ZTF-FCT
Zientzia eta Teknologia Fakultatea
Facultad de Ciencia y Tecnología

eman ta zabal zazu
Universidad del País Vasco
Euskal Herriko Unibertsitatea

Estudio de las estructuras cristalinas y de las transiciones de fase en nuevos materiales de wolframio ($Sr_2M^{2+}W^{6+}O_6$) y de antimonio ($A_2M^{3+}Sb^{5+}O_6$) con estructura de perovskita doble.

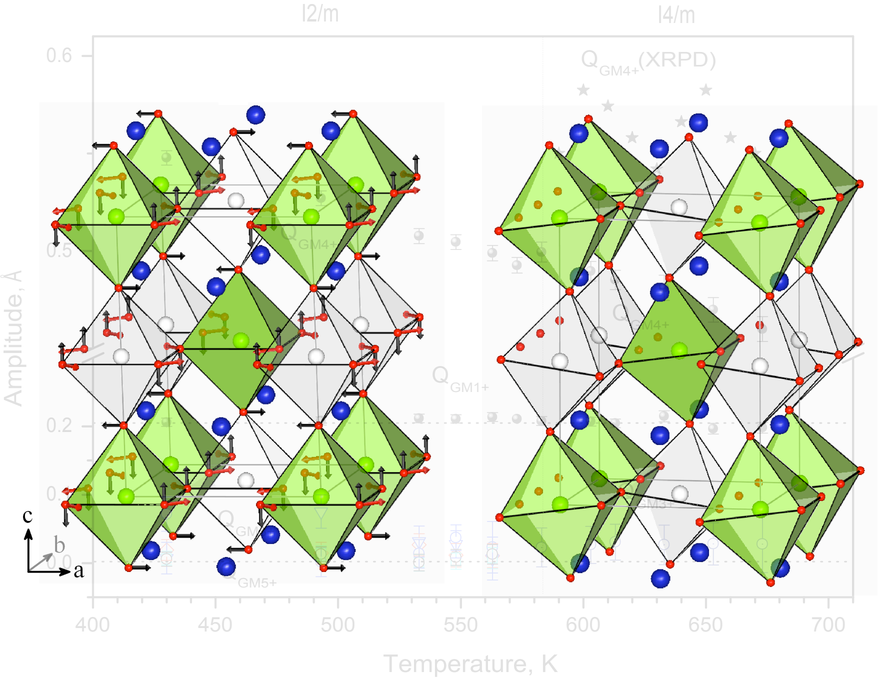
I2/m
I4/m
Q_{GM4+}(XRPD)
0.6
0.5
0.2
0
Amplitude, Å
Q_{GM4+}
Q_{GM1+}
GM5+
c
b
a
400
450
500
550
600
650
700
Temperature, K

Abdessamad FAIK

Memoria presentada para optar al grado de Doctor en Ciencias

Julio, 2009

ZTF-FCT
Zientzia eta Teknologia Fakultatea
Facultad de Ciencia y Tecnología

eman ta zabal zazu
Universidad del País Vasco
Euskal Herriko Unibertsitatea

Estudio de las estructuras cristalinas y de las transiciones de fase en nuevos materiales de wolframio ($Sr_2M^{2+}W^{6+}O_6$) y de antimonio ($A_2M^{3+}Sb^{5+}O_6$) con estructura de perovskita doble.

ABDESSAMAD FAIK

Director:
JOSU MIRENA IGARTUA ALDAMIZ

MEMORIA PRESENTADA PARA OPTAR AL GRADO DE DOCTOR EN CIENCIAS

Julio, 2009

a mi esposa Fadwa
a mis padres
a toda mi familia

Agradecimientos

La elaboración de una tesis doctoral no puede ser llevada a cabo en solitario. Afortunadamente, existen muchas personas a tu alrededor que de manera directa o indirecta contribuyen a la realización del trabajo. Por eso, hay distintas personas que merecen mucho más que un simple agradecimiento, porque sin ellas el presente trabajo no habría sido posible.

En el primer lugar, quiero manifestar la suerte de haber contado con *Josu M. Igartua Aldamiz* director de este trabajo y de la buena relación que nos ha acompañado durante todos estos años. Quiero expresar mi profundo agradecimiento por sus múltiples enseñanzas, buenos consejos, su ayuda, confianza y incontable tiempo dedicado durante estos años.

Al *Pr. Juan Manuel Pérez-Mato*, gracias por la cálida acogida en el grupo de investigación, y por concederme una beca de estudios predoctorales.

Al *Pr. Mois Aroyo* por sus apoyos y su ayuda en muchas ocasiones.

Al *Dr. Milen Gatheshki*, por su ayuda siempre a resolver los problemas en el mundo de las perovskitas dobles.

Al *Dr. Gabriel Cuello* por su ayuda en las medidas de neutrones en Grenoble.

Mes remerciements vont également à *Pr. Catherine Bessada*, pour avoir acceptée de faire partie de jury et apportée un regard critique sur ce travail.

A todos los profesores del grupo *Gotzon Madariaga*, *Iñigo Etxebarria*, *Tomasz Breczewski*, *Javier Zúniga*, *Andrzej Grzechnik*, *Karen Fariese*, *Luis Elcoro* y todos los demás profesores y funcionarios de los departamentos de Física Aplicada II y Física de la Materia Condensada.

Al *Dr. José Luis Pizarro*, por su trato, y por su bien hacer y colaboración con los experimentos de difracción de Rayos X.

A las *Dra. Maite Insausti* y *Dra. Izaskun Gil* por sus ayudas en la utilización de los diferentes equipos del laboratorio de química.

A los *Dr. Bouchaib Manoun*, *Dr. Said Benmoukhtar* y *Dr. Abdeslam El Bouari* por estar siempre dispuestos a apoyarme.

A *Irene* y *Edurne*, gracias por participar de manera directa en la realización del trabajo y por el buen tiempo que hemos compartido con Josu en diferentes sitios en el mundo (menos el tiempo duro a Castellón).

A mis compañeros con quines he tenido el placer de compartir muchos momentos de estos años (en orden alfabético): César, Danel, David, Edurne, Fermín, Irene, Jon, Josu, Josue, Leire, Luis, Mariano, Miguel, Nerea, Pablo(2), Raúl, Santi, Txema, Unai(2) y Urko(up25).

El trabajo de tesis doctoral, en parte resumido en la presente memoria, se ha realizado utilizando diferentes recursos (humanos, informáticos, económicos, de instalaciones, de equipamiento) de los departamentos de Física Aplicada II, Física de la Materia Condensada y Química Inorgánica de la Facultad de Ciencia y Tecnología de la Universidad del País Vasco/Euskal Herriko Unibertsitatea (UPV/EHU), así como de los Servicios Generales (SGIker) de la Universidad del País Vasco/Euskal Herriko Unibertsitatea (UPV/EHU).

Los laboratorios y servicios utilizados han sido los siguientes:

◇ Laboratorio de síntesis y crecimiento del departamento de Química Inorgánica: reactivos, material de laboratorio desechable, hornos etc.

◇ Laboratorio de difracción de rayos X del departamento de Física de la Materia Condensada.

◇ Laboratorios de difracción de rayos X de los Servicios Generales (SGIker)

El trabajo resumido en la presente memoria se ha realizado en un periodo de cuatro años: desde octubre de 2005, hasta julio de 2009.

Finalmente, el trabajo resumido en la presente memoria se ha financiado, casi en su totalidad, mediante dos proyectos de investigación:

◇ Grupos consolidados y de alto rendimiento

  Entidad financiadora: UPV/EHU (UPV 0063.310-13564/2001)

  Duración: 01/2001 hasta 01/2004 con sucesivas prórrogas anuales hasta hoy.

  Investigador responsable: *J.M. Pérez Mato*

  De este proyecto he recibido la beca predoctoral que me ha permitido realizar la tesis.

◇ Estructura cristalinas y propiedades de materiales funcionales en condiciones no ambientales

  Entidad financiadora: Ministerio de Ciencia y Tecnología (FIS2005-07090)

  Duración: 11/2005 hasta: 09/2008

  Investigador responsable: *A. Grzechnik*

Organización de la memoria

La presente memoria, que resume parte del trabajo, realizado durante los últimos cuatro años, que constituye mi tesis doctoral, se ha estructurado teniendo en cuenta que se ha realizado un estudio estructural y de las transiciones de fase similar pero en dos familias de materiales. Así, se ha dividido en cuatro partes:

(I) Primera parte: Introducción, Química Preparativa y Técnicas Experimentales

(II) Segunda parte: Familia del wolframio, Sr_2MWO_6

(III) Tercera parte: Familia del antimonio, A_2MSbO_6

(IV) Cuarta parte: Conlusiones, Trabajo futuro y Bibliografía

En la primera parte, a su vez subdividida en tres apartados, se describen los aspectos comunes a las dos familias analizadas. En el capítulo de introducción se repasan, si bien de una manera sucinta, las características principales de las perovskitas dobles, así como de las simples. Se hace especial hincapié en lo que se conoce como las distorsiones de las perovskitas dobles, que no son si no las configuraciones, que surgen por diversas razones, *distorsionando* la estructura prototipo cúbica de las perovskitas dobles.

En este punto quisiera subrayar que como novedad se describen las distorsiones usando la notación *clásica*, de Glazer, simplemente para relacionarlas con la notación más moderna, y que hemos empezando utilizar en los últimos trabajos publicados (el cambio se apreciará en las publicaciones), y más precisa, desde el punto de vista de la teoría de grupos, y que hace uso de los modos adaptados a la simetría.

Los procesos de preparación de las perovskitas dobles merecen un capítulo aparte, sobre todo, porque la ruta de preparación influye, por ejemplo, como se verá, en el grado de orden final que presentan los materiales. Así, en muchos casos se ha utilizado el método cerámico, pero en algunos otros se han ensayado otros métodos, que a la postre han resultado más convenientes.

Para terminar esta parte, en el apartado Técnicas Experimentales se describen, primero, los métodos y las técnicas utilizadas, y a continuación, el tipo de medidas que se han realizado. Este apartado es importante puesto que el trabajo recogido en la presente memoria es eminentemente experimental, y, por lo tanto es necesario conocer bien el método, la técnica y el tipo de medidas, así como sus características, para saber interpretar adecuadamente los resultados.

A continuación, en las partes dos y tres se recogen los resultados obtenidos en las familias de wolframio y de antimonio, respectivamente. Estas dos partes se han estructurado de la misma manera, conforme a los artículos publicados, en casi todos los casos, o por publicar, pero enviados, en el caso de los dos últimos trabajos de materiales de la familia del antimonio. (En el anexo de la memoria, en documento aparte, se recogen íntegramente los artículos.)

Cada una de las partes consta de un capítulo de introducción en el que se plantean los problemas y las motivaciones que han impulsado la realización del trabajo. Además, en esta misma parte introductoria, se recogen los datos previos conocidos sobre los materiales estudiados, tales como las estructuras a temperatura ambiente, o a altas y bajas temperaturas, las posibles propiedades físicas etc, simplemente para situar al lector en el punto de partida del trabajo. Esta introducción está escrita en castellano. A continuación, y por cada trabajo publicado, se presenta un capítulo con los resultados y la discusión de los mismos, junto con las conclusiones. Estos capítulos están escritos en inglés. Para esto hay dos razones. La principal, que el tribunal acceda fácilmente a la información, por un lado, y por otro, para facilitar mi incorporación a un puesto posdoctoral. Además, también se ha hecho así para aprovechar la estructura en artículos del trabajo realizado.

Finalmente, en la última parte se han resumido las Conclusiones Generales del trabajo y la Bibliografía utilizada. En este caso, tengo que decir que para facilitar el acceso a las referencias, éstas se han recogido según han ido apareciendo y una única vez por cada capítulo; pero, cuando aparecen en otro capítulo, se vuelven a recoger en éste.

Solo espero que el lector de la memoria encuentre no sólo su estructura adecuada, si no que así mismo estime que el trabajo recogido es coherente, está bien redactado y explicado, y sobre todo, está bien realizado.

Índice general

Indice general 1

I Introducción General 1

1. Introducción 3

1.1. Las perovskitas 3

1.2. Perovskitas dobles 5

1.3. Distorsiones de la estructura perovskita 7

1.4. Transiciones estructurales y distorsiones de la estructura tipo perovskita (I): *coordenadas atómicas* 11

1.5. Transiciones estructurales y distorsiones de la estructura tipo perovskita (II): *modos adaptados a la simetría* 15

1.6. Interés y Objetivos 26

2. Técnicas experimentales y equipos utilizados 29

2.1. Medidas de difracción de rayos X en muestras policristalinas 29

2.1.1. Rayos-X convecionales 30

2.1.2. Radiación sincrotrón 32

2.2. Medidas de difracción de neutrones en muestras policristalinas 32

2.3. Refinamiento de Rietveld 33

2.4. Espectroscopia de Resonancia paramagnética electrónica (RPE) 34

2.5. Espectroscopía de absorción de rayos X (XAS) 35

2.6. Espectroscopia Raman 36

3. Química preparativa **37**

3.1. Perovskitas dobles de tungsteno de fórmula general Sr_2MWO_6. 37

3.1.1. Sr_2CdWO_6 37

3.1.2. Sr_2MnWO_6 38

3.1.3. $Sr_2Cd_{1-x}Ca_xWO_6$ $(0 \leq x \leq 1)$ 39

3.2. Perovskitas dobles de antimonio de fórmula general $A_{2-x}A'_xMSbO_6$ 40

3.2.1. Sr_2AlSbO_6 40

3.2.2. $A_{2-x}A'_xMSbO_6$ 41

II Estructuras cristalinas y transiciones de fase en la familia de wolframio $Sr_2M_{1-x}M'_xWO_6$ **43**

4.1. Introducción 45

4.2. Sr_2CdWO_6 47

4.3. $Sr_2Cd_{1-x}Ca_xWO_6$ 48

4.4. Sr_2MnWO_6 48

5. Crystal structure and phase transitions of Sr_2CdWO_6 **51**

5.1. Results and discussion 51

5.2. Conclusions 57

6. Synthesis, Structures and Temperature-induced Phase Transitions of the $Sr_2Cd_{1-x}Ca_xWO_6$ $(0 \leq x \leq 1)$ Double Perovskite Tungsten Oxides **59**

6.1. Results and Discussion 59

6.1.1. Room-temperature structures 59

6.1.2. High-temperature structures and phase transitions 64

6.2. Conclusions 66

7. Crystal structures and temperature-induced phase transitions of $Sr_2Mn^{2+}W^{6+}O_6$, and of its transformation to $Sr_2Mn^{3+}W^{6+}O_{6+\delta}$ 69

7.1. Results and Discussion 69

7.1.1. Room-temperature structures 69

7.1.2. High-temperature phase transitions 76

7.2. Conclusions 80

III Estructuras cristalinas y transiciones de fase en la familia de antimonio AA′MSbO$_6$ 83

8.1. Introducción 85

9. Crystal Structures and Cation Ordering of Sr_2AlSbO_6 and Sr_2CoSbO_6 89

9.1. Introduction 89

9.2. Room-temperature Structure of Sr_2AlSbO_6 and
low-temperature Raman spectroscopy data 91

9.3. Room-temperature Structure of Sr_2CoSbO_6 92

9.4. High-temperature phase-transition in Sr_2CoSbO_6 98

9.5. Conclusions 100

10. Crystal Structures and phase transitions of Sr_2CrSbO_6 101

10.1. Results and Discussion 101

10.1.1. Room-temperature structure 102

10.1.2. Temperature-induced phase transitions: low- and high-temperatures 107

10.2. Conclusions 113

11. Crystal structures and high-temperature phase transitions of the new ordered double perovskites Sr_2SmSbO_6 and Sr_2LaSbO_6 115

11.1. Introduction 115

11.2. Room-temperature Structures of Sr_2SmSbO_6 and Sr_2LaSbO_6 116

11.3. High-temperature phase-transitions in Sr_2SmSbO_6 and Sr_2LaSbO_6 121

11.4. Conclusions 125

12. Cationic ordering and role of the A-site cation on the structure of the new double perovskites $Ca_{2-x}Sr_xLaSbO_6$ and $Ca_{2-x}Sr_xSmSbO_6$ $(x = 0, 0.5, 1)$ 127

12.1. Introduction 127

12.2. Room-temperature Crystal Structures 128

12.2.1. Ca_2LaSbO_6 and Ca_2SmSbO_6 128

12.2.2. $Ca_{2-x}Sr_xLnSbO_6$ (Ln=La,Sm) and $(x = 0.5, 1.0)$ 132

12.3. High-temperature phase-transitions in $Ca_{2-x}Sr_xLnSbO_6$ (Ln=La,Sm) and $(x = 0, 0.5, 1)$ 136

12.4. Conclusions 138

13. A study of the crystal structures and the phase transitions of the ordered double perovskites Sr_2ScSbO_6 and Ca_2ScSbO_6 139

13.1. Introduction 139

13.2. Room temperature crystal structures of Sr_2ScSbO_6 and Ca_2ScSbO_6 140

13.3. High-temperature x-ray diffraction of Sr_2ScSbO_6 and Ca_2ScSbO_6 151

13.4. Conclusions 159

14. A study of the crystal structures and the phase transitions of Sr_2FeSbO_6, $SrCaFeSbO_6$ and Ca_2FeSbO_6 double perovskite oxides 161

14.1. Introduction 161

14.2. Sr_2FeSbO_6 162

14.3. $SrCaFeSbO_6$ 169

14.4. Ca_2FeSbO_6 170

14.5. Conclusions 172

15. A study of the crystal structures and the phase transitions of Sr_2MSbO_6 (M=Al,Co,Cr,Ga,Mn,Fe,Sc,Sm,La) double perovskite oxides 173

15.1. Introduction 173

15.2. Results and Discussion 174

15.3. Sr_2GaSbO_6 174

15.4. Sr_2MnSbO_6 179

15.5. Cation ordering of Sr_2MSbO_6 (M=Al,Co,Cr,Ga,Mn,Fe,Sc,Sm,La) 183

15.6. Phase transition of Sr_2MSbO_6 (M=Al,Co,Cr,Ga,Mn,Fe,Sc,Sm,La) 183

15.7. Conclusions 186

IV Conlusiones y Trabajo Futuro 187

Conclusiones 189

Publicaciones 201

Resumen 203

Estudio de las estructuras cristalinas y de las transiciones de fase en nuevos materiales de wolframio ($Sr_2M^{2+}W^{6+}O_6$) y de antimonio ($A_2M^{3+}Sb^{5+}O_6$) con estructura de perovskita doble.

Memoria presentada por **Abdessamad Faik** para optar al grado de Doctor en Ciencias

Director: Josu M. Igartua Aldamiz

Parte I

Introducción General

Capítulo 1

Introducción

> *The perovskites have a habit of doing the unexpected.*
>
> A.M. Glazer

1.1. Las perovskitas

Los materiales que responden actualmente al nombre de "perovskitas" constituyen una extensa familia de compuestos cristalinos inorgánicos. Su nombre se deriva del mineral $CaTiO_3$, que presenta la estructura cristalina básica (perovskita simple) a la cual son análogas las estructuras de los compuestos pertenecientes a la mencionada familia. Este mineral se describió por primera vez en 1939, por el geólogo alemán Gustav Rose. En un acto que le dignifica, el profesor Rose decidió dedicar su descubrimiento al gran mineralogista ruso *Count Lev Alekeseevich Von Perovskii*.

La estructura ideal de una perovskita simple (ABX_3) es cúbica, con el grupo espacial $Pm\overline{3}m$ (N° 221) [1, 2]: se representa en la Figura 1.1. En ella se puede apreciar la coordinación cubo-octaédrica de los cationes A (12 vecinos próximos en la primera esfera de coordinación), y el entorno octaédrico de los cationes B. Los aniones X están coordinados, también, por 6 cationes: cuatro A y dos B).

Muchas perovskitas se consideran compuestos iónicos, de manera que en una primera aproximación los cationes que las constituyen se pueden tratar como esferas de radio iónico r. De esta forma, es posible predecir, por ejemplo, un parámetro de celda a_p=4.01Å para la perovskita $SrTiO_3$ utilizado los radios iónicos establecidos por R. D. Shannon [3], que es un valor muy próximo al determinado experimentalmente: a_p=3.905Å [4].

Muchos óxidos de perovskitas dobles se conocen desde los años 50 y 60. Los estudios sobre estos materiales han adquirido una especial relevancia desde que en 1998 fue descubierta la magnetorresistencia colosal en el compuesto Sr_2FeMoO_6 [5]. Desde entonces, se ha producido un aumento constante de trabajos dedicados a diferentes aspectos (estructura, propiedades magnéticas y dielécticas) de las perovskitas. Otras propiedades importantes que se han encontrado en perovskitas dobles son, por ejemplo, superconductividad en $Sr_2YRu_{0.95}Cu_{0.05}O_6$ [6] o ferroelectricidad en Pb_2CoWO_6 [7, 8]. Estas propiedades cambian mucho de un material a otro, sin que se observen grandes diferencias en la estructuras, aunque se ha observado experimentalmente un correlación entre las propiedades físicas y las estructuras y los cambios de estructura producidos en las transiciones de fase.

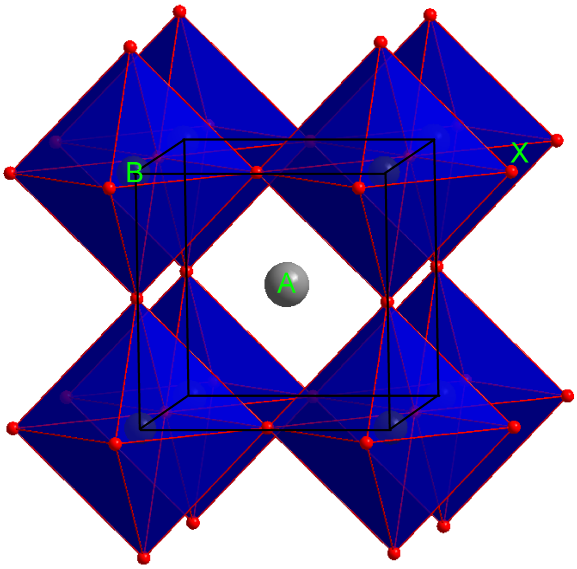

FIGURA 1.1: Representación esquemática de la estructura perovskita ABX_3. La estructura está formada por octaedros BX_6 interconectados a través de los aniones X; los cationes B están en los centros de los octaédros (sitios B); los aniones X, en los vértices de aquellos; y los cationes A ocupan los espacios intersticiales (sitios A) entre los octaédros.

Los cambios de las propiedades físicas son especialmente importantes cuando varían las condiciones externas, como la temperatura o la presión. Un ejemplo conocido es el compuesto $BaTiO_3$, cuya constante dieléctrica aumenta en un factor de 10^4 por encima de 380K. Generalmente, estos cambios ocurren en conexión con transiciones de fase, en los que la estructura cristalina cambia de forma continua o discontinua. Para comprender el comportamiento de las propiedades físicas en las proximidades de las transiciones de fase, es necesario conocer los cambios estructurales que se producen en cada material concreto.

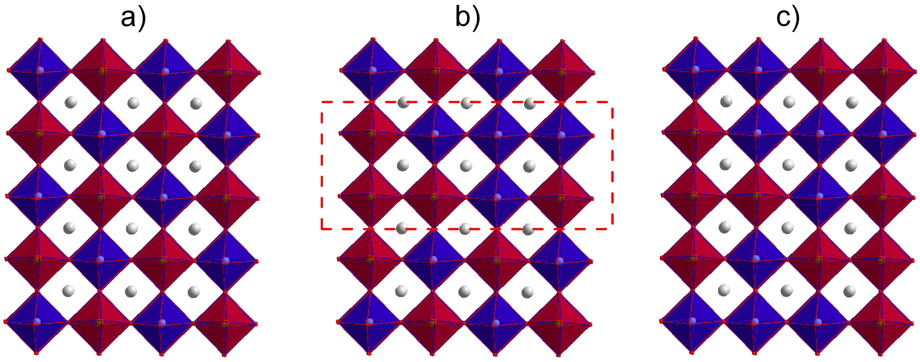

FIGURA 1.2: Representación esquemática de la estructura de la perovskita doble $A_2BB'X_6$: (a) completamente ordenada, (b) parcialmente ordenada y (c) completamente desordenada.

1.2. Perovskitas dobles

Desde el punto de vista cristalográfico, las perovskitas dobles, con fórmula general $A_2BB'O_6$, poseen una estructura similar a la de las perovskitas simples: la particularidad de las perovskitas dobles es que el sitio B es compartido por dos cationes, B y B′ en la proporción 1:1. Estos cationes, idealmente, se ordenan alternativamente en las tres direcciones del espacio (Figura 1.2(a)). Es común la existencia de defectos catiónicos en los que un catión B(B′) ocupa un sitio B′(B), en lo que se denomina un *antisite*. En la Figura 1.2(b) y la Figura 1.2(c) se muestran algunos esquemas que ilustran la presencia de este defecto en diferentes estructuras de perovskita doble: parcialmente ordenada, en la Figura 1.2(b), y totalmente desordenada, en la Figura 1.2(c). El grado de orden entre los cationes B y B′ depende de las diferencias de radio iónico, del estado de oxidación y de los potenciales de ionización de ambos. Por otro parte, como vamos a demostrar en este trabajo, es posible controlar la cantidad de *antisites* mediante una adecuada elección del protocolo de síntesis: se obtienen muestras con mayor grado de orden para procesos de síntesis a más alta temperatura.

La cantidad de *antisites* se suele cuantificar mediante la relación:

$$AS(\,\%) = \frac{\neq \text{cationes B en B}'}{\neq \textit{total} \text{ cationes B y B}'} \cdot 100 = \frac{\neq \text{cationes B}' \text{ en B}}{\neq \textit{total} \text{ cationes B y B}'} \cdot 100$$

Donde el número de cationes B en B′ puede ser extraído, al refinar mediante el método de Rietveld, de los factores de ocupación de las posiciones de Wyckoff correspondientes.

Compuestos ordenados, o parcialmente ordenados, se han observado sólo para el grupo de los óxidos (X=O); los materiales con otros cationes (F, Br, Cl, CN_6) se han encontrado siempre ordenados [9].

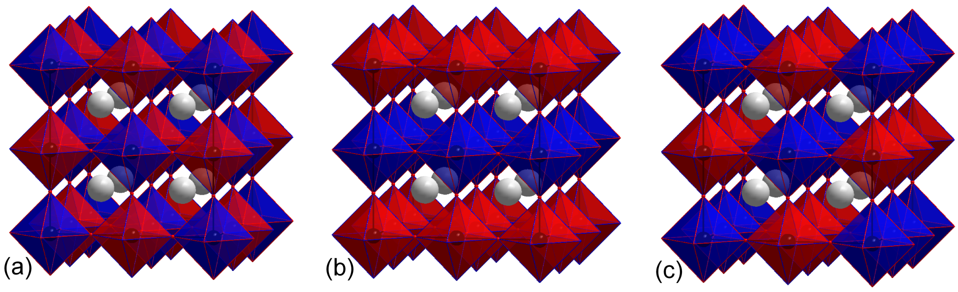

FIGURA 1.3: Representación esquemática de la estructura de perovskita doble ordenada $A_2BB'X_6$ (a). Teóricamente se han estudiado, también, otros tipos de ordenamientos: en planos (b) o en filas (c).

Los dos tipos de cationes B de los compuestos ordenados se distribuyen de manera similar a la que existe en la estructura del cloruro sódico (NaCl): los octaedros BX_6 comparten sus vértices con seis octaedros $B'X_6$ (Figura 1.3(a)). Esta estructura se conoce como perovskita doble ordenada o *elpasolita* (por el nombre del mineral K_2NaAlF_6); y la estructura arquetipo (sin distorsiones de ningún tipo) tiene la simetría del grupo espacial cúbico $Fm\overline{3}m$ (N° 225).

Aunque también se han estudiado teóricamente [10] otros tipos de ordenamientos (Figura 1.3(b) y 1.3(c)), todavía no se conocen compuestos que tengan los cationes distribuidos de esas maneras. La única excepción es el compuesto La_2CuSnO_6 [11], que tiene un ordenamiento como el que se muestra en la Figura 1.3(b). Se conocen, también, compuestos del tipo perovskita doble ordenada en el que los cationes B y B′ son del mismo elemento químico, pero se encuentran en diferentes estados de oxidación, por ejemplo: $Y_2Ni^{3-\delta}Ni^{3+\delta}O_6$ [12] y $Ba_2Bi^{3+}Bi^{5+}O_6$ [13].

También se han estudiado compuestos (óxidos de perovskita doble) en los que el catión A se sustituye por dos cationes de dos especies químicas (elementos) diferentes: A y A′, $AA'BB'O_6$. En todos los ejemplos que conocemos, los cationes A y A′ están distribuidos de forma desordenada en los sitios A de la estructura perovskita.

En [14] se han recopilado datos sobre más de 290 perovskitas dobles. De éstas, alrededor de 44 se han encontrado como desordenadas, y el resto como ordenadas. Una de las conclusiones del mencionado trabajo es que el factor más importante para el ordenamiento de los cationes es la diferencia de carga entre los cationes de tipo B. Así, todos la compuestos con diferencia de carga mayor o igual a 4 (por ejemplo, $B^{2+}B'^{6+}$, $B^{1+}B'^{6+}$ o $B^{1+}B'^{7+}$) están ordenados. Los compuestos con diferencia de carga igual a 3, puede decirse que también son siempre completamente ordenados, ya que el único compuesto con esta diferencia que se consideraba desordenado era $SrLaCu^{2+}Ru^{5+}O_6$, y recientemente [15], se ha demostrado que este material también esta ordenado.

En el grupo de las perovskitas dobles se pueden incluir los compuestos criolitas, con fórmula general A_3BO_6, en los que los cationes que ocupan los sitios B′ son del mismo elemento químico que los ocupan los sitios A.

La estructura de algunos de los compuestos con fórmula general $BB'X_6$ también se puede representar como una red tridimensional de octaedros BX_6 y $B'X_6$ interconectados, a través de los aniones X, y ordenados; pero, en este caso, los sitios A están sin ocupar (estructura de tipo ReO_3).

Mientras que las propiedades eléctricas y magnéticas de las perovskitas dobles se han estudiado ampliamente, las propiedades estructurales de estos materiales se han estudiado relativamente menos, solo hasta hace pocos años. Una de las razones de esto es la fuerte pseudosimetría cúbica que presentan estos materiales. Así, para obtener datos estructurales fiables, se necesitan tanto muestras de muy beuna calidad (con un buen grado de cristalización y baja cantidad de impurezas), como medidas de difracción de alta resolución. Una dificultad adicional para la determinación precisa de la estructura es el hecho de que rara vez se hayan crecido monocristales de estos materiales [16, 17]. De esta manera, la mayor parte de la información estructural se ha obtenido a partir de datos de difracción de muestras policristalinas.

En muchos casos, la resolución estructural se complica por la presencia de un desorden parcial, como ya se ha mencionado, de los cationes B y B′ y/o una deficiencia de oxígeno. Por ejemplo, en [18] se ha demostrado cómo una deficiencia de oxígeno de aproximadamente el 8 % en la estructura de Sr_2CoSbO_6 provoca que ésta cambie de una simetría trigonal a una cúbica. Otra dificultad es la poca sensibilidad de la difracción de rayos X a las posiciones de los átomos de oxígeno que, a menudo, no permite determinar la estructura con precisión; y, en muchos casos, la simetría propuesta está sobreestimada o mal asignada. En este sentido, es significativo el caso del compuesto Sr_2FeMoO_6. Para su estructura a temperatura ambiente, diferentes autores han propuesto cuatro grupos espaciales distintos: $I4/mmm$ [17], $I4/m$ [19], cúbica [20] (los autores mencionan que la técnica de síntesis utilizada puede modificar la estructura final) y $P4_2/m$ [21]. Estas dificultades, relacionadas con la determinación de la estructura de las perovskitas dobles, pueden explicar por qué no se ha dedicado la atención necesaria a las transformaciones estructurales presentes en estos materiales.

La importancia del estudio de las transiciones de fase estructurales para la comprensión de las propiedades de los óxidos con estructura del tipo perovskita doble se puede demostrar utilizando, de nuevo, como ejemplo el caso del compuesto Sr_2FeMoO_6 [19, 22]. En éste se ha encontrado una coincidencia entre la temperatura de la transición de fase estructural (de una fase tetragonal a una cúbica), la temperatura de la transición aislante-metal y la temperatura de Curie.

1.3. Distorsiones de la estructura perovskita

Aunque la estructura ideal de las perovskitas, tanto simples como dobles, es cúbica (grupos espaciales $Pm\bar{3}m$ y $Fm\bar{3}m$, respectivamente), las estructuras reales, a menudo, presenten diferentes distorsiones. (En este sentido, es significativo que el propio mineral perovskita, $BaTiO_3$, presenta, a temperatura ambiente, una estructura distorsionada con el grupo espacial *Pnma*.) En la mayoría de los casos, las distorsiones se deben a rotaciones (inclinaciones: *tilts*) de los octaedros.

Generalmente, en el caso de las perovskitas simples, se considera que una estructura distorsionada se puede observar cuando la longitud del enlace A$-$O es menor que $\sqrt{2}$ veces la longitud del enlace B$-$O. Una estimación cuantitativa de este efecto se puede conseguir utilizando el *factor de tolerancia*: t. Este factor fue introducido por Goldschmidt en 1926. La premisa de partida consiste en asumir que la estructura perovskita es puramente iónica y que los átomos son esferas que encuentran en contacto entre sí, estando cada una de ellas caracterizada por un radio iónico medio (r_i). De este modo, el factor de tolerancia se define, en el caso de una perovskita simple (ABO_3), de la siguiente manera:

$$t = \frac{r_{\mathrm{A}}+r_{\mathrm{O}}}{\sqrt{2}(r_{\mathrm{B}}+r_{\mathrm{O}})}$$

y, para sistemas más complejos como las perovskitas dobles ($AA'BB'O_6$), como sigue:

$$t = \frac{\frac{r_{\mathrm{A}}+r_{\mathrm{A}'}}{2}+r_{\mathrm{O}}}{\sqrt{2}(\frac{r_{\mathrm{B}}+r_{\mathrm{B}'}}{2}+r_{\mathrm{O}})}$$

Recientemente, se ha introducido [23] el factor de ajuste (*fitting factor*):

$$\Phi = \frac{\sqrt{2}r_{\mathrm{A}}}{\frac{r_{\mathrm{B}}+r_{\mathrm{B}'}}{2}+r_{\mathrm{O}}}$$

que, según los autores, describe mejor el desajuste entre el catión A y el espacio cuboctaédrico entre los octaedros BO_6 y $B'O_6$.

Si se toman como base los radios calculados por R.D. Shannon [3], se predice que sólo se obtendrá una perovskita cúbica ideal cuando $t = 1$. De este modo, para factores $t < 1$, se pueden observar estructuras distorsionadas (ortorrómbicas o tetragonales). En algunos casos, se han observado estructuras hexagonales para $t > 1$.

El primer estudio sobre las modificaciones de las estructuras de las perovskitas simples fue realizado por A.M. Glazer [24, 25]. Sus premisas fueron que la estructura perovskita simple (ABX_3) está constituida por octaedros rígidos e iguales; y que las estructuras distorsionadas se pueden describir en términos de inclinaciones de estos octaedros alrededor de los ejes cúbicos de la estructura arquetipo, cúbica, con grupo espacial $Pm\overline{3}m$. Glazer describió estas inclinaciones utilizando símbolos del tipo $a^{\sharp}b^{\sharp}c^{\sharp}$: las letras se refieren a las inclinaciones alrededor de las direcciones [100],[010] y [001] de la estructura cúbica. El símbolo $\sharp$ puede tener los valores 0, $+$ ó $-$, y su significado es el siguiente:

- ◇ 0, los octaedros no tienen inclinaciones alrededor del eje correspondiente.
- ◇ +, las inclinaciones de dos octaedros sucesivos tienen magnitudes iguales, y se producen en el mismo sentido.
- ◇ –, las inclinaciones de dos octaedros sucesivos tienen magnitudes iguales, pero se producen en sentido contrario.

Las letras se repiten para indicar que las inclinaciones son las mismas alrededor de los diferentes ejes cúbicos.

Una restricción del modelo de Glazer es que no tiene en cuenta posibles casos con inclinaciones $+$ y $-$ alrededor del mismo eje. Existen modelos alternativos [26] que sí permiten estas inclinaciones "combinadas", pero que también tienen sus limitaciones. La existencia de inclinaciones $+$ y $-$ alrededor del mismo eje se puede representar, también, como inclinaciones con diferentes magnitudes de los octaedros sucesivos.

Glazer encontró 23 tipos de posibles inclinaciones de los octaedros. Después, mediante simple inspección de las estructuras, asignó un grupo especial a cada uno de estos tipos de posibles inclinaciones: encontró 15 grupos espaciales diferentes. Esta clasificación ha sido objeto de discusiones durante años, pero se sigue utilizando hasta el día de hoy. Uno de los problemas (ver más adelante) de esta clasificación, y sus posibles alternativas, es que los materiales reales presentan sólo algunos de los posibles sistemas de inclinaciones. En el trabajo [27] se afirma que, para 8 de los sistemas de inclinaciones de Glazer, no se conocen ejemplos de compuestos reales que los presenten.

En lo que refiere al esquema de clasificación de las distorsiones en perovskitas simples, un avance importante ha sido el trabajo de Howard y Stokes [28], en el que, basándose en consideraciones de teoría de grupos, se reduce de 23 a 15 el número de posibles grupos espaciales. Para conseguirlo, los autores han identificado las representaciones irreducibles que corresponden a los sistemas de inclinaciones de los tipos $+$ y $-$; éstas son: $M_3^+ \oplus R_4^+$. Estos subgrupos representan todos los posibles sistemas de inclinaciones (25 en total) que se pueden obtener como combinaciones lineales de las seis inclinaciones básicas (inclinaciones $+$ y $-$ en torno a los tres ejes cúbicos). El paso final ha consistido en eliminar todos los subgrupos que permiten la existencia de inclinaciones $+$ y $-$ alrededor del mismo eje. Mediante este método se ha conseguido verificar las asignaciones de los grupos espaciales para todos los sistemas de inclinaciones; y eliminar algunos sistemas que, en realidad, no representan inclinaciones nuevas, sino que son casos especiales de otras. Por ejemplo, se ha eliminado el sistema $a^0b^+b^-$ que tiene el grupo espacial $Cmcm$. Este mismo grupo espacial tiene, también, el sistema $a^0b^+c^-$. Ya que en este grupo no existe un elemento de simetría que convierta las inclinaciones alrededor del eje y en inclinaciones alrededor del eje z, estas inclinaciones pueden ser sólo aproximadamente iguales. Esto significa que el sistema $a^0b^+b^-$ es un caso especial del $a^0b^+c^-$.

En 1997, Woodward [27] generalizó el esquema de clasificación de Glazer para el caso de los materiales con estructura de perovskita doble ordenada ($A_2BB'X_6$). Esta generalización consiste en encontrar un grupo espacial, para cada uno de los 23 tipos de posibles inclinaciones de Glazer, que permita el ordenamiento entre los cationes B y B′; y que, además, mantenga los octaedros no deformados. Se han encontrado 14 grupos espaciales diferentes.

Aparte de las inclinaciones de los octaedros, hay otros dos tipos de posibles distorsiones de las estructuras perovskitas dobles: deformación de las unidades octaédricas y desplazamientos de los cationes B. Estas modificaciones llevan, en general, a grupos espaciales que no están presentes en el esquema de Woodward. Éste es el caso, por ejemplo, de Ba_2CuWO_6 [29] y Sr_2MnSbO_6 [30], para los que se han propuesto los grupos espaciales $I4/mmm$ y $I4mm$, respectivamente. En estos dos compuestos, la presencia de los cationes Cu^{2+} y Mn^{3+}, que son activos para el efecto Jahn-Taller [31, 32], causa fuertes distorsiones de sus respectivos octaedros.

Las estructuras perovskitas dobles en las que los cationes B están desplazados de sus posiciones de alta simetría pierden el centro de inversión y, en general, se pueden describir con uno de los subgrupos polares del grupo de Woodward correspondiente. Por ejemplo, a la estructura de Pb_2CoWO_6 de 235K, se le ha asignado el grupo espacial $P2_1cn$ (setting no estándar de $Pna2_1$, N° 33) [7], en vez del grupo centrosimétrico $Pmcn$ ($Pnma$). Esta asignación se debe a las propiedades ferroeléctricas que se han observado en este compuesto.

Aunque existen muchos posibles tipos de distorsiones polares de las estructuras perovskitas, tenemos que mencionar que en una clasificación de los óxidos no centrosimétricos [33], basada en una búsqueda en la Base de Datos de Estructuras de Cristales Inorgánicos (ICSD), se han encontrado compuestos con estructuras con grupos espaciales no centrosimétricos: Sr_2MnSbO_6, con simetría tetragonal y grupo espacial $I4mm$; Sr_2TmNbO_6, con simetría ortorrómbica y grupo espacial $P2nn$ (setting no estándar del grupo N° 34); y, finalmente, Ca_2CaWO_6, para el que, en [26], se ha propuesto la simetría ortorrómbica y grupo espacial $Pmm2$.

Estructuras que presentan inclinaciones de los octaedros y, también, desplazamientos de los cationes se han estudiado, por ejemplo, en [34, 35].

Finalmente, las estructuras con simetría hexagonal, como es el caso de los compuestos Ba_2CrTaO_6 [36] y Ba_2CrNbO_6 [37], tienen una disposición de los octaedros distinta, y no se pueden representar como fases perovskitas distorsionadas. En el caso de Ba_2CrNbO_6, se conoce una transición de la fase hexagonal a una fase cúbica, aplicando simultáneamente alta temperatura (930 °C) y alta presión (80 kbar).

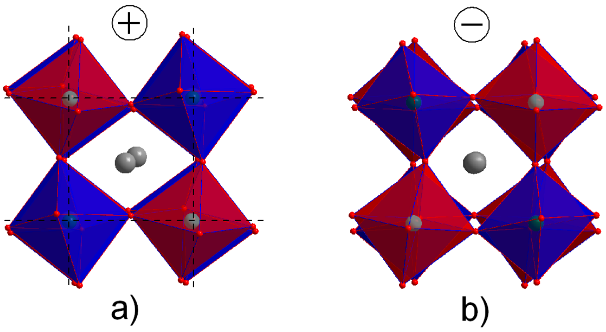

FIGURA 1.4: Inclinaciones de octaedros en perovskitas dobles ordenadas del tipo ⊕ (a); del tipo ⊖ (b).

1.4. Transiciones estructurales y distorsiones de la estructura tipo perovskita (I): *coordenadas atómicas*

En la práctica, se conocen muy pocos materiales (óxidos) con estructura, a temperatura ambiente (y presión atmosférica), de perovskita doble y simetría cúbica: la mayor parte de los óxidos que presentan este tipo de estructura se encuentran distorsionados a temperatura ambiente. Si pequeños desplazamientos en los cationes A y B causan fuertes cambios en las propiedades físicas de estos materiales, pequeños movimientos de los átomos de oxígeno en la red provocan el giro de los octaedros BO_6 y determinan la simetría final del compuesto. Los diferentes tipos de inclinaciones de los octaedros se representan en la Figura 1.4.

En [15] se ha llevado una revisión crítica de los estudios anteriores previos realizados sobre las posibles distorsiones estructurales presentes en las perovskitas y en las perovskitas dobles, y han propuesto las posibles transiciones estructurales entre todos tipos de estructuras distorsionadas. La Figura 1.5 muestra los 11 grupos espaciales que describen las diferentes distorsiones en estructuras tipo perovskita doble. En esta figura también se muestra las posibles transiciones de fase debidas a las inclinaciones de los octaedros.

Las líneas discontinuas representan las transiciones que tienen que ser de primer orden, según la teoría de Landau de transiciones de fase. Las líneas continuas representan que entre los dos grupos conectados es posible una transición de segundo orden. En la teoría de Landau, una transición de fase a un subgrupo particular puede ser continua, de según orden, si se cumplen las siguientes condiciones:

- ◇ Tiene que existir una relación grupo-subgrupo. También tiene que existir un *parámetro de orden primario*.

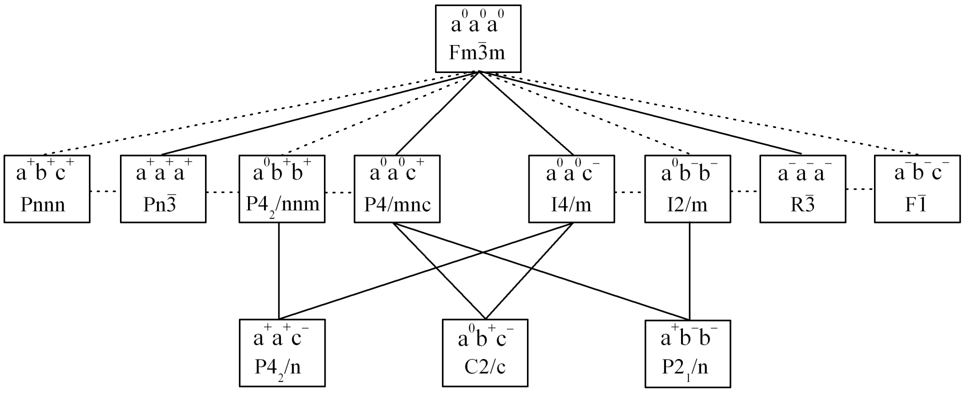

FIGURA 1.5: Posibles modificaciones de las estructuras de las perovskitas dobles, debidas a inclinaciones de los octaedros. Para cada modificación se muestran el símbolo del grupo espacial correspondiente y el tipo de inclinación. Las líneas discontinuas conectan los grupos espaciales entre los cuales sólo es posible una transición de fase de primer orden. Las líneas continuas representan algunas de las relaciones para las que transiciones de segundo orden están permitidas.

- ◇ El número de polinomios independientes de tercer orden en el desarrollo de la energía libre tiene que ser cero: condición de Landau.
- ◇ El número de veces que la representación vectorial aparece en el cubo antisimetrizado de la representación correspondiente al parámetro de orden tiene que ser cero: condición de Lifshitz.
- ◇ En la dirección del parámetro de orden debe existir un mínimo de la energía libre desarrollada hasta cuarto orden.

El resultado presentado en la Figura 1.5 tiene algunas características importantes:

- ◇ Contiene todos sistemas de inclinaciones observados experimentalmente. También contiene algunos que todavía no se han observado, tal como: $a^0b^+b^+$, $a^+b^+c^+$ ó $a^0b^+c^-$.
- ◇ Contiene algunas de las secuencias de transiciones de fase observadas en dobles perovskitas dobles: por ejemplo,

$$P2_1/n \rightarrow I2/m \rightarrow R\bar{3} \rightarrow Fm\bar{3}m$$

observada en $Ba_2Bi^{3+}Bi^{5+}O_6$ [38],

$$P2_1/n \rightarrow I2/m \rightarrow I4/m \rightarrow Fm\bar{3}m$$

observada en Cs_2RbDyF_6 [9]. En la Figura 1.6 se muestra este esquema ampliado. Para facilitar la comprensión de las rotaciones, se ha indicado el sentido de giro de los octaedros con los signos $\oplus$, $\ominus$ y ⊚,

$$P2_1/n \rightarrow P4/mnc \rightarrow Fm\bar{3}m$$

observada en $Cs_2LiCr(CN)_6$ [39]. Sin embargo, este esquema no incluye la transición directa $P2_1/n \rightarrow I4/m$, observada en muchos compuestos [9]

◇ El número de posibles sistemas de inclinaciones, en el caso de las perovskitas dobles, se ha reducido de 23 (que corresponden a 14 grupos espaciales) [27] a 12 (12 grupos espaciales). Los grupos que se han eliminado son: $P\bar{1}$ y $P2/c$, ya que estos dos grupos admiten inclinaciones del tipo $\pm$.

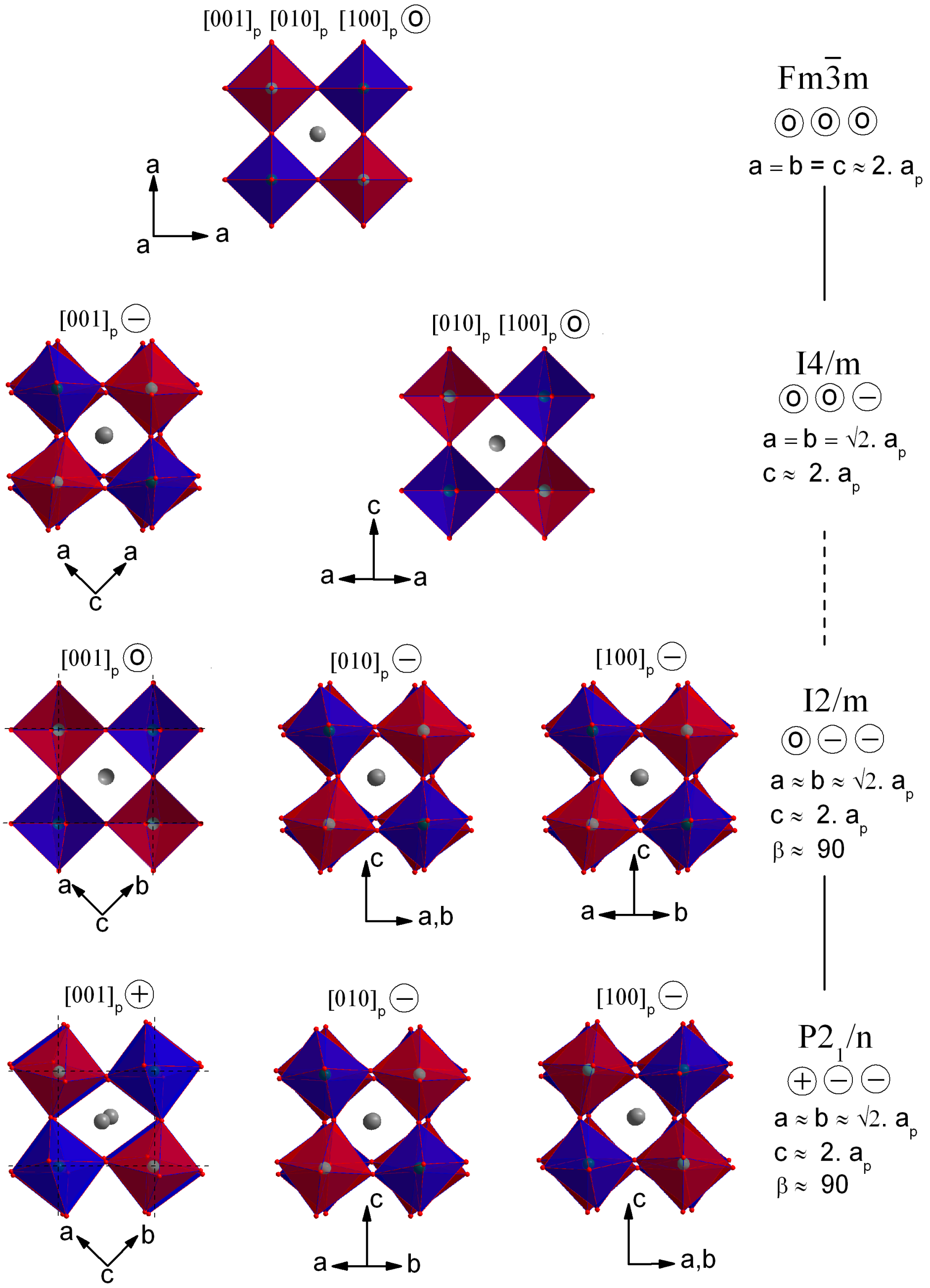
[001]p [010]p [100]p ⓞ
a
a
a
Fm3̄m
ⓞ ⓞ ⓞ
a = b = c ≈ 2. ap
[001]p ⊖
a a
c
[010]p [100]p ⓞ
c
a a
I4/m
ⓞ ⓞ ⊖
a = b = √2. ap
c ≈ 2. ap
[001]p ⓞ
a b
c
[010]p ⊖
c
a,b
[100]p ⊖
c
a b
I2/m
ⓞ ⊖ ⊖
a ≈ b ≈ √2. ap
c ≈ 2. ap
β ≈ 90
[001]p ⊕
a b
c
[010]p ⊖
c
a b
[100]p ⊖
c
a,b
P21/n
⊕ ⊖ ⊖
a ≈ b ≈ √2. ap
c ≈ 2. ap
β ≈ 90

FIGURA 1.6: Proyecciones (según los ejes de la perovskita simple cúbica) de la secuencia $P2_1/n - I2/m - I4/m - Fm\bar{3}m$. Se indica el giro de los octaedros respecto a cada eje de la perovskita simple y los parámetros relativos a la misma.

1.5. Transiciones estructurales y distorsiones de la estructura tipo perovskita (II): *modos adaptados a la simetría*

En lo que se refiere a las distorsiones de la estructura perovskita (a partir de este momento, me referiré sólo a las perovskitas dobles), durante el último año hemos empezado a utilizar una descripción diferente de las mismas; en realidad, no sólo de las distorsiones, si no de las propias estructuras y de las transicones de fase.

Se trata de una descripción equivalente, pero sin duda, más adecuada en el contexto de las transiciones de fase, que es justamente en el que se enmarca mi trabajo. La descripción consiste en utilizar como grados de libertad de la estructura, en los refinamientos o en las transiciones de fase, no las coordenadas atómicas si no los modos adaptados a la simetría; o, abusando del lenguaje, las *representaciones irreducibles* (irreps) mediante las cuales se transforman esos modos adaptados a la simetría.

Sólo en los últimos trabajos publicados hemos podido hacer uso de esta nueva descripción, utilizando para ello dos herramientas básicas: el Servidor Cristalográfico *Bilbao Crystallographic Server* (BCS) y el conjunto de programas FullProf Suite, y en concreto la última versión (Febrero de 2009) de un programa del mismo AMPLIMODES for FullProf. AMPLIMODES es una de las herramientas presentes en el BCS.

La estructura de muchos materiales puede ser el resultado de una distorsión con respeto a una estructura de más simetría: estructura prototipo (*parent*); ésta puede ser virtual o real. Necesariamente debe existir una relación grupo-subgrupo entre los grupos espaciales de las dos estructuras, y la distorsión que relaciona ambas, se puede identificar como *una distorisón que rompe la simetría*. Normalmente, si las distorsiones son pequeñas (en lo que sigue, me referiré sólo a distorsiones de tipo *displacivo*), significa que la fase de alta simetría puede (podría) ser estabilizada térmicamente, por ejemplo, y que se pueden (podrían) producir una o más transiciones de fase que llevan la estructura de baja simetría hacia la de alta, según aumenta la temperatura.

La distorisión presente en la estructura distorsionada contiene una componente *primaria* (*modo primario*), que se corresponde al modo o modos que son inestables en la configuración prototipo de alta simetría, que es fundamental para explicar (describir) la estabilidad de la estructura distorsionada. Además, la distorsión contiene también otras contribuciones secundarias, de menor importancia, asociadas a modos que están permitidos por simetría y que se congelan porque se acomplan con los modos primarios. Todos esos modos, tanto primarios como secundarios, están asociados a *irreps* del grupo espacial de la fase prototipo: se transforman mediante *irreps* del grupo espacial de la fase prototipo. La separación de las contribuciones a la distorsión de los diferentes modos se realiza mediante el análisis de los modos de simetría. Para realizar correctamente este análisis son dos los conceptos que hay que definir claramente: en primer lugar, (a) la distorsión estructural (*campo de desplazamientos*), que relaciona la estructura prototipo y las fases distorsionadas, y que se puede descomponer en dos contribuciones: deformación homogénea (grados de libertad elásticos) y el campo de los desplazamientos atómicos (grados de libertad internos de los átomos), que está constituido por los desplazamientos de cada átomo en la estructura de baja simetría respecto a las posiciones que ocupan en la fase prototipo de alta simetría. Y, en segundo lugar, (b) la base con respecto a la que se descompone el campo de desplazamientos y que está compuesta por los modos de simetría compatibles con la ruptura de simetría producida entre los dos grupos espaciales.

El programa AMPLIMODES consta de un módulo que prepara un archivo de entrada (.pcr) adecuado para realizar refinamientos de datos de difracción de polvo (independientemente de la fuente de radiación, rayos X o neutrones) mediante el paquete informático FullProf Suite [40]. En este caso, la nueva versión del mencionado programa de refinamiento utiliza modos adaptados a la simetría en vez de coordenadas atómicas como los grados de libertad refinables en el refinemiento. Se trata de un enfoque nuevo que aprovecha completamente el análisis de modos de simetría realizado por AMPLIMODES, y en el que se refinan las amplitudes de los modos adaptados a la simetría. Recientemente se ha demostrado que esta forma de realizar los refinamientos de datos de difracción de polvo es muy robusta y eficiente (ver más adelante).

Un aspecto importante de todo este análisis es que AMPLIMODES (en general, el análisis por modos adaptados) no necesita conocer la estructura prototipo real. Partiendo de la estructura distorsionada (cuyo grupo espacial sea H, por ejemplo), se puede construir una estructura prototipo ideal (con un grupo espacial G, G>H) mediante la pseudo-simetría, con una *estructura pseudosimétrica* respecto de la fase de baja simetría. Entonces, las diferencias estructurales entre la fase prototipo real y al construida de la manera descrita, se deben sólo a contribuciones de modos compatibles con G (el grupo espacial de la fase de alta simetría); esto es, modos que se transforman según la *irrep* totalmente simétrica, *modos totalmente simétricos*.

AMPLIMODES, con caracter general, calcula los desplazamientos atómicos que relacionan ambas estructuras, y si los tamaños de esos desplazamientos son menores de un valor determinado (fijado por el experimentador) el programa sigue adelante. Determina y define un conjunto completo de modos adaptados a la simetría. Posteriormente, descompone la distorsión en términos de esos modos, y calcula la amplitud con que cada uno de esos modos contribuye a la distorsión. Los modos se describen en términos de desplazamientos de los átomos de la unidad asimétrica de la fase distorsionada, expresados en unidades relativas.

En lo que sigue, explicaré el procedimiento general de los nuevos tipos de refinamientos, así como el análisis general de los resultados, usando como ejemplo el compuesto Sr_2ScSbO_6, que como se verá más adelante presenta una secuencia de tres transiciones de fase según aumenta la temperatura: $P2_1/n \rightarrow I2/m \rightarrow I4/m \rightarrow Fm\overline{3}m$. He elegido este caso puesto que sirve para analizar la transición de fase entre la fase prototipo y la de más baja simetría observada en las dos familias que he estudiado. Además, también sirve para describir las transiciones de fase a las fases intermedias tanto tetragonal $I4/m$ (de las dos familias) como monoclínica $I2/m$ (de algunos de los miembros de la familia del antimonio; queda fuera de este análisis la fase trigonal intermedia $R\overline{3}$ de la familia del antimonio).

El procedimiento a seguir, en general, es el siguiente. Se cuenta con datos de difracción (en nuestro caso siempre de difracción de polvo, lo mismo de rayos-X que de neutrones) de la fase de temperatura ambiente, que suponemos que es la fase de baja simetría. Además, se ha indexado el difractograma y, por lo tanto, se conocen el grupo espacial y los parámetros de celda. Todavía no se ha resuelto la estructura (no se ha refinado). Se espera que a alta temperatura, la fase evolucione a la fase prototipo cúbica, con lo que se considera ésta como la fase de referencia. Como se ha dicho, esta fase de referencia puede ser conocida o no, y no importa si es la fase conocida para otro material, de la misma familia, por ejemplo, o no necesariamente. A continuación, se introducen los datos de la fase de referencia, el grupo espacial y los parámetros de celda (siempre en la descripción estándar), en AMPLIMODES for FullProf. No se introduce en AMPLIMODES, en este caso, puesto que no se conoce la estructura de baja simetría: el módulo AMPLIMODES for FullProf trabaja sólo con las métricas y devuelve el conjunto de *irreps* que permiten romper la simetría desde la fase de referencia hasta la de baja simetría. En el ejemplo que nos ocupa, los datos de entrada suministrados al módulo son los mostrados en la Figura 1.7.

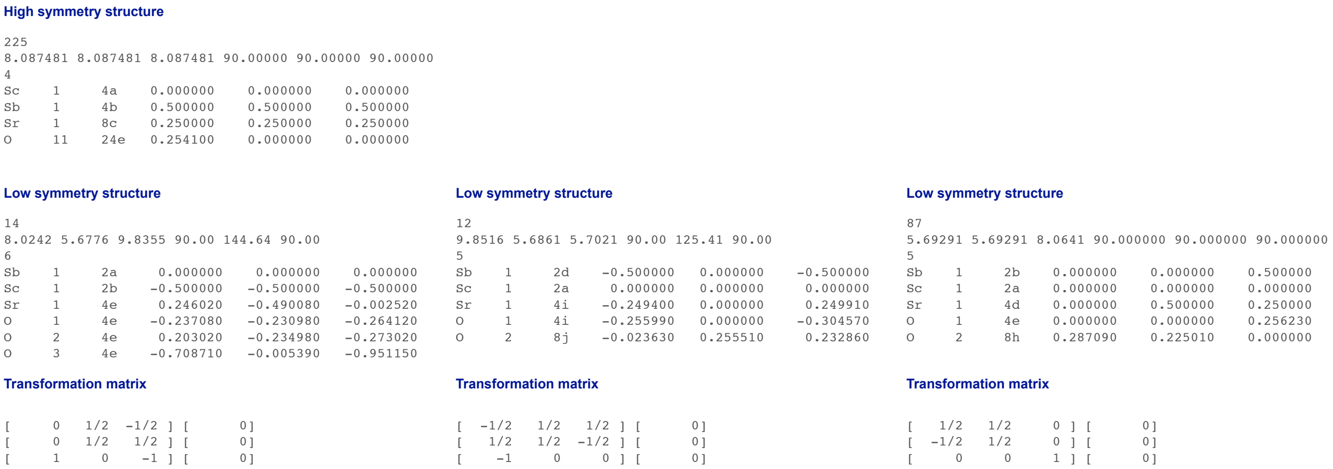

High symmetry structure

```
225
8.087481 8.087481 8.087481 90.00000 90.00000 90.00000
4
Sc    1     4a    0.000000    0.000000    0.000000
Sb    1     4b    0.500000    0.500000    0.500000
Sr    1     8c    0.250000    0.250000    0.250000
O     11    24e   0.254100    0.000000    0.000000
```

Low symmetry structure

```
14
8.0242 5.6776 9.8355 90.00 144.64 90.00
6
Sb    1     2a     0.000000    0.000000    0.000000
Sc    1     2b    -0.500000   -0.500000   -0.500000
Sr    1     4e     0.246020   -0.490080   -0.002520
O     1     4e    -0.237080   -0.230980   -0.264120
O     2     4e     0.203020   -0.234980   -0.273020
O     3     4e    -0.708710   -0.005390   -0.951150
```

Transformation matrix

```
[     0   1/2  -1/2 ] [       0]
[     0   1/2   1/2 ] [       0]
[     1     0    -1 ] [       0]
```

Low symmetry structure

```
12
9.8516 5.6861 5.7021 90.00 125.41 90.00
5
Sb    1     2d    -0.500000   0.000000   -0.500000
Sc    1     2a     0.000000   0.000000    0.000000
Sr    1     4i    -0.249400   0.000000    0.249910
O     1     4i    -0.255990   0.000000   -0.304570
O     2     8j    -0.023630   0.255510    0.232860
```

Transformation matrix

```
[  -1/2   1/2   1/2 ] [       0]
[   1/2   1/2  -1/2 ] [       0]
[    -1     0     0 ] [       0]
```

Low symmetry structure

```
87
5.69291 5.69291 8.0641 90.000000 90.000000 90.000000
5
Sb    1     2b    0.000000    0.000000    0.500000
Sc    1     2a    0.000000    0.000000    0.000000
Sr    1     4d    0.000000    0.500000    0.250000
O     1     4e    0.000000    0.000000    0.256230
O     2     8h    0.287090    0.225010    0.000000
```

Transformation matrix

```
[   1/2   1/2     0 ] [       0]
[  -1/2   1/2     0 ] [       0]
[     0     0     1 ] [       0]
```

FIGURA 1.7: Parte de la entrada de AMPLIMODES for FullProf.

Y los datos de salida (esto es, la clasificación de las *irreps*, modos) son los siguientes:

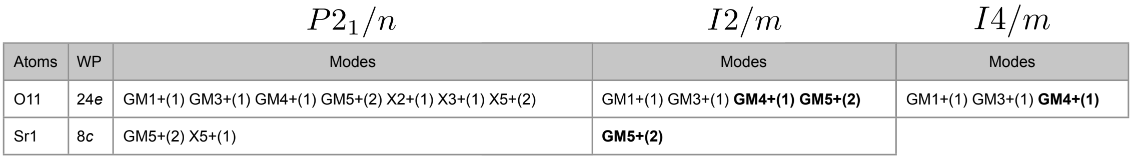

		$P2_1/n$	$I2/m$	$I4/m$
Atoms	WP	Modes	Modes	Modes
O11	*24e*	GM1+(1) GM3+(1) GM4+(1) GM5+(2) X2+(1) X3+(1) X5+(2)	GM1+(1) GM3+(1) **GM4+(1) GM5+(2)**	GM1+(1) GM3+(1) **GM4+(1)**
Sr1	*8c*	GM5+(2) X5+(1)	**GM5+(2)**	

FIGURA 1.8: Parte de la salida de AMPLIMODES for FullProf. La etiqueta para las *irreps* en el punto Γ de la unidad asímetrica que utiliza AMPLIMODES es GM, en vez de Γ.

En la tabla anterior, los números entre paréntesis indican la dimensión de las *irreps*.

El paso de la simetría cúbica a la monoclínica ($P2_1/n$) supone ganar 12 grados de libertad, si nos fijamos sólo en las coordenadas atómicas. En la fase cúbica, en la undidad asimétrica, sólo hay una coordenada no fijada por la simetría: la coordenada x del oxígeno. Sin embargo, en la fase $P2_1/n$, hay tres oxígenos en posiciones generales ($3 \times (x, y, z) = 9$), y el catión Sr también se encuentra en una posicón general ($1 \times (x, y, z) = 3$, en total $9 + 3 = 12$ grados de libertad), con lo que hay doce grados de libertad posicionales en la estructura monoclínica. Por supuesto, las distorsiones que se transforman según estas *irreps*, sólo pueden involucrar al (los) oxígeno(s) y al estroncio, cuyas etiquetas de las posiciones de Wyckoff en la fase cúbica son 24e y 8c, respectivamente. De la misma manera, en la transición $Fm\overline{3}m \rightarrow I2/m$ se pasa a dos oxígenos independientes en la unidad asimétrica, con dos y tres coordenadas libres, y a un estroncio con dos coordenadas libres; lo que hace un total de 7 grados de libertad posicionales. Finalmente, en el caso de la transicón $Fm\overline{3}m \rightarrow I4/m$, en la unidad asimétrica de la fase tetragonal los dos oxígenos independientes tienen una y dos coordenadas libres; con lo que el número de grados de libertad es 3.

Las 7 posibles *irreps* Γ_1^+, Γ_3^+, Γ_4^+, Γ_5^+, X_2^+, X_3^+ y X_5^+, asociadas con la primera transición, *desplazan* el oxígeno (de la fase cúbica); y sólo 2 (Γ_5^+ y X_5^+) desplazan el estroncio de la fase cúbica. Las 4 posibles *irreps* Γ_1^+, Γ_3^+, Γ_4^+ y Γ_5^+, asociadas con la segunda transición, *desplazan* el oxígeno; y sólo 1 (Γ_5^+) desplaza el estroncio. En el caso de la tercera transición, las posibles *irreps*, Γ_1^+, Γ_3^+ y Γ_4^+, sólo desplazan el oxígeno.

En las figuras siguientes, 1.9 y 1.10, se presenta el resto de los resultados del análisis de modos de la transicón de fase $Fm\overline{3}m \rightarrow P2_1/n$, proporcionado por AMPLIMODES. Estos datos también se pueden utilizar para representar las dos transiciones intermedias, ya que para este caso concreto, el paso desde la simetría de la fase prototipo hasta la de temperatura ambiente incluye los otros dos cambios de simetría. Como es sabido, los subgrupos de isotropía representan el grupo espacial de simetría (subgrupo del de alta simetría) de la fase que resulta de distorsionar la fase de referencia mediante el campo de desplazamientos que se transforma según la correspondiente *irrep*. Por otro lado, el campo de desplazamientos (los vectores de polarización) de los modos adaptados a la simetría, están representados en la siguientes tabla (el resultado de AMPLIMODES) y figura (para que sea más sencillo visualizar los desplazamientos, modificado según se obtiene de FullProf STUDIO).

K vector: GM = (0,0,0)

Irrep	GM1+	GM3+	GM4+	GM5+
Order Parameter	(a)	(a,0)	(a,-a,0)	(b,a,a)
Isotropy Subgroup H	225 Fm-3m Oh-5	139 I4/mmm D4h-17	12 C2/m C2h-3	12 C2/m C2h-3

Transformation Matrix

```
GM1+:
[      1      0      0 ] [      0]
[      0      1      0 ] [      0]
[      0      0      1 ] [      0]

GM3+:
[    1/2   -1/2      0 ] [      0]
[    1/2    1/2      0 ] [      0]
[      0      0      1 ] [      0]

GM4+:
[   -1/2   -1/2    1/2 ] [      0]
[   -1/2    1/2    1/2 ] [      0]
[     -1      0      0 ] [      0]

GM5+:
[   -1/2    1/2    1/2 ] [      0]
[   -1/2   -1/2    1/2 ] [      0]
[      1      0      0 ] [      0]
```

GM1+

WP 24e	Displacements
(x,0,0)	(1,0,0)
(x+1/2,0,-1/2)	(1,0,0)
(-x,0,0)	(-1,0,0)
(-x+1/2,0,-1/2)	(-1,0,0)
(0,0,x)	(0,0,1)
(1/2,0,x-1/2)	(0,0,1)
(0,0,-x)	(0,0,-1)
(1/2,0,-x-1/2)	(0,0,-1)
(0,x,0)	(0,1,0)
(1/2,x,-1/2)	(0,1,0)
(0,-x,0)	(0,-1,0)
(1/2,-x,-1/2)	(0,-1,0)

GM3+

WP 24e	Displacements
(x,0,0)	(0.500,0,0)
(x+1/2,0,-1/2)	(0.500,0,0)
(-x,0,0)	(-0.500,0,0)
(-x+1/2,0,-1/2)	(-0.500,0,0)
(0,0,x)	(0,0,-1)
(1/2,0,x-1/2)	(0,0,-1)
(0,0,-x)	(0,0,1)
(1/2,0,-x-1/2)	(0,0,1)
(0,x,0)	(0,0.500,0)
(1/2,x,-1/2)	(0,0.500,0)
(0,-x,0)	(0,-0.500,0)
(1/2,-x,-1/2)	(0,-0.500,0)

GM4+

WP 24e	Displacements
(x,0,0)	(0.500,0,0)
(x+1/2,0,-1/2)	(0.500,0,0)
(-x,0,0)	(-0.500,0,0)
(-x+1/2,0,-1/2)	(-0.500,0,0)
(0,0,x)	(0,0,-1)
(1/2,0,x-1/2)	(0,0,-1)
(0,0,-x)	(0,0,1)
(1/2,0,-x-1/2)	(0,0,1)
(0,x,0)	(0,0.500,0)
(1/2,x,-1/2)	(0,0.500,0)
(0,-x,0)	(0,-0.500,0)
(1/2,-x,-1/2)	(0,-0.500,0)

GM5+

WP 24e	Displacements
(x,0,0)	(0,0,1),(0,1,0)
(x+1/2,0,-1/2)	(0,0,1),(0,1,0)
(-x,0,0)	(0,0,-1),(0,-1,0)
(-x+1/2,0,-1/2)	(0,0,-1),(0,-1,0)
(0,0,x)	(1,1,0),(0,0,0)
(1/2,0,x-1/2)	(1,1,0),(0,0,0)
(0,0,-x)	(-1,-1,0),(0,0,0)
(1/2,0,-x-1/2)	(-1,-1,0),(0,0,0)
(0,x,0)	(0,0,1),(1,0,0)
(1/2,x,-1/2)	(0,0,1),(1,0,0)
(0,-x,0)	(0,0,-1),(-1,0,0)
(1/2,-x,-1/2)	(0,0,-1),(-1,0,0)

WP 8c	Displacements
(1/4,1/4,1/4)	(1,1,0),(0,0,1)
(3/4,1/4,-1/4)	(1,1,0),(0,0,1)
(-1/4,-1/4,-1/4)	(-1,-1,0),(0,0,-1)
(1/4,-1/4,-3/4)	(-1,-1,0),(0,0,-1)

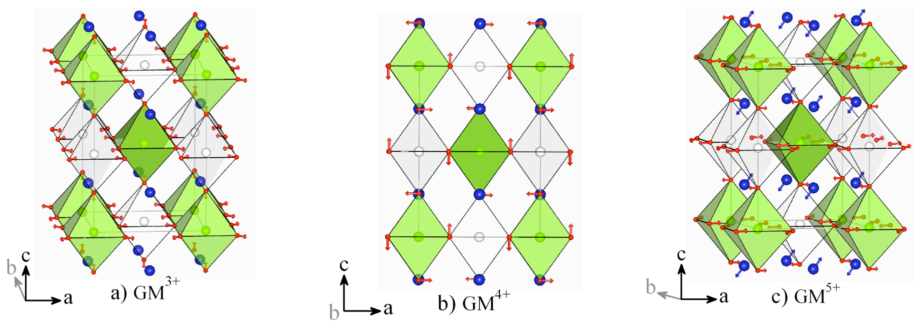

a) GM^{3+} b) GM^{4+} c) GM^{5+}

FIGURA 1.9: Resultados del análisis de los modos que participan en la transición $Fm\bar{3}m \rightarrow P2_1/n$ y sus correspondientes *irreps*, en el punto Γ: Γ_1^+, Γ_3^+, Γ_4^+ y Γ_5^+. Se indica el efecto de cada modo sobre la estructura de la perovskita doble ideal.

K vector: X = (0,1,0)

Irrep	X2+	X3+	X5+
Order Parameter	(0,a,0)	(0,a,0)	(a,a,0,0,-a,a)
Isotropy Subgroup H	136 P4_2/mnm D4h-14	128 P4/mnc D4h-6	58 Pnnm D2h-12
Transformation Matrix	[1/2 1/2 0] [0] [-1/2 1/2 0] [0] [0 0 1] [0]	[1/2 1/2 0] [0] [-1/2 1/2 0] [0] [0 0 1] [0]	[0 1/2 -1/2] [0] [0 -1/2 -1/2] [0] [-1 0 0] [0]

WP 24e	Displacements
(x,0,0)	(-1,0,0)
(x+1/2,0,-1/2)	(1,0,0)
(-x,0,0)	1,0,0
(-x+1/2,0,-1/2)	(-1,0,0)
(0,0,x)	(0,0,0)
(1/2,0,x-1/2)	(0,0,0)
(0,0,-x)	(0,0,0)
(1/2,0,-x-1/2)	(0,0,0)
(0,x,0)	(0,1,0)
(1/2,x,-1/2)	(0,-1,0)
(0,-x,0)	(0,-1,0)
(1/2,-x,-1/2)	(0,1,0)

WP 24e	Displacements
(x,0,0)	(0,1,0)
(x+1/2,0,-1/2)	(0,-1,0)
(-x,0,0)	(0,-1,0)
(-x+1/2,0,-1/2)	(0,1,0)
(0,0,x)	(0,0,0)
(1/2,0,x-1/2)	(0,0,0)
(0,0,-x)	(0,0,0)
(1/2,0,-x-1/2)	(0,0,0)
(0,x,0)	(-1,0,0)
(1/2,x,-1/2)	(1,0,0)
(0,-x,0)	(1,0,0)
(1/2,-x,-1/2)	(-1,0,0)

WP 24e	Displacements	
(x,0,0)	(0,0,0)	(0,0,-1)
(x+1/2,0,-1/2)	(0,0,0)	(0,0,1)
(-x,0,0)	(0,0,0)	(0,0,1)
(-x+1/2,0,-1/2)	(0,0,0)	(0,0,-1)
(0,0,x)	(-1,1,0)	(0,0,0)
(1/2,0,x-1/2)	(1,-1,0)	(0,0,0)
(0,0,-x)	(1,-1,0)	(0,0,0)
(1/2,0,-x-1/2)	(-1,1,0)	(0,0,0)
(0,x,0)	(0,0,0)	(0,0,1)
(1/2,x,-1/2)	(0,0,0)	(0,0,-1)
(0,-x,0)	(0,0,0)	(0,0,-1)
(1/2,-x,-1/2)	(0,0,0)	(0,0,1)

WP 8c	Displacements
(1/4,1/4,1/4)	(-1,1,0)
(3/4,1/4,-1/4)	(1,-1,0)
(-1/4,-1/4,-1/4)	(1,-1,0)
(1/4,-1/4,-3/4)	(-1,1,0)

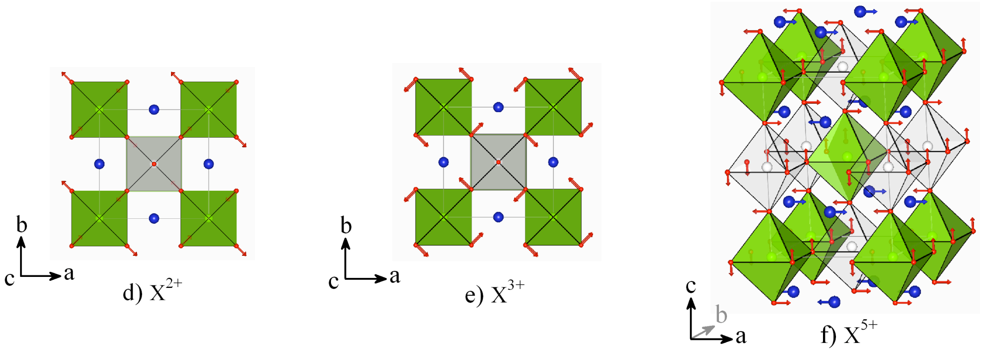

d) X^{2+} e) X^{3+} f) X^{5+}

FIGURA 1.10: Resultados del análisis de los modos que participan en la transición $Fm\bar{3}m \rightarrow P2_1/n$ y sus correspondientes *irreps*, fuera del punto Γ: X_2^+, X_3^+, y X_5^+. Se indica el efecto de cada modo sobre la estructura de la perovskita doble ideal.

Para seguir con el procedimiento general, ahora, lo único que queda es refinar las amplitudes de los modos adaptados a la simetría, en vez de las coordenadas atómicas; aquellas son los nuevos grados de libertad. Sin embrago, antes de ver cuáles son los resultados de esos refinamientos, con el fin de entender mejor las transiciones de fase en términos de los modos, describo un estudio paralelo que es recomendable hacer, antes de seguir; por supuesto, son varias las herrmientas del BCS las que permiten hacerlo de la manera en la que lo describo a continuación.

En la Figura 1.11 se muestra el esquema del conjunto de (sub)grupos espaciales obtenido mediante CELLSUB (otra herramienta del BCS) y que describen la ruptura de simetría desde la fase cúbica hasta la monoclínica $P2_1/n$, en vertical; en horizontal, se describe la ruptura de simetría hasta la fase tetragonal intermedia $I4/m$. En el esquema vertical, se ha indicado con fondo azul la ruptura de simetría a la fase intermedia monoclínica $I2/m$, que como puede apreciarse está incluida en la otra ruptura monoclínica. La simetría de la fase de referencia se ha marcado en rojo; mientras que las simetrías de las fases de *llegada* (de baja simetría) se han marcado en rosa. En la misma figura, se han representado la relación de las celdas unidad (en definitiva, la relación de las métricas en cada una de las transiciones de fase). Así, en azul se ha representado la celda cúbica de la perovskita simple; en línea de puntos, la celda cúbica de la estructura de referencia; y en trazo contínuo negro, la celda correspondiente a cada fase. También se indica la relación entre los parámetros de celda. Finalmente, también se indican las posiciones de los ejes característicos, tetragonal (en rojo) y monoclínico (en verde), que perteneciendo a la fase de referencia cúbica, permanencen en las sucesivas fases de más baja simetría. Como puede apreciarse, el eje monoclínico está orientado de la misma manera en las dos fase monoclínicas: a lo largo de una de las diagonales de cara cúbicas; sin embargo, el eje tetragonal está orientado a lo largo de una arista cúbica. Esto significa que si bien se puede pasar de manera contínua de la fase de simetría $P2_1/n$ a la de simetría $I/2m$, no ocurre lo mismo con la otra transción: $I2/m \rightarrow I4/m$, ya que los ejes característicos están orientados perpendicularmente. Así, la primera transición es contínua, y la segunda es discontínua. En realidad, si nos fijamos en las *irreps*, y bajamos de la fase de referencia, sólo hay una *irrep* que rompe la simetría totalmente hasta la fase de interés tetragonal ($I4/m$): Γ_4^+; que es la misma que rompe la simetría hasta la primera fase monoclínica de interés ($I2/m$): Γ_4^+, pero que está orientada de manera distinta. Para darse cuenta ello hay que fijarse en la orientación (descrita en la fase de referencia) que tiene el vector de desplazamiento correspondiente a esa irrep (AMPLIMODES): Γ_4^+ para $Fm\overline{3}m \rightarrow I4/m$ está en la dirección $(a, 0)$, mientras que Γ_4^+ para $Fm\overline{3}m \rightarrow I2/m$ está en la dirección $(a, a, 0)$. Por supuesto, ésta no es la única posibilidad, para la orientación relativa de las celdas (de los ejes característicos): es una de las posibles y la que normalmente se utiliza.

Desde el punto de vista de la simetría, pasar de la fase cúbica de referencia a la tetragonal, supone que ha de conservarse un eje tetragonal, sólo uno, dicho de otra manera: se pierden los ejes ternarios. Los ejes tetragonales en la fase cúbica se encuentran a lo largo de las aristas del cubo (celda unidad), por lo que cualquiera de las aristas es la que puede *conservarse*. Por otra lado, pasar desde la fase de referencia a la fase monoclínica $I2/m$, supone conservar un eje binario. El

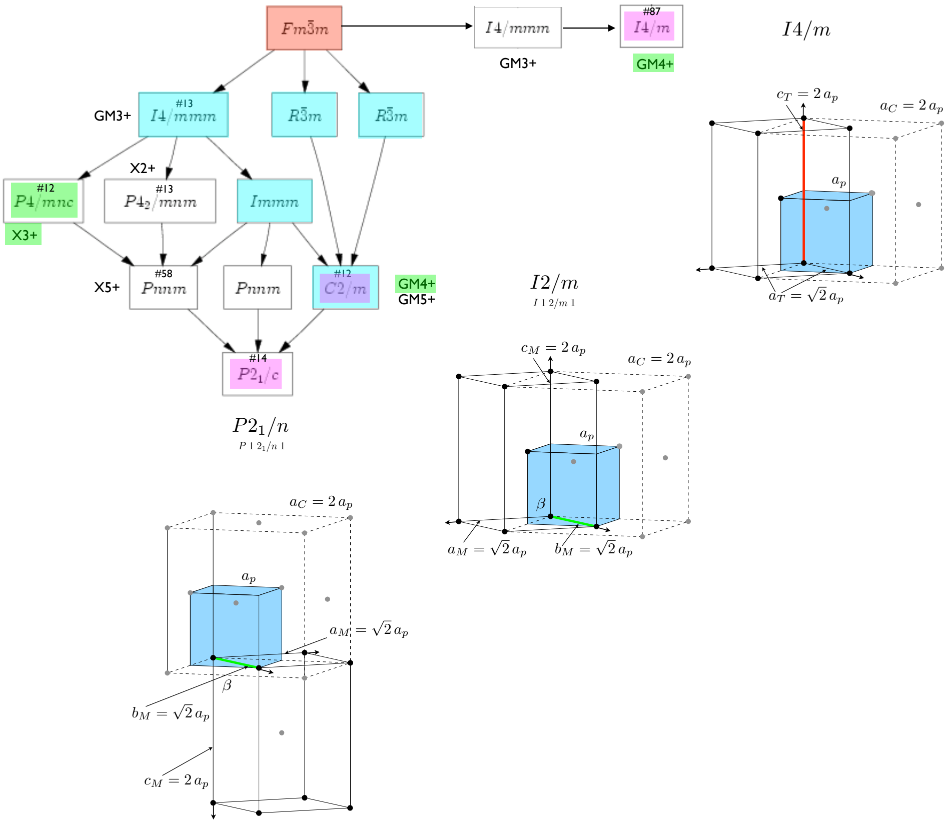
$Fm\bar{3}m$
$I4/mmm$
#87
$I4/m$
GM3+
GM4+
$I4/m$
GM3+
#13
$I4/mmm$
$R\bar{3}m$
$R\bar{3}m$
X2+
#12
$P4/mnc$
X3+
#13
$P4_2/mnm$
$Immm$
X5+
#58
$Pnnm$
$Pnnm$
#12
$C2/m$
GM4+
GM5+
#14
$P2_1/c$
$c_T = 2\,a_p$
$a_C = 2\,a_p$
a_p
$a_T = \sqrt{2}\,a_p$
$I2/m$
$I\,1\,2/m\,1$
$c_M = 2\,a_p$
$a_C = 2\,a_p$
a_p
β
$a_M = \sqrt{2}\,a_p$
$b_M = \sqrt{2}\,a_p$
$P2_1/n$
$P\,1\,2_1/n\,1$
$a_C = 2\,a_p$
a_p
$a_M = \sqrt{2}\,a_p$
β
$b_M = \sqrt{2}\,a_p$
$c_M = 2\,a_p$

FIGURA 1.11: Esquema del conjunto de subgrupos espaciales obtenidos mediante CELLSUB, y la relación de las celdas unidad de las estructuras que experimentales.

grupo tetragonal $I4/m$ no posee al monoclínico $I2/m$ como subgrupo. Esto significa que a pesar de que el grupo tetragonal tiene un eje binario (orientado, por supuesto como el eje cuaternario), éste nunca puede ser el de $I2/m$, porque si no sí habría relación grupo-subgrupo. Esto quiere decir que de todos los ejes binarios presentes en la fase cúbica de referencia sólo aquellos que no estén orientados según los ejes cuaternarios son los que se pueden conservar al reducir la simetría hasta $I2/m$; y éstos son o perpendiculares (como en el caso de la figura) u oblícuos (esto es, los ejes binarios que en la fase cúbica se encuentran en las diagonales principales del cubo).

En relación con este último punto, tengo que decir que, gracias a los cálculos realizados por el Dr. Iñigo Etxebarria y por su estudiante Urko Petralanda, así como gracias a las discusiones mantenidas con ellos y con el Dr. Gotzon Madariaga, he sabido que desde el punto de vista *energético* (haciendo cálculos de dinámica molecular) parece que es más favorable (menos costoso) pasar de manera discontínua de la fase tetragonal a la monoclínica cuyo eje monoclínico está orientado oblícuamente respecto al cuaternario de la tetragonal, en vez de perpendicularmente (como normalmente se ha considerado y como yo he representado en la figura). Sin embargo, también tengo que decir que experimentalemente no hay forma de comprobar que eso sea así.

Ahora, sólo queda referirme a las marcas verdes en las etiquetas de las *irreps* de la Figura 1.11: representan las *irreps activas*, las asociadas a los *modos primarios*, responsables de la transición de fase. Cuando se plantea una ruptura de simetría, se pueden presentar dos casos: (1) que alguna de las *irreps* sea capaz de romper la simetría hasta el grupo espacial de baja simetría, o (2) que no sea así, esto es, que la distorsión presente en la fase de baja simetría necesariamente cuente con al menos dos *irreps* (modos). Esta información la proporciona AMPLIMODES: cuando puede existir alguno modo primario, el programa indica la *irrep* en negrita. Como se puede apreciar en la Figura 1.8, Γ_4^+ y Γ_5^+, para $Fm\overline{3}m \rightarrow I2/m$; y Γ_4^+, para $Fm\overline{3}m \rightarrow I4/m$, aparecen en negrita. Esto quiere decir que cualquiera de ellas rompe totalmente la simetría hasta donde se necesita, y que por lo tanto representan *irreps* asociadas a modos primarios. En el caso de la transformación $Fm\overline{3}m \rightarrow P2_1/n$ (figura más arriba) ninguna de las *irreps* aparece en negrita, lo que significa que se necisitan al menos dos *irreps* para provocar la ruptura total de simetría. Es el experimento, es decir, el conocimiento de las correspondientes estructuras, el que dirá cuál de las posibles *irreps* primarias lo es realmente, o cuáles de las que se necesitan conjuntamente para romper totalmente la simetría. Para eso, por tanto, lo que hay que hacer es refinar la estructura de interés o indicarle a AMPLIMODES, no sólo la estructura de referencia si no también la de baja simetría. De esta forma, AMPLIMODES calculará la amplitudes de los modos asociados con cada *irrep*, y de entre los posibles modos primarios lo serán aquellos cuyas amplitudes sean mayores. En cualquier caso, el resultado del refinamiento de las amplitudes de las irreps correspondientes a cada una de las transiciones es el siguiente:

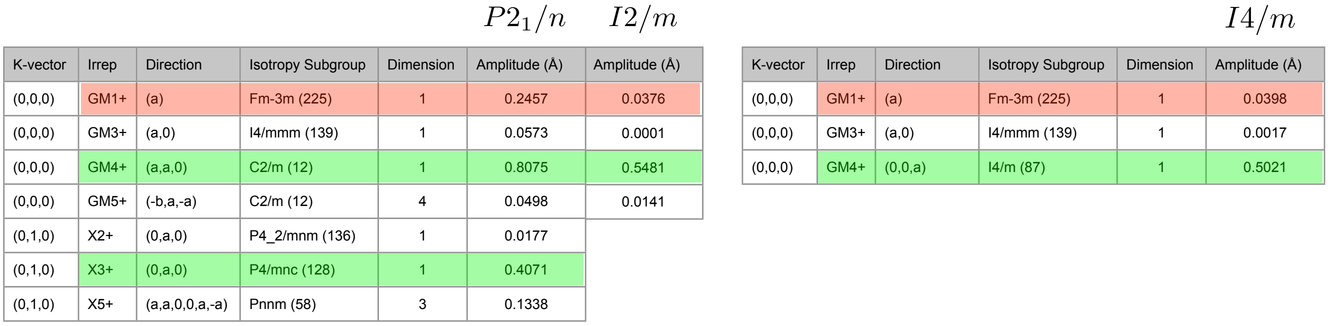

$P2_1/n$ $I2/m$

K-vector	Irrep	Direction	Isotropy Subgroup	Dimension	Amplitude (Å)	Amplitude (Å)
(0,0,0)	GM1+	(a)	Fm-3m (225)	1	0.2457	0.0376
(0,0,0)	GM3+	(a,0)	I4/mmm (139)	1	0.0573	0.0001
(0,0,0)	GM4+	(a,a,0)	C2/m (12)	1	0.8075	0.5481
(0,0,0)	GM5+	(-b,a,-a)	C2/m (12)	4	0.0498	0.0141
(0,1,0)	X2+	(0,a,0)	P4_2/mnm (136)	1	0.0177	
(0,1,0)	X3+	(0,a,0)	P4/mnc (128)	1	0.4071	
(0,1,0)	X5+	(a,a,0,0,a,-a)	Pnnm (58)	3	0.1338	

$I4/m$

K-vector	Irrep	Direction	Isotropy Subgroup	Dimension	Amplitude (Å)
(0,0,0)	GM1+	(a)	Fm-3m (225)	1	0.0398
(0,0,0)	GM3+	(a,0)	I4/mmm (139)	1	0.0017
(0,0,0)	GM4+	(0,0,a)	I4/m (87)	1	0.5021

FIGURA 1.12: Valores de las amplitudes de los modos que participan en la transición $Fm\overline{3}m \rightarrow P2_1/n$ según se han obtenido del refinamiento por modos.

Los resultados anteriores se han obtenido liberando a la vez en el proceso de refinamiento todas las amplitudes (las posibles en cada caso). En rojo he indicadao la *irrep* Γ_1^+, la totalmente simétrica. Esta amplitud representa lo *lejos* que se encuentra la fase de referencia respecto a la fase de baja simetría. Como se ha indicado más arriba, en realidad, el resultado importante no depende del valor de esta amplitud. Si nos fijamos en los valores obtenidos, lo que se ve es que poco a poco, nos vamos acercando a la fase cúbica, ya que las amplitudes del modo toalmente simétrico van disminuyendo. En verde he marcado las *irreps* primarias. Ya he comentado más arriba que en el caso de la ruptura de simetría hasta $P2_1/n$ ninguna de las posibles *irreps* puede producirla, con lo que al menos se necesitan dos: el experimento, el refinamiento, nos dice que aquellas con la mayor amplitud serán las primarias. Este es el caso de Γ_4^+ y X_3^+, con los valores 0.8075 Å y 0.4071 Å, respectivamente. Del resto de amplitudes, Γ_3^+, Γ_5^+ y X_2^+ son un orden de magnitud menores. Y Γ_1^+, es incluso la mitad de la más pequeña de las dos primarias, y, a su vez X_5^+ (0.1338 Å) es la mitad de la Γ_1^+. En lo que respecta a las otras dos transiciones, el experimento está de acuerdo con las predicciones teóricas: en ambos casos la única *irrep* primaria, con la misma etiqueta en ambos casos (Γ_4^+), es la que tiene el mayor valor.

Finalmente, me gustaría hacer un comentario sobre la nueva forma de refinar implementada en FullProf y que hace uso de los modos adaptados a la simetría. Al introducirlo, un poco más arriba, he afirmado que es equivalente utilizar las amplitudes de los modos adaptados a la simetría a utilizar directamente las coordenadas atómicas individuales; también he afirmado que es más conveniente desde el punto de vista de la teoría de grupos. Para demostrar ambas afirmaciones desde un punto de vista práctico, a continuación, presento los datos de diferentes refinamientos realizados en el caso del compuesto Sr_2CrSbO_6 para la transición $I4/m \to Fm\bar{3}m$.

El procedimiento seguido en los refinamientos mostrados en la Figura 1.13 ha sido el siguiente. Se trata de observar en la evolución de los modos la presencia de la transición de fase. Así, se han refinado todos los difractogramas utilizando el modelo tetragonal, la métrica tetragonal, para todas las temperaturas. Como se ha dicho antes, para esta transición de fase la *irrep* activa es Γ_4^+, que por lo tanto, tendrá una amplitud diferente de cero en la fase tetragonal, pero que según la estructura tetragonal evolucione hacia la cúbica, aquella irá disminuyendo, hasta que en la fase cúbica, por definición, desaparezca: se haga cero. Sin nos fijamos en la coordenadas atómicas individuales, la diferencia entre la fase tetragonal y la cúbica, como se ha dicho en el apartado anterior, es que los octahedros están girados un cierto ángulo en torno al eje tetragonal; según la estructura se acerca a la fase cúbica el giro va disminuyendo hasta que se hace cero. Por supuesto, la amplitud del modo (primario) asociado a Γ_4^+ debe se proporcional al ángulo de giro.

El primer refinamiento se ha hecho usando coordenadas atómicas, el refinamiento clásico. Seguidamente, se ha utilizado AMPLIMODES para calcular, en cada temperatura, la amplitud de los diferentes modos. El resultado se muestra en la figura mediante puntos negros; sin errores, ya que AMPLIMODES todavía no calcula los errores. Tengo que indicar que en estos refinamientos por coordenadas atómicas, nos vimos obligados a fijar la coordenada de uno de los oxígenos $(0,0,z) \to (0,0,0.25)$ (posición cercana a la que toma en la fase cúbica), ya que no conseguíamos que los refinamientos convergieran.

El siguiente refinamiento se ha hecho usando modos, en vez de coordenadas. En este caso también se ha impuesto una restricción: la amplitud de Γ_3^+ se ha fijado a cero. Viendo, en la Figura

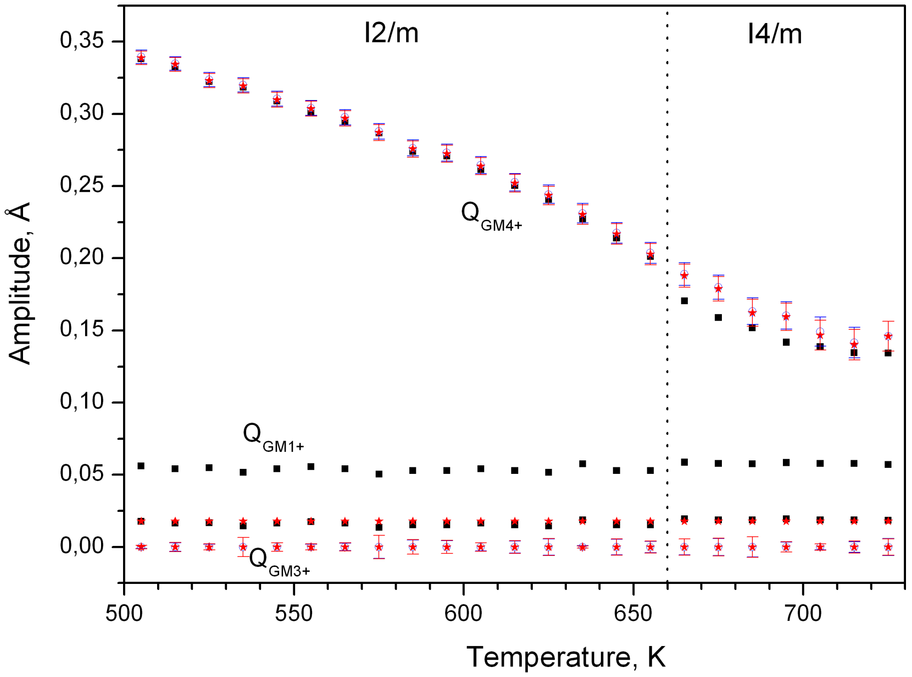

FIGURA 1.13: Evolución de las amplitudes de los modos cuyas *irrpes* son Γ_1^+, Γ_3^+ y Γ_4^+ (modo primario) en la transición $I4/m \rightarrow Fm\overline{3}m$, para tres tipos de refinamientos diferentes: puntos negros, refinamiento mediante coordenadas atómicas, con una restricción sobre una coordenada de uno de los oxígenos; estrellas en rojo, refinamiento mediante modos adaptados, también con una restricción, la amplitud del modo Γ_3^+ se fija en cero; estrellas en azul, refinamiento por modos, con una restricción, la amplitud del modo con Γ_3^+ fijada al valor que toma en la primera temperatura (ver texto).

1.11, que el resultado obtenido para la amplitud de esa *irrep* (aunque los materiales sean diferentes, los valores de las amplitudes son muy similares, ya que las transiciones son esencialemente iguales) es dos órdenes de magnitud inferior a la del modo primario, físicamente tiene sentido decir que apenas tiene importancia en la transición, y que apenas se introduce error si no se refina; lo cual, por un lado supone que el refinamiento será más eficiente, puesto que se estará haciendo con un grado de libertad menos. Pero, por otro lado, lo que es más importante todavía es que desde el punto de vista de la simetría es más adecuada esta restricción que la de fijar *arbitrariamente* una coordenada atómica individual. En los modos adaptados a la simetría pueden participar varios átomos de la celda unidad, con lo que al hacer nula la amplitud asociada al mismo, se están dejando fijas todas las posiciones de esos átomos. Sin embargo, cuando se fija, *arbitrariamente*, la posición individual de un átomo, en general, se estarán afectando a los valores de las amplitudes de varias *irreps*, que, en realidad, son las importantes (o no, dependiendo de su caracter) en la transición. Este refinamiento se muestra en azul en la figura. Dos consecuencias importantes: primero, el valor de la amplitud del modo primario, si tenemos en cuenta los errores, es el mismo (esto es cierto en toda la parte tetragonal, no así en la cúbica) que en refinamiento en el que se han considerado todos los grados de libertad mediante coordenadas, pero en el segundo refinamiento tenemos un grado de libertad menos. Segundo, el valor de Γ_1^+ ha bajado un orden de magnitud, oscila en torno a cero: esto significa que la restricción (arbitraria) *fijar la posición de un oxígeno* desvía innecesariamente la estructura, que el refinamiento se encarga de compensar.

El siguiente refinamiento también se ha hecho con modos, y en él también se ha aplicado una restricción: se ha fijado (arbitrariamente, sólo para ver qué supone) el valor de la amplitud de Γ_3^+ para todas las temperaturas con el valor que toma al dejarlo libre en la primera temperatura, los cuadrados rojos. En este caso, también, dos conclusiones: primero, de nuevo los valores de la amplitud del modo primario, en todo el rango de temperatura, y teniendo en cuenta los errores, que ahora sí son prácticamente los mismos, son iguales. Segundo, la restricción arbitraria empleada en este caso tampoco desvía la estructura como la anterior, ya que el valor que se obtiene para Γ_1^+ es, con el error, el mismo que en el segundo refinamiento.

1.6. Interés y Objetivos

Como se ha mencionado anteriormente, los óxidos mixtos con estructura tipo perovskita doble $A_2BB'O_6$ presentan gran interés desde el punto de vista científico y tecnológico debido a la gran variedad de propiedades que poseen. Entre éstas, destacan las propiedades superconductoras, catalíticas, magnéticas y magnetorresistentes que presentan muchos de estos compuestos en función de los elementos constituyentes, de las transiciones estructurales que se producen por efectos de la temperatura, y de los diferentes grados de orden posibles entre los cationes B y B′.

El presente trabajo de investigación se enmarca en una línea iniciada en el año 2000, basada en la síntesis, caracterización estructural y de las transiciones de fase de materiales con estructura de tipo perovskita doble. Por ello se han utilizado las siguientes técnicas: difracción de rayos X y neutrones, espectroscopía de absorción de rayos X (XAS), espectroscopia de resonancia paramagnética electrónica (ERP) y espectroscopia Raman.

En un trabajo interior realizado en el grupo de investigación en el que he realizado mi tesis doctoral, se ha presentado el estudio experimental mediante difracción rayos X (de laboratorio y radiación sincrotrón) y de neutrones en muestras policristalinas, de la evolución con la temperatura de las estructuras cristalinas de la familia de óxidos de perovskitas dobles de wolframio $Sr_2M^{2+}W^{6+}O_6$ (M= Ni, Zn, Co, Ca, Mg, Cu) [41, 42, 43, 44]. Sr_2NiWO_6 y Sr_2MgWO_6 presentan una transición de fase de la estructura tetragonal de temperatura ambiente, con el grupo espacial $I4/m$, a una estructura cúbica ($Fm\overline{3}m$), de alta temperatura. Sr_2ZnWO_6, Sr_2CoWO_6 y Sr_2CaWO_6 muestran secuencias de dos transiciones de fase estructurales: $P2_1/n \rightarrow I4/m \rightarrow Fm\bar{3}m$. La secuencia de transiciones que se ha encontrado en Sr_2CuWO_6 es $I4/m \rightarrow I4/mmm \rightarrow Fm\bar{3}m$. Se han demostrado que las transiciones $I4/m \rightarrow Fm\bar{3}m$ en Sr_2MWO_6 (M= Ni, Zn, Co, Ca, Mg) y la transición $I4/m \rightarrow I4/mmm$ en Sr_2CuWO_6 son de segundo orden.

El objetivo de mi trabajo de tesis doctoral, es doble: por un lado, se trata de completar el estudio de la citada familia de wolframio $Sr_2M^{2+}W^{6+}O_6$, analizando los siguientes materiales, algunos de los cuales se sintetizan y estudian por primera vez: (M= Mn, Cd) y la solución sólida $Sr_2Cd_{1-x}Ca_xWO_6$ $(0 \leq x \leq 1)$ y estudiar una nueva familia de Antimonio de fórmula general $Sr_{2-x}Ca_xM^{3+}Sb^{5+}O_6$ (M= Al, Co, Cr, Ga, Mn, Fe, Sc, Sm, La) $(0 \leq x \leq 1)$.

Por otro lado, se trata de extender el estudio realizado en la familia $Sr_2M^{2+}W^{6+}O_6$, a la familia de óxidos de perovskitas dobles de antimonio $Sr_2M^{3+}Sb^{5+}O_6$. He indicado explícitamente el estado de oxidación de los cationes B y B′ en los sitios B para poner de manifiesto que no sólo se está cambiando de familia de óxidos, de wolframio a antimonio, si no que también se está cambiando de sistema: (2+,6+) a (3+,5+), que es como a menudo se designan los tipos generales de combinaciones de estados de oxidación de los cationes B y B′ en los sitios B de la perovskita doble. Este cambio de sistema proporciona un nuevo grado de libertad a la estructura de la perovskita doble, ya que como ya se ha mencionado, una diferencia de carga entre los cationes B y B′ igual o inferior a 2 puede dar lugar a desorden parcial o total de los cationes B y B′ en los sitios B. Así, se pretende estudiar los esquemas de ordenamiento posibles en la familia $Sr_2M^{3+}Sb^{5+}O_6$, así como los factores que principalmente afectan a esos esquemas de ordenamiento.

Capítulo 2

Técnicas experimentales y equipos utilizados

En este capítulo se describen las características básicas de las técnicas experimentales, así como de los equipos experimentales utilizados en el desarrollo del trabajo, parte de cuyos resultados de recogen en la presente memoria

2.1. Medidas de difracción de rayos X en muestras policristalinas

Los rayos X son una forma de radiación electromagnética de elevada energía y pequeña longitud de onda; del orden de los espacios interatómicos de los sólidos. Cuando un haz de rayos X incide en un material sólido, parte de este haz se dispersa en todas direcciones a causa de los electrones asociados a los átomos o iones que encuentra en el trayecto, pero el resto del haz puede dar lugar al fenómeno de difracción de rayos X, que tiene lugar si existe una disposición ordenada de átomos y si se cumplen las condiciones que vienen dadas por la *Ley de Bragg* que relaciona la longitud de onda de los rayos X y la distancia interatómica con el ángulo de incidencia del haz difractado. Si no se cumple la *ley de Bragg*, la interferencia es de naturaleza no constructiva y el campo del haz difractado es de muy baja intensidad.

Una de las ventajas más importantes de la difracción de rayos X, respecto a otros tipos de difracción (neutrones, por ejemplo), es precisamente la alta resolución en d_{hkl} con que se cuenta cuando se mide un difractograma de polvo en condiciones idóneas. Sin embargo, esta técnica, también presenta un inconveniente importante: la magnitud de la interacción de la radiación incidente con los átomos del cristal es proporcional al número atómico (Z) de aquellos. Así, si un material se compone de átomos que se encuentran próximos en la Tabla Periódica, esta técnica no será capaz de distinguirlos debido a su pequeña diferencia porcentual en el número atómico. Esto mismo ocurre cuando en el mismo material se encuentran átomos con Z muy diferentes: unos grandes (átomos pesados) y otros pequeños (átomos ligeros), la dispersión de estos últimos queda enmascarada por la de los primeros, al ser más pesados. Asimismo, la dispersión de rayos X también depende del ángulo de dispersión θ: cuanto mayor es el ángulo, menor es el poder de dispersión. Así, la intensidad difractada disminuye drásticamente con el ángulo de difracción. Sin embargo, conviene recoger intensidad también a altos ángulos, ya que, a pesar de la mencionada disminución de intensidad y de que, como ocurre con los materiales presentados en la memoria, a altos ángulos los picos de difracción se superponen, lo que complica su tratamiento, es a altos ángulos donde se encuentra, sobre todo la información sobre los parámetros de desplazamiento térmico de los átomos.

La difracción de rayos X se ha usado con dos objetivos: determinar la estructura a temperatura ambiente y estudiar la evolución con la temperatura de aquella. Esta técnica sirve, además, para la identificación de las fases cristalinas, así que se ha utilizado en cada paso de los tratamientos térmicos en la ruta de síntesis.

Para el estudio de las estructuras cristalinas de los compuestos sintetizados y analizados, se han realizado medidas de difracción utilizando diferentes difractómetros.

2.1.1. Rayos-X convecionales

- ◇ Stoe STADI-P

  Las medidas de difracción utilizadas para caracterizar las muestras después de cada tratamiento térmico y las medidas a temperatura ambiente de la solución sólida $Sr_2Cd_{1-x}Ca_xWO_6$ $(0 \leq x \leq 1)$ se han realizado con este difractómetro, en geometría de transmisión.

  El difractómetro STOE STADI-P esta equipado con un detector PSD. Cu$K\alpha1$, λ=1.5406(Å), y un monocromador primario de germanio. Los datos de intensidad difractada se han recogido con un paso en 2θ de 0.02°, mediante barrido continuo y tiempos de contaje entre 10 y 50 segundos por cada punto. El rango de 2θ cubierto en las medidas ha sido de 15° a 100°.

- ◇ Philips X'Pert MPD

  Philips X'Pert MPD System con radiación Cu$K\alpha$, equipado con un detector proporcional PW3011/10, dos rendijas Soller de 0.02 rad (una para el haz incidente y otra para el haz difractado), rendija de divergencia de 0.5°, rendija anti-scattering de 0.5°, rendija programable de recepción, máscara de 10 mm y monocromador secundario de grafito curvado. En estas medidas se ha utilizado la geometría focalizadora Bragg-Brentano. Esta geometría se caracteriza por un menor nivel de fondo continuo, que permite observar reflexiones de muy baja intensidad; también, es la geometría adecuada para estudiar materiales que tienen alta absorción (como es el caso de los materiales estudiados) para la longitud de onda utilizada. Como desventaja se puede mencionar que el área iluminada por el haz de rayos X es distinta para diferentes valores de 2θ (si no se utiliza rendija de divergencia variable); y, también, que esta geometría es más propicia a provocar orientación preferente de los granos cristalinos de la muestra. Para reducir el efecto de la orientación preferente y mejorar la distribución de los cristalitos en posición de difracción, la muestra se gira, durante la medida, con una frecuencia de 1 revolución por segundo.

En las medidas a temperatura ambiente, los datos de intensidad difractada se han recogido con un paso en 2θ de 0.01°, mediante barrido continuo y tiempos de contaje entre 8 y 20 segundos por cada punto. El rango de 2θ cubierto en las medidas ha sido de 15° a 120°. Los difractogramas de rayos X a altas temperaturas se han obtenido utilizando una cámara de temperatura Anton-Paar HTK16, montada sobre el mismo difractómetro. Se han utilizado dos rendijas Soler de 0.04 rad, una rendija de divergencia de 1° y una rendija anti-scattering de 1°. Los demás componentes coinciden con los utilizados para las medidas a temperatura ambiente.

◇ Bruker Advance D8

Difractómetro Bruker D8 Advance equipado con monocromador primario de germanio, geometría Bragg-Brentano y con una longitud de onda Cu$K_{\alpha1}$ de 1.5406 Å. Se ha empleado un detector de energía dispersiva Sol-X con una ventana optimizada para Cu$K_{\alpha1}$ limitando la radiación de fluorescencia. La toma de datos se ha realizado en modo continuo, de 15° a 100° en 2θ, paso de 0.01° (2θ) y tiempo de medida por paso de 10 segundos.

Las medidas de difracción a baja y alta temperatura se han realizado en un difractómetro Bruker D8 Advance igual al anterior equipado con una cámara de baja temperatura de rango TC-ancha de MRI con refrescamiento directo de la muestra, una cámara de alta temperatura variable Anton Paar HTK2000 y portamuestras de platino, excepto que en este caso no cuenta con monocromador primario, por lo que en los difractogramas se recogen las reflexiones correspondientes a las dos longitudes de onda Cu$_{K\alpha1}$ y Cu$_{K\alpha2}$. La recogida de intensidades se ha realizado empleando un detector Väntec monodimensional de alta velocidad con abertura angular de 3 grados.

Las muestras para el estudio a bajas y altas temperaturas se han preparado mezclando el material estudiado con la acetona. La mezcla obtenida se ha ”pintado” sobre el calefactor de aleación de platino de la cámara. Se han realizado dos tipos de medidas en temperatura:

- Medidas en rangos 2θ amplios y pasos en temperatura de 10 ó 15K, para determinar la variación de los parámetros de celda.
- Medidas en rangos 2θ cortos y pasos en temperatura entre 5 y 10K, para observar la evolución con la temperatura de reflexiones escogidas, que presentan una mayor sensibilidad a las distorsiones de la celda unidad y a las rotaciones de los octaedros.

2.1.2. Radiación sincrotrón

Datos de difracción de radiación sincrotrón se han recogido de la muestra Sr_2CdWO_6 a temperatura ambiente en la línea de haz X7A de NSLS (Brookhaven National Laboratory, EE.UU.). Se ha utilizado radiación con una longitud de onda 0.8005Å. Ésta se ha obtenido con un monocromador de Si(111); y se ha calibrado con una muestra estándar de CeO_2.

Las medidas a altas temperaturas se han realizado utilizando la geometría Debye-Scherrer con un capilar de cuarzo con diámetro de 0.2 mm y un detector PSD. Para el calentamiento de la muestra se ha utilizado un calefactor cerámico. El capilar se gira durante las medidas.

Medidas a altas temperaturas se han realizado para la misma muestra Sr_2CdWO_6. Se han obtenido datos de difracción a temperaturas entre 773K y 1120K.

2.2. Medidas de difracción de neutrones en muestras policristalinas

Durante este trabajo, se han realizado experimentos de difracción de neutrones en la mayoría de los compuestos estudiados, con el objeto de estudiar en detalle la evolución de su estructura cristalina con la temperatura. Se han utilizado tres difractómetros diferentes: D20 de alta intensidad y D2B de alta resolución en el Instituto Laue-Langevin (Grenoble, Francia), y E9 (BENSC) de alta resolución en el Instituto Hahn-Meitner (Berlín Alemania).

- **D20 de alta intensidad**

  Se han utilizado neutrones con longitud de onda 1.30Å obtenidos con un monocromador Cu(200) con la resolución $\triangle d/d \approx 16 \times 10^{-3}$. Este instrumento está equipado con un detector que cubre 153.4° en el espacio 2θ; y que está constituido por 1534 celdas de ^{3}He. Las muestras se han colocado en un capilar de vanadio con diámetros de 5mm. La velocidad de calentamiento ha sido de 1K/min.

- **D2B de alta resolución**

  Las medidas de difracción de neutrones se han obtenido a altas y bajas temperaturas en el rango $2\theta = 0 - 160^\circ$ con longitud de onda 1.59432Å obtenidos con un monocromador (Ge 335), que tiene un mosaico relativamente grande extienda de $20'$ para compensar la correspondiente pérdida de intensidad. Es 300 mm de alto, mientras enfocando verticalmente hacia aproximadamente 50 mm; esta divergencia vertical incidente grande se empareja por descubridores de 200 mm de altos detectores y colimadores. Las muestras se han colocado en un capilar de vanadio con diámetros de 5mm.

- **E9 de alta resolución**

  Las medidas de difracción de neutrones se han obtenido a bajas y altas temperaturas en el rango $2\theta = 0 - 160°$, y que está constituido por 1534 celdas de ^{3}He. La longitud de onda es 1.79776Å con una resolución de aproximadamente de 10 min. Las muestras se han colocado en un capilar de vanadio con diámetros de 8mm. Un sistema crióstato-horno permite realizar medidas a Bajas y altas temperaturas se usó entre 15 y 900K.

Es importante mencionar que en las medidas con radiación de neutrones las temperaturas de las transiciones de fase en los diferentes compuestos no se corresponden, siendo considerablemente más bajas, con las encontradas en las medidas con rayos X convencionales. Estas diferencias las hemos atribuido al hecho de que el equipo de alta temperatura utilizado no ha sido suficientemente calibrado.. Por esto, puede que exista una diferencia entre la temperatura medida y la temperatura real de la muestra.

2.3. Refinamiento de Rietveld

Para "determinar"(refinar) las estructuras cristalinas de los compuestos estudiados se ha utilizado el método Rietveld. En este método, se utiliza un modelo inicial de la estructura cristalina (grupo espacial y posiciones atómicas aproximadas) y de los parámetros experimentales (factor de escala, forma de los picos de difracción) para calcular un perfil de difracción simulado.

El perfil simulado se compara con el perfil obtenido experimentalmente; y mediante aproximaciones sucesivas se intentan encontrar los parámetros estructurales y experimentales que resultan en el mejor acuerdo posible entre los perfiles observado y calculado. Esto se consigue minimizando la función:

$$M = \sum w_i (y_i - y_{ci})^2$$

donde y_i es la intensidad observada en el punto **i** del diagrama, y_{ci} es la intensidad calculada en el punto **i** y $w_i = \frac{1}{\sigma^2}$ es el peso asignado a cada punto **i** de intensidad y_i (σ es la varianza asignada a la observación y_i).

La evaluación de la calidad de un refinamiento se realiza mediante las siguientes figuras de mérito (también se utilizan los términos "factores de desacuerdo" y "parámetros de fiabilidad"):

- Factor de desacuerdo de perfil,

$$R_p = \frac{\sum |y_i - y_{ci}|}{\sum y_i}$$

- Factor de desacuerdo de perfil ponderado,

$$R_{wp} = \sqrt{\frac{M}{\sum w_i (y_i)^2}}$$

- Bondad del ajuste,

$$\chi^2 = \frac{M}{N - P - C}$$

  donde N, P y C representan el número de puntos utilizados en el refinamiento, número de parámetros refinados y el número de restricciones del refinamiento (si existen).

- Factor de desacuerdo esperado,

$$R_{exp} = \frac{R_{wp}}{\chi^2}$$

El refinamiento Rietveld de las estructuras se ha realizado utilizando el programa FullProf [40]. Para las medidas de difracción (con la geometría Bragg-Brentano) el fondo continuo se ha aproximado con un polinomio de orden cinco. La forma de los picos de difracción se ha aproximado mediante una función del tipo Pseudo-Voigt.

2.4. Espectroscopia de Resonancia paramagnética electrónica (RPE)

La RPE aporta datos relevantes sobre las propiedades eléctricas y magnéticas de los materiales que poseen átomos con electrones desapareados: en general, proporciona información precisa sobre el estado fundamental y la anisotropía geométrica del entorno del ión paramagnético, así como de posibles interacciones magnéticas entre ellos. De igual manera, la RPE puede proporcionar información sobre los niveles de energía de los elementos estudiados.

La técnica se base en el hecho de que el espín de un electrón puede perder su degeneración natural cuando se aplica un campo magnético, y adoptar cualquiera de las dos orientaciones definidas a lo largo de la dirección del campo. Esta ruptura de la degeneración da lugar a los estados Zeeman caracterizados por una determinada diferencia de energía. Ésta puede estudiarse haciendo incidir sobre la nuestra una radiación electromagnética de frecuencia constante, y variando el campo magnético aplicado. El máximo de absorción se produce cuando la diferencia de energía provocada por el campo coincide con la energía suministrada por la radicación electromagnética. La curva que representa la absorción puede ser lorentziana o gaussiana, y lo que se registra experimentalmente es la derivada de dicha curva. Conociendo la altura a media altura de la curva de los espectros RPE, es posible conocer las posibles interacciones de canje entre iones paramagnéticos próximos, o la existencia de estados de energía excitados cercanos al fundamental. También es de interés conocer la integral de la curva de absorción, ya que es proporcional a la cantidad de espines que resuenan en la muestra.

Dependiendo del estado de oxidación del ión que se esté estudiando, éste dará lugar a señal de RPE o no. Para esto es, precisamente, para lo que se ha hecho uso de esta técnica: para determinar, sin lugar a dudas, el estado de oxidación de los iones Mn: Mn^{2+}, Mn^{3+} y Mn^{4+}. Mn^{2+} y Mn^{4+} dan lugar a señal RPE, distinta, con lo que la técnica se puede utilizar para distinguirlos; y Mn^{3+} no da señal RPE. Así, esta técnica se puede utilizar, como se ha hecho, para saber si el material estudiado contiene Mn^{2+}, Mn^{3+} ó Mn^{4+}.

Los espectros de EPR sobre muestra policristalina de $Sr_2Mn^{2+}WO_6$ y $Sr_2Mn^{3+}WO_{6+\delta}$ han sido registrados a temperatura ambiente en banda X en un espectrómetro Bruker ESP300 equipado con un gausómetro broker ER035M.

2.5. Espectroscopía de absorción de rayos X (XAS)

La Espectroscopia de Absorción de rayos X (XAS) es una de las técnicas más potentes para describir la estructura local de los átomos en diferentes tipos de sistemas, resulta de la absorción de rayos X de alta energía por los átomos en una muestra. Esta absorción ocurre a energías definidas correspondiente a la energía de enlace de los electrones en el material. El electrón expulsado interactúa con los átomos del entorno para producir el espectro observado.

XAS comúnmente se divide en dos regiones espectrales. La primera es absorción de rayos X cerca de la estructura de borde (XANES). El espectro XANES permite determinar su estado electrónico o valencia y la geometría de coordinación. La región más distante del espectro de absorción se denomina Estructura Fina de la Absorción Extendida de Rayos X (EXAFS). El espectro EXAFS proporciona información sobre el número y tipo de átomos vecinos del átomo absorbente, así como los valores de las respectivas distancias entre átomos vecinos. Los experimentos de XAS en Mn K- y WL3- bordes se han realizado en la línea español CRG (SpLine-BM25) del ESRF (European Synchrotron Radiation Facility, Grenoble, Francia). Se ha utilizado como monocromador un doble cristal de Si(111) que produce un haz de salida fija. La eliminación de armónicos se ha llevado a cabo resintonizando en un 70 % la alineación en paralelo de los cristales del monocromador. La energía del electrón haz del anillo era 6 GeV, y la media corriente era 200 mA.

Los espectros de absorción en Mn K-borde y W L3-borde fueron registrados en modo de transmisión utilizando cámaras de ionización como detectores. Se realizaron varias medidas en cada borde para asegurar una proporción de la señal de ruido buena. Las muestras estaban montadas en un horno y se tomaron espectros a varias temperaturas, mientras subiendo la temperatura hasta 875K, y entonces de nuevo a la temperatura ambiente, con un paso de 50K, para observar cualquier variación entre los dos espectros a temperatura ambiente antes y después de tratamiento térmico. El tratamiento de los datos del XANES espectros se realizaron con el programa ATENA [45].

2.6. Espectroscopia Raman

La espectroscopia Raman es una técnica fotónica de alta resolución que proporciona en pocos segundos información química y estructural de casi cualquier material. El análisis de la espectroscopia Raman se basa en el examen de la luz dispersada por un material al incidir sobre aquel un haz de luz monocromático. Una pequeña porción de esa luz es dispersada inelásticamente experimentando ligeros cambios de frecuencia que son característicos del material analizado e independientes de la frecuencia de la luz incidente. Los iones, enlazados químicamente para formar moléculas y redes cristalinas, están sometidos a constantes movimientos vibracionales y rotacionales, estas oscilaciones en torno a las posiciones de equilibrio de los iones se realizan con frecuencias bien determinadas en función de iones que intervienen y del comportamiento dinámico de los enlaces existentes. Un cambio de simetría de la estructura cristalina dará lugar a un cambio en las características de los enlaces, lo que se traducirá en un cambio en el espectro Raman característico del material objeto de estudio.

Se trata de una técnica de análisis que se realiza directamente sobre el material sin que éste, que puede estar en forma policristalina, precise de ningún tipo de preparación especial: es una técnica no destructiva. Los experimentos de espectroscopia Raman son muy fácilmente realizables en condiciones de temperatura variable, así, la espectroscopia Raman se ha convertido en una técnica ampliamente utilizada para caracterizar las posibles secuencias de transiciones de fase inducidas por la temperatura.

Los espectros de Raman sobre muestra policristalina han sido registrados en un espectrómetro HORIBA JOBIN YVON LabRam-HR 800 Raman micro-spectrometer. Las muestras se excitaron con longitud de onda 514.5 nm y una potencia de 30 mW mediante un láser de Ar^+ y un OLIMPUS 100 × objetivo (N.A.=0,5). El enfriamiento y el control de la temperatura se ha realizado con nitrógeno líquido y el calentamiento simultáneo dentro de un calefacción LINKAM THMS 600. La muestra está colocada en un crisol de cuarzo. La temperatura dentro del crisol se verificó midiendo el cambio de TA-LO del phonon de la pulida del cristal de Si. La estabilidad de la temperatura durante la registro de los espectros y la excitación de las medidas estaba alrededor de ∓ 1 °C. Los espectros se registran sin filtro de polarización para el láser incidente y la luz de Raman dispersada. El tamaño y la potencia de la mancha del láser en la superficie son aproximadamente $3\mu m$ y $5mW$. La resolución espectral, determinada por cálculo de la línea Rayleigh es aproximadamente 1.8 cm^{-1}.

Capítulo 3

Química preparativa

En la literatura, se han descrito un gran número de métodos para sintetizar óxidos de perovskitas dobles. No queremos ser exhaustivos, pero, sólo en los últimos años, hemos recogido los siguientes métodos: método cerámico [41, 42], sol-gel [46, 47], método de liofilización [48, 49], reacción de intercambio iónico [50]. Cada uno de ellos tiene sus propias ventajas y desventajas.

En este capítulo vamos a presentar los métodos de preparación utilizados para obtener los materiales estudiados. El objetivo es determinar la influencia del método de preparación sobre la calidad del material y comprender el papel de los parámetros del proceso síntesis, para conseguir sintetizar los compuestos con una buena calidad y de forma reproducible.

3.1. Perovskitas dobles de tungsteno de fórmula general Sr_2MWO_6.

3.1.1. Sr_2CdWO_6

Para preparar la muestra Sr_2CdWO_6 se ha utilizado el método estándar de reacción química en estado sólido. Cantidades estequiométricas de los compuestos primarios se han mezclado de acuerdo con la siguiente ecuación:

$$2SrCO_3 + CdO + WO_3 \rightarrow Sr_2CdWO_6 + 2CO_2\uparrow$$

Los materiales primarios mezclados se han molido y se han calentado en aire sucesivamente a 1120K (24 h), 1170K (24 h) y 1250K (48 h). Después de cada calentamiento, la muestra se ha enfriado lentamente (3K/min), y se han vuelto a moler para mejorar la homogeneidad. Para controlar la calidad de los materiales obtenidos, se han realizado medidas de difracción de rayos X después de cada calentamiento. Hemos obtenido una cantidad de $SrWO_4$ como impureza $\approx$1.7 % (en fracción del peso) en el material.

3.1.2. Sr_2MnWO_6

Para estudiar la influencia del método de preparación sobre la fase $Sr_2Mn^{2+}W^{6+}O_6$, hemos preparado este material utilizando tres métodos: el método cerámico, el método de disolución en Acido Diethylene Triamine Pentaacetic (DTPI) y el método de co-precipitación. A continuación, se describirá el proceso de síntesis de $Sr_2Mn^{2+}W^{6+}O_6$ en el caso de los dos métodos más eficaces: DTPI y co-precipitación; más eficaces en el sentido de tiempo y esfuerzo, y, también, en el sentido de obtener un material de buena calidad. Lo principal de estos métodos consiste a comenzar con una disolución homogénea de los productos de partida.

Muestra 1: $Sr_2Mn^{2+}W^{6+}O_6$, método DTPI

No hemos encontrado ninguna referencia sobre la síntesis de perovskitas dobles por el método DTPI.

Inicialmente, se pesaron cantidades estequiométricas de los correspondientes precursores: WO_3, $SrCO_3$ y $MnCO_3$. Se disolvió la mezcla de los reactivos en una solución diluida de ácido nítrico. Posteriormente, a la disolución resultante se le añadieron cantidades convenientes de $C_{12}H_{20}N_3O_8$ (DTPI) (el número de los moles de DTPI es igual a la suma de los moles de los reactivos) y el amoníaco para conseguir un pH final entre 8 y 10. Se obtuvo una solución completamente homogénea de color amarillo transparente, después de calentar a 370K durante 30 min, y con un control del pH entre 8 y 10. Esta solución llevó a ebullición, hasta que se formó un residuo viscoso (el gel). Este gel, el precursor orgánico, se solidificó después de someterlo a un calentamiento en el horno a 440K, durante 4h. Una vez obtenido este precursor se precedió a la molienda y a la calcinación, a 570K durante 5h y, más tarde, a 720K durante 10 h, para descomponer al precursor orgánico.

El tratamiento térmico final del polvo resultante se realizó en atmósfera de nitrógeno, y fue el siguiente: 1170K (10 h), 1220K (10 h) y 1270K (10 h). Después de cada calentamiento, la muestra se enfrió lentamente, y se volvió a moler para mejorar la homogeneidad. Para controlar la calidad de los materiales obtenidos, se realizaron medidas de difracción de rayos X después de cada calentamiento. Se obtuvo una cantidad pequeña de $SrWO_4$ como impureza (3.35 %) en la fase final de $Sr_2Mn^{2+}W^{6+}O_6$. Por lo tanto, la muestra se obtuvo después de cuatro días de tratamiento, y con una temperatura máxima 1270K.

Muestra 2: $Sr_2Mn^{2+}W^{6+}O_6$, método co-precipitación

El método co-precipitación consiste en utilizar como productos de partida sales, nitratos o compuestos orgánicos, fácilmente solubles en agua. Para sintetizar el material $Sr_2Mn^{2+}W^{6+}O_6$ con el método co-precipitación hemos utilizado cantidades estequiométricas de los nitratos $Sr(NO_3)_2$ (I) , $(OOCH_3)_2Mn{\cdot}4H_2O$ (II), y $(NH_4)_{10}W_{12}O_{41}$ (III). Tras la adición, gota a gota, de la disolución de $(NH_4)_{10}W_{12}O_{41}$ (III) a la mezcla de los disoluciones (I+II) con agitación magnética a temperatura ambiente, hemos obtenidos un precipitado blanco. Después de la evaporación lenta, a una temperatura aproximadamente de 330K, de la disolución final obtenida, hemos obtenido un polvo.

El tratamiento térmico final del polvo resultante se realizó en atmósfera de nitrógeno, y fue el siguiente: 570K, 670K, 770K (8 h a cada temperatura) y 1170K (24 h). Después de cada calentamiento, la muestra se enfrió lentamente, y se volvió a moler para mejorar la homogeneidad. Para controlar la calidad de los materiales obtenidos, se realizaron medidas de difracción de rayos X después de cada calentamiento. El polvo final obtenido de $Sr_2Mn^{2+}W^{6+}O_6$ es de color castaño. En este caso, se obtuvo una cantidad de MnO como impureza ($< 1\,\%$) menor que en el caso anterior. Por lo tanto, la muestra se obtuvo después de 2 días de tratamiento, y con una temperatura máxima 1170K.

Mediante el método co-precipitación se produce un material más puro, se precisa de un tiempo de síntesis más corto y la temperatura de síntesis es más baja.

Muestra 3: $Sr_2Mn^{3+}W^{5+}O_{6+\delta}$

Hemos preparando $Sr_2Mn^{3+}W^{5+}O_{6+\delta}$ a partir de la transformación del material $Sr_2Mn^{2+}W^{6+}O_6$ en aire a 870K, durante 24 h. La muestra se ha calentado y enfriado lentamente (3K/min).

3.1.3. $Sr_2Cd_{1-x}Ca_xWO_6$ ($0 \leq x \leq 1$)

La síntesis de los compuestos de fórmula general $Sr_2Cd_{1-x}Ca_xWO_6$ (x=0, 0.2,0.25,0.4,0.5,0.6,0.75,0.8,1) se ha realizado con el método co-precipitación, a partir de los compuestos primarios $Sr(NO_3)_2$, $Cd(NO_3)_2{\cdot}4H_2O$, $Ca(OOCH_3)_2$ y $(NH_4)_{10}W_{12}O_{41}$. El tratamiento térmico que se ha realizado para todas muestras, ha sido el siguiente: 470K (12 h), 670K (12 h), 870K (12 h), 1170K (24 h) y 1270K (24 h). Para controlar la calidad de los materiales obtenidos, se han realizado medidas de difracción de rayos X después de cada calentamiento. Hemos obtenido una fase pura para los compuestos ($x = 0.2, 0.8, 1$), y una cantidad pequeña de $SrWO_4$ como impureza ($\leq 3\,\%$) en los compuestos. ($x = 0, 0.4, 0.6$).

Después de la comparación de las dos muestras de Sr_2CdWO_6 preparadas con el método cerámico y el método co-precipitación (el caso de la solución sólida), se observa que la muestra preparada con el segundo método presenta un material con menos impureza.

Después de preparar los materiales de la familia de wolframio con fórmula general Sr_2MWO_6 con los diferentes métodos: método cerámico, método sol-gel y el método co-precipitación, podemos concluir que el método co-precipitación produce el material más puro.

3.2. Perovskitas dobles de antimonio de fórmula general $A_{2-x}A'_xMSbO_6$

Como se ha mencionado, el método de co-precipitación consiste en utilizar como productos de partida sales, nitratos o compuestos orgánicos, fácilmente solubles en agua. El antimonio existe sólo en dos formas de óxido como compuesto primario: Sb_2O_3 y Sb_2O_5. Estos dos óxidos de antimonio no se disuelven totalmente en agua, por eso, no es posible preparar los compuestos de la familia de antimonio con este método.

El formato óxido de los compuestos primarios nos permiten de preparar los materiales de antimonio con el método cerámico y con el método sol-gel. Para estudiar la influencia del método de preparación sobre la calidad de los materiales de la familia de antimonio, hemos preparado en el primer lugar el material Sr_2AlSbO_6 mediante estos dos métodos.

3.2.1. Sr_2AlSbO_6

Muestra 1: Sr_2AlSbO_6, método sol-gel

El método sol-gel está basado en la obtención de complejos metálicos, a partir de soluciones concentrados de ácidos polifuncionales y sales u óxidos de los cationes necesarios para la formación de los óxidos mixtos. El acido orgánico utilizado en este preparación es el ácido cítrico de fórmula general $C_3H_4OH(COOH)_3$.

La muestra Sr_2AlSbO_6 se preparó a partir de cantidades equimoleculares de los siguientes compuestos primarios: Sb_2O_5, $Al(NO_3)_3 \cdot 9H_2O$ y Sr_2CO_3. Inicialmente, se disolvió 1 mol de Sb_2O_5 en una solución de ácido cítrico (en una relación metal-ácido 1:3), y se revolvió hasta conseguir la disolución total del óxido. Después, cantidades estequiométricas de de Sr_2CO_3 y $Al(NO_3)_3 \cdot 9H_2O$ se disolvieron en la misma solución, y se dejaron durante 1 hora para asegurar la complexación. Posteriormente, a la disolución resultante se le añadieron cantidades adecuadas de etilenglicol ($OH - CH_2 - CH_2 - OH$) (3/4 mol de etileno por 1 mol de ácido cítrico), para evaporarla posteriormente hasta la formación de un polímero intermedio, cuyo tiempo de obtención aproximado fue de 1 h. Este compuesto se solidificó a 370K en un baño de arena, formándose un gel. Este gel se solidificó después de someterlo durante 24 h en el horno a la temperatura de 720K para eliminar el precursor orgánico. Una vez obtenido este precursor se procedió a la molienda y a la calcinación en aire a 1220K (10 h) y a 1270K (10 h). El último calentamiento se realizó a 1370K en atmósfera de oxígeno, para asegurar el contenido adecuado de oxígeno en la muestra.

Al final, hemos obtenido un material puro y con un grado de ordenamiento entre los cationes Al^{3+} y Sb^{5+} del 91 %.

Muestra 2: Sr_2AlSbO_6, método cerámico con acetona.

Para preparar la muestra Sr_2AlSbO_6 se ha utilizado el método cerámico con acetona. Cantidades estequiométricas de los compuestos primarios se han mezclado de acuerdo con la siguiente ecuación:

$$4SrCO_3 + Al_2O_3 + Sb_2O_5 \rightarrow 2Sr_2AlSbO_6 + 4CO_2.$$

Los materiales primarios mezclados se han molido con acetona para obtener asegurar la mayor homogeneidad posible, y se han calentado en aire sucesivamente a 870K (6 h), 1270K (24 h) y 1470K (24 h), 1670K (24 h) y, finalmente, a 1770K durante 72 h. Después de cada calentamiento, la muestra se ha enfriado lentamente, y se han vuelto a moler con acetona para mejorar la homogeneidad. Se ha obtenido un material puro y con mayor grado de ordenamiento (98 %, casi completo) entre los cationes Al^{3+} y Sb^{5+}.

El material obtenido mediante los dos métodos tiene una buena calidad (puro), pero con un grado de ordenamiento entre los cationes Al^{3+} y Sb^{5+} mayor, 98 % obtenido en el caso del método cerámico.

3.2.2. $A_{2-x}A'_xMSbO_6$

Después de comparar los dos métodos, hemos decidido de preparar todos los compuestos de este familia con el método cerámico con acetona y los mimos tratamientos térmicos, para eliminar sus efectos sobre el estudio del ordenamiento catiónico en este trabajo. Cantidades estequimétricas de los correspondientes compuestos precursores se han mezclado de acuerdo con las siguientes ecuaciones:

◇ Sr_2CoSbO_6

$$4SrCO_3 + 2Co(C_5H_7O_2)_3 + 10O_2 + Sb_2O_5 \rightarrow 2Sr_2CoSbO_6 + 14CO_2 + 14H_2O.$$

◇ A_2MSbO_6 (A=Ca,Sr) (M=Cr,Ga,Fe,Mn,Sc,Sm,La)

$$4SrCO_3 + M_2O_3 + Sb_2O_5 \rightarrow 2Sr_2MSbO_6 + 4CO_2.$$

◇ $Ca_{2-x}Sr_xLnSbO_6$ (Ln=La,Sm) $(x = 0, 0.5, 1)$

$$2(2\text{-}x)CaCO_3 + 2xSrCO_3 + Ln_2O_3 + Sb_2O_5 \longrightarrow 2Ca_{2-x}Sr_xLnSbO_6 + 4CO_2.$$

Parte II

Estructuras cristalinas y transiciones de fase en la familia de wolframio $\mathrm{Sr_2M_{1-x}M'_xWO_6}$

4.1. Introducción

En la figura 1, se resumen parte de los resultados experimentales obtenidos por el Dr. Gateshki, durante la realización de su trabajo de tesis doctoral, para los miembros estudiados de la familia de wolframio (Sr_2BWO_6, B=Ca,Zn,Co,Ni,Mg,). La figura recoge la secuencia de transiciones de fase en los diferentes materiales frente al factor de tolerancia; son varias las conclusiones que se pueden deducir.

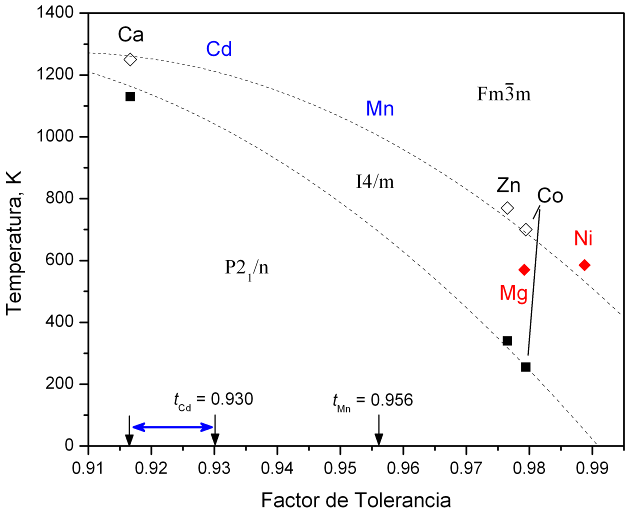

- Primero, tres compuestos (Sr_2BWO_6, B=Ca,Zn,Ni), representados mediante cuadrados negros y rombos blancos, muestran la misma secuencia de dos transciones de fase:

  $$P2_1/n \text{ (monoclínico, “setting” no estándar)} \longrightarrow I4/m\text{(tetragonal)}\longrightarrow Fm\bar{3}m,$$

  mientras que Sr_2MgWO_6 y Sr_2NiWO_6, en rojo, solo presentan una transición de fase

  $$I4/m \longrightarrow Fm\bar{3}m,$$

  y las correspondientes temperaturas de transción no parecen estar relacionadas con las de los tres primeros compuestos.

- Segundo, por lo dicho, parece que los tres compuestos, no sólo presentan una secuencia de transciones de fase común, si no que parece que las temperaturas de transción están relacionadas: cuanto mayor es el factor de tolerancia menores son las temperaturas de transición, y, además, parece que de una manera más o menos lineal (línea punteada).
  Dicho de otra manera, una relación adecuada de tamaños de cationes en las posiciones de

tipo B de la perovskita doble (estando fijo el catión en la posición) B′, W, decrece el tamaño del catión B), estabiliza a temperaturas menores, eventualmente a temperatura ambiente, una fase con una simetría cada vez mayor.

- ◇ Tercero, de igual modo, cuanto mayor es el factor de tolerancia, mayor es el rango de estabilidad de la fase tetragonal ($I4/m$), intermedia entre la $P2_1/n$ monoclínica de temperatura ambiente y la cúbica prototipo $Fm\overline{3}m$.

En la siguiente figura se recoge la evolución de los vólumenes, a temperatura ambiente, frente al factor de tolerancia de las celdas unidades de los diferentes materiales estudiados por el Dr Gateshki, cuadros negros; en círculos blancos se ha representado lo mismo, pero calculado teóricamente, mediante el programa SPUDS [51]. En este caso también, se pueden deducir varias conclusiones.

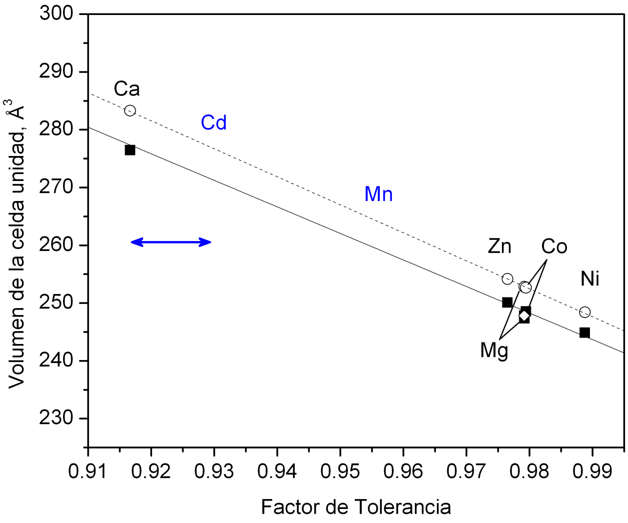

- ◇ Primero, los resultados experimentales concuerdan bastante bien con los teóricos: la diferencia entre los valores experimentales y teóricos es del 10 %.
- ◇ Segundo, a pesar de que las simetrías de las fases de temperatura ambiente son diferentes, los volúmenes de las celdas unidades están correlacionados: cuanto mayor es el tamaño del catión en la posición B, tanto mayor es el volumen de la celda unidad correspondiente.
- ◇ Tercero, además, la mencionada correlación es lineal.

El objetivo de la primera parte del estudio resumido en la presente memoria ha sido comprobar que efectivamente existe una correlación entre el factor de tolerancia y las temperaturas de transición, las secuencias de las transiciones de fase, la extensión del rango de estabilidad de la fase tetragonal intermedia y el volúmen de la celda unidad a temperatura ambiente (independientemente de la simetría). Como el factor de tolerancia es una medida del tamño relativo de los cationes presentes en las posciones B y B′ de la perovskita doble, y como uno de los cationes está fijo (B′=W), y el factor de tolerancia es una medida de la distancia entre los cationes B y B′ (mediada por los oxígenos que comparten). En definitiva, el objetivo ha sido completar el diagrama de fases presentado en la figura 1: esto es, obtener un diagrama de fase en términos de un factor geométrico (estérico).

El objetivo se abordó de la siguiente forma:

- ◇ Se decidió intercalar algún material con factor de tolerancia intermedio entre el de los compuestos de Ca y Zn. Se eligierón los cationes Cd y Mn. (En color azul en la figura 1.)

- ◇ Además, se intentó saber si podrí cambiar de manera contínua el factor de tolerancia, sintetizando una solución sólida, en este caso entre los compuestos con Ca y Cd. (Flecha azul en la figura 1.)
  En este caso, también, se buscaba saber si incluso para una solución sólida se mantenían las características observadas para los miembros “puros” de la familia.

- ◇ Finalmente, el caso del Mn se consideró especialmente interesante puesto una publicación relativamente reciente asignaba a temperatura ambiente un grupo espacial que no era ninguno de los observados en el resto de los miembros de la familia

4.2. Sr$_2$CdWO$_6$

El primer estudio sobre Sr$_2$CdWO$_6$ se presentó en [52]. A la estructura de este compuesto a temperatura ambiente se le asignó el grupo espacial $Pmm2$, debido a las propiedades piezoeléctricas observadas; aunque en el trabajo no se presentaron evidencias experimentales piezoeléctricas. La estructura propuesta permite ordenamiento de los cationes de tipo B y además permite, también, la presencia de momento dipolar. La estructura se resolvió haciendo uso de datos de difracción de rayos x de laboratorio: ésta se caracteriza por tener los octaedros WO$_6$ y CdO$_6$ deformados, pero no girados; además, los cationes W^{6+} y Cd^{2+} se encuentran desplazados de los centros de sus respectivos octaedros. En el trabajo [53] la estructura de Sr$_2$CdWO$_6$ se ha determinado como tetragonal, pero sin especificar más detalles.

El estudio en temperatura presentado en [52] incluye medidas DTA y una resolución estructural a 860 °C (1133 K). Las medidas DTA presentan una anomalía térmica reversible alrededor de 807 °C. La estructura a 860 °C se refinó en el grupo cúbico $Fm\bar{3}m$.

4.3. $Sr_2Cd_{1-x}Ca_xWO_6$

Ésta no es la primera vez que se sintetizan y se estudian soluciones sólidas de materiales que presentan estructuras de perovskita doble; por ejemplo, en los trabajos [54, 55, 56] se estudia el efecto en la posible aparación de transiciones de fase estructurales del tamaño del catión de tipo A, y en los trabajos [57, 58], se estudia el efecto del tamaño del catión de tipo B. De todas formas, en todos los casos citados, sólo se presentan las resoluciones estructurales a temperatura ambiente y las transiciones de fase inducidas por la sustitución sólo a temperatura ambiente. Por lo tanto, hasta donde sabemos, ésta es la primera vez que se obtienen las estruturas y las transiciones de fase inducidas por la evolución en temperatura en una solución sólida con estructura de perovskita doble.

4.4. Sr_2MnWO_6

La primera vez que se referencia el compuesto Sr_2MnWO_6 es en [59], y se afirma que es cúbico, con el siguiente parámetro de celda: $a = 8.01$ Å; el estudio se realizó a temperatura ambiente y se utilizó difracción de neutrones. Posteriormente, el grupo de A.K. Azad describió este material como tetragonal y le asignó el grupo espacial $P4_2/n$ [60], que es uno de los posibles grupos tetragonales permitidos para las perovskitas dobles, pero que hasta ese momento no se había asignado nunca a una perovskita doble de la familia del wlframio, y, demás, rara vez ha sido asignado a perovskitas dobles. Existe un tercer trabajo [61] sobre este material, en el que en este caso se afirma que es monoclínico, con el grupo espacial $P2_1/n$. Como se afirma en [61], en la descripción tetragonal en el grupo espacial $P4_2/n$ aparecen tres posiciones independientes para los cationes Sr^{2+}, y el volumen de la celda unidad es prácticamente el doble que el de la celda unidad en la descripción monoclínica en el grupo $P2_1/n$. Estos mismo autores realizaron un refinamiento de sus datos utilizando como modelo de partida la descripción tetragonal de [60], y encontraron que los factores de acurdo en este caso eran algo peores que en la descripación monoclínica. Así, su conclusión fue que la estructura podía describirse mejor utilizando una celda menor y menos parámetros libres, y se inclinaron por asignar el grupo monoclínico. Es más, estos mismos autores encuentraron que la distorsión monoclínica era muy pequenña, que es un efecto muy conocido en la perovskitas dobles con una caracter marcadamente pseudo-cúbico. Finalmente, el grupo de A.K. Azad ha realizó un estudio a altas temperaturas (295, 573, 773 y 973 K), mediante difracción de neutrones. Según sus datos, la estructura de Sr_2MnWO_6 sigue siendo tetragonal a 573 K; sin embargo, a más altas temperaturas encuentran dos transiciones de fase estructurales: a 773 K la estructura pasa de un grupo espacial con una celda primitiva a uno con una celda centrada en el cuerpo ($I4/m$), y a 973 K, la estructura transforma al grupo cúbico $Fm\overline{3}m$ de la fase prototipo de las perovskitas dobles.

Todavía queda trabajo por hacer en esta familia: no está claro porqué los compuestos Sr_2MgWO_6 y Sr_2NiWO_6 quedan fuera del esquema, en cuanto a las temperaturas de transición y en lo que respecta a las secuencias de las transiciones de fase. Además, sería conveniente introducir algún otro material, con un factor de tolerancia intermedio, pero que resulte de una sustitución, por un lado; y, por otro lado, habría que intentar conseguir un material que siendo una sustitución tenga el mismo valor del factor de tolerancia que otro que sea del tipo "puro" (Sr_2BWO_6). Si estos dos materiales encajan en las dos figuras anteriores, la conclusión es que, al menos en esta familia de perovskitas dobles (totalmente ordenadas), son factores estéricos los que gobiernan las posibles transiciones de fase (sin tener en cuenta la simetría) y las temperaturas de las transiciones de fase.

En esta familia del wolframio, los estados de oxidación de los cationes B y B′ (W) son 2+ y 6+, respectivamente.

Capítulo 5

Crystal structure and phase transitions of Sr_2CdWO_6

5.1. Results and discussion

At all temperatures covered, the 2θ region chosen (71.5-73.5) for the phase transition search contains a group of diffraction peaks that has been identified as especially sensitive to the structural changes occurring in double perovskite materials [43]. This experiment showed that the only changes that can be interpreted as indications of phase transitions are the appearance of a shoulder on the low-angle side of the peak, at 1105K (Fig. 1); and the subsequent unification of this shoulder with the main peak, occurring at about 1220K. This behavior is very similar to that observed in Sr_2CaWO_6 [43], where these changes were interpreted as evidences of the material undergoing two phase transitions; first, from monoclinic structure to tetragonal one, and (at higher temperature) from tetragonal to cubic. To clarify the structural changes occurring in Sr_2CdWO_6, high-resolution diffraction measurements using synchrotron radiation were performed at three different temperatures: 300K, 770K and 1120K. It was not possible to reach higher temperatures due to instrument limitations.

The diffraction pattern collected at 300K is shown in Fig. 2. The attempt to refine the structure of Sr_2CdWO_6 using a structural model with the $Pmm2$ space group, as suggested previously [52], gave a reasonably good fit of the diffraction profile: no unindexed lines or large differences between the experimental and calculated intensities were observed. However, many fine details in the pattern were not well accounted for by the model. These problems were successfully solved by performing a refinement based on the monoclinic structure with space group $P2_1/n$ observed in many double perovskite compounds [54, 55, 62, 63], including several compounds with the general formula Sr_2MWO_6 [41, 42, 64]. One example of a diffraction reflection where the monoclinic

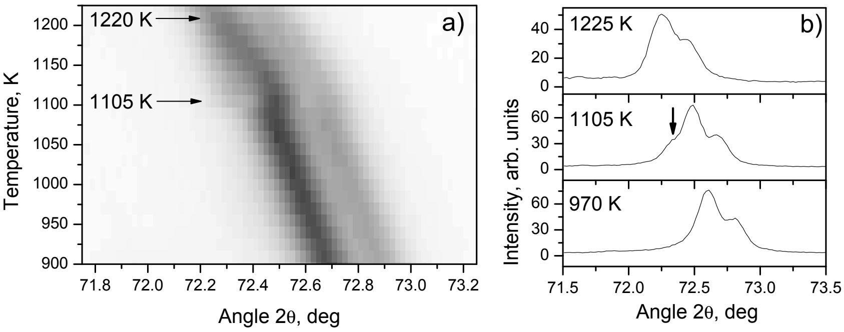

FIGURA 5.1: Temperature evolution of the (620) cubic reflection of Sr_2CdWO_6. In (a), scattered intensity is represented with shades of gray–black corresponds to high intensity and white to low intensity. The tetragonal splitting existing in the temperature range from 1105 to about 1220K can be observed. The shoulder appearing at 1105K is marked with an arrow in (b).

model gives improvement, is shown on Fig. 3. The peak located at higher 2θ angle is considerably broader than the peak at lower angle, also shown on the figure. This difference in the widths of the two peaks can be easily explained as a result of a monoclinic distortion of the unit cell, while the orthorhombic structural model is not able to reproduce this experimental observation. The better visual fit of the experimental data with the $P2_1/n$ model is accompanied, also, with significant improvement in the agreement factors of the refinement.

In the diffraction data collected at 770K, the presence of the monoclinic distortion is even clearer. There is a visible splitting (middle panel of Fig. 4c) of the peak, caused by the difference in 2θ positions of the (-404) and (404) reflections. The structural details of Sr_2CdWO_6 at room temperature and 770K, refined by assuming monoclinic lattice and the $P2_1/n$ space group, are shown in Table 1.

With respect to the piezoelectric properties observed for Sr_2CdWO_6 in [64], it should be pointed out that a structure with the $P2_1/n$ space group, which is centrosymmetric, can not present such properties. If the crystal structure had a symmetry described by some of the non-centrosymmetric subgroups of $P2_1/n$: $P2_1$, Pn or $P1$, additional diffraction peaks should be observed, since these space groups have different extinction conditions. Such additional peaks could not be observed in our diffraction data, and it was not possible, on the base of the collected X-ray powder diffraction data, to confirm that Sr_2CdWO_6 is non-centrosymmetric.

Before analyzing the structure of Sr_2CdWO_6 at 1120K, it should be noted that the diffraction experiment at this temperature (Fig. 5) shows that the weight fraction of $SrWO_4$ increases to about 4 %, indicating partial decomposition of the sample. Also, at this temperature, several low intensity peaks appear that are incompatible with the perovskite structure. Through search-match procedure, these peaks were identified as originating from quartz, and are probably due to crystal-

TABLA 5.1: Crystal structure data and refinement results for Sr_2CdWO_6 at 300K, 770K and 1120K. The atomic positions (in fractional coordinates) and isotropic atomic displacement parameters were refined in the space group $P2_1/n$, $P2_1/n$ and $I4/m$, respectively.

Temp. Space Group R. factors	Lattice Parameters (Å)	Atom	Wyck. Pos.	x	y	z	B_{iso}(Å^2)
300K	$a = 5.7463(1)$	W	2a	0	0	0	0.5(1)
$P2_1/n$	$b = 5.8189(1)$	Cd	2b	$1/2$	$1/2$	0	0.7(1)
$R_{wp} = 7.18\,\%$	$c = 8.1465(1)$	Sr	4e	0.0081(7)	0.5375(1)	0.2508(3)	0.9(1)
$R_B = 4.29\,\%$	$\beta = 90.071(1)$	O1	4e	0.089(1)	0.021(2)	-0.23(1)	2.7(1)
$\chi^2 = 11.6$		O2	4e	0.254(2)	-0.194(2)	0.032(2)	2.7(1)
		O3	4e	0.182(2)	0.250(2)	0.058(2)	2.7(1)
773K	$a = 5.7905(1)$	W	2a	0	0	0	0.7(1)
$P2_1/n$	$b = 5.8122(1)$	Cd	2b	$1/2$	$1/2$	0	1.2(1)
$R_{wp} = 7.19\,\%$	$c = 8.1974(1)$	Sr	4e	0.0050(1)	0.5261(3)	0.2512(5)	1.8(1)
$R_B = 4.06\,\%$	$\beta = 90.091(1)$	O1	4e	0.073(3)	0.024(2)	-0.216(2)	3.9(1)
$\chi^2 = 9.86$		O2	4e	0.282(2)	-0.203(2)	0.009(3)	3.9(1)
		O3	4e	0.179(3)	0.264(3)	0.046(2)	3.9(1)
1120K	$a = 5.8273(1)$	W	2a	0	0	0	1.5(1)
$I4/m$	$c = 8.2564(1)$	Cd	2b	0	0	$1/2$	2.2(1)
$R_{wp} = 8.02\,\%$		Sr	4d	0	$1/2$	$1/4$	3.4(1)
$R_B = 4.5\,\%$		O1	4e	0	0	0.230(2)	6.1(1)
$\chi^2 = 14.1$		O2	8h	0.265(2)	0.181(3)	0	6.1(1)

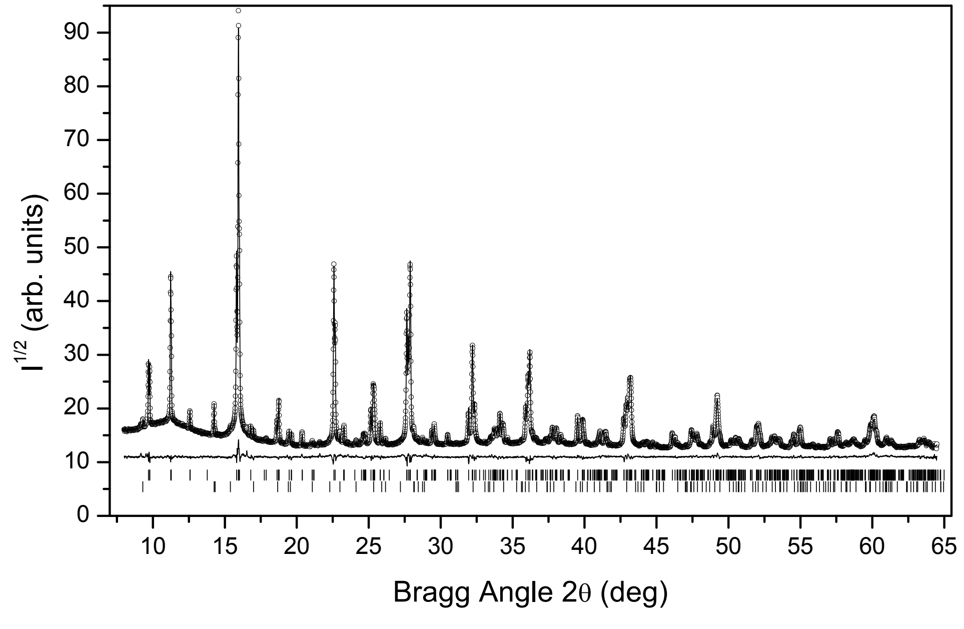

FIGURA 5.2: Experimental (symbols) and calculated (line) powder diffraction profiles for the Rietveld refinement of Sr_2CdWO_6 at room temperature using a structural model with $P2_1/n$ space group. The bars in the lower part of the graphics represent the Bragg peak positions of main phase and the $SrWO_4$ impurity (lower set of bars).

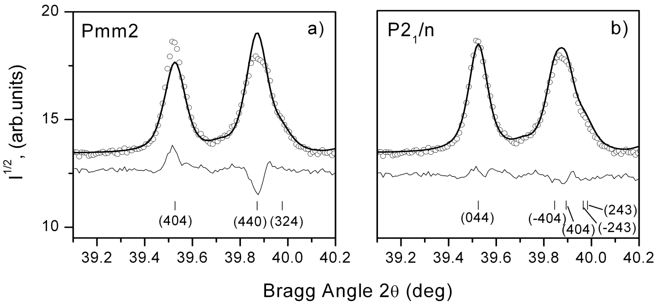

FIGURA 5.3: Experimental diffraction data for Sr$_2$CdWO$_6$ at 300K (symbols) compared with the diffraction patterns calculated after refinement (lines) using structural models with symmetries $Pmm2$ (a) and $P2_1/n$ (b). Only the monoclinic model reproduces correctly the diffraction intensities observed in the experiment.

lization process in the material of the capillary tube.

Regarding the Sr$_2$CdWO$_6$ material under study, there are several important observations that can help identify its structural type at 1120K. For example, all diffraction peaks with indices of the type $h + k + l = 2n + 1$ present at lower temperatures are missing at 1120K (see Fig. 4a). This shows that there is a change from a primitive unit cell to a body-centered one. Also, while some of the peaks remain split (Fig. 4b) at this temperature, others are well represented by a single diffraction reflection (Fig. 4c). Analyzing the peak splitting, it becomes clear that at 1120K the unit cell is tetragonal.

If this result is compared with the list of the possible double perovskite structures suggested by group-theorethical analysis (Fig. 1 [41], Fig. 1 [38]), it can be assumed that at 1120K Sr$_2$CdWO$_6$ has the symmetry $I4/m$ (tilt $a^0a^0c^-$). The pattern calculated using this symmetry accounts for all important features of the experiment (Fig. 5) and provides reasonably good agreement factors. Structural details for Sr$_2$CdWO$_6$ at 1120K are given in Table 1. It can be seen that the isotropic atomic displacements of the oxygen atoms are rather large even considering that the experiment is performed at high temperature. Refinement of the structure was attempted also with the space group $I4$ which allows not only octahedral rotations but also atomic displacements along the c-axis. This did not lead to any improvement of the agreement factors despite the increased number of refinable atomic coordinates. One likely cause for for the unusually large isotropic displacements of the oxygen atoms is the modified chemical composition of the material due to the ongoing decomposition process.

The tetragonal distortion of the unit cell at 1105K also is responsible for the peak splitting observed in Fig 1. As already mentioned, this splitting gradually disappears at higher temperature (upper panel of Fig 1b), and suggests that at a temperature of about 1220K the unit cell is converted to cubic. This cubic phase most probably has the symmetry of the aristotype double perovskite structure with space group $Fm\bar{3}m$. It was not possible to confirm this hypothesis through structural

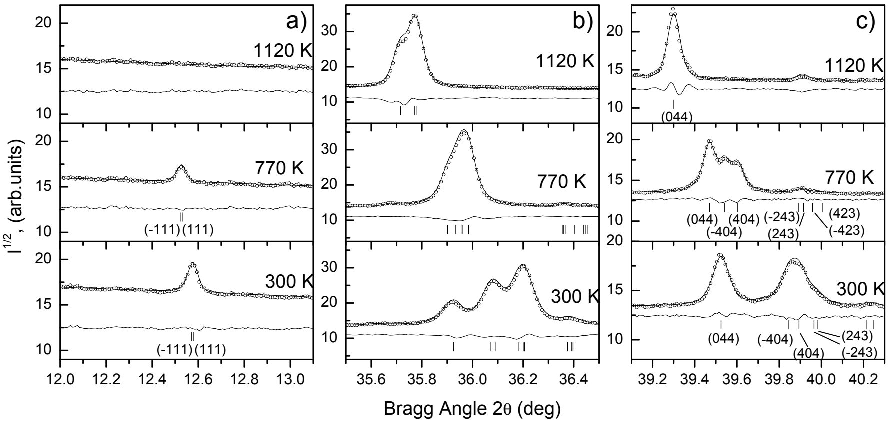

FIGURA 5.4: Temperature evolution of three groups of diffraction peaks located at different 2θ positions. The calculated and difference diffraction profiles (lines) are obtained after Rietveld refinement of the structure at each temperature. The structural models used in the refinement have the following symmetries: $P2_1/n$ for 300 and 770K, and $I4/m$ for 1120K. For clarity, only the Bragg positions of the main phase are shown as bars in the lower part of the graphics.

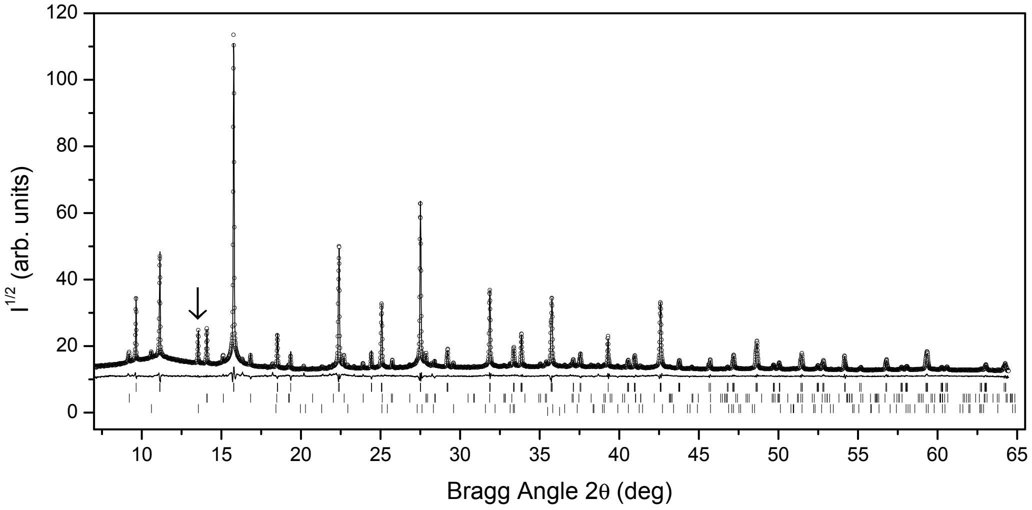

FIGURA 5.5: Experimental (symbols) and calculated (line) powder diffraction profiles for the Rietveld refinement of Sr_2CdWO_6 at 1120K using a structural model with $I4/m$ space group. The bars in the lower part of the graphic represent the Bragg peak positions of the main phase, the $SrWO_4$ impurity (middle set of bars) and SiO_2 (lower set of bars). The arrow points to the most intense diffraction peak of SiO_2.

refinement, due to the instrumental limitations, and to the fact that at this temperature the decomposition process accelerates (note the diminished intensity of the peak shown in the upper panel of Fig 1b, compared to the other two temperatures). Further studies are required to confirm the presence of the cubic phase at high temperatures and to establish its symmetry.

The structural analysis based on the presented temperature-dependent high-resolution diffraction experiments suggests that the phase transition sequence existing in Sr_2CdWO_6 is $P2_1/n \rightarrow I4/m \rightarrow Fm\overline{3}m$; being the first transition discontinuous, and the second one continuous. The same sequence is known to exist in many other double perovskites [65], including Sr_2BWO_6 (B=Co,Zn,Ca) [41, 42], suggesting that the temperature evolution of their structures is governed by the same principles. It is usually assumed [65] that the driving force of the structural changes in this kind of materials is the mismatch between the size of the A cation (Sr^{2+} in this case) and the interstitial space between the BO_6 and $B'O_6$ octahedra. This mismatch is measured by means of the so-called tolerance factor [66]:

$$t = \frac{d_{A-O}}{\frac{1}{\sqrt{2}}\left(d_{B-O}+d_{B'-O}\right)}$$

The mean d_{A-O}, d_{B-O} and $d_{B'-O}$ bond lengths can be obtained from tables of ionic radii [3] or by calculating the distances that give the nominal oxidation states of the cations in the bond-valence method [67, 68]. Fig. 6 shows the phase transition temperatures as a function of the tolerance factor t, calculated using the second method. As the figure shows, the phase transition temperatures increase at lower values of t. Also, the temperature range in which the tetragonal phase exists is narrower at low t. These results are very similar to those observed in Rb_2KBF_6 (B=Sc,In,Lu,Er,Ho) elpasolites [69], and confirm that the most important factor governing the appearance of octahedral tilts in the double perovskite structure and the temperature range in which they exist is the mismatch between the size of the A cation and interstitial space between the BO_6 and $B'O_6$ octahedra. There is one exception, however, and this is the case of Sr_2MgWO_6. This compound has a tolerance factor that is very close to that of Sr_2CoWO_6 but considerably lower temperature of the cubic-to-tetragonal transition. Also, the low-temperature studies of this compound [43] showed that the tetragonal structure is preserved at least down to 26K, while in Sr_2CoWO_6 the monoclinic phase is observed below 250K [41, 42]. This suggests that other factors can also influence the phase transition temperatures. Such factors could be the presence of oxygen or cation vacancies, and the electronic properties of the particular cations. If the lattice parameters of Sr_2MgWO_6 [43] are compared with those obtained in other recent studies, [70, 71, 72] using also different precursor materials and synthesis temperatures, it can be seen that they are within 0.1 % of each other. This makes unlikely the presence of excessive amount of vacancies in our sample and also any other synthesis related effect. The temperature of the tetragonal-cubic phase transition reported in [70] is identical (570K) to the one observed in our previous study. Similarly, low temperature studies of Sr_2MgWO_6 [72] show that the tetragonal phase is retained down to 15K. Further studies are required to establish the reason for Sr_2MgWO_6 not following the general trend observed in Fig 6.

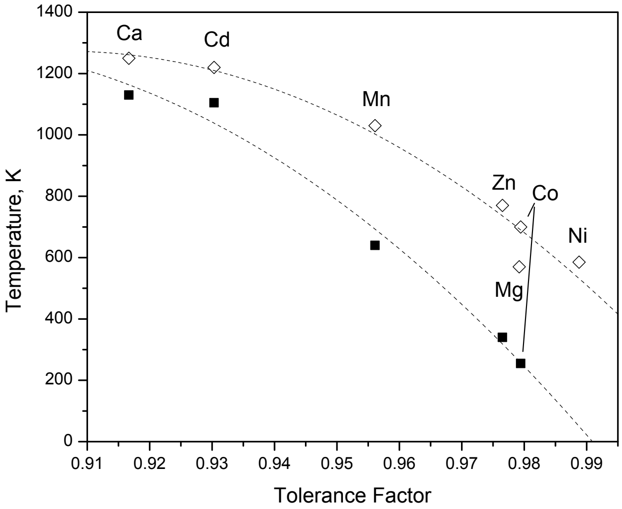

FIGURA 5.6: Phase transition temperatures of Sr_2MWO_6 compounds, as a function of their tolerance factors. The temperature values used were taken from previously reported studies: [43], for M=Ca,Mg; [41], for M=Zn,Co,Ni; and [73], for M=Mn. Open diamonds represent the tetragonal-cubic transition, and solid squares represent the monoclinic-tetragonal transition (if existing) in each compound. Lines are guides to the eye.

If the unit cell volumes at ambient temperature of the studied double perovskite oxides is plotted as a function of the tolerance factor (Fig. 7), a linear dependence can be observed. This, again, reinforces the result that structural properties of double perovskites are predetermined by the cationic radii. On the same figure the unit cell volumes calculated for the studied compounds using the program SPuDS (Version2–Creation date December 2005) [51, 62] are given. For each compound the tilt pattern observed in the experiment was used in the calculation. The calculated values have a linear dependence on the tolerance factor with the same slope observed in the experiment. The only difference is that the calculated values slightly overestimate the unit cell volumes for all compounds.

5.2. Conclusions

The crystal structure of Sr_2CdWO_6, prepared by solid state reaction, was determined by high-resolution X-ray diffraction at different temperatures. At ambient temperature, the crystal structure of Sr_2CdWO_6 was found to be monoclinic with the space group $P2_1/n$, which is different from the previously reported orthorhombic ($Pmm2$) structure. Sr_2CdWO_6 undergoes a phase transition at 1105K above which the structure becomes tetragonal ($I4/m$). The high-temperature diffraction data also suggest that there is another phase transition at around 1220K, which transforms the

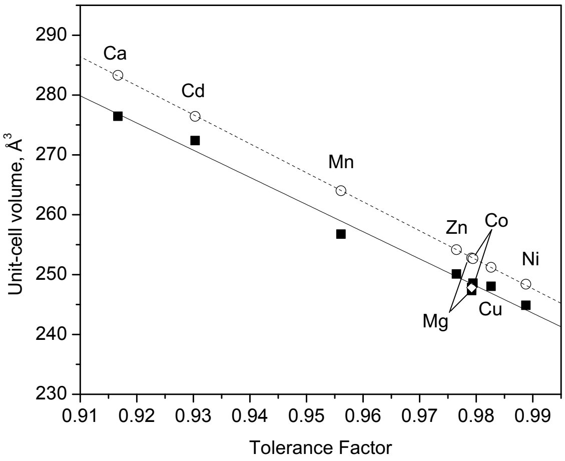

FIGURA 5.7: Variation of the unit-cell volumes at ambient temperature of Sr_2MWO_6 compounds, as a function of the tolerance factor. Both the experimental values (solid squares) and those calculated with the program SPuDS (open circles) show linear dependence with the same slope. The unit-cell volume of Sr_2MgWO_6, obtained from the structural data given in the work by Khalyavin *et al.* [51], is also included as a reference (open diamond).

structure to cubic. The mechanism of these phase transitions is related to the mismatch of the size of the A cation and the cuboctahedral space between the WO_6 and CdO_6 octahedra. The bigger size of the Cd^{2+} cation, with respect to that of some other members of the Sr_2MWO_6 family, such as Co^{2+} and Ni^{2+} cations, for instance, leads to a structure with lower symmetry at room temperature. When the phase transition temperatures of Sr_2CdWO_6 are compared with those of other compounds of the Sr_2MWO_6 family reported previously, it becomes clear that the transition temperatures increase at low tolerance factors, and, that, at the same time, the temperature range in which the intermediate tetragonal phase exists is reduced. This comparison also showed that the temperature-dependent structural evolution of the Sr_2MgWO_6 compound considerably deviates from the general trend observed in the rest of the Sr_2MWO_6 materials.

Capítulo 6

Synthesis, Structures and Temperature-induced Phase Transitions of the $Sr_2Cd_{1-x}Ca_xWO_6$ ($0 \leq x \leq 1$) Double Perovskite Tungsten Oxides

6.1. Results and Discussion

6.1.1. Room-temperature structures

Figure 1a shows the room-temperature x-ray powder diffraction patterns for the various compositions of $Sr_2Cd_{1-x}Ca_xWO_6$, in the 17–82 degree 2θ range. Based on a visual inspection of the room-temperature x-ray powder diffractograms (Fig. 1b), as there is a continuous change in the position of the peaks and in their form, evolving from the Cd-containing compound to the Ca-containing one, it is clear that the substitution of the Cd cation by Ca gives rise to a continuous solid solution: all the compositions are in a double perovskite phase with good homogeneity. As mentioned, the end-members of this solid-solution crystallize, at room-temperature, in a monoclinic symmetry ($P2_1/n$) [41, 43]. Thus, we expected that the members of the solid solution also crystallize in the same space group. Indeed, for all the studied compositions, all the reflections in each diffractograms, could be indexed in the $P2_1/n$ space group. We performed two sets of refinements: in

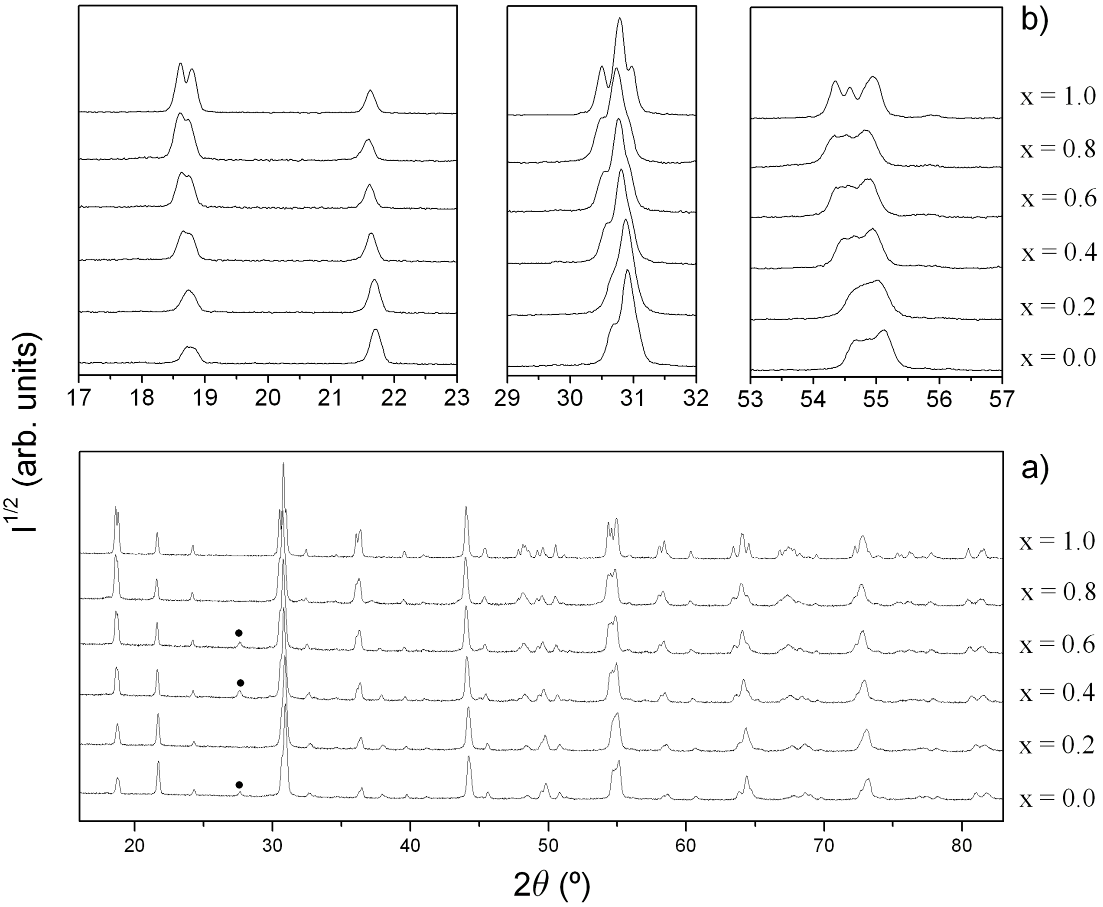

FIGURA 6.1: (a) Evolution of the laboratory x-ray powder diffraction patterns of $Sr_2Cd_{1-x}Ca_xWO_6$: $x = 0.0, 0.2, 0.4, 0.6, 0.8, 1.0$. The bullet (●) indicates the small impurity, $SrWO_4$, only present in the $x = 0.0, 0.4, 0.6$ compositions. (b) Details from the x-ray powder diffraction patterns of $Sr_2Cd_{1-x}Ca_xWO_6$ ($x = 0.0, 0.2, 0.4, 0.6, 0.8, 1.0$) in the 17-23°, 29-32° and 53-57° 2θ ranges, to show the continuous evolution of the patterns with the increasing Ca-content.

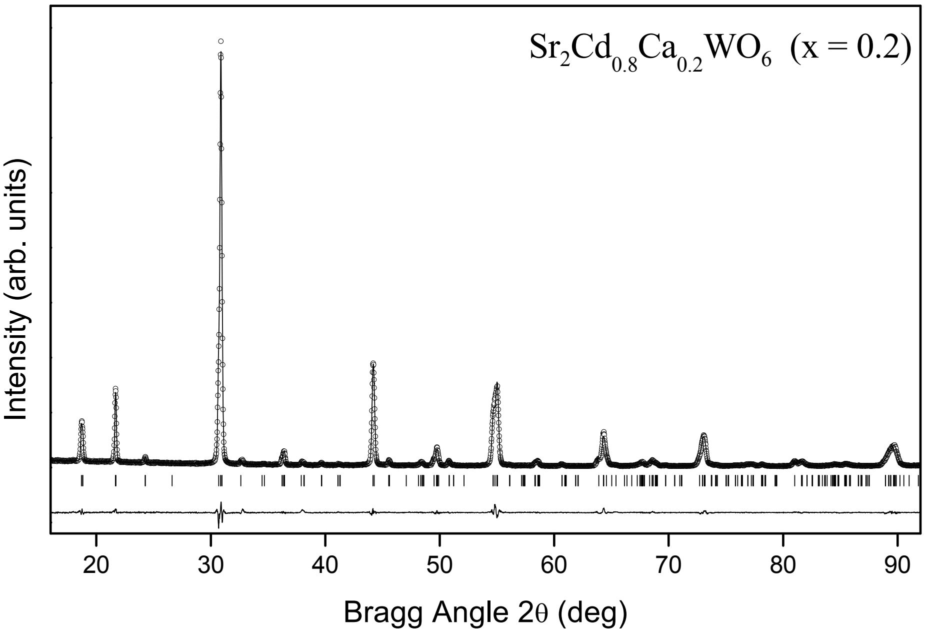

FIGURA 6.2: Observed (·), calculated (–) and difference profiles for the Rietveld refinements of $Sr_2Cd_{1-x}Ca_xWO_6$ ($x = 0.2$), at room temperature, space group $P2_1/n$.

the first one, we used the room-temperature structure of Sr_2CdWO_6 as the starting model; in the second one, we used the room-temperature structure of Sr_2CaWO_6. In both cases we obtained the same refined structural model for each of the solid solution members.

As a representative, in figure 2, we show the results of the refinements for the $x = 0.2$ composition. For all phases we obtained a good agreement between the experimental and the calculated diffraction profiles. Table 1 summarizes the room-temperature unit cell parameters, atomic positions and isotropic independent atomic displacement parameters and the reliability factors of the Rietveld refinements for the studied compositions; except for the $x = 0.25, 0.50, 0.75$ values, not to overload the table. In these refinements, the atomic positions and unit cell parameters of Sr_2CdWO_6 and Sr_2CaWO_6 are very close to those found in our recent works [41, 43]. The small differences are attributed to the different methods of preparation (co-precipitation method for the materials of this work, and solid state method for the materials of our recent works) and to the different experimental equipments used.

Figure 3 shows the (a) a, b and c lattice parameters, (b) monoclinic angle (β) and the (c) unit-cell volume of the synthesized materials. All those parameters increase linearly with the Ca amount, a clear evidence that the Vegard's law holds for this solid solution.

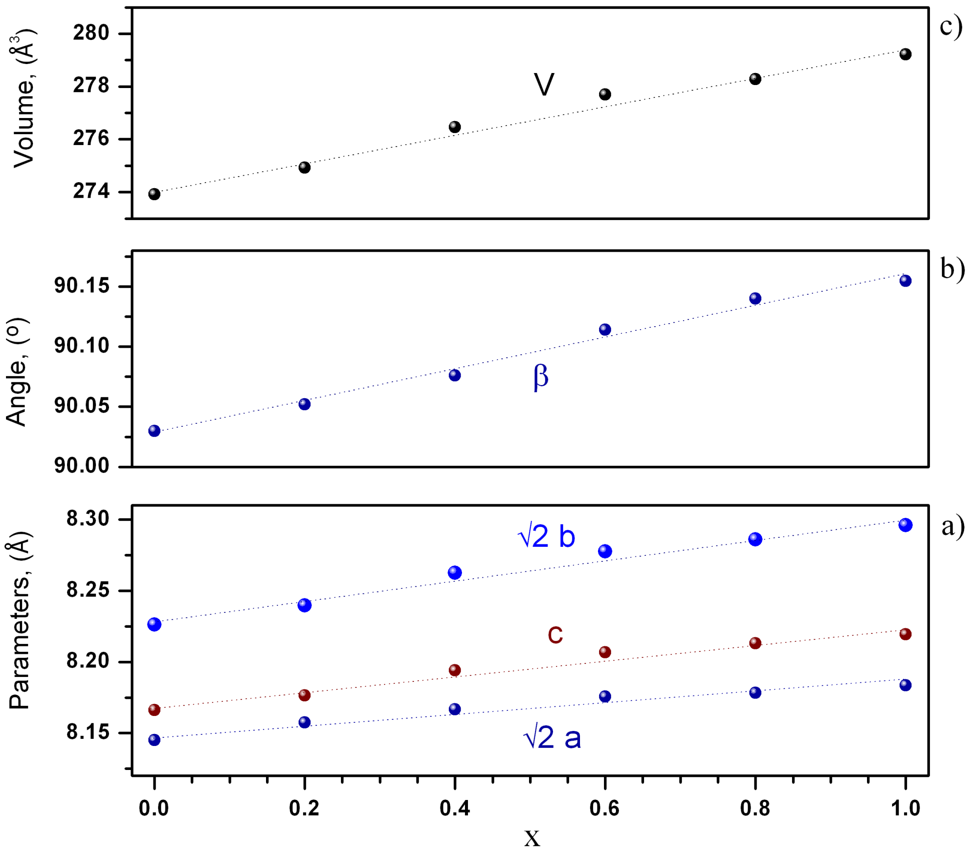

FIGURA 6.3: Evolution, as a function of increasing calcium content, (x = 0, 0.2, 0.4, 0.6, 0.8, 1.0), at room temperature, of the (a) unit-cell volume, (b) monoclinic angle (β) and the (c) unit-cell parameters of the synthesized materials. Dotted line is a guide for the eyes.

TABLA 6.1: Refined structural parameters for the $Sr_2Cd_{1-x}Ca_xWO_6$ solid solution, at room temperature, as a function of calcium content ($x = 0.0, 0.2, 0.4, 0.6, 0.8, 1.0$). The atomic positions (in fractional coordinates) and the isotropic independent atomic displacement parameters were refined in the space group $P2_1/n$. W atoms occupy the site 2a(0,0,0); and Cd and/or Ca occupy the site 2b(1/2,1/2,0). O and Sr atoms occupy the site 4e(x,y,z).

Composition			x = 0	x = 0.2	x = 0.4	x = 0.6	x = 0.8	x = 1
Atom	Sr	x	0.0090(9)	0.0065(2)	0.0110(9)	0.0098(8)	0.0088(7)	0.0091(3)
		y	0.5362(2)	0.5356(2)	0.5374(3)	0.5380(2)	0.5362(3)	0.5391(2)
		z	0.2513(4)	0.2519(4)	0.2509(4)	0.2513(3)	0.2517(3)	0.2506(2)
	O1	x	-0.087(2)	-0.080(3)	-0.077(3)	-0.078(2)	-0.089(2)	-0.082(1)
		y	-0.025(2)	-0.014(2)	-0.017(2)	-0.018(2)	-0.026(2)	-0.023(1)
		z	0.221(2)	0.223(3)	0.223(2)	0.221(2)	0.224(2)	0.228(1)
	O2	x	0.251(3)	0.270(3)	0.249(3)	0.248(3)	0.254(2)	0.269(1)
		y	-0.188(2)	-0.198(3)	-0.186(3)	-0.191(2)	-0.175(2)	-0.1840(1)
		z	0.042(3)	0.036(2)	0.049(3)	0.051(3)	0.043(3)	0.039(2)
	O3	x	0.190(2)	0.186(3)	0.188(3)	0.188(3)	0.183(2)	0.190(1)
		y	0.240(2)	0.243(2)	0.235(3)	0.239(2)	0.248(2)	0.264(1)
		z	0.054(3)	0.045(3)	0.058(3)	0.060(3)	0.051(2)	0.045(1)
	B(^{2})	W	0.11(3)	0.09(3)	0.33(4)	0.41(3)	0.09(3)	0.30(2)
		Ca,Cd	0.53(5)	0.21(5)	0.73(6)	1.03(6)	1.12(8)	0.69(6)
		Sr	0.69(3)	0.76(4)	0.22(4)	0.13(4)	0.51(4)	0.32(2)
		O1,O2,O3	0.47(16)	1.60(2)	0.65(2)	0.55(2)	0.50(2)	0.54(2)
Cell param.	a()		5.7594(2)	5.7682(3)	5.7747(2)	5.7809(2)	5.7839(3)	5.7867(7)
	b()		5.8209(2)	5.8296(2)	5.8426(3)	5.8531(3)	5.8592(3)	5.8688(9)
	c()		8.1663(3)	8.1762(4)	8.1939(4)	8.2067(4)	8.2133(4)	8.2193(2)
	$\beta(^\circ)$		90.040(1)	90.052(2)	90.076(6)	90.114(4)	90.140(3)	90.155(7)
	V(^{3})		273.91(6)	274.92(8)	276.46(4)	277.69(6)	278.28(4)	279.22(2)
Reliability fact.	R_p(%)		8.02	8.72	10.30	10.50	9.86	6.95
	R_{wp}(%)		9.28	10.40	12.10	11.30	11.60	8.36
	R_{bragg}(%)		7.12	7.84	7.78	8.50	7.83	5.69
	χ^2 (%)		1.70	1.77	2.41	1.78	2.18	2.16

6.1.2. High-temperature structures and phase transitions

As the room-temperature results indicated that Vegard's law holds, for the high-temperature study we analyzed only three compositions, $x = 0.25, 0.50, 0.75$. For the high-temperature phase-transitions search, we have chosen two 2θ regions: the first one centered at about 24 deg, and the second one, depending on the material, between 71.0 and 74.0 deg. At all temperatures covered, these regions contain a group of diffraction peaks that have been identified as especially sensitive to the structural changes occurring in double perovskite materials [43]. These experiments showed that, in the low-angle interval, the peak disappears at a certain temperature; and the only changes that can be interpreted as indications of phase transitions, in the high-angle interval, are the appearance of a very weak shoulder on the low-angle side of the peak (in coincidence with the disappearance of the peak in the low-angle interval); and the subsequent unification of this shoulder with the main peak. Those changes were interpreted as evidences of the material undergoing two phase transitions; first, from the monoclinic structure to tetragonal one, and (at higher temperature) from tetragonal to cubic.

It should be noted that the diffraction experiments at the highest measured temperatures show that the weight fraction of $SrWO_4$ increases, indicating partial decomposition of the sample. This fact has also been clearly observed in Sr_2CdWO_6 [43].

The peak present in the low-angle interval, in all the materials of the solid solution (Fig. 4), is of the type $h + k + l = 2n + 1$, and disappears, which means that the there is a change from a primitive unit cell to a body-centered one. Also, while some of the peaks remain split at those temperatures, others are well represented by a single diffraction reflection (Fig. 5). Analyzing the peak splitting, and taking into account the phase-transition sequence shown by the end-members of the solid solution, it becomes clear that at 1080K, 1090K and 1100K the unit cells of $Sr_2Cd_{1-x}Ca_xWO_6$ $(x = 0.25, 0.5, 0.75)$, respectively, are all tetragonal: $I4/m$ space group.

This tetragonal distortion gradually disappears at higher temperature, and suggests that at the highest measured temperatures, the unit cells are converted to cubic. This cubic phase most probably has the symmetry of the aristotype double perovskite structure with space group $Fm\overline{3}m$. This is the result we obtained for the Ca containing compound, and this is what we suggested for the Cd containing compound.

For the case of the monoclinic-to-tetragonal phase transition we have assigned the first temperature at which the (-111) and (111) reflections are absent (Fig. 4) and the left shoulder (which is indicated by arrows in Fig. 5 (b) panel) is observed. For the tetragonal-to-cubic ones, the first temperature at which the mentioned left shoulder disappears. The temperatures assigned to the successive phase transitions, at the measured compositions, are included in the corresponding panels in Fig. 5.

The structural analysis based on the presented temperature-dependent conventional diffraction experiments suggests that the phase transition sequence existing in the continuous $Sr_2Cd_{1-x}Ca_xWO_6$ $(0 \leq x \leq 1)$ solid solution is $P2_1/n \rightarrow I4/m \rightarrow Fm\bar{3}m$. As we pointed out in [43], the same phase-transition sequence is observed in the Sr_2BWO_6 double perovskite oxide family, suggesting that the temperature evolution of their structures is governed by the same principles.

It is usually assumed [74] that the driving force of the structural changes in this kind of materials is the mismatch between the size of the A cation (Sr^{2+} in this case) and the interstitial space between the BO_6 and $B'O_6$ octahedra. This mismatch is measured by means of the so-called tolerance factor [66]: $t = \sqrt{2}\frac{d_{A-O}}{(d_{B-O}+d_{B'-O})}$. In the present case, $d_{B-O} = (1-x)d_{Cd-O} + xd_{Ca-O}$. We have obtained the mean d_{Sr-O}, d_{Cd-O}, d_{Ca-O} and d_{W-O} bond lengths by calculating the room-temperature distances that give the nominal oxidation states of the cations in the bond-valence method [43, 67]. In Fig. 6 we show the phase transition temperatures of the successive phase transitions as a function of the tolerance factor t at room-temperature.

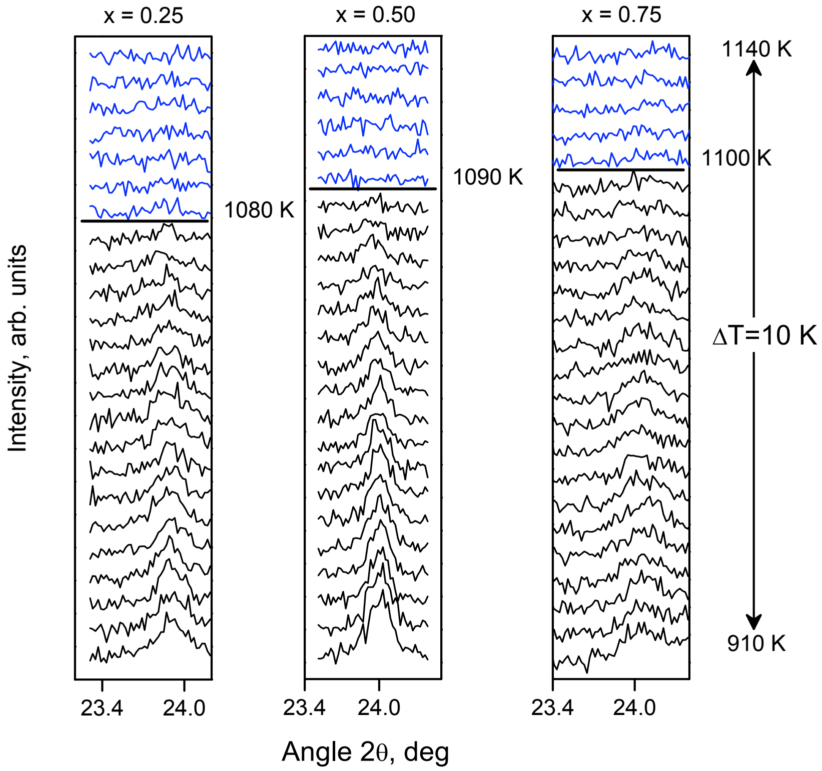

FIGURA 6.4: Evolution with temperature and as a function of calcium content, (a) $x = 0.25$,(b) $x = 0.50$ and (c) $x = 0.75$, of the (111) and (-111) monoclinic reflections. Their disappearance marks the transition from a primitive cell ($P2_1/n$) to a centered one ($I4/m$). As the Ca content is increased, the temperature at which the transitions takes place also increases linearly: (a) $x = 0.25$, ≈1080K, (b) $x = 0.50$, 1090K and (c) $x = 0.75$, 1100K.

A clear linear behavior of the cubic-to-tetragonal phase-transition temperature is observed, in accordance with the result obtained for the whole Sr_2BWO_6 (B=Ca,Cd,Mn,Zn,Mg,Co,Cu,Ni) family [41, 43, 68]. The same is true for the tetragonal-to-monoclinic transition, if the value for that phase transition in Sr_2CdWO_6 is revisited [43]. The actual temperature (1070K) for the tetragonal-to-monoclinic transition in Sr_2CdWO_6, belonging to the preparation presented in this work, is a slightly lower than the previously reported one (1105K) [43] in a sample from another preparation, measured in another equipment, and that showed, at high temperatures, a progressive decomposition which could be responsible for a slightly different stoichiometry, affecting the symmetry, and, in turn, influencing in the temperature value for the phase transition.

These results confirm that the most important factor governing the appearance of octahedral tilts in the double perovskite structure and the temperature range in which they exist is a geometrical one: the mismatch between the size of the A cation and interstitial space between the BO_6 and $B'O_6$ octahedra, irrespective of having a solid solution in the B-site, at least for the studied solid solution.

6.2. Conclusions

The solid solution with double perovskite structure and general chemical formula $Sr_2Cd_{1-x}Ca_xWO_6$ ($0 \leq x \leq 1$) has been synthesized by the co-precipitation method. The Cd^{2+} cation progressive substitution by Ca^{2+} in the Sr_2CdWO_6 double perovskite led to a continuous solid solution in the whole ($0 \leq x \leq 1$) fraction range. The crystal structures, at room temperature, of all the

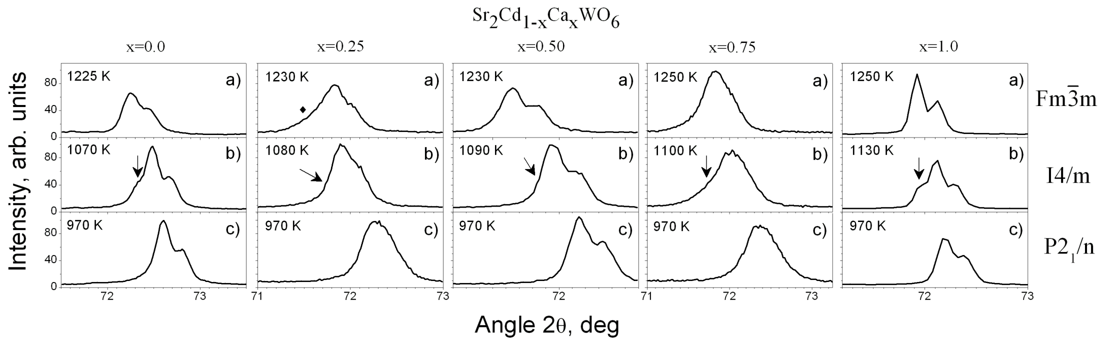

FIGURA 6.5: Evolution with temperature and as a function of calcium content, of the (620) cubic reflection, (a) panel. The tetragonal distortion, (b) panel, is evidenced by the appearance of a weak shoulder at the left side of the reflection, indicated by the arrow. Finally, in the (c) panel, the monoclinic distortion is shown. The bullet in the $x = 0.25$ Ca fraction content, in the (a) panel, indicates the shoulder attributed to the formation of the $SrWO_4$ impurity as the sample decomposes at high temperature.

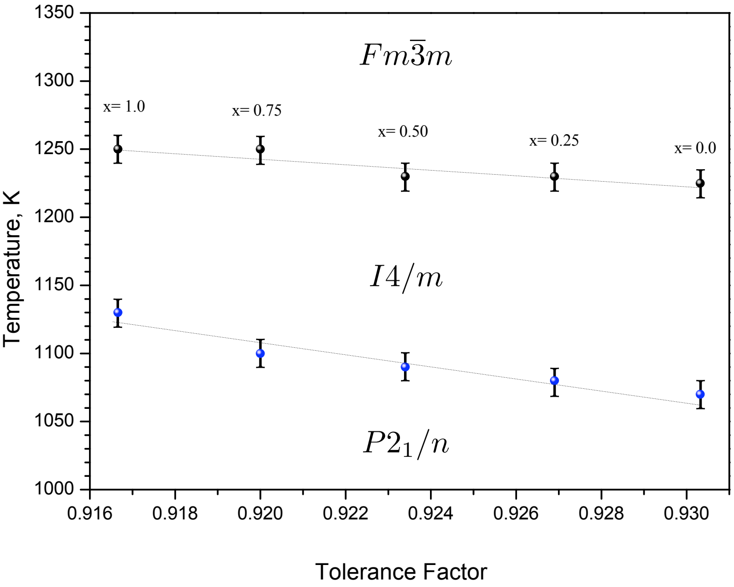

FIGURA 6.6: Phase transition temperatures of the successive phase transitions of the $Sr_2Cd_{1-x}Ca_xWO_6$ solid solution, as a function of their respective tolerance factors at room temperature Continuous line is a guide for the eyes.

members of the solid solution were determined from the Rietveld refinements of laboratory X-ray powder diffraction data: they crystallize in the $P2_1/n$ space group. The high-temperature study revealed the following two phase-transition sequence, for all the members of the solid solution: $P2_1/n \rightarrow I4/m \rightarrow Fm\overline{3}m$. The cation substitution does not induce a phase transition, and the phase transition sequence observed in the end members of the solid solution is also observed in the solid solution. The phase transition temperatures of both successive phase transitions showed a linear behavior in the whole ($0 \leq x \leq 1$) fraction range. It was observed that the transition temperatures are higher in compounds with low tolerance factors, as in the case of the members of the Sr_2MWO_6 family.

Capítulo 7

Crystal structures and temperature-induced phase transitions of $Sr_2Mn^{2+}W^{6+}O_6$, and of its transformation to $Sr_2Mn^{3+}W^{6+}O_{6+\delta}$

7.1. Results and Discussion

7.1.1. Room-temperature structures

In figure 1 we show the X-ray diffraction results, at room temperature, for samples 1 and 2. As mentioned, $P4_2/n$ [60] and $P2_1/n$ [61] space groups have been proposed, using neutron powder diffraction data, for the room-temperature structure of Sr_2MnWO_6. We tried both structures as the starting models for our refinements; the R-factor values obtained (sample 2) for both space groups are: $R_\mathrm{p} = 10.6\,\%$; $R_\mathrm{wp} = 16.0\,\%$; $R_\mathrm{exp} = 10.11\,\%$; $\chi^2 = 2.50$ for $P4_2/n$ with 8 atoms per unit cell; and $R_\mathrm{p} = 7.96\,\%$; $R_\mathrm{wp} = 12.5\,\%$; $R_\mathrm{exp} = 8.77\,\%$; $\chi^2 = 2.02$ for $P2_1/n$ with 6 atoms per unit cell; as we can see, the best R-factor values were obtained for the monoclinic model with fewer atoms per unit cell and smaller primitive unit cell volume ($V_T \simeq 2V_M$). Thus, we suggest that the room-temperature space group of $Sr_2Mn^{2+}WO_6$ is $P2_1/n$. There are three facts that support this affirmation. First, it is very easy to confirm that the $P4_2/n$ space group is not common; indeed it is very strange, as

TABLA 7.1: Crystal structure data and refinement results for $Sr_2Mn^{2+}WO_6$ at room temperature. The atomic positions (in fractional coordinates) and temperature factors were refined in the space group $P2_1/n$. (Note: $a = 5.6764(1)$; $b = 5.6752(1)$; $c = 8.0144(1)$; $\beta = 90.12(1)^\circ$ and $V = 258.18(1)^3$; $R_p = 7.96\,\%$; $R_{wp} = 12.5\,\%$; $R_{exp} = 8.77\,\%$; $\chi^2 = 2.02$).

Atom	Site	x	y	z	B(Å^2)
W	2a	0	0	0	0.27(3)
Mn	2b	1/2	1/2	0	0.10(1)
Sr	4e	0.0054(7)	0.5166(3)	0.2464(7)	0.67(4)
O1	4e	0.057(2)	0.020(2)	-0.236(1)	0.92(8)
O2	4e	0.252(1)	-0.221(5)	0.042(4)	0.92(8)
O3	4e	0.210(5)	0.264(5)	0.038(2)	0.92(8)

a space group preferred by double perovskites (although it is a possible one). Secondly, there is a çrystallographic reason.^{a}lso used by Muñoz [14]: there is a little improvement in the R factors when the structure is described using the $P4_2/n$ space group, which needs a bigger unit cell (primitive) and which gives rise to more degrees of freedom, as, for instance, instead of having only one Sr cation position, there are three. Thirdly, in a previous paper [10], we presented a phase diagram (transition temperature vs. tolerance factor) in the Sr_2MWO_6 family. The data in that figure demonstrate that the Sr_2MWO_6 family (including a continuous solid solution $Sr_2Cd_{1-x}Ca_xO_6$ [75]) shows the same phase-transition sequence $P2_1/n - I4/m - Fm\bar{3}m$, and the feature of increasing the stable temperature range of the more distorted monoclinic phase and the diminishing of the tetragonal $I4/m$ phase as the tolerance factor diminishes at room temperature. We see no "physicalreason to take out the present work compound from that general behaviour (trend) proven to exist in the mentioned family. With all these arguments, we conclude that the correct space group assignation for the room-temperature structure of Sr_2MnWO_6 is undoubtedly the monoclinic $P2_1/n$. The results obtained for the crystal structure of $Sr_2Mn^{2+}WO_6$ at room temperature and the reliability parameters of the refinement are given in table 1. Similar results were obtained using samples 1 and 2 data.

In figure 2 we show the X-ray diffraction measurement results obtained using sample 2 at different temperatures between 470K and 1090K, in three selected 2θ ranges: (44.0°–46.0°), (55.0°–57.0°) and (73.5°–76.0°). The main goal of this experiment was to determine precisely the temperature of the known to exist two phase transitions [76]: in that work, the authors reported three different structures: $P4_2/n$, at room-temperature; $I4/m$, at 573K and $Fm\bar{3}m$, at 773K. At a first glance to figure 2, it seemed that our results could be compatible with the known two phase-transition sequence in Sr_2MnWO_6. We thought that the phase-transitions temperatures were approximately 630K and 820K, as indicated by the white dot-lines in figure 2. Nevertheless, the behavior between 820 and 1020K temperatures puzzled us: in that temperature interval, the cell parameters of the

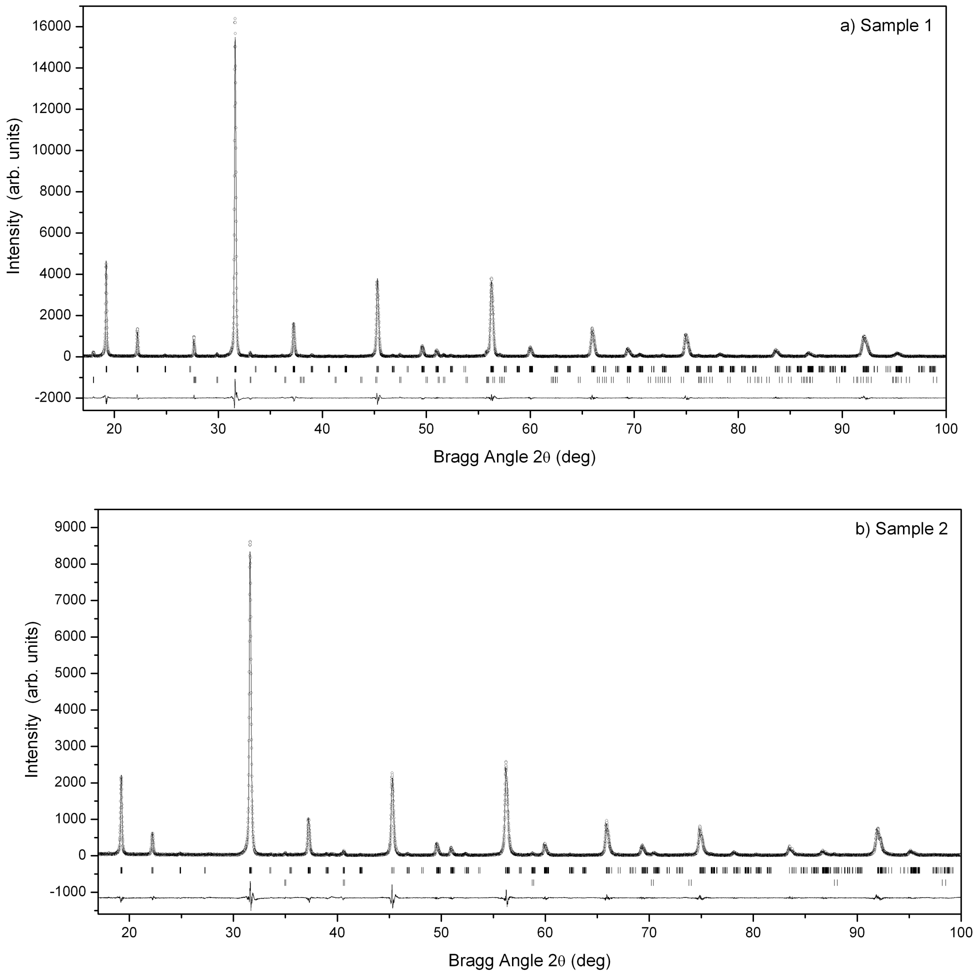

FIGURA 7.1: Observed (·), calculated (–) and difference profiles for the Rietveld refinement of $Sr_2Mn^{2+}WO_6$ at room temperature using a structural model with the $P2_1/n$ space group. In (a), the impurity $SrWO_4$ (<3.35 %) is included in the refinement as a known additional phase. In (b), the impurity MnO (< 1 %) is included in the refinement as a known additional phase. The top barred pattern corresponds to $Sr_2Mn^{2+}WO_6$ and the bottom barred pattern to the impurity.

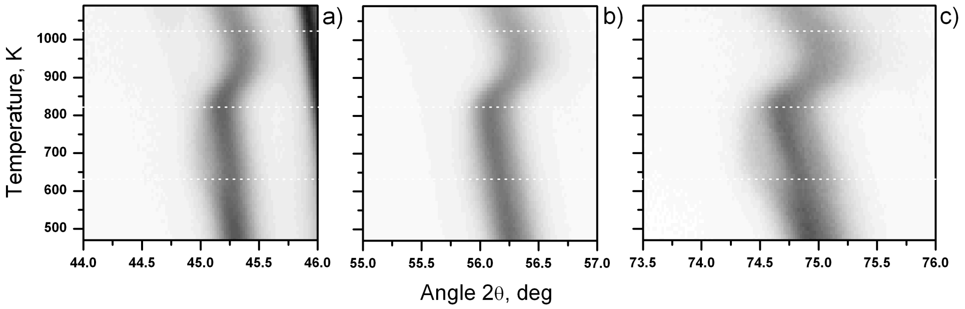

FIGURA 7.2: Temperature evolution of the three diffraction line-set at $2\theta \approx 45°;56°;75°$, obtained by X-ray diffraction measurement in air of $Sr_2Mn^{2+}WO_6$ (sample 2). At 640K, the compound transforms to the tetragonal $I4/m$ space group. Before the expected high-temperature cubic ($Fm\bar{3}m$ space group) phase appears, the $Sr_2Mn^{2+}WO_6$ compound starts to transform irreversibly to $Sr_2Mn^{3+}WO_{6+\delta}$, at about 820K.

compound diminished. We interpreted it as a possible irreversible transformation, taking place continuously in temperature, to another compound; in fact, the color of the recovered sample had changed from brownish to black; and, besides, a great increase in the amount of impurity present in the sample was noticed.

In figure 3 we show the results obtained in the 2θ angular range (15°–100°) for sample 2: (a) before increasing the temperature from room temperature to 875K and (b) after recovering the room-temperature conditions. The amount of impurity has noticeably increased; and, what is more important, the starting phase is not recovered; hence, the compound has, undoubtedly, transformed irreversibly (see below, next sub-section $Sr_2Mn^{3+}WO_{6+\delta}$). Having this fact in mind, we re-interpreted the results shown in figure 2: up to approximately 820K, the compound keeps the structure of $Sr_2Mn^{2+}WO_6$, and at that temperature, it starts to transform irreversibly. Thus, the temperature interval of interest to observe the previously reported phase transitions is 473K to 773K; although in our results, in that temperature interval only one clear anomaly was seen.

The behavior of the three sets of reflections, shown in figure 2, is qualitatively the same. At $\approx$ 810K, the evolution with temperature of all them changes and instead of evolving to lower 2θ values, they move to higher values. This is a sign of a decreasing of the cell parameters. As a possible explanation to this observation, we thought that the $Sr_2Mn^{2+}W^{6+}O_6$ compound transformed to $Sr_2Mn^{3+}W^{5+}O_6$; thus, we thought of an oxidation-reduction transformation. There are some facts supporting that conclusion. First, the conventional X-ray measurements have been done in air, and it is known how easily Mn^{2+} oxides in air. Second, we can compare the ionic radii of Mn^{3+} (0.645) and W^{5+} (0.620) to those of Mn^{2+} (0.830) and W^{6+}(0.600). Although the ionic radius reduction in the tungstate is very small ($\Delta r_W = 0.02$), in the manganese after the proposed transformation the reduction is one order of magnitude bigger ($\Delta r_{Mn} = 0.195$), and, relatively, it is a 30 % decrease.

So, it is quite reasonable to think of a general unit cell reduction, as the inter-atomic distances are governed by the ionic radii. This reduction, in turn, will appear as an evolution with temperature of the position of the reflections to bigger values of 2θ, at least, while the oxidation-reduction transformation takes place. Once it has finished, it is supposed that the cell parameters will be evolve with temperature as usual.

We made a thermal treatment in $Sr_2Mn^{2+}W^{6+}O_6$: we heated it in air at 875K, during 24 h. The sample was heated up and cooled down slowly 3K/min. After the treatment, we obtained the same two features in the recovered sample (sample 3): color had changed to black, and a big amount of impurity was present.

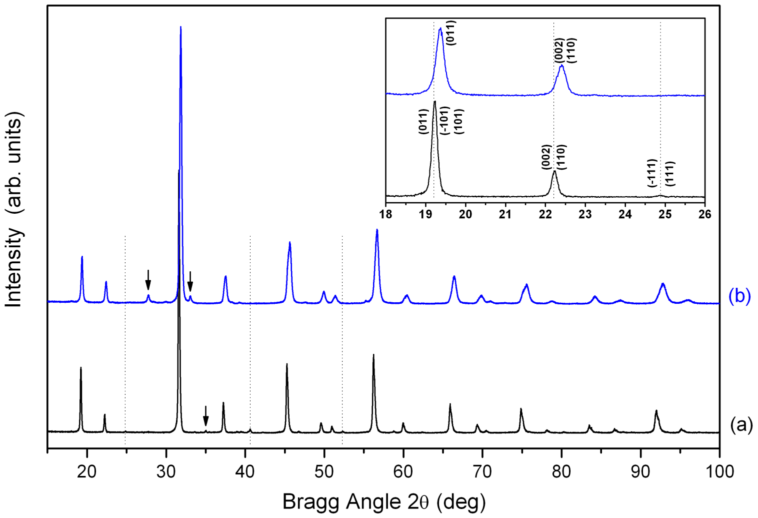

FIGURA 7.3: X-ray diffraction patterns of (a) $Sr_2Mn^{2+}WO_6$ (sample 2) and (b) $Sr_2Mn^{3+}WO_{6+\delta}$ (sample 3). In the inset we have enlarged the 2θ-interval, and we have indicated the indices of the reflections in the $P2_1/n$ and $I4/m$ space groups, for (a) and (b), respectively. The $(\bar{1}11/111)$ reflections characteristic of a primitive cell are clearly seen in (a). Another two peaks which are absent are highlighted by dashed vertical lines. The arrows at 27.7°, 32.9° and 34.9° show the Peaks due to the impurities of $SrWO_4$, $Sr_2Mn_2O_5$ and MnO, respectively.

To confirm our assumption about the mechanism of the observed transformation, we recorded an EPR spectrum, at room temperature, for both samples: $Sr_2Mn^{2+}W^{6+}O_6$ (sample 2) and sample 3. Figure 4 shows the EPR spectra obtained. The EPR signal shows a broad isotropic signal centred at a resonance field of 3367.4(2) Oe, corresponding to g value of 1.998(1), indicating that manganese ions are in the 2+ oxidation state in sample 2; besides, there is no signal at all in the case of sample 3, indicating that there is no manganese cations in it in the 2+ oxidation state, and, thus, that all the manganese present is in 3+ oxidation state.

As we performed the thermal treatment on $Sr_2Mn^{2+}W^{6+}O_6$ in air, it could had happened that while Mn^{2+} oxided to Mn^{3+}, the sample had gained some oxygen, maintaining the W^{6+} oxidation state; thus, transforming to $Sr_2Mn^{3+}W^{6+}O_{6+\delta}$; or, otherwise, to maintain charge neutrality, the W^{6+} cation could had transformed to W^{5+}, therefore, the compound in sample 3 should be $Sr_2Mn^{3+}W^{5+}O_6$. In order to see if the sample gains oxygen or W^{6+} transforms to W^{5+}, while the temperature is increased in air, we focused on the oxidation states of manganese and tungsten at room temperature, after and before the thermal treatment at 875K.

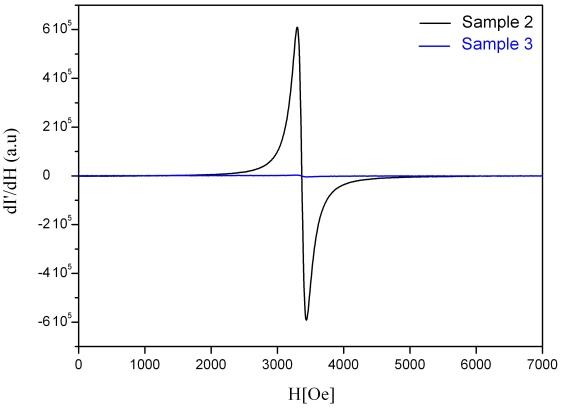

FIGURA 7.4: Room–temperature EPR spectrum of samples 2 and 3. The EPR signal shows a broad isotropic signal, centred at a resonance field of 3367.4(2) Oe, corresponding to g value of 1.998(1), indicating that manganese ions are in the 2+ oxidation state in sample 2; besides, there is not signal at all in the case of sample 3, indicating that there is no manganese cations in it in the 2+ oxidation states, and, thus all the manganese present is in 3+ oxidation state.

The XANES experiments at the Mn K-edge and W L3-edge were carried out for the starting material $Sr_2Mn^{2+}W^{6+}O_6$ and the treated sample, and normalized spectra are shown in figure 5. The Mn K-edge XANES spectra recorded at room temperature on sample 2, as prepared and after the thermal treatment at 875K are depicted in Figure 5(a). As it is clear form the figure, changes in the absorption edge occurred after the thermal treatment: the edge position shifts from 6543 to 6550 eV, revealing the transition from Mn^{2+} to Mn^{3+}. Furthermore, the spectrum profile of the starting Mn^{2+} double perovskite resembles to analogue perovskites with Fe^{2+}, whereas the shape of the Mn^{3+} treated sample is very similar to Fe^{3+} perovskites [77, 78]. The W L3-edge XANES spectra recorded at room temperature, before and after thermal treatment are extremely similar to each other, as shown in Figure 5(b). The position of the W edge absorption at the half jump in the as-prepared sample is found at 10205 eV, a typical value for tungsten in the 6+ oxidation state [78, 79]. The treated sample has the same edge energy, the W L3 edge usually does not present an important shift in the edge energy, in this case the edge position is the same, suggesting the maintenance of a W^{6+} oxidation state [78]. The L3 absorption edge comes from a direct dipolar $2p \rightarrow 5d$ transition, so the slight differences in the double structure in the white line may suggest a weakening of the crystal field effect in the WO_6 octahedra, due to increase in the W-O distances in the transition to the tetragonal symmetry. Thus, from the combined EPR and XANES measurements results, we conclude that $Sr_2Mn^{2+}W^{6+}O_6$ transforms, at 875K in air, to $Sr_2Mn^{3+}W^{6+}O_{6+\delta}$. Of course, the non-stoichiometric excess in oxygen compensates the change in the oxidation state in Mn and the maintenance of the oxidation state in W. This transformation is irreversible, and, thus, in turn, gives rise to a new material.

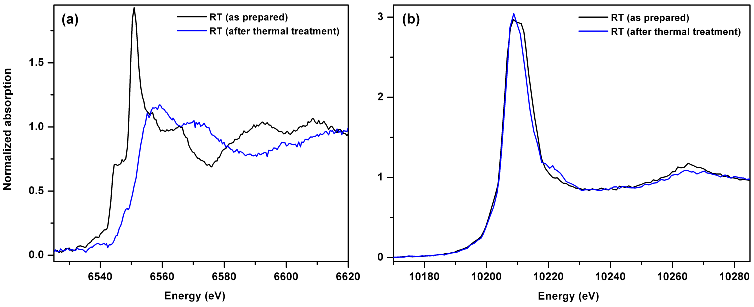

FIGURA 7.5: XANES spectra, at room temperature, of sample 2 (as prepared) and sample 3 (after the thermal treatment at 875K): (a) Mn K-edge, (b) W L3-edge.

We focused in this new material and we made a room-temperature X-ray diffraction measurement in $Sr_2Mn^{3+}WO_{6+\delta}$ (sample 3). In addition to the already mentioned color change and impurity increase, the diffractogram has two more features: (i) it is relatively shifted to higher angles (figure 3, in comparison to the results obtained before the thermal treatment, sample 2), what is consistent with a decrease in the cell parameters; and (ii) there are some reflections pertaining to the monoclinic phase that have disappeared (marked with dashed lines); a fact that can be interpreted as a symmetry increase. The reflections that disappear are of the type (hkl) with $h + k + l = 2n + 1$, which are characteristic of a primitive cell. Bearing in mind that the are characteristic of a primitive cell, we performed a refinement with a tetragonal space group, $I4/m$, and using the structural results obtained for sample 2 with the tetragonal phase as the starting structural model. The results of the refinement are shown in figure 6, and the final structural results and refinement parameters obtained are summarized in table 2. The results of refinements shown the presence of 2.90 % of $SrWO_4$ and 1.37 % of $Sr_2Mn_2O_5$, which mean a partial decomposition of the compound to 2:1 mole proportional portion of $SrWO_4$ and $Sr_2Mn_2O_5$,respectively , according to the following chemical reaction:

$$Sr_2MnWO_6 + {}^1/_2O_2 \longrightarrow 2\,SrWO_4 + Sr_2Mn_2O_5.$$

We conclude that the sample 3 allows for 2:1:1 proportional portion of Sr, Mn and W, respectively.

Unfortunately, the refinement of oxygen site occupancy was not very conclusive, due to the insensitivity of powder X-ray diffraction to small variations in oxygen content in the presence of higher atomic number elements. Nevertheless, the refinement results are consistent with fixed occupancy of these sites. The oxygen occupancy at the $4e$ and $8h$ sites ($I4/m$ space group) was fixed during the refinement at 1 and 1.125, respectively, as the initial stoichiometry seemed most likely to be $Sr_2Mn^{3+}WO_{6.5}$. The mean interatomic distances of Mn and W in $Sr_2Mn^{2+}WO_6$ and $Sr_2Mn^{3+}WO_{6+\delta}$ are listed in Table 3. In the case of $Sr_2Mn^{2+}WO_6$, the bond lengths of $Mn - O1$, $Mn - O2$ and $Mn - O3$ are 2.139(3)Å, 2.145(8)Å and 2.144(8)Å, respectively, which are very close and similar to the value predicted by bond valence calculations 2.196Å. The same results are observed for the bond lengths of WO_6 octahedra. In the other compound $Sr_2Mn^{3+}WO_{6+\delta}$, the bond lengths in the axial position of Mn are elongated due to a Jahn- Taller distortion. In consequence, we have obtained two large distances 2.076(1)Å and four short distances 2.024(7)Å, the average value of the Mn bond distances within the octahedra 2.041(2)Å are in good agreement with the value predicted by bond valence calculations 2.0461Å. As sequences we have obtained deformed WO_6 octahedra, with two short axial distances 1.930(1)Å and four large distances 1.986(7)Å.

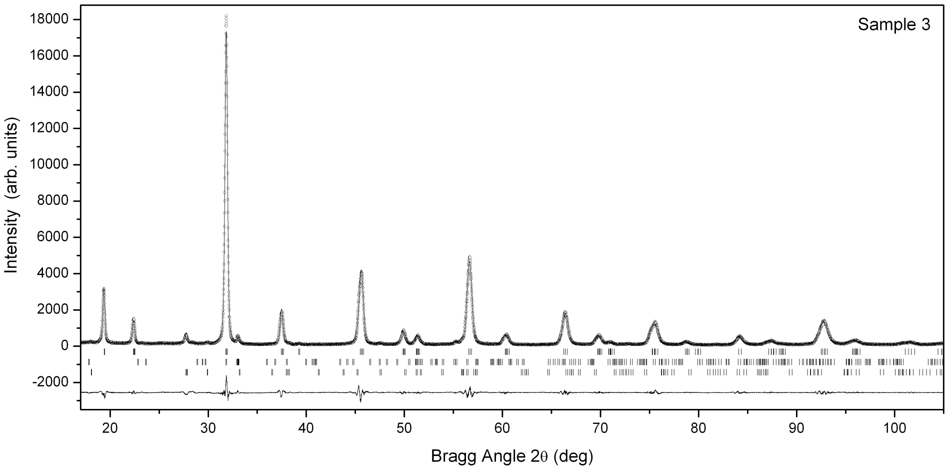

FIGURA 7.6: Observed (·), calculated (–) and difference profiles for the Rietveld refinement of $Sr_2Mn^{3+}WO_{6+\delta}$ (sample 3) at room temperature using a structural model with the $I4/m$ space group. The top barred pattern corresponds to $Sr_2Mn^{3+}WO_{6+\delta}$, and the middle and bottom barred patterns to the impurities $SrWO_4$ (2.90) and $Sr_2Mn_2O_5$ (1.37), respectively, which have been included in the refinement as known additional phases.

7.1.2. High-temperature phase transitions

$Sr_2Mn^{2+}WO_6$

To determine precisely the temperatures of the expected phase transitions in $Sr_2Mn^{2+}WO_6$ (sample 2), we performed neutron and X-ray powder diffraction (XRPD) measurements at different temperatures, under vacuum (to avoid the sample transformation to $Sr_2Mn^{3+}WO_{6+\delta}$). In figures 7(a) and

TABLA 7.2: Crystal structure data and refinement results for $Sr_2Mn^{3+}WO_{6+\delta}$ at room temperature. The atomic positions (in fractional coordinates) and temperature factors were refined in the space group $I4/m$. (Note: $a = 5.6353(1)$Å; $c = 8.0149(1)$Å and $V = 254.53(1)^3$; $R_p = 10.6\,\%$; $R_{wp} = 15.1\,\%$; $R_{exp} = 5.42\,\%$; $\chi^2 = 7.73$).

Atom	Site	x	y	z	B(Å^2)
W	2a	0	0	0	0.33(7)
Mn	2b	0	0	1/2	0.37(2)
Sr	4d	0	1/2	1/4	0.74(3)
O1	4e	0	0	0.241(2)	1.05(4)
O2	8h	0.219(2)	0.276(1)	0	1.05(4)

TABLA 7.3: Main bond distances (Å) for $Sr_2Mn^{2+}WO_6$ and $Sr_2Mn^{3+}WO_{6+\delta}$ from XRPD at room temperature.

	$Sr_2Mn^{2+}WO_6$	$Sr_2Mn^{3+}WO_{6+\delta}$
Mn-O1	2.139(3) (×2)	2.076(1) (×2)
Mn-O2	2.145(8) (×2)	2.024(7) (×4)
Mn-O3	2.144(8) (×2)	-
Average distance	2.143(9)	2.041(2)
Predicted distance	2.196	2.046
W-O1	1.926(3) (×2)	1.930(1) (×2)
W-O2	1.931(8) (×2)	1.986(7) (×4)
W-O3	1.938(8) (×2)	-
Average distance	1.932(9)	1.967(2)
Predicted distance	1.917	1.946

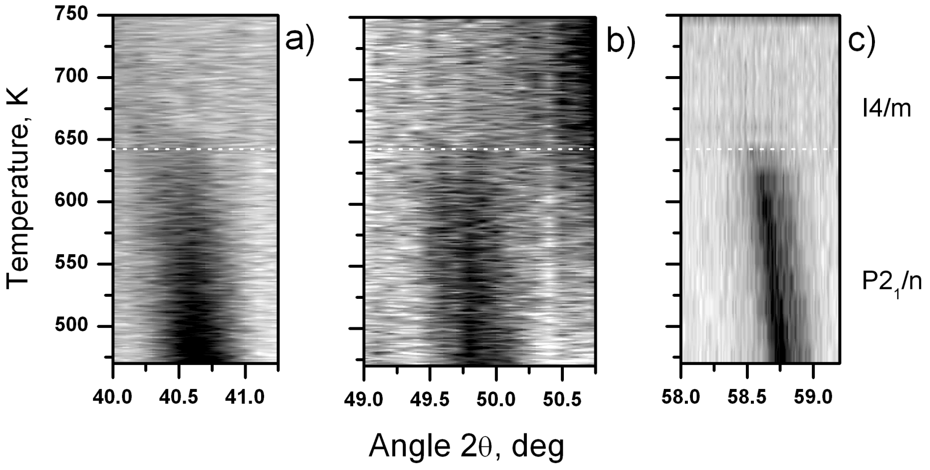

FIGURA 7.7: Thermal evolution of the primitive Bragg peaks of Sr$_2$Mn^{2+}WO$_6$ obtained under vacuum from neutron powder diffraction (a,b) and from XRPD experiments (c). The scattered intensity is represented with gray scale, black being high intensity and white lowest intensity. Thermal evolution of (131/$\bar{1}$31/311/$\bar{3}$11) in (a) and (124/$\bar{1}$24/214/230/$\bar{2}$14/320) in (b,c), showing the disappearance of these peaks at about 640K.

(b) we show the results obtained from neutron measurements, in the 430K to 750K temperature interval, with a 1K step, in the (44.0°–41.5°) and (49.0°–50.75°) selected 2θ intervals, corresponding to the primitive Bragg peaks (131/$\bar{1}$31/311/$\bar{3}$11) and (124/$\bar{1}$24/214/230/$\bar{2}$14/320), respectively. It can be seen clearly that these peaks, of the type hkl which not satisfy the $h+k+l = 2n$ reflection condition, gradually disappear at about 640K. This observation indicates that at about 640K, the structure transforms from primitive unit cell to a centered unit cell. Unfortunately the neutron diffraction measurement could not show significant changes for the rest of the peaks in the temperature range 430–1200K. This is because D20 is a resolution limited instrument. The disappearance of the primitive Bragg peaks is also observed in the X-ray diffraction measurement results. For example, in figure 7(c), the peaks (124/$\bar{1}$24/214/230/$\bar{2}$14/320), observed in (58.0°–59.5°) 2θ interval, disappear at the same temperature 640K. Figure 8 shows the results obtained by X-ray diffraction measurements in the (73°–76°) 2θ selected interval, corresponding to (620) cubic reflection. At all temperatures covered, the 2θ region chosen for the phase transition search contains a group of diffraction peaks that has been identified as especially sensitive to the structural changes occurring in double perovskite materials [43]. The monoclinic triplet converts to a tetragonal doublet reflection at the same temperature at which the primitive Bragg peaks disappear, and, eventually, the tetragonal splitting disappears and the double reflection evolves to a single cubic one at about 960K. This behavior is very similar to that observed, for instance, in Sr$_2$CaWO$_6$ [43], where these changes were interpreted as evidence of the material undergoing two phase transitions: first, from a monoclinic structure to a tetragonal one, and (at higher temperature) then from tetragonal to cubic.

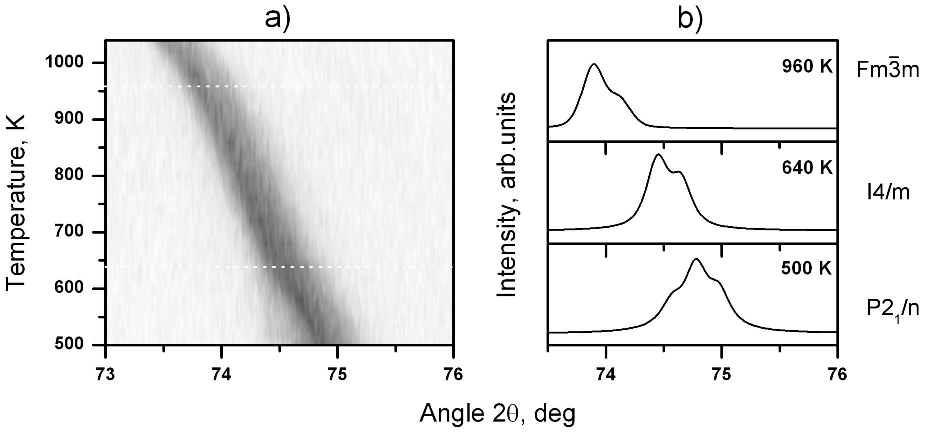

FIGURA 7.8: Thermal evolution of (620) cubic reflections as obtained from XRPD experiments under vacuum of $Sr_2Mn^{2+}WO_6$. The scattered intensity is represented with gray scale, black being high intensity and white lowest intensity. The monoclinic triplet converts to a tetragonal doublet reflection at the same temperature of disappearance of the primitive Bragg peaks, and, eventually, the tetragonal splitting disappearance and the double reflection evolves to a single cubic one at about 960K.

Next, we measured sample 2 in the (17°–80°) 2θ range and in the temperature interval from 500K to 1040K, with a temperature step of 20K, to have good enough data to determine the variation of the cell parameters with temperature. In figure 9 we show the results obtained for the variation with temperature of the cell parameters (a) and unit cell volume (b), in sample 2. Up to 640K the compound is monoclinic ($P2_1/n$); from 640K to 940K it is tetragonal ($I4/m$); and it remains cubic ($Fm\bar{3}m$), from 960K up to 1040K. It can be observed that, in the monoclinic phase, the metric parameters ($b\sqrt{2}$, c) change continuously, and, at 640K, become almost equal. The observed phase-transition sequence, $P2_1/n \rightarrow I4/m \rightarrow Fm\bar{3}m$, is the "usual" two phase-transition sequence encountered in some of the members of the double perovskite tungstate oxide family, and connects the three space groups most frequently found for the ordered perovskites.

$Sr_2Mn^{3+}WO_{6+\delta}$

As in the previous case, the search for phase transitions was carried out by performing diffraction measurements of sample 3, in the (17°–80°) 2θ range and in the temperature interval from 320K to 870K, with a temperature step of 20K, to have good enough data to determine the variation of the cell parameters with temperature. The temperature dependence of the cell parameters (a) and unit cell volume (b), is shown in figure 9. At about 710K a strong discontinuous phase transition is observed. The high temperature phase is indexed as cubic $Fm\bar{3}m$ and the low temperature one as tetragonal, body centered. No changes in the set of observed reflections were found below this temperature, suggesting that the unit cell does not change in the temperature range from 700K to room temperature. However, at about 490K a very small change in the slope of the curve of variation of the c tetragonal cell parameter is observed (in figure 9 we have shown the prolongation of the temperature evolution of the $I4/m$ c cell parameter with a dashed line as guide for the eyes). This behavior is compatible with a continuous phase transition.

In a double perovskite structure with the $I4/mmm$ space group the octahedra are not rotated, therefore, there is no change in the intensity of some reflections with temperature. In a double perovskite structure with the $I4/m$ space group, however, the octahedra are rotated. In this case, there is a change in the intensity of some reflections with the rotation angle: the bigger the value of the rotation angle, the smaller the height of the peaks. Thus, the assumption that there is a continuous phase transition at 490K, for which the order parameter is proportional to the rotation angle, could explain the change of the cell parameters observed in figure 9. The XRPD are not suitable for these observations, and the NPD data that we have are not good enough for seeing these intensity changes. But, if we assume that at 490K there is a phase transition under way, this (very small) anomaly could be explained as produced by the homogeneous strain coupled to the order parameter. It is not easy to observe a transition of the type $I4/m \rightarrow I4/mmm$, because the two space groups have the same extinction conditions (no peak splitting or appearance of new peaks is expected). It should also be pointed out that the refinement of the room temperature structure in the $I4/m$ space group gives better reliability parameters than the refinement in the $I4/mmm$ group, although the difference is small. This is due to the fact that X-ray diffraction is not very sensitive to the positions of the oxygen atoms. The fact that the transition is continuous makes most of the thermal analysis methods unsuitable for its detection. The evidence presented here is not enough to affirm the existence of such a transition. However, in the analysis that we made in $Sr_2Cu^{2+}WO_6$ double perovskite [42], we showed that due to the Jahn-Teller character of the Cu^{2+} cation there was an intermediate phase between the low-temperature $I4/m$ and the High-temperature $Fm\overline{3}m$ phase, $I4/mmm$: we suggested that the lowering of the symmetry from $Fm\overline{3}m$ to $I4/m$ in $Sr_2Cu^{2+}WO_6$ was performed in two steps, $Fm\overline{3}m \rightarrow I4/mmm \rightarrow I4/m$. Now, we suggest that, being Mn^{3+} Jahn-Teller active, the same behavior could be expected for $Sr_2Mn^{3+}WO_{6+\delta}$.

The variations of the lattice parameters $a\sqrt{2}$, c and V with temperature in $Sr_2Mn^{3+}WO_{6+\delta}$ are presented in figure 9, all of them increase monotonously with increasing temperature. They are smaller than those observed for $Sr_2Mn^{2+}WO_6$, due to the difference between the ionic radii of Mn^{3+} (0.645) and Mn^{2+} (0.830).

7.2. Conclusions

We present, the new effective route for synthesizing Sr_2MWO_6 double perovskite oxides as the co-precipitation method because it needs a lower maximum temperature of thermal treatment and only two days of preparation. Moreover, the samples obtained in this way contain a very low quantity of impurity. Using conventional X-ray diffraction methods, we have confirmed the room-temperature space group of $Sr_2Mn^{2+}WO_6$ to be $P2_1/n$, and we have shown that the compound presents the following temperature induced phase-transition sequence: $P2_1/n \rightarrow I4/m \rightarrow Fm\bar{3}m$. After a thermal treatment, 24 hours at 870K in air, the $Sr_2Mn^{2+}WO_6$ compound transforms irreversibly to $Sr_2Mn^{3+}WO_{6+\delta}$. This transformation has been confirmed by EPR and XANES measurements. Also, we have confirmed the room-temperature space group of $Sr_2Mn^{3+}WO_{6+\delta}$ to be $I4/m$, and we have shown that the compound presents the following temperature induced phase-transition sequence: $I4/m(\rightarrow I4/mmm) \rightarrow Fm\bar{3}m$. The tetragonal-to-tetragonal phase transition is suggested to be present (taking into account the behavior of Sr_2CuWO_6), not seen as it is very weak; and it is attributed to the presence of the Jahn-Teller active Mn^{3+} cation.

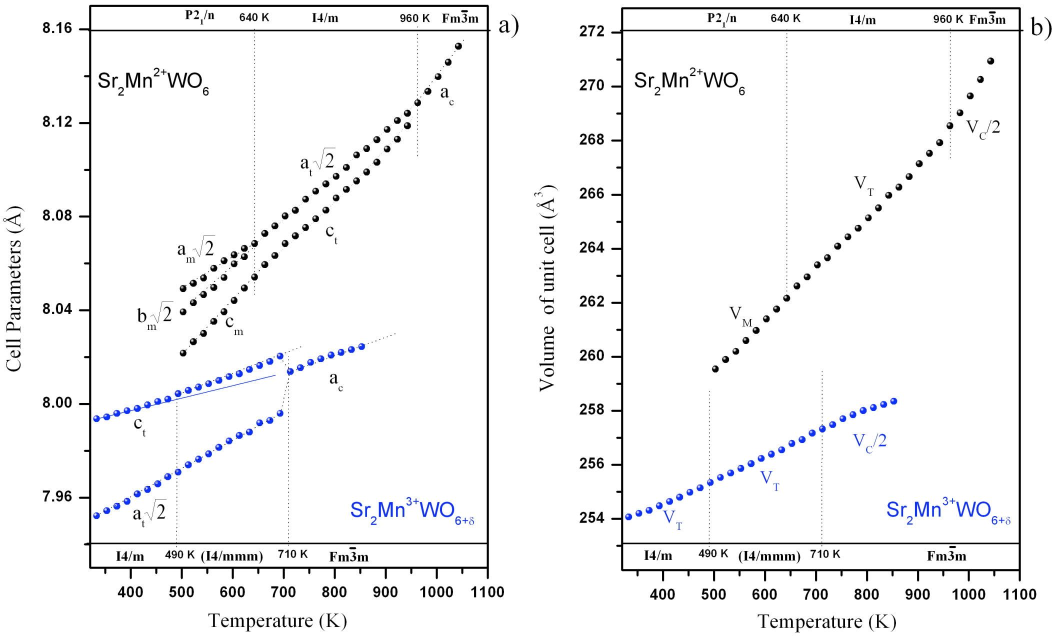

FIGURA 7.9: Variation with the temperature of the cell parameters (a) and unit cell volume (b) of $Sr_2Mn^{2+}WO_6$ and $Sr_2Mn^{3+}WO_{6+\delta}$, as indicated.

Parte III

Estructuras cristalinas y transiciones de fase en la familia de antimonio AA’MSbO$_6$

8.1. Introducción

Tras haber analizado los materiales pertenecientes a la familia del wolframio, se pasó a estudiar la familia del antimonio. La familia del wolframio responde a la siguiente fórmula general: $Sr_2M^{2+}W^{6+}O_6$. Uno de los resultados encontrados en el trabajo anterior, es que debido a la gran diferencia de carga que existe entre los cationes situados en las posiciones de tipo M de la perovskita, en todas las estructuras resueltas se ha visto un ordenamiento completo de los cationes M^{2+} y W^{6+}. La familia del antimonio, por su parte, responde a la siguiente fórmula general: $Sr_2M^{3+}W^{5+}O_6$. En este caso la diferencia de carga entre los dos cationes en las posiciones B y B′ de la perovskita es menor que en el caso de la familia del wolframio, con lo que se espera que el ordenamiento pueda no ser total, como en la familia del wolframio. Uno de los factores que gobierna el ordenamiento de los cationes es, además del método de síntesis, o el tamaño relativo de los cationes, precisamente la diferencia de carga. Por esta razón se elgió esta familia, porque pertenece al sistema (3+,5+): se ha tratado de estudiar, etre otras cosas, el grado de ordenamiento de los cationes B en estos tipos de materiales.

Otras de las razones por las que se decidió estudiar el sistema (3+,5+) con Sb en la posición B′ es que muy pocos materiales de esta familia han sido sintetizados y analizados, estructuralmente, tanto a temperatura ambiente, como a bajas y altas temperaturas. De esta manera, todo hacía indicar que la familia del antimonio era una candidata muy adecuada para dilucidar hasta qué punto un cambio de sistema (pasar del sistema (2+,6+) al (3+,5+)) podía modificar las características observadas en el diagrama de fases de la familia del wolframio, que como ya se ha indicado en esta memoria, son tres: primero, la secuencia de transiciones de fase observadas es $P2_1/n \rightarrow I4/m \rightarrow Fm\bar{3}m$, con dos transiciones; segundo, a temperatura ambiente, según disminuye el factor de tolerancia menor es la simetría de las estructuras observadas; tercero, conforme disminuye el factor de tolerancia se estabiliza en un intervalo de temperatura mayor la fase monoclńica de baja temperatura $P2_1/n$, y, además, la fase tetragonal intermedia disminuye su intervalo de estabilidad.

El trabajo que se planteó quiso responder, entre otras, a las siguientes preguntas:

- ¿Cómo evluciona con el factor de tolerancia la fase de temperatura ambiente?
- ¿Cuántas transiciones de fase se producen?
- ¿Cuáles son?
- ¿Hay más de una fase intermedia?
- ¿Cómo es su rango de estabilidad, varía?
- ¿Hay alguna relación entre estas transiciones y las de la familia del wolframio?

En la figura 1, se resumen los resultados experimentales conocidos para los miembros estudiados de la familia de antimonio (Sr_2BSbO_6, B=Sm,La,Fe,Cr,Mn,Ga,Co).

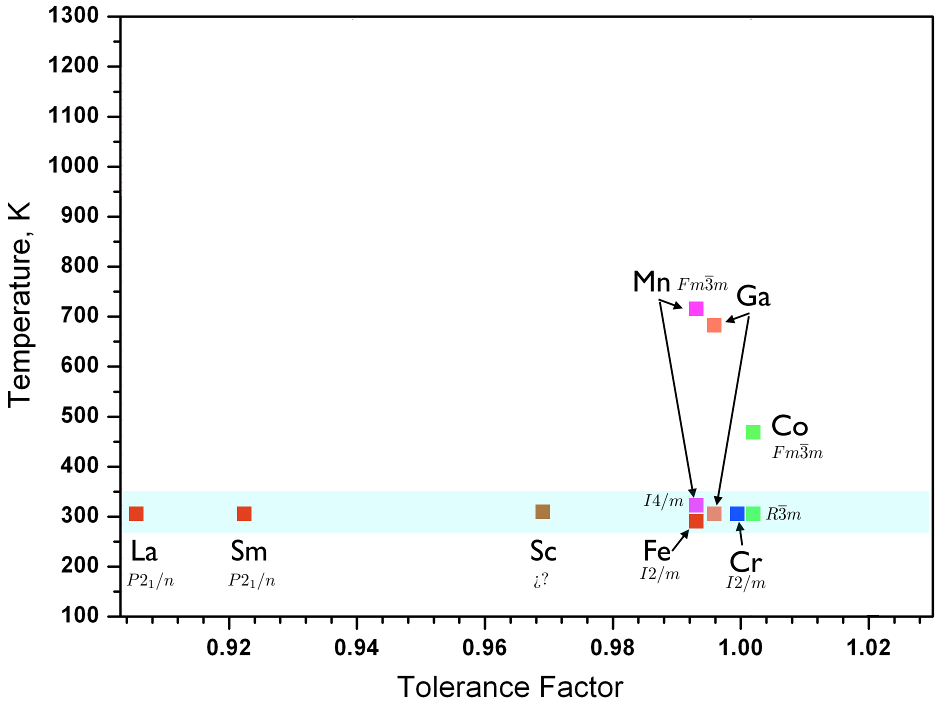

Por lo que se puede deducir, la mayoría de los materiales se han analizado sólo a temperatura ambiente; hay tres casos en los que se han estudiado las secuencias de transciones de fase de alta temperatura: Mn, Ga (sólo con Rayos-X) y Co.

Llama la atención que a temperatura ambiente ya hay tres grupos espaciales más, $I2/m$, $I4/m$ y $R\bar{3}m$, que en el caso de la familia del wolframio, y, además con una simetría mayor. Podría tratarse de alguna fase intermedia entre la de baja temperatura, monoclínica $P2_1/$ (también de la familia del wolframio) y la de alta temperatura $Fm\bar{3}m$, que también se observa en los tres casos medidos a alta temperatura.

También llama la atención la presencia de otra fase (¿itermedia?) trigonal, $R\bar{3}m$, no observada nunca en la familia del wolframio y muy pocas veces observada en otras familias, a pesar de estar permitida por simetría.

Otro aspecto interesante es el cambio brusco de simetría, de monoclínica ($I2/m$) a tetragonal ($I4/m$) e incluso trigonal ($R\bar{3}m$), que se produce entre los compuestos de Fe, Mn, Ga, Cr y Co, con un factor de tolerancia muy similar (en el caso del Fe y del Mn iguales): la experiencia en la familia del wolframio indica que deberían comportarse de manera similar, o si no es así, en el diagrama de fase de la familia de antimonio existe una frontera o la familia presenta un comportamiento totalmente distinto.

Los objetivos de la segunda parte del estudio resumido en la presente memoria han sido los siguinetes:

- ◇ Por una parte, comprobar las asignaciones de los grupos espaciales en las fases de temperatura ambiente de los materiales conocidos, y asignar correctamente los grupos espaciales a los no conocidos (Sc, por ejemplo).
- ◇ Por otra parte, se han querido obtener las secuencias de las transiciones de fase en temperatura, tanto a altas como a bajas temperaturas.
- ◇ También se ha querido comprobar que efectivamente existe una correlación entre el factor de tolerancia y las temperaturas de transición, las secuencias de las transiciones de fase, la extensión del rango de estabilidad de la fase o fases intermedias y el volúmen de la celda unidad a temperatura ambiente (independientemente de la simetría).
  Como el factor de tolerancia es una medida del tamaño relativo de los cationes presentes en las posciones B y B′ de la perovskita doble, y como uno de los cationes está fijo (B′=Sb), y el factor de tolerancia es una medida de la distancia entre los cationes B y B′ (mediada por los oxígenos que comparten). En definitiva, el objetivo ha sido completar el diagrama de fases presentado en la figura 1: esto es, obtener un diagrama de fase en términos de un factor geométrico.

El objetivo se abordó de la siguiente forma:

- ◇ Lo mismo que en el caso de la familia del wolframio, se decidió intercalar algún material con factor de tolerancia intermedio entre el de los compuestos de Sm y Fe (por ejemplo). Se eligió el catión Sc. En la sección Trabajo Futuro se describen más compuestos a intercalar en esta zona.
- ◇ Además, se intentó saber si podrí cambiar de manera contínua el factor de tolerancia, sintetizando una solución sólida de los compuestos con La y Sm.
  En este caso, también, se buscaba saber si incluso para una solución sólida se mantenían las características observadas para los miembros “puros” de la familia.
- ◇ Finalmente, como ya se ha mencionado los casos del Mn, Fe, Cr, Ga y Co se consideraron especialmente interesantes puesto que presentas simetrías distintas con factoresde tolerancia muy similares, en el caso del Ga el estudio en temperatura (muy alta temperatura se hace mediante Rayos-X), y al Co se le asigna un grupo espacial nada común.

Capítulo 9

Crystal Structures and Cation Ordering of Sr_2AlSbO_6 and Sr_2CoSbO_6

9.1. Introduction

The family of strontium antimony oxides with double perovskite structure has attracted considerable attention because of the magnetic properties of some of its members, such as Sr_2FeSbO_6 [80, 81]. From structural point of view, different symmetries have been reported for these materials: monoclinic, tetragonal, trigonal and cubic (Table 1). Despite this variety, very few temperature-dependent structural studies have been conducted [82].

Structural data of previously studied Sr_2MSbO_6 double perovskite oxides are summarized in Table 1. All materials were prepared by solid state reaction method with the exception of the Al-containing material reported in this work for which sol-gel method was also used. The table shows the synthesis temperatures, the tolerance factors, $t = \frac{r_{\mathrm{Sr}}+r_{\mathrm{O}}}{\left(\frac{r_{\mathrm{B}}+r_{\mathrm{B}'}}{2}\right)+r_{\mathrm{O}}}$, [66] (calculated using the ionic radii suggested in [3]), the degree of ordering between the M^{3+} and Sb^{5+} cations over the B-sites of the perovskite structure, and the reported symmetry at room temperature. The compound Sr_2MnSbO_6 was not included in the table because its crystal structure is strongly distorted due to the Jahn-Teller effect [86] and does not follow the trends observed in the other Sr_2MSbO_6 materials. As seen in Table 1, only the Al-containing material reported in this work has a cubic structure at room temperature and a tolerance factor well above 1. Sr_2CoSbO_6 and Sr_2GaSbO_6 are two materials with tolerance factors very close to 1 and with trigonal and tetragonal symmetries, respectively. The rest of the materials are monoclinic and with tolerance factors below 1.

The aim of the present work is to analyze the structures and the possible structural phase transitions of Sr_2AlSbO_6 and Sr_2CoSbO_6, as there are no previous studies on the temperature-dependent structural modifications of these materials. This work is a part of a systematic study that we have undertaken on the $AA'BSbO_6$ (AA'=Ca_2,SrCa,Sr_2), and (B=Al,Co,Cr,Fe,Sc. . .) family of materials.

TABLA 9.1: Structural details and preparation conditions of Sr_2MSbO_6 compounds. The data shown are as follows: Highest temperature of treatment; tolerance factor calculated from the ionic radii in [3]; experimentally observed degree of cation ordering; symmetry of the crystal structure at room temperature; literature reference. "PW"stands for present work.

Compound	Syn. Temp.(K)	t	D.O. (%)	S.G. at 300K	Ref.
Sr_2AlSbO_6	1770	1.021	98	$Fm\bar{3}m$	PW
	1375*		91	$Fm\bar{3}m$	PW
Sr_2CoSbO_6	1570-1620	1.002	77	$R\bar{3}m$	[18]
	1770		80	$R\bar{3}$	PW
Sr_2GaSbO_6	1570-1870	0.999	100	Tetragonal	[83]
	–		100	$I4/m$	[82]
Sr_2FeSbO_6	1570	0.993	80	$P2_1/n$	[80]
	–		80	$P2_1/n$	[81]
Sr_2InSbO_6	1470	0.956	100	$P2_1/n$	[84]
Sr_2YSbO_6	1545	0.934	100	$P2_1/n$	[84]
Sr_2HoSbO_6	1670	0.934	100	$P2_1/n$	[85]
Sr_2DySbO_6	1670	0.931	100	$P2_1/n$	[85]

The structure and magnetic properties of Sr_2CoSbO_6 were first studied in [87] and [88], and it was reported that this material is pseudo-cubic. In addition, it was claimed that this is the first oxide with Co^{3+} being completely in the high-spin ($S = 2$) state, due to the high value found (5.2 μ_B) for the effective magnetic moment. More recently, the room-temperature structure of Sr_2CoSbO_6 (together with $Sr_2CoSbO_{5.63}$) was re-investigated [18], and the suggestion was made that it has a trigonal symmetry with space group $R\bar{3}m$ (No. 166); lattice constants $a = 5.5992(2)$ Å and $c = 13.6609(2)$ Å, and a partial ordering (77 %) of the Co^{3+} and Sb^{5+} cations.

Finally, in [89] Sr_2CoSbO_6 was studied using x-ray and neutron powder diffraction methods. It was confirmed that this material is a trigonal perovskite, but due to the lack of cation ordering, the author assigned the $R\bar{3}c$ (No. 167) space group.

It is interesting to note that the assignation of $R\bar{3}m$ space group suggested in [18] is rather unusual for a double perovskite material. The reason is that $R\bar{3}m$ allows the constituent octahedra to be distorted, but not rotated, which is by far the most common modification of the perovskite structure. On the other hand, many trigonal perovskites are reported with $R\overline{3}$ (No. 148) space group which allows out-of-phase rotations of the octahedra around the $[111]_p$ direction of the simple perovskite and corresponds to the $(a^-a^-a^-)$ tilt system [24, 25]. The space group $R\overline{3}c$ suggested in [89], corresponds to the $(a^-a^-a^-)$ tilt system in the cases of disordered double perovskites and simple perovskites.

These peculiarities of the previous structural determinations warranted a re-investigation of the room-temperature crystal structure of Sr_2CoSbO_6. In a similar re-examination [90] the structure of Ba_2BiSbO_6, which was initially reported to have $R\overline{3}m$ space group, was later shown [91] to be described better by $R\overline{3}$. With respect to Sr_2AlSbO_6, to the best of our knowledge this is the first time that it has been prepared and its room-temperature structure determined.

9.2. Room-temperature Structure of Sr_2AlSbO_6 and low-temperature Raman spectroscopy data

X-ray measurements of sample 1 and sample 2 of Sr_2AlSbO_6 (Figs. 1a and 1b) revealed that the structure of this material is cubic (undistorted) double perovskite with the $Fm\overline{3}m$ space group. Refined structural parameters for the two samples are given in Table 2. Cubic perovskite structures are especially suitable for the study of the degree and the extension of the cation ordering, since in this case the superstructure reflections, i.e. those related to the B-cation ordering, are not overlapping with the order-independent reflections and there is no peak splitting due to unit cell distortion.

Fig. 2 shows a comparison between the diffraction data collected from samples 1 and 2 and a Williamson-Hall plot of the diffraction peaks in the two samples. It can be seen that the superstructure reflections arising from the presence of rock-salt type ordering between the B-site cations (solid squares) are clearly broader than those of the rest of the peaks. From the Rietveld refinement it was obtained that the average crystallite size is about 110±1 nm, and that the effective size of the ordered regions within the crystallites is 17±1 nm. A similar result was obtained in [92] for Sr_2AlTaO_6 and it was interpreted as an evidence for the presence of anti-phase domains. The presence of anti-phase boundaries is also the cause for the increased lattice strain, given by the slope in Fig. 2b. The Rietveld refinement of the diffraction data for sample 1, with variable occupancy factors for the Al and Sb cations, and anisotropic broadening rules accounting for the larger peak widths of the superstructure $(h + k + l = 2n + 1)$ reflections showed that about 91 % of the B-cations occupy their respective sites (see Table 2). For sample 2, no *hkl* specific broadening was observed in the diffraction data and the refined cation ordering was $\approx$98 %.

It is well known [14] that the degree of cation ordering depends mostly on the charge, size and polarization properties of the the B-site cations. However it can be also affected by the synthesis temperature, sintering time and the method of preparation. In the case of the two Sr_2AlSbO_6

TABLA 9.2: Crystal structure parameters for Sr_2AlSbO_6 (sample 1 and sample 2) at room temperature. The atomic positions are: Sr(8c: 1/4,1/4,1/4), Sb1/Al2(4a: 0,0,0), Al1/Sb2(4b: 1/2,1/2,1/2), O1(24e: x,0,0) in the space group $Fm\overline{3}m$.

		Sample 1	Sample 2
a (Å)		7.7662(1)	7.7634(1)
Vol (Å^3)		468.40(1)	467.92(1)
O_{1x}		0.252(1)	0.251(1)
B_{iso}(Å^2)	Sr	0.64(5)	0.37(4)
	Al/Sb	0.22(3)	0.55(3)
	O	0.68(7)	0.65(7)
Occupancy	Sb1/Al2(4a)	0.91(1)/0.09(1)	0.98(1)/0.02(1)
	Al1/Sb2(4b)	0.91(1)/0.09(1)	0.98(1)/0.02(1)
R_p (%)		14.1	11.9
R_{Bragg} (%)		3.81	3.31
χ^2		1.93	1.30

samples discussed here, the difference in the degrees of cation ordering found in samples 1 and 2 is probably related to the methods of preparation and to the sintering temperatures. As mentioned above, samples 1 and 2 were prepared following different routes: sol-gel method with highest temperature treatment at 1373K and conventional ceramic method with 1770K.

The Raman spectroscopic measurements of Sr_2AlSbO_6 (sample 2) performed from room temperature down to 79K are shown in Fig. 3. As seen, there are no notable changes at lower temperatures, and it can be concluded that the cubic structure observed at room temperature remains stable down to, at least, 79K.

9.3. Room-temperature Structure of Sr_2CoSbO_6

The diffraction pattern collected from Sr_2CoSbO_6 at room temperature is shown in Fig. 4. Many diffraction lines are clearly split, indicating that the unit cell of this material is not cubic. The observed splitting is consistent with the trigonal symmetry suggested in [18]. For example, the inset in Fig. 4 shows the splitting of the (444) cubic reflection into (440) and (0012) reflections of $R\overline{3}m$.

As a starting model for the Rietveld refinement we used the structure with space group $R\overline{3}m$ suggested in [18]. The results of the refinements are shown in Fig. 4, and the structural details of Sr_2CoSbO_6 at room temperature, refined by assuming the $R\overline{3}m$ space group, are given in Table 3.

It can be seen that the isotropic displacement parameter for the oxygen atoms is larger than

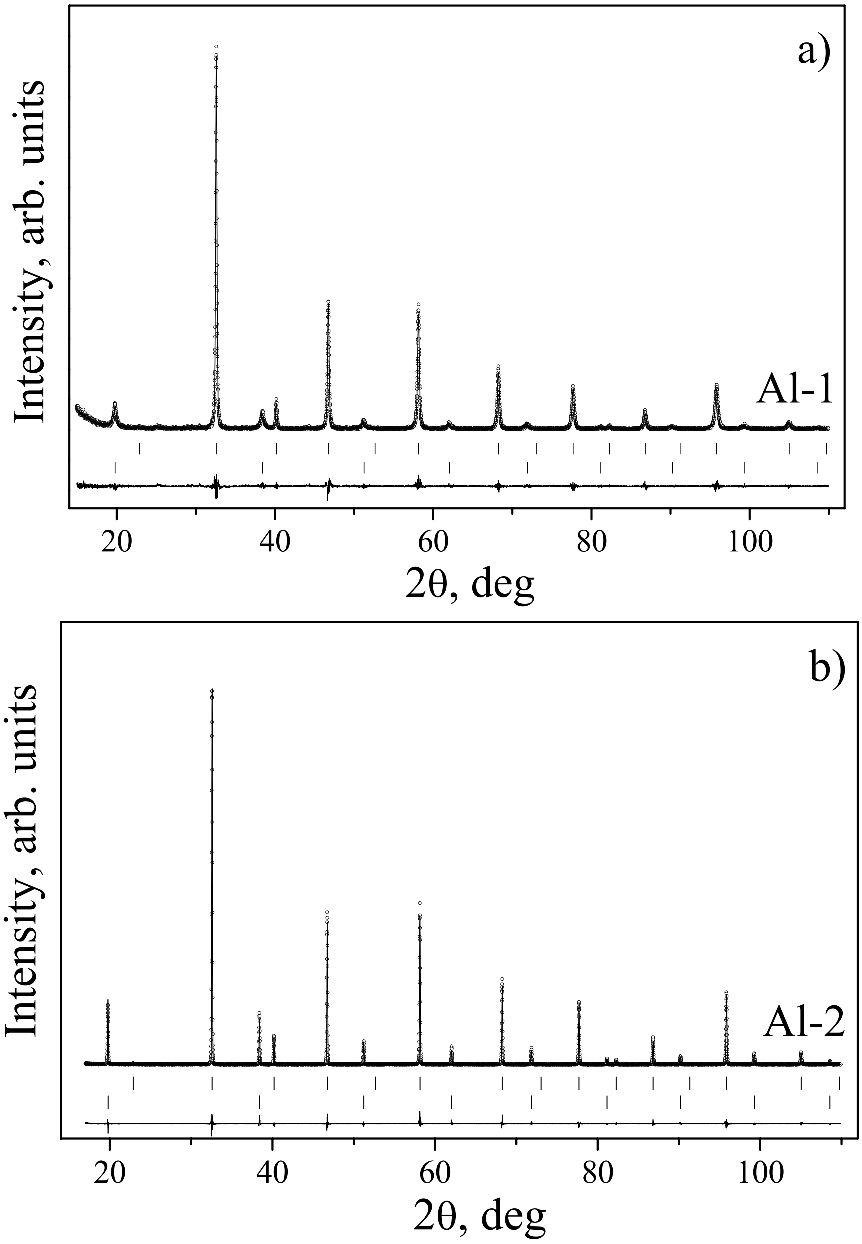

FIGURA 9.1: Experimental (symbols) and calculated (line) powder diffraction profiles for the Rietveld refinement of Sr_2AlSbO_6 at room temperature using a structural model with $Fm\bar{3}m$ space group: (a) sample 1 and (b) sample 2. The bars in the lower part of the graphics represent the Bragg peak positions. The upper set of bars correspond to the simple perovskite structure (sub-cell); and the lower set of bars give the positions of peaks arising from the presence of the B-site cation ordering (super-cell).

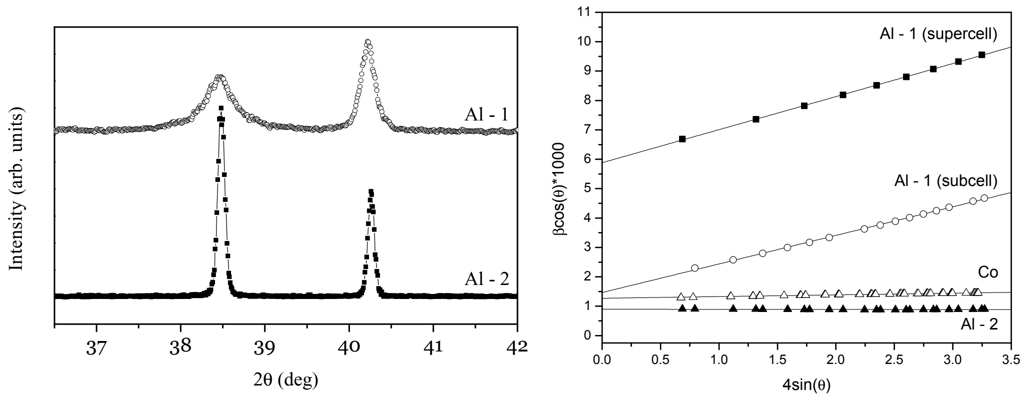

FIGURA 9.2: (a) Comparison between the diffraction data from sample 1 and sample 2. (b) A Williamson-Hall plot of the diffraction peaks in sample 1 and sample 2: β denotes the integral breadth corrected for instrumental effects, θ is the diffraction angle. It can be seen that in the case of sample 1 β of the superstructure reflections (solid squares), are clearly larger than those of the rest of the peaks.

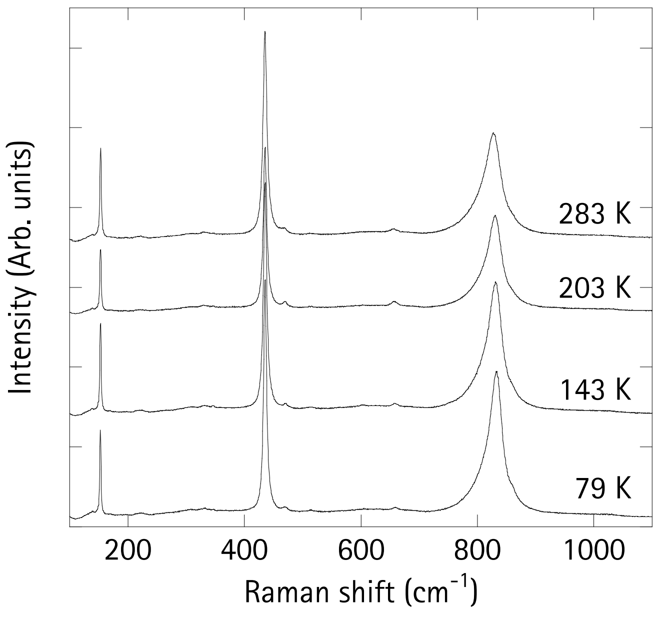

FIGURA 9.3: Raman spectra of Sr$_2$AlSbO$_6$ (sample 1) at different temperatures (excitation 514.5 nm). No significant changes are observed at lower temperatures, indicating that the cubic structure observed at 300K remains stable down to, at least, 79K.

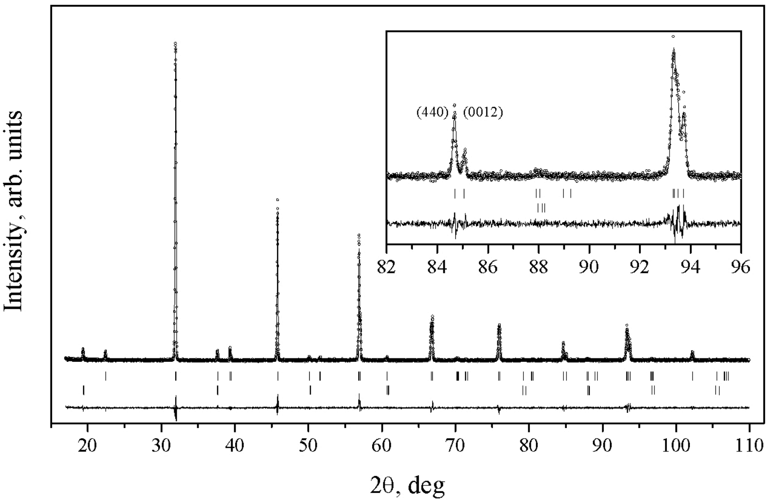

FIGURA 9.4: Experimental (symbols) and calculated (line) powder diffraction profiles for the Rietveld refinement of Sr_2CoSbO_6 at room temperature using a structural model with $R\overline{3}m$ space group. The bars in the lower part of the graphics represent the Bragg peak positions. The upper set of bars correspond to the simple perovskite structure (sub-cell). The lower set of bars give the positions of the superlattice reflections, indicating partial order in the B-site of the double perovskite structure. The inset shows the splitting of the (444) cubic reflection

the usually observed in similar materials at room temperature (compare with Table 2). The same result was obtained in [18], but no satisfactory explanation was given. Such high isotropic displacement parameters could be an indication that the actual symmetry of the structure is lower than the one used in the refinement. As mentioned above, the most common trigonal space group observed in double perovskite oxides is $R\overline{3}$. As a next step in our study, we attempted a refinement with this space group. The difference between the structural models with $R\overline{3}m$ and $R\overline{3}$ space groups is that in the former the oxygen atoms are located on the plane m $(x, -x, z)$, and in the latter they are allowed to be displaced out of it (see figures 5a and 5b). These two trigonal space groups have the same extinction conditions, and the only way to distinguish between them is to compare the refined structural parameters and agreement factors. The structural details of the room-temperature structure of Sr_2CoSbO_6 refined with the $R\overline{3}$ space group are summarized in table 3.

Comparing the two structural models shown in table 3, it can be seen that these models are very similar to each other: the same position ($z = 0.249$) for the Sr^{2+} cation; and very similar values for the isotropic atomic displacements parameters of Co^{3+}, Sb^{5+} and Sr^{2+} cations. However, it can be also observed that the x and y fractional coordinates of the oxygen atoms are slightly different, and that their isotropic atomic displacement are lower (0.88 Å^2) in the $R\overline{3}$ model compared to the $R\overline{3}m$ model (2.11 Å^2). Also, the refinement with $R\overline{3}$ is both visually (Fig. 6) and statistically (compare agreement factors) better than the one with $R\overline{3}m$. Based on these results, we suggest that

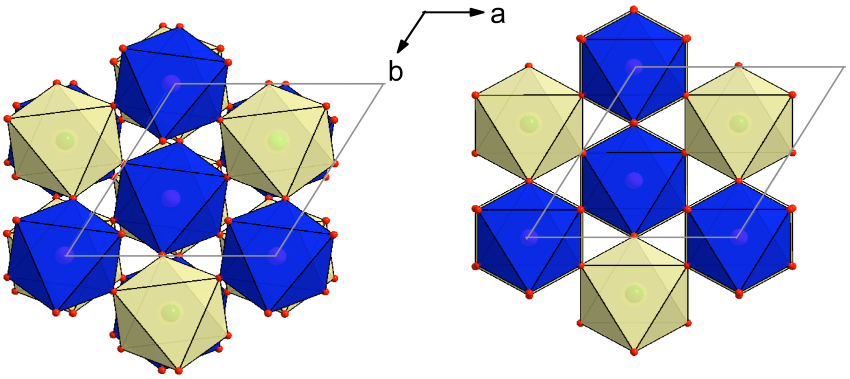

a) R$\bar{3}$

b) R$\bar{3}$m

FIGURA 9.5: Projections, along z axis, of the structure of Sr$_2$CoSbO$_6$ using the two trigonal models, as indicated. The difference between them is the m mirror plane present in $R\bar{3}m$ and absent in $R\bar{3}$.

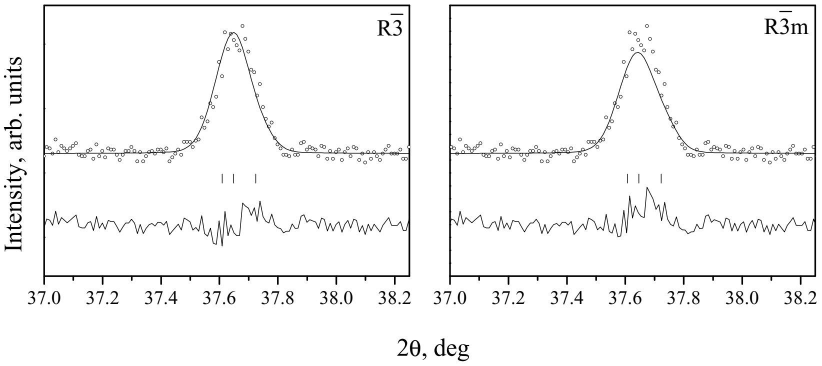

FIGURA 9.6: Rietveld refinement of Sr$_2$CoSbO$_6$, at room temperature, using the $R\bar{3}$ and $R\bar{3}m$ space groups. Experimental (symbols) and calculated (line) and difference powder diffraction profiles. The bars represent the Bragg peak positions. The structural model in $R\bar{3}$ fits better the intensity of the peak.

TABLA 9.3: Crystal structure for Sr_2CoSbO_6, at room temperature, in the $R\bar{3}m$ and $R\bar{3}$ space groups. The atomic positions in the $R\bar{3}m$ space group are: Sb1/Co2(3b: $0, 0, 1/2$), Co1/Sb2(3a: $0, 0, 0$), Sr(6c: $0, 0, z$), O1(18h: $x, -x, z$). The atomic positions in the $R\bar{3}$ space group are: Sb1/Co2(3b: $0, 0, 1/2$), Co1/Sb2(3a: $0, 0, 0$), Sr (6c: $0, 0, z$), O1(18f: x, y, z).

		$R\bar{3}m$	$R\bar{3}$
a (Å		5.6060(1)	5.6058(1)
c (Å		13.6762(3)	13.6758(3)
Vol (Å^3		372.23(1)	372.19(1)
O_{1x}		0.2498(3)	0.128(1)
O_{1y}		-0.170(1)	-0.207(1)
O_{1z}		0.584(1)	0.583(1)
B_{iso}(Å^2)	Sr	0.75(5)	0.75(5)
	Co/Sb	0.23(5)	0.26(7)
	O	2.11(5)	0.88(2)
Occupancy	Sb1/Co2(3b)	0.80(1)/0.20(1)	0.80(1)/0.20(1)
	Co1/Sb2(3a)	0.80(1)/0.20(1)	0.80(1)/0.20(1)
R_p (%)		11.8	8.47
R_{Bragg} (%)		4.28	1.77
χ^2		1.41	1.15

the room-temperature structure of Sr_2CoSbO_6 is better described by the $R\bar{3}$ space group, and that the CoO_6 and SbO_6 octahedra are rotated according to the $a^-a^-a^-$ tilt system. Neutron diffraction studies are under way to confirm this result.

The presence of ordering between the Co^{3+} and Sb^{5+} cations is indicated by the super-lattice reflections in the room-temperature diffractogram (lower set of reflections in Fig. 4). The degree of this ordering deduced from the final Rietveld refinement in the $R\bar{3}$ space group model is $\approx$80 %.

In the case of Sr_2CoSbO_6, despite the high synthesis temperature (1770K), the degree of ordering is relatively low. This can be explained by the small difference between the radii of the B-site cations: $\Delta r = 0.01$ Å [3]. For comparison, in Sr_2AlSbO_6 this difference is $\Delta r = 0.065$ Å. Another interesting fact is that the sample-related broadening of the diffraction peaks of Sr_2CoSbO_6 does not show any significant *hkl*-dependence, see fig. 2b. This suggests that no extended anti-phase boundaries are formed within the crystallites and the observed low degree of ordering is caused by randomly distributed anti-site defects. In the case of trigonal perovskites the effect of the cation ordering on the peak widths cannot be visualized easily as in the case of cubic perovskites (Fig.2a) due to the overlapping of the order-related reflections with sub-cell reflections (see Fig. 4) and the peak splitting due to the trigonal distortion of the unit cell. The results in this section are based on the independent refinement of the profile parameters of the super-cell and sub-cell reflections.

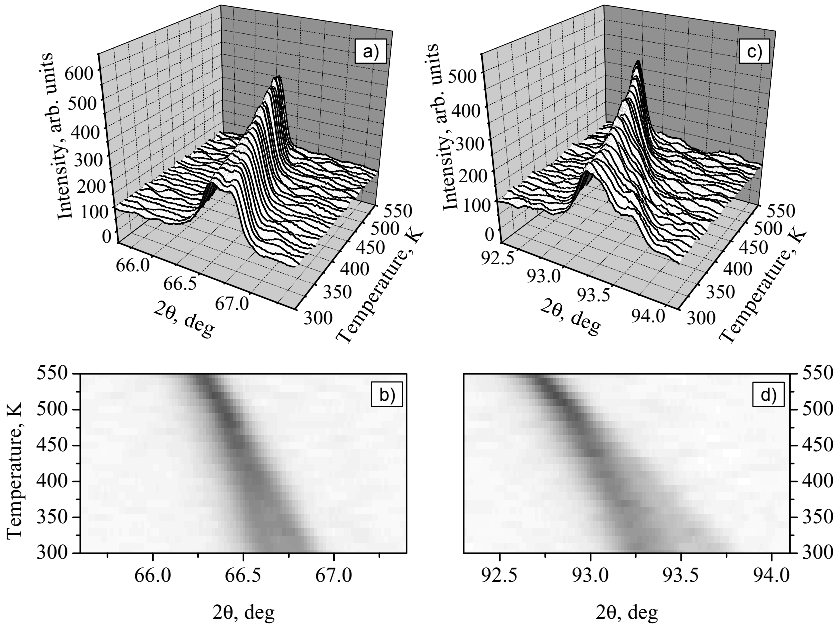

FIGURA 9.7: Thermal evolution of the (440) and (642) cubic reflections, (a) and (c) respectively. In panels (b) and (d) the scattered intensity of the same reflections is projected and represented with shades of gray. Black corresponds to high intensity, and white to low intensity. The trigonal splitting disappears at about 470K.

A remark on the oxygen content of our sample is in order. In [18] it was shown that the oxygen content of the Sr_2CoSbO_6 sample can strongly influence its structure. For example, a sample synthesized in air had about 6 % oxygen deficiency and a cubic structure, while a second sample prepared under a high-pressure oxygen atmosphere showed no deficiency and a trigonal structure. Both samples were synthesized using Sb_2O_3 as a source of antimony. In our preparation method no oxygen atmosphere is required to obtain the stoichiometric compounds.

9.4. High-temperature phase-transition in Sr_2CoSbO_6

The diffraction patterns collected from Sr_2CoSbO_6 at high temperatures revealed that the peak splitting caused by the trigonal distortion of the unit cell disappears in a continuous way at about 470K (Fig. 7). This indicates the change of the structure from trigonal to cubic. The patterns collected at temperatures higher than 470K were well fit by a structural model with the space group $Fm\overline{3}m$, corresponding to the undistorted aristotype double perovskite structure (tilt-system $a^0a^0a^0$). No further changes in the set of observed reflections were found above this temperature, suggesting that the type of unit cell does not change in the temperature range from 470 to 650K.

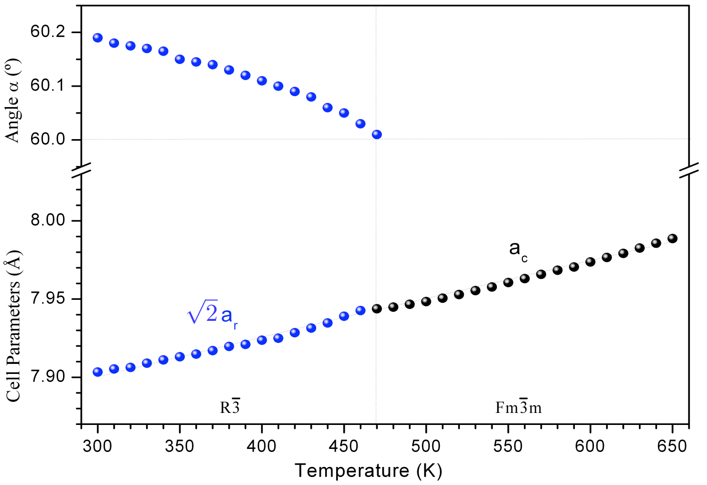

FIGURA 9.8: Temperature evolution of the lattice parameters of Sr_2CoSbO_6 in rhombohedral notation. The rhombohedral angle α decreases continuously with temperature and at ≈470K becomes equal to 60 deg and the unit cell becomes cubic.

Fig. 8 shows the evolution with temperature of the lattice parameters of Sr_2CoSbO_6. In this figure we have represented the unit cell in the rhombohedral description (a=b=c, α=β=γ), instead of the hexagonal one (a=b, $\gamma = 120°$). This representation is more convenient for observing the disappearance of the trigonal distortion. As it can be observed in Fig. 8, the rhombohedral angle α decreases continuously with the temperature, and at ≈470K it becomes equal to 60 deg, the value at which the cubic symmetry is attained.

Thus, the structural analysis of Sr_2CoSbO_6 suggests that there is a high-temperature continuous phase transition $R\bar{3} \longrightarrow Fm\bar{3}m$ in this compound. Phase transitions of the same type have been observed also in some other double perovskite oxides [65]. The mechanism of these phase transition i related to the mismatch of the size of the A cation and the cuboctahedral space between the SbO_6 and CoO_6 octahedra. In the particular case of antimony double perovskites the temperature of the phase transition is most likely influenced also by the polarization properties of Sb^{5+}.

It was not possible to perform low-temperature Raman experiments of Sr_2CoSbO_6 due to the high absorption for the used laser wavelengths (514.5 and 488.0 nm). Further studies will be required to establish whether the trigonal structure observed at room temperature is preserved at lower temperatures.

9.5. Conclusions

The new double perovskite oxide Sr_2AlSbO_6 was prepared and its structure studied with X-ray powder diffraction method. At room temperature the crystal structure of this compound is cubic ($Fm\overline{3}m$) and the performed low-temperature Raman spectroscopic measurements demonstrated that this cubic phase is stable down to at least 79K. Depending on the preparation conditions, the Al^{3+} and Sb^{5+} cations can be either entirely or partially ordered. In the case of the partially ordered Sr_2AlSbO_6 sample, the extension of cation ordering was found to be much smaller than the crystallite size, which suggests the formation of anti-phase domains in the material. At room temperature, the structure of the second compound studied here Sr_2CoSbO_6 was found to be trigonal with space group $R\overline{3}$, which is different from the previously suggested $R\overline{3}m$. The material has partially ordered Co and Sb cations with degree of ordering of $\approx$80 % deduced from the structural refinement. In this case however no evidence of the formation of anti-phase boundaries was found. Sr_2CoSbO_6 undergoes a continuous phase transition at 470K above which the structure transforms to cubic ($Fm\overline{3}m$).

Capítulo 10

Crystal Structures and phase transitions of Sr_2CrSbO_6

10.1. Results and Discussion

In [93] we have studied the structures of Sr_2AlSbO_6 and Sr_2CoSbO_6 with the X-ray powder diffraction method. At room temperature the crystal structure of Sr2AlSbO6 is cubic ($Fm\bar{3}m$). It was found that depending on the preparation conditions, the Al^{3+} and Sb^{5+} cations can be either entirely or partially ordered. In the case of the partially ordered Sr_2AlSbO_6 sample, the extension of cation ordering was estimated from the hkl-dependent broadening of the diffraction peaks and the results were interpreted as evidence of the formation of anti-phase domains in the material. Low-temperature Raman spectroscopic measurements demonstrated that the cubic phase of Sr_2AlSbO_6 is stable down to 79K. The room-temperature crystal structure of Sr_2CoSbO_6 is trigonal (space group $R\bar{3}$, No. 148). At 470K, however, the material undergoes a continuous phase transition and its structure is converted to cubic (space group $Fm\bar{3}m$). The studied $Sr_2CoSbO6_6$ sample was partially ordered, but unlike Sr_2AlSbO_6, no indication of the formation of anti-phase domains was observed.

The aim of the present work is to analyze the structures and the possible structural phase transitions of Sr_2CrSbO_6, as there are no previous studies on the (high) temperature-dependent structural modifications of this material. This work is a part of a systematic study that we have undertaken on the AA'BSbO$_6$ (AA'=Ca$_2$,SrCa,Sr$_2$), and (B=Al,Sc,Cr,Fe,Co,La, Sm...) family of materials. Sr_2CrSbO_6 was first reported by Sleight and Ward (1964) [94], and subsequent X-ray diffraction studies by Blasse (1965) [87] lead to the conclusion that this compound was cubic with 1:1 M-cation ordering. Woodward (1997) [95] reported Sr_2CrSbO_6 to be a monoclinic ordered double perovskite (space group $P2_1/n$, No. 14) based on the presence of small extra reflections and peak splitting in the XRPD diffractograms. Similar reflection splitting was observed in the XRPD data reported in [89], and they did full pattern Rietveld refinements (with constraints) using the $P2_1/n$ space group.

Finally, in [96], the most recent study on Sr_2CrSbO_6, the crystal structures at room-temperature and the magnetic properties of the double perovskites Sr_2CrSbO_6 and Ca_2CrSbO_6 were studied by X-ray (XRD) and neutron powder diffraction (NPD) data. Rietveld refinements showed that the room-temperature crystal structure was monoclinic (space group $P2_1/n$), and that contained an almost completely ordered array of alternating CrO_6 and SbO_6 octahedra sharing corners, tilted along the three pseudocubic axes according to the Glazer notation $a^-a^-b^+$. The monoclinic distortion was larger in Ca_2CrSbO_6 than in Sr_2CrSbO_6, which was associated with the tilting of the CrO_6 and SbO_6 octahedra, displaying tilting angles $\phi = 13.5°$ and $\phi = 5.5°$, respectively. Magnetization measurements and low-temperature NPD data showed that Sr_2CrSbO_6 is an antiferromagnet with a Néel temperature of 12K, with an ordered magnetic moment of 1.64(4) μ_B per Cr^{3+}, being the propagation vector $k = 0$. This work is very important in relation to the magnetic properties of Ca_2CrSbO_6 as they report the first example of a ferromagnetic double perovskite containing a non-magnetic element in the B positions of the perovskite structure.

10.1.1. Room-temperature structure

We have calculated the tolerance factor for Sr_2CrSbO_6, using ionic radii from [3]: t=1.000. This value is between the values calculated for Sr_2CoSbO_6 [93], t=1.002, and for Sr_2GaSbO_6 [82], t=0.999. Being the three values so close, and knowing that the symmetries of Sr_2CoSbO_6 and Sr_2GaSbO_6 are $R\bar{3}$ and $I4/m$, respectively, we have tried both space groups as the starting models for the room-temperature refinements of the structure of Sr_2CrSbO_6.

In table 1 we show four 2θ ranges and the corresponding (hkl) indices for the $I2/m$ (monoclinic, No. 12, non-standard setting of $C2/m$), $I4/m$, $R\bar{3}$ and $Fm\bar{3}m$ (the aristotype cubic symmetry) space groups. In figure 1 we show sections, at two of those intervals, of the experimental (symbols), calculated (line) powder diffraction profiles for the Rietveld refinements of Sr_2CrSbO_6, at room temperature, using a structural model with the three different space groups: $I2/m$, $I4/m$ and $R\bar{3}$. In figure 1a and 1b we compare the monoclinic and the tetragonal space groups, and in figure 1c and 1d, the monoclinic and the trigonal. The important point in those comparisons is the splitting, which are evident, and from which neither the tetragonal nor the trigonal symmetries should be assigned, despite the high tolerance factor found for the title compound.

It is known [38] that the diffraction pattern for a compound that has $P2_1/n$ symmetry must have reflections indicative of A-cation displacements (eeo), in-phase tilting distortions (ooe), out-of-phase tilting distortions and cation ordering (ooo). As revealed by the above careful examination of the peak splitting patterns from our XRPD diffractograms the unit cell is monoclinic, but the absence of reflections with (ooe) cubic indices indicates that there is no in-phase tilting. Besides, the usually small reflections corresponding to atomic displacements (eeo) are not observed; only (eee) and (ooo) reflections can be observed when the NPD pattern (figure 2b) is indexed with a doubled cubic lattice parameter. Thus, the peak splitting pattern and cubic Miller indices indicate that the true symmetry of the compound is $I2/m$, and not $P2_1/n$ as has been assigned very recently [96], or as it was pointed out in [95].

TABLA 10.1: 2θ ranges and the (hkl) indices of the reflections for the $I2/m$, $I4/m$, $R\bar{3}$ and $Fm\bar{3}m$ (the ideal cubic symmetry) space groups.

Peak (2θ, deg)	$I2/m$	$I4/m$	$R\bar{3}$	$Fm\bar{3}m$
39.2-40.2	022 -202 202	022		222
45.6-46.6	220 004		024	400
84.2-86.2	044 -404 404	044		444
101-105	440 008		048	800

Another fact that corroborates the $I2/m$ space group assignment can be inferred by comparing the reflection conditions for the two monoclinic space groups. A compound with $I2/m$ symmetry must show (*hkl*) reflections with $h+k+l$=2n. Table 2 lists the first four reflections corresponding to in-phase tilting and cation displacements in the cubic unit cell and their corresponding monoclinic indices. Those peaks are not observed in the diffraction data (shown on XRPD and NPD data in Figures 2a and 2b, respectively), indicating that correct space group symmetry for Sr_2CrSbO_6 is $I2/m$.

Refinement results for the XRPD data with the $I2/m$ space group are given in Table 3. The mean interatomic distances and some selected bond angles are listed in Table 4. The $I2/m$ space group allows for 1:1 positional ordering of the B and B′ cations to form a rock-salt sub-lattice of corner-shared CrO_6 and SbO_6 octahedra. The Sr^{2+} cations are located in the cavities formed by the corner-sharing octahedra, and the average Sr−O distance 2.783Å is typical for Sr^{2+} cations in a twelve-coordinate environment. For the Sb−O bonds, the average value of the bond distances within the octahedra 1.991Å are in good agreement with the value predicted by bond valence calculations 2.0095Å; and for the Cr−O bonds, the average value 1.952Å is somewhat shorter than the expected one 1.9805Å. The small discrepancies (bigger in the case of the Cr octahedra) can be associated to the grade of disorder in the B-site present in the material.

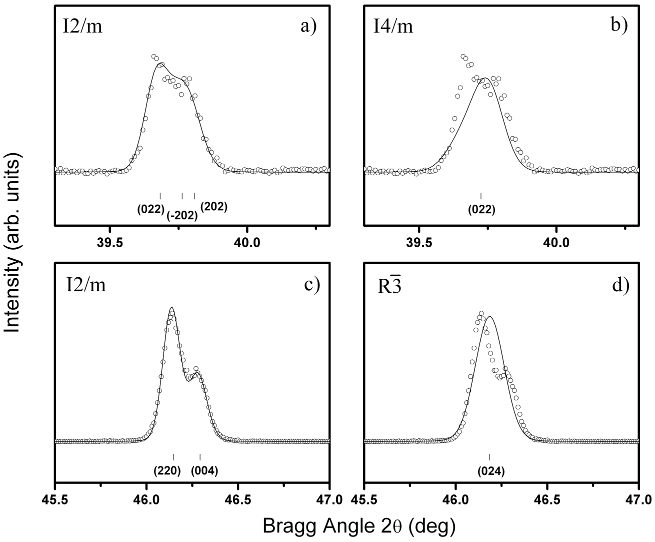

FIGURA 10.1: (a) and (b) Section of the diffractogram of the XRPD measurements refined in the $I2/m$ and $I4/m$ space groups, respectively, to show that the tetragonal symmetry does not take into account the observed splitting. (c) and (d) Another section of the diffractogram comparing the results of the refinements using the $I2/m$ and the $R\bar{3}$ space groups. The trigonal space group does not take into account the observed splitting.

TABLA 10.2: List of the first four reflections corresponding to A-cation displacements (eeo) and to in-phase tilting distortions (ooe) in the cubic unit cell and their corresponding monoclinic indices. XRPD and NPD wavelengths are 1.5406Å and 1.3Å, respectively.

Peak	$\approx 2\theta$		Monoclinic	Cubic *hkl*	
	XRPD	NPD	indices	(eeo) A-cation	(ooe) in-phase
			($P2_1/n$)	displacement	tilting
1	25	21.4	-111 111	-210	
2	27	23.6	012		-211
3	34	29	021	300 221	
4	36	30.5	120 210	-310	

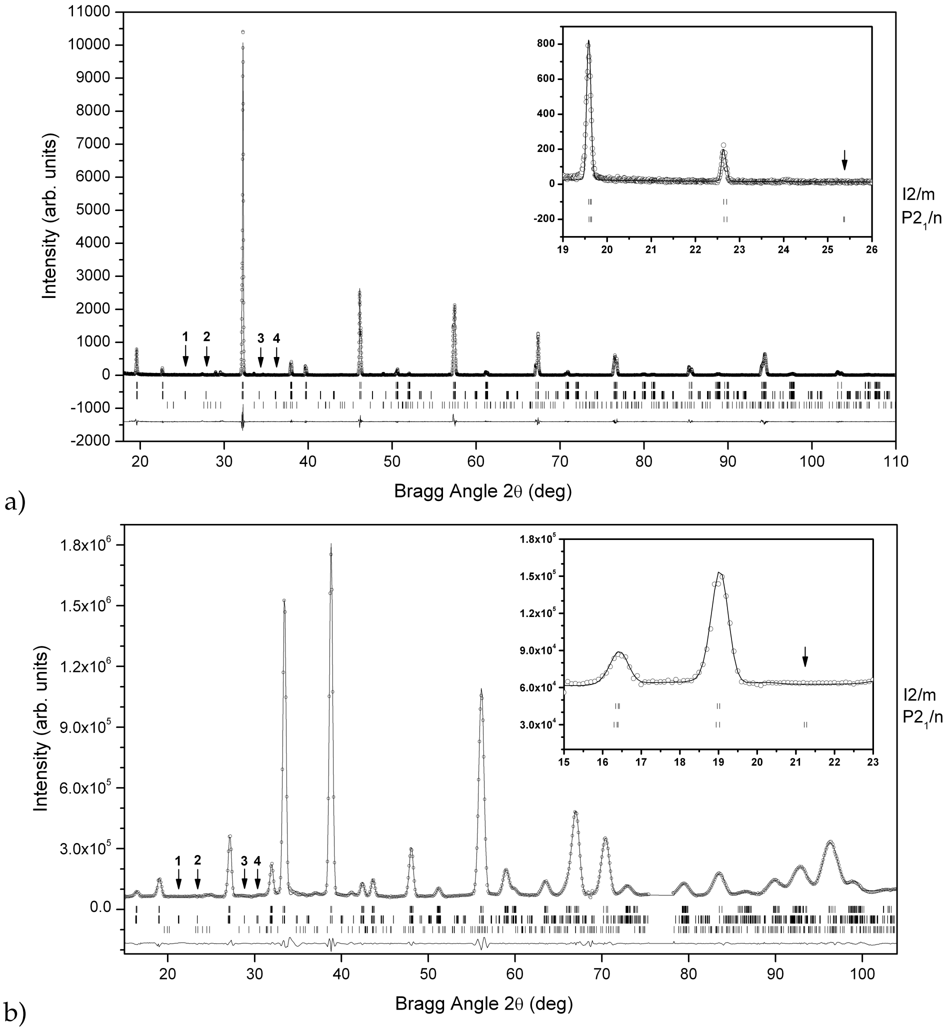

FIGURA 10.2: (a) Experimental (symbols) (XRPD), calculated (line) and difference powder diffraction profiles for the Rietveld refinement of Sr_2CrSbO_6 at room temperature using a structural model with $I2/m$ space group. The impurity $Sr_2Sb_2O_7$ (1.18 %) is included as a known additional phase. The vertical bars indicate the Bragg reflections: those in the top row correspond to the $I2/m$ space group; those in the middle row, to $P2_1/n$, and the ones in the bottom row, correspond to the impurity. Arrows indicate the positions of the reflections summarized in table 2. Inset shows in detail the absence of the (double) peak of the form $h+k+l$=2n+1, corresponding to the $P2_1/n$ symmetry. (b) Experimental (symbols), calculated (line) and difference neutron powder diffraction (NPD) profiles for the Rietveld refinement of Sr_2CrSbO_6 at room temperature using a structural model with $I2/m$ space group. The same comments apply.

TABLA 10.3: Crystal structure at room temperature (XRPD). The atomic positions were refined in the $I2/m$ space group. The cell parameters are: a=5.5574(1)Å; b=5.5782(1)Å; c=7.8506(2)Å; $\beta = 90.06(2)°$; V=243.37(1)Å^3 for the XRPD.

Atom	x	y	z	B(Å^2)	Occupancy
Sr	0.4999(1)	0	0.2504(3)	0.71(3)	1.000
Sb1/Cr2	0	0	1/2	0.24(3)	0.994(1)/0.006(1)
Cr1/Sb2	0	0	0	0.53(6)	0.994(1)/0.006(1)
O1	-0.039(4)	0	0.249(5)	1.10(3)	1.000
O2	0.246(2)	0.249(4)	0.015(5)	1.10(3)	1.000

Reliability factors (XRPD): $R_{\mathrm{p}} = 10.0\,\%$, $R_{\mathrm{wp}} = 17.5\,\%$, $R_{\mathrm{exp}} = 14.1\,\%$, $\chi^2 = 1.54$, $R_{\mathrm{Bragg}} = 2.63$

TABLA 10.4: Main bond distances (Å) and selected angles (°) for Sr$_2$CrSbO$_6$ from XRPD at room temperature. rCr^{3+}(VI)= 0.615Å rSb^{5+}(VI)= 0.6Å.

	Sr$_2$CrSbO$_6$
SrO$_{12}$ polyhedra	
Sr-O1 (×1)	2.955(1)
Sr-O1 (×1)	2.602(5)
Sr-O1 (×1)	2.795(6)
Sr-O2 (×2)	2.702(9)
Sr-O2 (×2)	2.886(5)
Sr-O2 (×2)	2.857(7)
Sr-O2 (×2)	2.877(9)
Average distance	2.783(2)
Predicted distance	2.781
CrO$_6$ polyhedra	
Cr-O1 (×2)	1.959(8)
Cr-O2 (×4)	1.948(7)
Average distance	1.952(4)
Predicted distance	1.9805
SbO$_6$ polyhedra	
Sb-O1 (×2)	1.982(5)
Sb-O2 (×4)	1.996(4)
Average distance	1.991(8)
Predicted distance	2.0095
Sb-O1-Cr (×2)	169(1)
Sb-O2-Cr (×4)	173(1)
<Sb-O-B>	172

In previous works published on double perovskite oxides, it has been shown that the $I4/m$ space group is not the "standardroom-temperature structure space group [97, 98, 99]. The mono-clinic splitting is to be taken into account, but the space groups $P2_1/n$ and $I2/m$ (another possible mono-clinic space group, $a^0a^-a^-$ tilt system) give rise to the same splitting, although the former gives also rise to primitive-cell reflections: (hkl) with $h+k+l$=2n+1. These kind of primitive reflections usually are very weak, and from their presence undoubtedly a primitive lattice has to be assigned. Nonetheless, if they can't be seen in the diffractogram, as it is our case, a non-primitive cell can be assumed. In that assumption, if the R-factors do not increase in a nonphysical way, the higher symmetry is usually assigned.

We have checked the possible symmetry miss-assignment of the structure reported in [96], analyzing the possible presence of pseudosymmetry, making use of PSEUDO [100]. The results show that displacing the Sr cation by 0.003Å and O1 by 0.111Å (absolute units), the $I2/m$ space group can be achieved ($I2/m$ is a super group of index 2 of $P2_1/n$). As it has been shown [101, 102] an overall displacement of 0.75Å is taken as a good value to assure a mis-assignment of symmetry. Hence, changing slightly the location of the oxygens [96] and assigning the antimony cation a more realistic (lower) B_{iso} value, gives rise to the $I2/m$ space group. Thus, our data show that the space group $I2/m$ gives a better description of the room-temperature structure of Sr_2CrSbO_6 (at least for the sample we have worked with) than that reported with the $P2_1/n$ space group structure in [96]; moreover, with the former description no physical or chemical inconsistencies are remaining.

In figure 3 we show the projections along the cubic (simple) perovskite axes, ($[100]_p$, $[010]_p$ and $[001]_p$), corresponding to a section of the unit cell of the double perovskite with $A_2MM'O_6$ general formula in the $I2/m$ and $P2_1/n$ space groups. The difference between both structural models consists in the losing of the tilt angle around the $[001]_p$ axis, which coincides with the c axis of the double perovskite.

10.1.2. Temperature-induced phase transitions: low- and high-temperatures

Although Sr_2CrSbO_6 has been studied at low temperature [96], no structural phase transition has been reported and, as far as we know, this is the first time that the temperature-induced structural phase-transitions at high temperature are reported in this compound. We have explored the low-temperature interval, 110-300K, and from our XRPD results we have to conclude that the room-temperature $I2/m$ monoclinic symmetry seems to be stable down to at least 100K.

In figure 4 we show the evolution of the scattering intensity with temperature for three 2θ intervals corresponding to (a) (444), (b) (800) and (c) (660) cubic ($Fm\bar{3}m$, space group) reflections. As it can be concluded from the figure, Sr_2CrSbO_6 undergoes two successive temperature-induced phase transitions taking place at 500 and 660K, respectively. The first one, discontinuous, changes the symmetry from monoclinic $I2/m$ to tetragonal $I4/m$. The discontinuous character of the phase

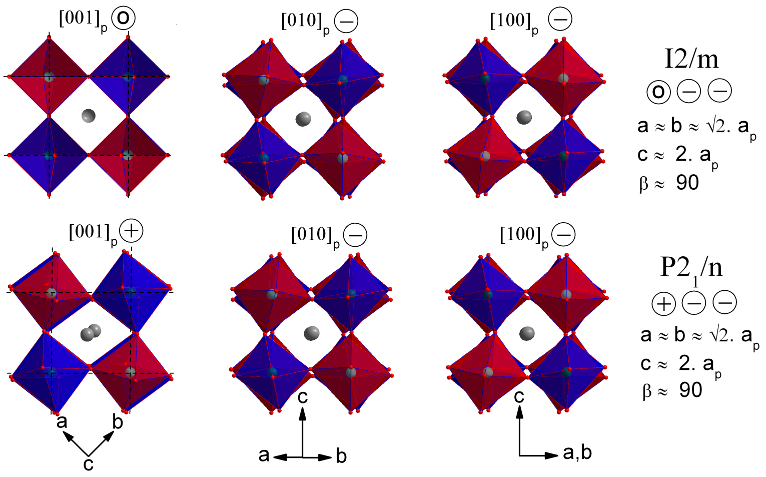

FIGURA 10.3: Projections along the cubic (simple) perovskite axes, ($[100]_p$, $[010]_p$ and $[001]_p$), of a section of the unit cell of the double perovskite with $A_2MM'O_6$ general formula in the $I2/m$ and $P2_1/n$ space groups.

transition can be readily appreciated in figure 4(b); nevertheless, in figure 4(a) we have represented the reflection that gives the difference between both space groups: (044), (-404), (404) in the $I2/m$ space group go to a single reflection in $I4/m$, (044). The reflections shown in figure 4(b) are (440) and (008) in both space groups, $I2/m$ and $I4/m$, but as they are interchanged in position, the transition is obvious. In figure 4(c) the continuous (see below) character of the $I4/m$ to $Fm\bar{3}m$ phase transition is .^{ea}sily.^{a}ppreciated: at that symmetry change, nearly all reflections increase intensity as all the splitting disappears.

In figure 5 we show the same 2 intervals as in figure 4, but this time only the profile at a single temperature is plotted: (a) 110K, (b) 310K (both in the $I2/m$ monoclinic phase), (c) 510K ($I4/m$ tetragonal phase) and (d) 670K ($Fm\bar{3}m$ cubic phase). The tetragonal splitting of the (800) cubic reflection (102-104.5° interval (c) panel) is very clear; the interchange in the positions of the (008) and (440) $I4/m$ tetragonal reflections going to (440) and (008) $I2/m$ monoclinic is also true (same interval and (b) panel). From the comparison of the (a) and (b) panels the decreasing of the monoclinic splitting as temperature increases can be observed.

Finally, in figure 6 we plot the evolution with temperature of the cell parameters of Sr_2CrSbO_6 in the whole temperature range, from 110K to 870K, as obtained from the refinements of the XRPD data of three different measurements: the first one, a low temperature measurement from 110 to 300K, represented in the figure by open squares; the second one, a high-temperature measurement from 300K to 870K, represented in the figure by open circles; and the third one, a measurement using the low-temperature camera from the lowest to the highest temperatures, 110K and 700K, at four temperatures as indicated, represented in the figure by stars. The evolution with temperature of the cell parameters is very similar to that observed for the members of the Sr_2MWO_6 family

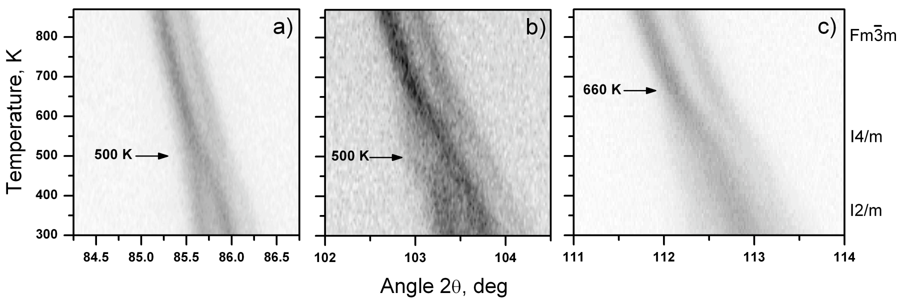

FIGURA 10.4: Thermal evolution of the (a) (444), (b) (800) and (c) (660) cubic reflections as obtained from XRPD experiments. The scattered intensity is represented with shades of gray–black corresponds to high intensity, and white, to low intensity. In (a), the $I2/m$ monoclinic triplet [(044),(-404),(404)] converts to a single $I4/m$ tetragonal reflection: (044). In (b), two monoclinic reflections maintain as two tetragonal but with the positions interchanged, and, eventually, the tetragonal splitting disappears and the double reflection evolves to a single cubic one. (c) Temperature evolution of the (660) cubic reflections: the tetragonal splitting existing in the temperature range from 500 to about 660K can be observed.

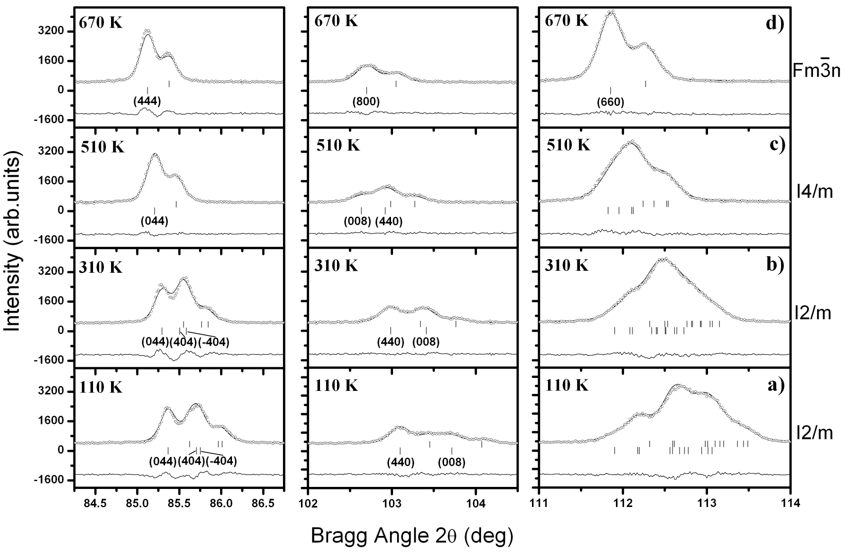

FIGURA 10.5: The thermal evolution of the (444), (800) and (600) cubic reflections as determined from XRPD measurements are shown in left, middle and right column panels, respectively. Each panel represents a single profile section at a fixed temperature: (a) 110K, (b) 310K, (c) 510K and (d) 670K.

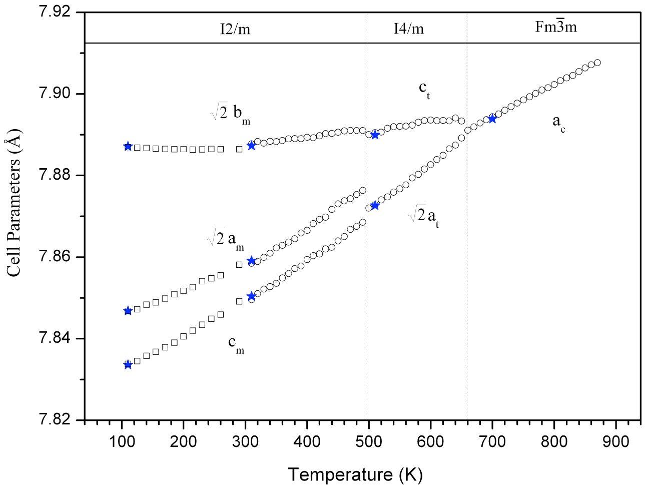

FIGURA 10.6: The temperature evolution of the cell parameters of Sr_2CrSbO_6 as obtained from the three different XRPD measurement series: open circles up to 300K, were obtained in the first low-temperature measurement; open circles from 300 to 900K were obtained with the high-temperature camera, in both cases in the same conditions; finally, stars were obtained using the low-temperature camera and with a counting time in each step (long enough) so that we had the required statistics to determine the structure. The high-temperature structure of the compound is cubic ($Fm\bar{3}m$); below 660K it transforms to tetragonal ($I4/m$); and at 500K the compound transforms to monoclinic ($I2/m$).

which show a two successive phase-transitions. Although in the tungsten containing family the low temperature monoclinic phase has the $P2_1/n$ space group and not $I2/m$, both space groups give rise to the nearly the same structural model (see figure 3): the extra $P2_1/n$ distortion is not appreciated in the cell parameters. The same is true for the cell parameters' evolution in the tetragonal phase: the characteristic feature of the tungsten family members is the negative thermal expansion of the c parameter, as is the case in the title compound.

Despite the fact that the XRPD and NPD measurements have been carried out obviously in different equipments, under different measuring conditions and using distinct ancillary equipment, they are in complete agreement. Although there is an obvious splitting in the monoclinic phase, the overlapping of the reflections in the NPD data makes impossible the structural determination: there is no enough resolution. The third set of XRPD measurements have been carried out to be able to extract structural data: shown in table 5.

We have analyzed the temperature evolution of the tetragonal structure, as deduced from the NPD data, until it undergoes the phase transition to the cubic phase, using the AMPLIMODES program [103]. AMPLIMODES carries out a symmetry-mode analysis of a displacive phase transition. Starting from the experimental structures of the high- and low-symmetry phases, the program determines the global structural distortion that relates the two phases. The symmetry modes compat-

TABLA 10.5: Crystal structure data and refinement results for Sr_2CrSbO_6 from XRPD at 110K, 310K, 510K and 700K.

Temperature (K)		110	310	510	700
Space group		$I2/m$	$I2/m$	$I4/m$	$Fm\bar{3}m$
Sb1/Cr2		0,0,1/2	0,0,1/2	0,0,1/2	0,0,0
Cr1/Sb2		0,0,0	0,0,0	0,0,0	0,0,1/2
Sr	x	0.5008(1)	0.4978(2)	0	1/4
	y	0	0	1/2	1/4
	z	0.2493(2)	0.2493(3)	1/4	1/4
O1	x	-0.0627(6)	-0.0638(8)	0	0.2584(3)
	y	0	0	0	0
	z	0.2473(8)	0.2468(2)	0.2431(3)	0
O2	x	0.2484(8)	0.2469(8)	0.2825(2)	
	y	0.2362(9)	0.2379(7)	0.2053(9)	
	z	0.0279(8)	0.0256(8)	0	
v B(Å^2)	Sb1,Cr2	0.28(2)	0.44(2)	0.68(2)	0.58(2)
	Cr1,Sb2	0.75(4)	0.92(4)	1.11(3)	1.22(4)
	Sr	0.52(2)	0.81(2)	1.16(2)	1.40(2)
	O1,O2	0.34(7)	0.73(8)	1.61(8)	2.15(1)
Cell parameters					
a(Å)		5.5485(1)	5.5572(1)	5.5668(1)	7.8939(1)
b(Å)		5.5770(1)	5.5772(1)	-	-
c(Å)		7.8336(1)	7.8503(1)	7.8899(1)	-
$\beta(^\circ)$		89.97(4)	90.04(3)	-	-
V(Å^3)		242.40(1)	243.31(1)	244.50(1)	491.89(1)
Reliability factors					
$R_p(\%)$		7.80	4.29	4.39	5.95
$R_{wp}(\%)$		8.87	6.08	6.08	8.26
$R_{Bragg}(\%)$		4.19	2.90	2.97	2.95
χ^2		4.48	4.40	4.18	7.83

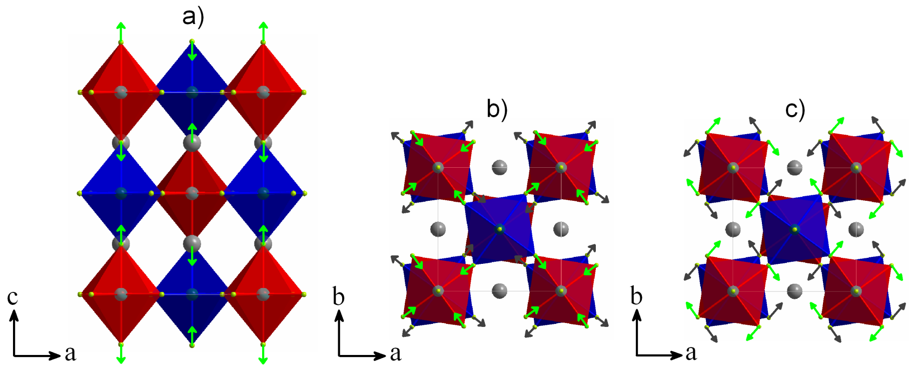

FIGURA 10.7: (a) and (b) The components of the GM^{3+} mode, responsible for the breaking of the symmetry to the $I4/mmm$ tetragonal space group from the $Fm\bar{3}m$, observed experimentally at high. This mode involves the movements of all the oxygen atoms in the octahedra: those located in the (00z) positions move to the center (or out of) of the octahedra, as shown in (a); and the oxygen atoms located in the xy plane move outwards (inwards) along the diagonals of the basal plane of the octahedra (b). As the octahedra are corner sharing if one octahedra stretches the other one expands. (c) On the other hand, the mode GM^{4+} is responsible for the breaking of the symmetry down to the $I4/m$ space group, and involves movements only of the oxygen atoms located in the xy plane (c): those displacements can be viewed as rotations (tilts) of the octahedra around the tetragonal axis.

ible with the symmetry break are then calculated. Their orthogonality allows the decomposition of the global distortion, obtaining the amplitude of each symmetry mode, as well as the corresponding eigenvectors. In the tetragonal ($I4/m$) to cubic ($Fm\bar{3}m$) phase transition there are three unidimensional modes: GM^{1+}, GM^{3+} and GM^{4+}. The GM^{3+} mode is responsible for the breaking of the symmetry to the $I4/mmm$ tetragonal space group (intermediate between the $Fm\bar{3}m$ and the $I4/m$, observed experimentally at high and low temperature, respectively). This mode involves the movements of all the oxygen atoms in the octahedra, in a way that those located in the (00z) positions move to the center of the octahedra; and the oxygen atoms located in the xy plane move outwards along the diagonals of the basal plane of the octahedra (see figure 7a and 7b). On the other hand, the mode GM^{4+} is responsible for the breaking of the symmetry down to the $I4/m$ space group, and involves movements only of the oxygen atoms located in the xy plane (figure 7c). We show the amplitude of each mode in figure 8(a). It can be readily appreciated that the amplitude of the first ones, the totally symmetric one (GM^{1+}) and GM^{3+} are negligible, of the order of magnitude of the error in the data, and that they maintain at a constant value. On the other hand, the GM^{4+} mode amplitude is considerable and shows a clear evolution with temperature: diminishes as temperature increases, and at the transition temperature (650K) it reaches its lowest (non null) value.

This is the typical behavior of the primary order parameter of a continuous phase transition

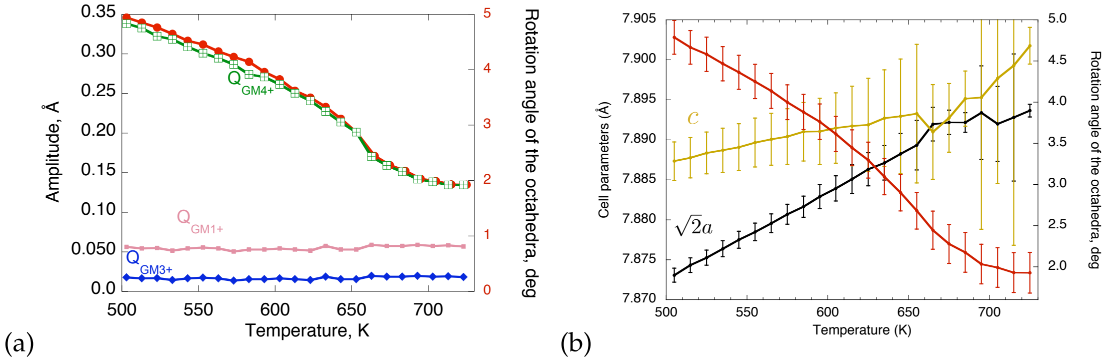

FIGURA 10.8: (a) The temperature evolution of the amplitudes of the GM^{1+}, GM^{3+} and GM^{4+} modes, in the left axis, as calculated by AMPLIMODES from the NPD data, and in the right axis, temperature evolution of the angle of rotation of the octahedra around the tetragonal axis. Both magnitudes are proportional, and show the typical behavior of a primary order parameter. The temperature at which the tetragonal structure disappears is 625K (there is a temperature-shift in comparison to the XRPD data). (b) The temperature evolution of the cell parameters a $\sqrt{2}$ and c, in the left axis; in the right one, the evolution with temperature of the rotation angle of the octahedra around the tetragonal axis, as in (a).

[42]: continuous decreasing and a smooth change to zero at the critical temperature. Indeed, in the same figure, in the right axis, we have plotted the evolution of the angle of rotation of the octahedra around the tetragonal axis (the only distortion allowed by symmetry in the $I4/m$ tetragonal phase, $a^0a^0c^-$ tilt system): the matching of both magnitudes is perfect, indicating that they are proportional and, thus, showing that the rotation of the octahedra around the tetragonal axis is the primary order parameter associated to the tetragonal-to-cubic phase transition.

All these facts allow us concluding that the symmetry changes taking place in Sr_2CrSbO_6, which belongs to the $Sr_2M^{3+}Sb^{5+}O_6$ system, have the same origins that those driving the structural change (tetragonal-to-cubic) in the $Sr_2M^2+W^6+O_6$ family [74]; that is, the tetragonal distortion of the unit cell is the result of an homogeneous strain coupled to the order parameter (the angle of rotation of the octahedra around the tetragonal axis). The transition takes place due to the mismatch of the Sr^{2+} cation and the cubo-octahedral interstitial space between the MO_6 and SbO_6 octahedra, and, also, due to the softening of the T^{4+} phonon [104].

10.2. Conclusions

Sr_2CrSbO_6 was synthesized by the conventional solid-state reaction process. X-ray powder diffraction (XRPD) and neutron Powder diffraction (NPD) has been used to reinvestigate the structure at room temperature and to study the phase transitions at high- and low-temperature. Rietveld analysis revealed that Sr_2CrSbO_6 crystallizes at room temperature in a monoclinic system having a space group $I2/m$, with a=5.5574(1)Å; b=5.5782(1)Å; c=7.8506 (2)Åand $\beta = 90.06(2)^{\circ}$, no $P2_1/n$ space group as was previously reported. The high-temperature study (300-870K) has shown that the compound presents the following temperature induced phase-transition sequence: $I2/m - I4/m - Fm\bar{3}m$. The low-temperature study (100-300K) demonstrated that the room-temperature $I2/m$ monoclinic symmetry seems to be stable down to 100K.

Capítulo 11

Crystal structures and high-temperature phase transitions of the new ordered double perovskites Sr_2SmSbO_6 and Sr_2LaSbO_6

11.1. Introduction

In two recent works, we analyzed the double perovskite oxides Sr_2AlSbO_6, Sr_2CoSbO_6 [93] by means of X-ray powder diffraction, and we have reinvestigated the structure at room temperature and the phase transitions at high- and low-temperature of Sr_2CrSbO_6 [105], by X-ray and neutron powder diffraction. At room temperature the crystal structure of Sr_2AlSbO_6 is cubic (space group $Fm\overline{3}m$), with $a = 5.6058(1)$Å. Low-temperature Raman spectroscopic measurements demonstrated that the cubic phase of Sr_2AlSbO_6 is stable down to 79K. The room-temperature crystal structure of Sr_2CoSbO_6 is trigonal (space group $R\overline{3}$) with $a = 5.6058(1)$Å and $c = 13.6758(3)$Å. At 470K, however, the material undergoes a continuous phase transition and its structure is converted to cubic (space group $Fm\overline{3}m$). The studied Sr_2CoSbO_6 sample was partially ordered, but unlike Sr_2AlSbO_6, no indication of the formation of anti-phase domains was observed. The Rietveld analysis revealed that Sr_2CrSbO_6 crystallizes at room temperature in a monoclinic system having a space group $I2/m$, with $a = 5.5574(1)$Å, $b = 5.5782(1)$Å, $c = 7.8506(2)$Å and

$\beta = 90.06(2)^\circ$, and no $P2_1/n$ space group, as was previously reported. The high-temperature study has shown that the compound presents the following temperature induced phase-transition sequence: $I2/m \rightarrow I4/m \rightarrow Fm\overline{3}m$. The low-temperature study demonstrated that the room-temperature $I2/m$ monoclinic symmetry seems to be stable down to 100K.

The aim of the present work is to analyze the room-temperature structures and the possible temperature-induced structural phase transitions of Sr_2SmSbO_6 and Sr_2LaSbO_6, as there are no previous studies neither on room-temperature nor on the temperature-dependent structural modifications of these materials. This work is a part of a systematic study that we have undertaken on the $AA'BSbO_6$ (AA'=Ca_2,SrCa,Sr_2), and (B=Al,Co,Cr,Fe,Sc. . .) family of materials.

11.2. Room-temperature Structures of Sr_2SmSbO_6 and Sr_2LaSbO_6

The diffraction patterns collected from Sr_2SmSbO_6 and Sr_2LaSbO_6 at room temperature are shown in Fig. 1(a) and (b), respectively. Many diffraction lines are clearly split, indicating that the unit cells of these materials are distorted, with respect to the aristotype cubic phase characteristic of the double perovskites. The profile matching results suggested the monoclinic symmetry. The usual monoclinic space groups encountered in the double perovskite oxides are $P2_1/n$ and $I2/m$, which give rise, apparently, to the same distortion (in Glazer's notation [24, 25], the tilt-systems are ($a^+a^-a^-$) and ($a^0a^-a^-$), respectively, thus in the former there is a tilt not present in the later), but $P2_1/n$ space group, as is associated to a primitive unit cell, gives rise to super-cell reflections, forbidden in the case of $I2/m$. This is a common place in distorted double perovskites. It is known in [38], that the diffraction pattern for a compound that has $P2_1/n$ symmetry must have reflections indicative of A-cation displacements (eeo), in-phase tilting distortions (ooe), out-of-phase tilting distortions and cation ordering (ooo). As revealed by the careful examination of the peak splitting patterns from our X-ray powder diffraction (XRPD) diffractograms in both compounds, the unit cells are monoclinic, and the presence of reflections with (ooe) cubic indices indicates that there is in-phase tilting. Besides, the usually small reflections corresponding to atomic displacements (eeo) are clearly observed in both compounds. Thus, the peak splitting pattern and cubic Miller indices indicate that the symmetry of these compounds is $P2_1/n$. As the starting model for the Rietveld refinements we used the structure reported for another member of the antimony family (Sr_2FeSbO_6), which has been reported to have a room-temperature monoclinic symmetry with the $P2_1/n$ space group [80].

In the insets graph of Fig. 1(a) and 1(b), we have plotted two 2θ intervals: the first one corresponds to the monoclinic primitive peaks $(\overline{1}11)$ and (111), observed about $2\theta \approx 24^\circ$; and the second one, at about $2\theta \approx 80^\circ$, corresponds to the monoclinic splitting of the (444) cubic reflection into the (044), $(\overline{4}04)$ and (404) reflections. The refinements show that the Sm^{3+} (La^{3+}) and Sb^{5+} ions are regularly ordered at the B and B' sites of the double perovskite. The ionic radii of Sm^{3+} and La^{3+} are 0.958Å and 1.032Å, respectively. The big difference between the ionic radii of Sm^{3+} (La^{3+}) and

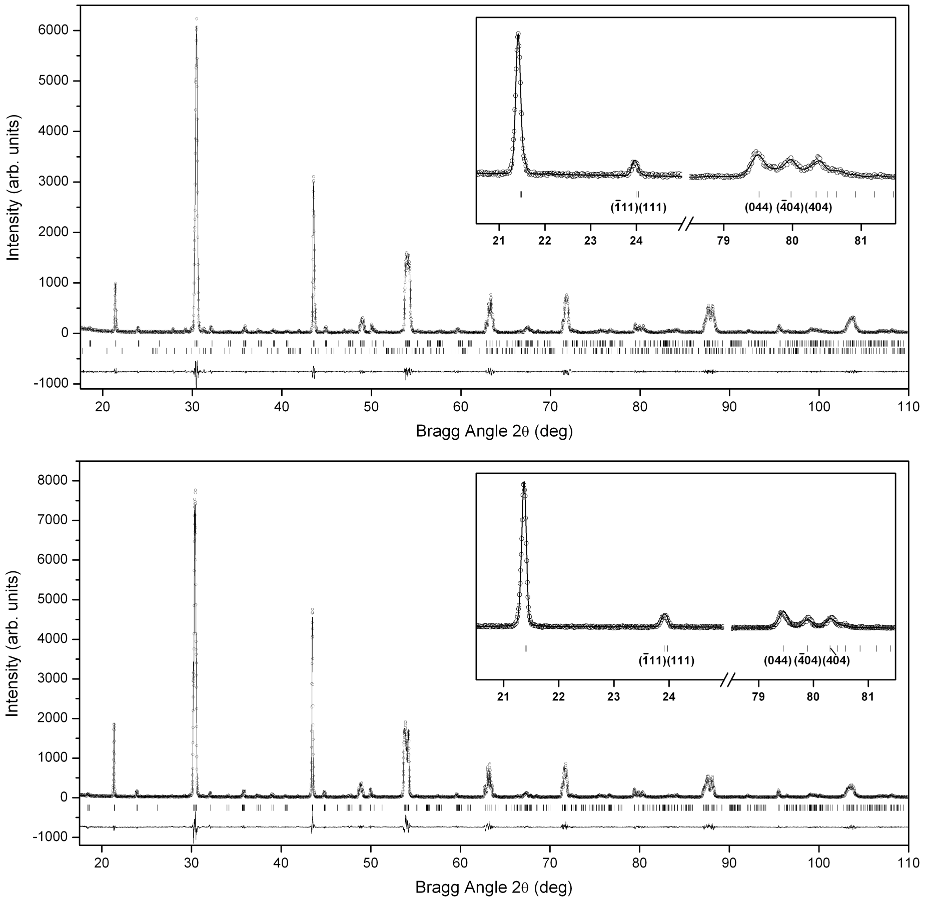

FIGURA 11.1: Experimental (symbols) and calculated (line) powder diffraction profiles for the Rietveld refinement of (a) Sr_2SmSbO_6 and (b) Sr_2LaSbO_6 at room temperature, using a structural model with $P2_1/n$ space group. The bars in the lower part of the graphics represent the Bragg peak positions. In (a), the upper set of bars correspond to the main phase Sr_2SmSbO_6, and the lower set of bars correspond to the impurity Sm_2O_3 (2.7 %).

TABLA 11.1: Crystal structure data and refinement results for Sr_2SmSbO_6 at room temperature. The atomic positions (in fractional coordinates) and isotropic atomic displacement parameters were refined in the space group $P2_1/n$. (Note: $a = 5.8580(1)$Å; $b = 5.9160(1)$Å; $c = 8.3136(1)$Å; $\beta = 90.23(1)°$; $R_p = 14.3\,\%$; $R_{wp} = 20.4\,\%$; $R_{exp} = 15.6\,\%$; $\chi^2 = 1.70$.)

Atom	Site	x	y	z	B(Å^2)
Sm	2d	1/2	0	0	0.27(3)
Sb	2c	0	1/2	0	0.19(3)
Sr	4e	0.0085(9)	0.0333(3)	0.2528(8)	0.61(5)
O1	4e	0.286(2)	0.325(2)	0.040(3)	0.88(1)
O2	4e	0.309(3)	0.266(3)	0.436(2)	0.88(1)
O3	4e	0.905(2)	0.460(3)	0.229(1)	0.88(1)

TABLA 11.2: Crystal structure data and refinement results for Sr_2LaSbO_6 at room temperature. The atomic positions (in fractional coordinates) and isotropic atomic displacement parameters were refined in the space group $P2_1/n$. (Note: $a = 5.8613(1)$Å; $b = 5.9220(1)$Å; $c = 8.3245(1)$Å; $\beta = 90.26(1)°$; $R_p = 11.8\,\%$; $R_{wp} = 16.9\,\%$; $R_{exp} = 10.85\,\%$; $\chi^2 = 2.41$.)

Atom	Site	x	y	z	B(Å^2)
La	2d	1/2	0	0	0.34(2)
Sb	2c	0	1/2	0	0.35(2)
Sr	4e	0.0094(4)	0.0344(2)	0.2509(3)	0.85(3)
O1	4e	0.269(7)	0.321(6)	0.075(5)	1.08(3)
O2	4e	0.312(4)	0.259(8)	0.417(5)	1.08(3)
O3	4e	0.879(1)	0.459(1)	0.223(9)	1.08(3)

Sb^{5+} (r=0.60Å), has a strong tendency to order B^{3+} and Sb^{5+} in B and $B^{'}$ sites, respectively.

The results of the refinements are also shown in Fig. 1 (a) and (b), and the structural details of Sr_2SmSbO_6 and Sr_2LaSbO_6 at room temperature are given in Table 1 and Table 2, respectively. It can be observed a large deviation of the monoclinic β angle from 90° for both structures. For the double perovskites with $P2_1/n$ symmetry, it has been reported that, in general, the deviations of the monoclinic angle from 90° are sometimes larger in compounds where one of the octahedral cations, such a rare earth cation, has a fairly large radius [85]. This large deviation can be attributed to the high distortions of the octahedra caused by the large cationic radius.

The tolerance factor values t, $t = \frac{(r_{Sr}+r_O)}{\sqrt{2}(\bar{r}_{B,Sb}+r_O)}$ where $\bar{r}_{B,Sb}$ is the averaged ionic radii of the B and Sb cations in the double perovskite, for Sr_2SmSbO_6 and Sr_2LaSbO_6 are 0.922 and 0.906, respectively (calculated using the ionic radii suggested in [3]). Increasing the cation size of the central cation in one of the octahedra, gives rise to a more distorted structure: this behaviour has also been observed in the tungsten family. In this case, the difference between the sizes of the cations, Sm^{3+} and La^{3+}, is not too big: $\Delta r_{\text{La-Sm}} = 0.074$Å; although it is bigger than the difference, for instance, between the Ca^{2+} and Cd^{2+} cations' radii: $\Delta r_{\text{Ca-Cd}} = 0.05$Å, in the tungsten family, in which different grade of distortions where also observed. On the other hand, if we take into account the t values of some other members of the antimony family (Table 1 in [93]), both compounds match perfectly in the table. Both values of t are lower than $t = 0.931$ calculated for Sr_2DySbO_6, which has the lowest t value in the table, with the lowest symmetry $P2_1/n$, which is the one we have obtained for the title compounds.

The mean interatomic distances and some selected bond angles for Sr_2SmSbO_6 and Sr_2LaSbO_6 are listed in Table 3. For the Sb-O bonds, the average values of the bond distances within the octahedra are 1.998Å and 2.007Å, for Sr_2SmSbO_6 and Sr_2LaSbO_6, respectively. For the B-O bonds, the average values are 2.332Å for the samarium compound and 2.417Å for the lanthanum compound. As mentioned, there is a large size difference between the two B-type cations, the Sb^{5+} cation is much smaller than the Sm and La cations. In both compounds, the Sm and La cations are overbonded, 3.09 for both cations Sm and La, with the Sm-O (La-O) bond lengths being (a little bit) shorter than the expected values obtained by calculating the distances in the bond-valence method [106]. On the other hand, the mean B-O bond lengths of Sb, Sm and La are the expected value from ionic radii giving bond-valence sums in agreement with the formal valence of Sb^{5+}, Sm^{3+} and La^{3+} cations.

The Sr^{2+} cations are located in the cavities formed by the corner-sharing octahedra. The analysis of Sr-O bond lengths shows that Sr atoms form a highly distorted SrO_8 polyhedron, with a Sr-O mean bond-length being 2.699Å and 2.676Å for Sr_2SmSbO_6 and Sr_2LaSbO_6, respectively; but, in both cases also the distribution of lengths is quite large, ranging from 2.429Å to 3.115Å in the samarium compound, for instance. The average values of Sr-O bond distances are larger, than the optimal value 2.631Å for Sr^{2+} cations in a eight-coordination environment, in both compounds. As mentioned, there is a large size difference between the two B-type cations; the Sb^{5+} cation is very much smaller than the Sm^{3+} and La^{3+} cations: consequently, the distortion is bigger, and, as a result, this gives rise to more enlarged Sr-O bonds. In Fig. 2 we show a clinographic projection of the room-temperature unit cells of Sr_2SmSbO_6, although the angle of rotation of the octahedra is bigger and can be appreciated clearly in the figure. Nevertheless, the distortion is bigger, which, as a result, gives rise to a more distorted coordination sphere assigned to Sr^{2+}.

The high distortion, with respect to the prototype structure, observed in both compounds is inferred from the large deviation of the Sb-O-B angle, in both compounds, from the ideal value (180°), as can bee seen in Table 3.

TABLA 11.3: Main bond distances (Å) and selected angles (°) for Sr_2SmSbO_6 and Sr_2LaSbO_6 from XRPD at room temperature.

	Sr_2SmSbO_6	Sr_2LaSbO_6
Sb-O1 (×2)	1.993(2)	2.000(7)
Sb-O2 (×2)	2.002(7)	2.010(8)
Sb-O3 (×2)	1.998(6)	2.011(2)
Average distance	1.998(5)	2.007(3)
Predicted distance	2.009	2.009
B-O1 (×2)	2.324(2)	2.418(7)
B-O2 (×2)	2.342(7)	2.420(8)
B-O3 (×2)	2.331(6)	2.414(2)
Average distance	2.332(5)	2.417(3)
Predicted distance	2.344	2.428
Sr-O1 (×1)	2.965(2)	2.715(7)
Sr-O1 (×1)	2.429(2)	2.309(7)
Sr-O1 (×1)	2.849(2)	3.167(7)
Sr-O2 (×1)	2.698(7)	2.614(8)
Sr-O2 (×1)	2.471(7)	2.391(8)
Sr-O2 (×1)	3.115(7)	3.239(7)
Sr-O3 (×1)	2.603(7)	2.637(8)
Sr-O3 (×1)	2.466(3)	2.330(5)
Average distance	2.699(6)	2.676(3)
Predicted distance	2.631	2.631
Sb-O1-B (×2)	149.1(5)	140.8(3)
Sb-O2-B (×2)	146.6(7)	140.0(3)
Sb-O3-B (×2)	147.4(2)	140.1(7)
<Sb-O-B>	147.7	140.3

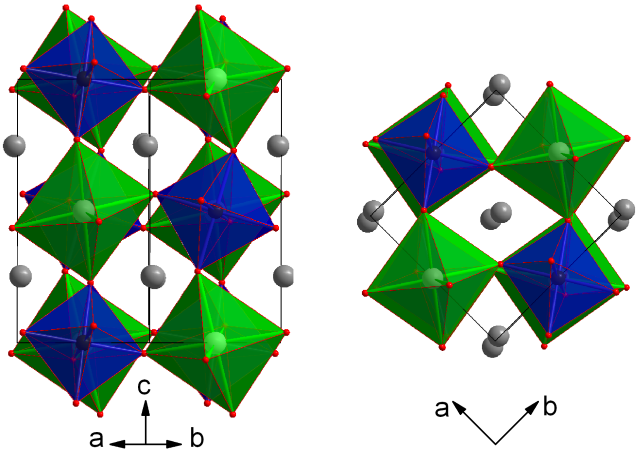

FIGURA 11.2: Clinographic projections of the structures of Sr_2SmSbO_6, along the $[010]_p$ and $[001]_p$ directions, as indicated, in the right and in the left panels, respectively. SmO_6 octahedra are shown green, SbO_6 in blue and Sr cations in gray.

11.3. High-temperature phase-transitions in Sr_2SmSbO_6 and Sr_2LaSbO_6

The thermal evolution of the structures of Sr_2SmSbO_6 and Sr_2LaSbO_6 was studied by means of laboratory X-ray diffraction measurements at different temperatures. In Fig. 3 we show the scattered intensity in the 86-88.5° 2θ interval, projected and represented with shades of gray. Black corresponds to high intensity, and white to low intensity: we have plotted the experimental results for Sr_2SmSbO_6 in panel (a) and for Sr_2LaSbO_6 in panel (b).

As seen in Fig. 3, the distortion of the unit cells gets smaller at higher temperatures: the diffraction lines get closer to each other. At about 885K and 945K in Sr_2SmSbO_6 and Sr_2LaSbO_6, respectively, as indicated in the figure, the splitting of the diffraction lines reduces appreciably. At those temperatures also, the reflections of the type hkl, with $h+k+l=2n+1$ also disappear in the patterns of both compounds (Fig. 5, panels (b) and (c)). As mentioned, these reflections are characteristic for a primitive unit cell. These observations indicate that, at the mentioned temperatures, the structures transform from the monoclinic symmetry (at low temperature) to another structure of higher symmetry (at high temperature), not with a primitive cell. At about 1170 and 1185K, in Sr_2SmSbO_6 and in Sr_2LaSbO_6, respectively, the splitting of the diffraction lines disappears, in a continuous way (Fig. 3). This indicates the presence of another phase transition, in each case, that changes the structures from the intermediate to a higher symmetry one, cubic ($Fm\bar{3}m$).

As mentioned in the Introduction, from the structural point of view, different symmetries have been reported for antimony double perovskite materials at room temperature: monoclinic, tetragonal, trigonal and cubic; although, very few temperature-dependent structural studies have

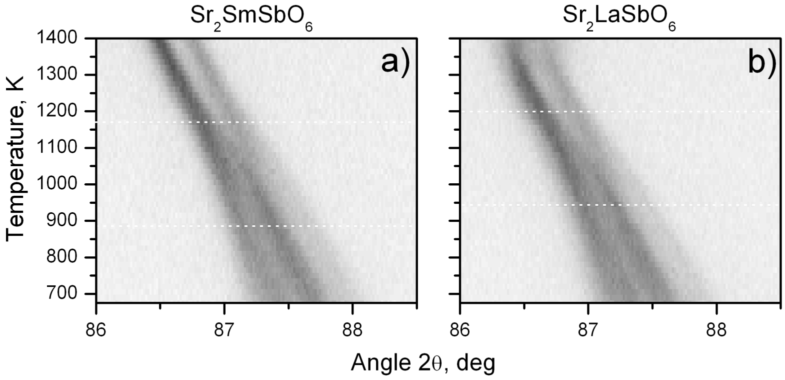

FIGURA 11.3: Thermal evolution of the the scattered intensity in the 86-88.5° 2θ interval, projected and represented with shades of gray. Black corresponds to high intensity, and white to low intensity. The horizontal lines are a guide to the eye, and mark the temperatures at which the distortions in both compounds get smaller, first, and, then, disappear; thus, indicating the presence of two successive phase transitions: at 885 and 1170K in Sr_2SmSbO_6; and at 945 and 1185K in Sr_2LaSbO_6.

been conducted [93, 105], so ïť is not easy to guess"*a priori*, which could be the expected phase-transition sequences. On the other hand, the usual intermediate symmetry between the high- (cubic, $Fm\overline{3}m$) and low-temperature phases (monoclinic, $P2_1/n$) in the tungstate double perovskites is tetragonal ($I4/m$) [41, 43, 74]. So, we attempted to refine the patterns at 970K, for Sr_2SmSbO_6 and Sr_2LaSbO_6, in the $I4/m$ space group, trying to reproduce the observed splittings, but the results were not satisfactory, as shown in Fig. 4 for Sr_2SmSbO_6 and Sr_2LaSbO_6, respectively. Nevertheless, the structural temperature evolution of the Sr_2CoSbO_6 has been studied and, as reported, shows a first order phase transition from the room-temperature trigonal phase ($R\overline{3}$ space group) to the cubic $Fm\overline{3}m$ space group. The calculated tolerance factors t for both compounds, matched perfectly in Table 1 of [93]. As it can be seen in that table, as the t value increases the stable symmetry at room-temperature changes following the next sequence: $P2_1/n \rightarrow I4/m \rightarrow R\overline{3} \rightarrow Fm\overline{3}m$. Increasing temperatures stabilizes more symmetric structures, and as the attempt to refine the structures after the first phase transition using the $I4/m$ space group failed, we tried to refine the patterns of Sr_2SmSbO_6 and Sr_2LaSbO_6 after the first transition in the $R\overline{3}$ space group; the results for the same splittings in Fig. 4. These good results confirm that the observed discontinuous phase transition for both compounds is $P2_1/n \rightarrow R\overline{3}$.

The refinement of the structures at 1220K has confirmed that, at those temperatures, the structures can be described with the $Fm\overline{3}m$ space group (panel (c) Fig. 5). And the patterns collected at temperatures higher than 1185 and 1200K were well fit by a structural model with the space group $Fm\overline{3}m$, corresponding to the undistorted aristotype double perovskite structure (tilt-system $a^0a^0a^0$). No further changes in the set of observed reflections were found above this temperature, suggesting that the type of unit cell does not change up to the highest temperature measured.

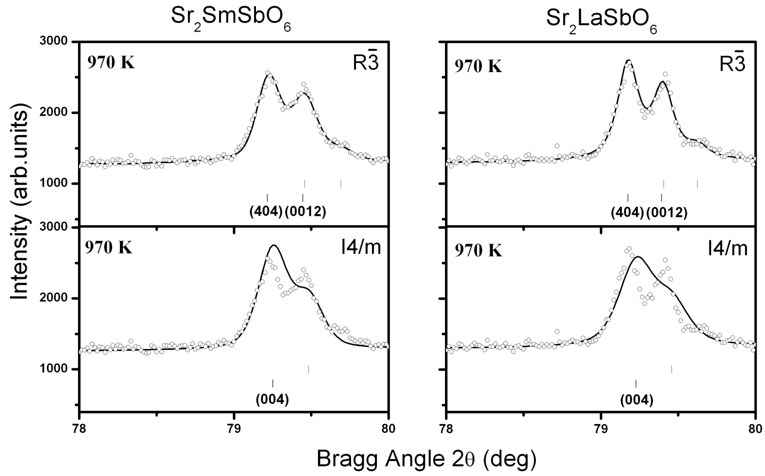

FIGURA 11.4: Results of the refinements, in the 78-80° 2θ interval, in Sr_2SmSbO_6 and Sr_2LaSbO_6, using two different models with the $I4/m$ and $R\bar{3}$ space groups. The bars indicate the Bragg reflections: the lower bars are associated to $k_{\alpha1}$, and the upper ones, to $k_{\alpha2}$. The tetragonal space group has only one reflection in this 2θ interval, and is unable to take into account of the observed splitting; on the contrary, the trigonal space group has two reflections and takes perfectly into account the splitting.

Finally, in Fig. 6 we show the variation with the temperature of the lattice constants of (a) Sr_2SmSbO_6 and (b) Sr_2LaSbO_6. The monoclinic and hexagonal parameters have been scaled to be comparable with the edge of the centered cubic as it appears in the final structure. In both compounds Sr_2SmSbO_6 and Sr_2LaSbO_6, the transitions are clearly seen. At about 885 and 945K in Sr_2SmSbO_6 and Sr_2LaSbO_6, respectively, we can see a discontinuous variation of parameters indicative of the first order nature of the corresponding transition from monoclinic symmetry $P2_1/n$ to trigonal symmetry $R\bar{3}$. And about 1170K for samarium compound and about 1185K for the lanthanum compound, a continuous variation of parameters is observed, indicative of the second order nature of the corresponding transition from $R\bar{3}$ to $Fm\bar{3}m$.

Thus, the structural analysis of Sr_2SmSbO_6 and Sr_2LaSbO_6 suggests that there is a two phase-transitions at high temperatures, the first one being discontinuous and the second one continuous as a following phase-transition sequence: $P2_1/n \rightarrow R\bar{3} \rightarrow Fm\bar{3}m$. As far as we know, this is the first time that a double phase-transition sequence, from primitive monoclinic $P2_1/n$ at room temperature to cubic symmetry $Fm\bar{3}m$ at high temperature with a trigonal intermediate phase, is observed in the antimony double perovskites. The $R\bar{3}$ space group as a high-temperature intermediate symmetry was previously reported for Ba_2PrNbO_6, but with a centred monoclinic symmetry ($I2/m$) at room temperature [65, 105]. Phase transitions sequences with two phase transitions have been observed also for Sr_2CrSbO_6 with a different phase-transition sequence: $I2/m \rightarrow I4/m \rightarrow Fm\bar{3}m$ [105], for instance, in which the intermediate phase is tetragonal. The mechanism of these discontin-

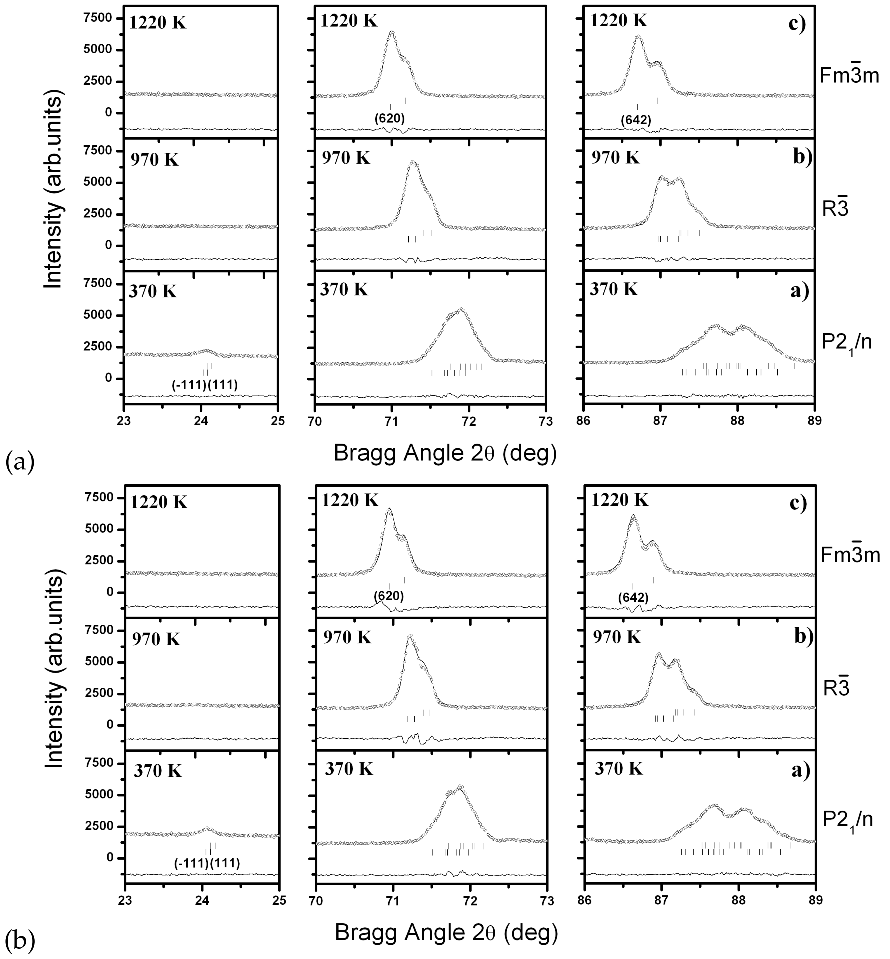

FIGURA 11.5: Temperature evolution of three groups of diffraction peaks located at different 2θ positions. The calculated and difference diffraction profiles (lines) are obtained after Rietveld refinement of the structure at each temperature. The structural models used in the refinement, for Sr_2SmSbO_6 (upper set) and Sr_2LaSbO_6 (lower set), have the following symmetries: (a) $P2_1/n$ for 370K, (b) $R\bar{3}$ for 970K and (c) $Fm\bar{3}m$ for 1120K. The bars indicate the Bragg reflections: the lower bars are associated to $k_{\alpha 1}$, and the upper ones, to $k_{\alpha 2}$. In the first interval (first column) the monoclinic (-111) and (111) reflections disappear as temperature increases. In the second columns it is shown the (620) cubic reflection, which does not split in the trigonal phase. Finally, in the third column, the (642) cubic reflection, clearly splits into two in the trigonal phase.

uous phase transitions is related to the mismatch of the size of the A cation and the cuboctahedral space between the BO_6 and SbO_6 octahedra. The big difference between the B cations' radii could be responsible for bringing the intermediate phase to a trigonal structure, more symmetric than the tetragonal structure.

11.4. Conclusions

The new double perovskites Sr_2SmSbO_6 and Sr_2LaSbO_6 have structures with $P2_1/n$ space group symmetry at room temperature, resulting from Sm(La)/Sb ordering and ($a^+b^-b^-$) tilt-system. The temperature evolution of the structures of Sr_2SmSbO_6 and Sr_2LaSbO_6 show the following sequence of two phase transitions: $P2_1/n \rightarrow R\overline{3} \rightarrow Fm\bar{3}m$, a discontinuous one, at 885 and 945K, for Sr_2SmSbO_6 and Sr_2LaSbO_6, respectively; and a continuous one, at 1170 and at 1185K, for Sr_2SmSbO_6 and Sr_2LaSbO_6, respectively. This sequence $P2_1/n \rightarrow R\overline{3} \rightarrow Fm\bar{3}m$ of structural transitions has been observed for the first time in the antimony double perovskite family.

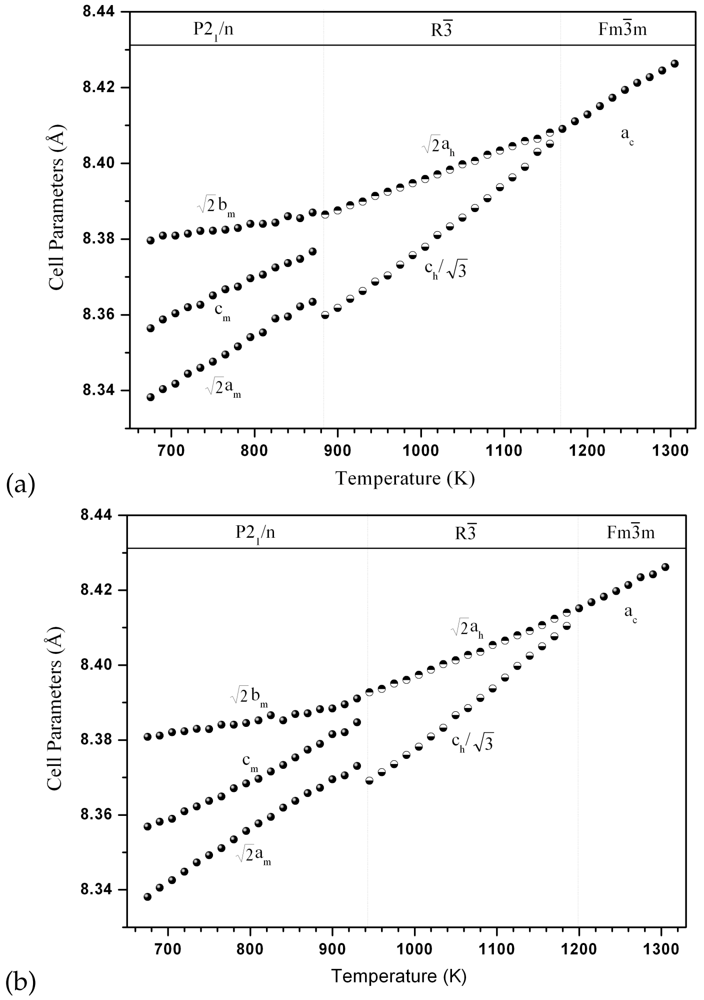

FIGURA 11.6: Temperature evolution of the lattice parameters of (a) Sr_2SmSbO_6 and (b) Sr_2LaSbO_6. We show the cell parameters of the trigonal phase in the hexagonal notation. The monoclinic and hexagonal parameters have been scaled to be comparable with the edge of the centered cubic.

Capítulo 12

Cationic ordering and role of the A-site cation on the structure of the new double perovskites $Ca_{2-x}Sr_xLaSbO_6$ and $Ca_{2-x}Sr_xSmSbO_6$ $(x = 0, 0.5, 1)$

12.1. Introduction

In previous articles [105, 108, 109, 110, 111], we have studied the structural phase transitions occurring in the materials with general formula A_2BSbO_6, A=Ca,Sr and B=Al,Co,Cr,Fe,Sc,Sm,La. These antimony oxide materials undergo a different temperature-induced phase transition sequences with rhombohedral or tetragonal tilt system as intermediate symmetry. the intermediate rhombohedral tilt system is favored by the presence of the big difference between the B cations' radii.

The aim of the present work is to analyze the room-temperature structures and the possible temperature-induced structural phase transitions of the double perovskite system by chemical substitution of the smaller Ca^{2+} ions by the bigger Sr^{2+} ions resulting in the system $Sr_{2-x}Ca_xLnSbO_6$ (Ln=Sm,La) and $(x = 0, 0.5, 1)$, as there are no previous studies neither on room-temperature nor on the temperature-dependent structural modifications of these materials.

12.2. Room-temperature Crystal Structures

12.2.1. Ca_2LaSbO_6 and Ca_2SmSbO_6

The diffraction patterns collected from Ca_2LaSbO_6 and Ca_2SmSbO_6 at room temperature are shown in Fig. 1(a) and (b), respectively. All diffraction lines, in both patterns, are clearly split, indicating that the unit cells of these materials are distorted, with respect to the aristotype cubic phase ($Fm\overline{3}m$) characteristic of the double perovskites. The profile matching results suggested the monoclinic symmetry. Following the discussion made in [109], and as revealed by the careful examination of the peak splitting patterns from our XRPD diffractograms in both compounds, the presence of reflections with (ooe) cubic indices indicates that there is in-phase tilting; and, besides, the usually small reflections corresponding to atomic displacements (eeo) are not small in these cases, and clearly observed in both compounds. Thus, the peak splitting pattern and cubic Miller indices indicate that the symmetry of these compounds is $P2_1/n$. As the starting model for the Rietveld refinements we used the structure reported for the strontium counterparts of the title compounds (Sr_2LnSbO_6, Ln=Sm,La), which we reported to have a room-temperature monoclinic symmetry with the $P2_1/n$ space group [109]. In this work, our aim was to substitute the Sr^{2+} cation by the Ca^{2+} in the A-site position of the double perovskite. Being the ionic radius of the later smaller than that of the former, $r_{Ca^{2+}_{XII}} = 1.34$Å and $r_{Sr^{2+}_{XII}} = 1.44$Å, we expected that the new double perovskite structures would be more distorted. This is a common place in double perovskite oxides: decreasing the ionic radius of the A-site cation, deforms, shrinking the cubooctahedral space among the oxygen corner sharing octahedra, because the octahedra have more room to rotate (tilt), thus, increasing the distortion of the structure.

In the insets of Fig. 1(a) and 1(b), we have plotted the 18-26°, 2θ interval. In this interval, we are showing the first three sets of Bragg monoclinic reflections. The first set corresponds to the cubic (111) reflection, split in both cases into the monoclinic $(011), (-101), (101)$ reflections, and when present, indicates that the cation distribution over the B-sites of the double perovskite is ordered. The second set, observed at about $2\theta \approx 22$, corresponds to the monoclinic splitting of the (200) cubic reflection into the (002) and (110) reflections. Finally, the third set corresponds, as indicated, to the monoclinic primitive peaks (-111) and (111), observed at about $2\theta \approx 24$. On the other hand, the first of the two insets in each (a) and (b) corresponds to Sr_2LnSbO_6, and the second one to Ca_2LnSbO_6, with Ln=La,Sm.

The important point is that the intensity distribution of the Bragg peaks in the Sr and Ca containing compounds is completely different. The total intensity for (002) and (110) is significantly small, compared with the compounds Sr_2LaSbO_6 and Sr_2SmSbO_6 in which the A site is occupied completely by Sr. This fact reflects that Ca^{2+} ions partially occupy the A site. which means that the cation distribution is different. We have tried all the possible cation distributions as models for the refinement of the patterns, and we have obtained that, in the Ln=La case, the distribution that

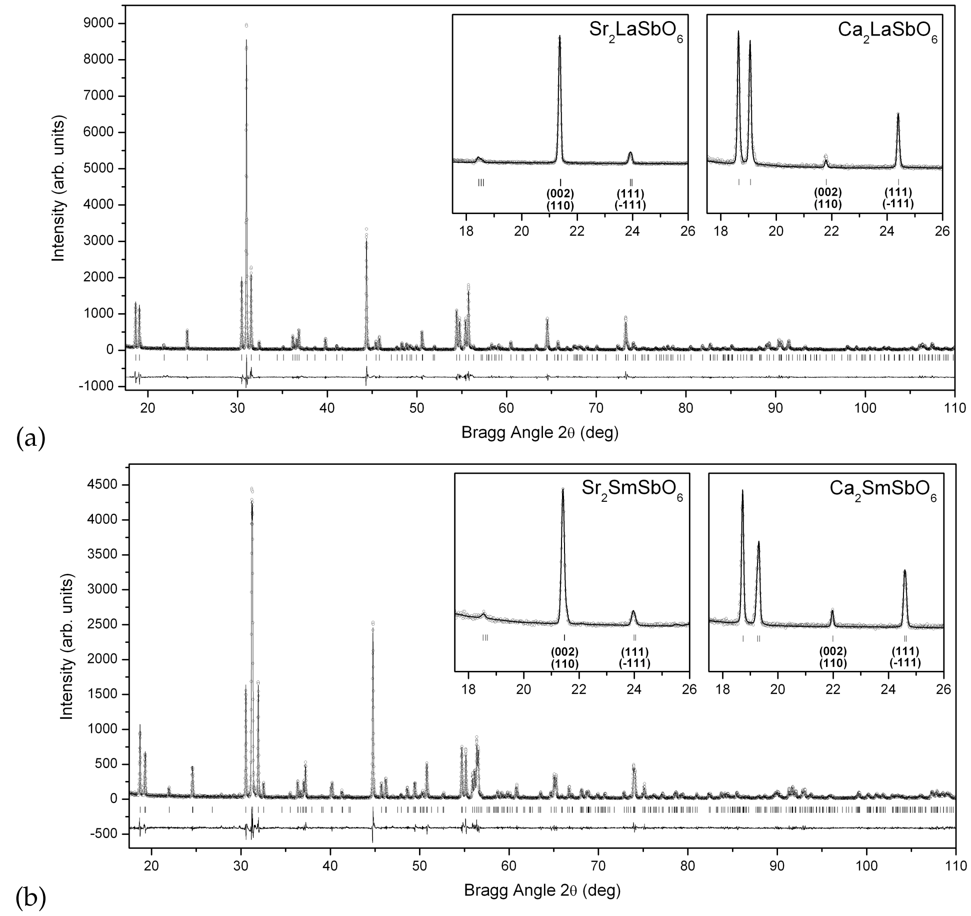

FIGURA 12.1: Experimental (symbols) and calculated (line) powder diffraction profiles for the Rietveld refinement of (a) $[CaLa]_A[Ca]_BSbO_6$ and (b) $[Ca_{1.08}Sm_{0.92}]_A[Sm_{0.08}Ca_{0.92}]_BSbO_6$ at room temperature, using a structural model with $P2_1/n$ space group, and the cation distribution as indicated by the general formula. The bars in the lower part of the graphics represent the Bragg peak positions. The insets show the first three sets of Bragg monoclinic reflections: $[(011),(-101),(101)]$, $[(002),(110)]$ and the monoclinic primitive peaks $[(-111),(111)]$ (see text). In both insets we compare the Sr_2LnSbO_6 from [109] with Ca_2LnSbO_6 (present work), to show that the intensity distributions are different.

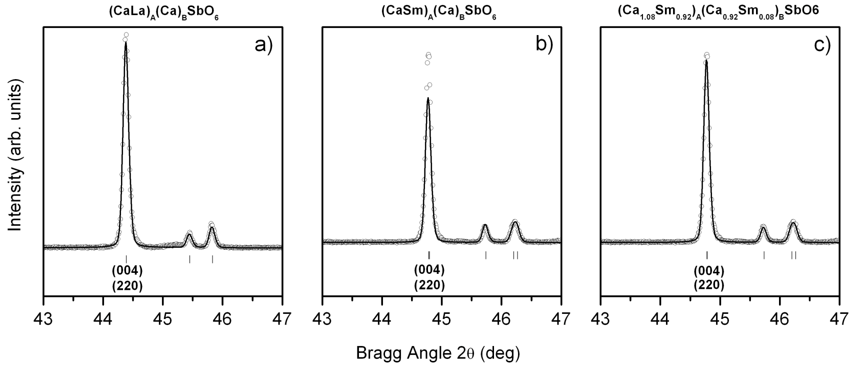

FIGURA 12.2: Experimental (symbols) and calculated (line) sections (around the (004) and (220) monoclinic reflections) of the powder diffraction profiles for the Rietveld refinement of (a) $[CaLa]_A[Ca]_BSbO_6$, (b) $[CaSm]_A[Ca]_BSbO_6$ and (c) $[Ca_{1.08}Sm_{0.92}]_A[Sm_{0.08}Ca_{0.92}]_BSbO_6$ at room temperature, using a structural model with $P2_1/n$ space group, and the cation distribution as indicated by the general formula. The bars in the lower part of the graphics represent the Bragg peak positions. The cation distribution of (a) can not be used to reproduce the patter in (b), and it has to be changed to the distribution indicated in (c).

reproduces satisfactorily all the features of the pattern is: Ca^{2+}/La^{3+} (4e), Ca^{2+} (2d) and Sb^{5+} (2c), which corresponds to the $[CaLa]_ACaSbO_6$ general formula. Hence, the La^{3+} cation *has displaced* the Ca^{2+} cation from the A-site position of the double perovskite. In the Ln=Sm case, though, the distribution that reproduces satisfactorily all the pattern features is different from the previous one: we need to distribute the Sm^{3+} cation between the A-site and B-site, because otherwise the model is not able to reproduce the correct intensity of many peaks in the pattern, as shown in Fig. 2. The final distribution found for Ln=Sm corresponds to the $[Ca_{1+x}Sm_{1-x}]_A[Sm_xCa_{1-x}]_BSbO_6$ general formula, with $x = 0.08$. The final results of the refinements are shown in Fig. 1 (a) and (b), and the structural details of Ca_2laSbO_6 and Ca_2SmSbO_6 at room temperature are given in Table 1 and Table 2, respectively.

In general, In the double perovskite with general formula $A_2BB'O_6$, the A-sites are occupied by ions of larger size and the B-sites by ions of relatively lower size. Alkaline earth metal ions like Ba or Sr have larger size in comparison of that of the rare earth and transition metal ions, and therefore occupy the A-site. As a result the B-site is occupied either by the transition metal ions or the rare earth metal. In the case of Ca alkaline earth metal ions, this cation is relatively smaller than Ba and Sr, as a consequence the distribution of this cation is depend of the size of the others cations. The Ca occupied totaly the A-sites in presence of smaller cations as be found in Ca_2MSbO_6 (M=Cr,Fe,Sc) [110, 111, 112]. In this case, the La ($r_{La^{3+}_{XII}} = 1.36$Å) and Sm ($r_{Sm^{3+}_{XII}} = 1.24$Å) have a larger cation size, as a result the La^{3+} and Sm^{3+} are replaced the Ca^{2+} in the A-site.

In the work by Sakai *et al.* [113], they analyzed the Ca_2LnRuO_6 (Ln=La-Lu) system, and they concluded that their diffraction measurements, which have the same intensity distribution as the

TABLA 12.1: Crystal structure data and refinement results for Ca_2LaSbO_6 at room temperature. The atomic positions (in fractional coordinates) and isotropic atomic displacement parameters were refined in the space group $P2_1/n$. (Note: $a = 5.6820(1)$Å; $b = 5.8729(1)$Å; $c = 8.1676(1)$Å; $\beta = 89.98(1)^\circ$; $R_{wp} = 12.2\,\%$; $R_B = 5.37\,\%$; $\chi^2 = 2.17$.)

Atom	Site	x	y	z	B(Å^2)	Occupancy
Sb	2c	0	1/2	0	0.70(3)	1.00
La	2d	1/2	0	0	0.70(3)	1.00
Ca/La	4e	0.0108(3)	0.0496(3)	0.2486(2)	1.01(4)	1.00
O1	4e	0.326(1)	0.295(1)	0.064(1)	1.07(1)	1.00
O2	4e	0.295(1)	0.311(1)	0.451(1)	1.07(1)	1.00
O3	4e	0.899(1)	0.457(1)	0.263(1)	1.07(1)	1.00

TABLA 12.2: Crystal structure data and refinement results for Ca_2SmSbO_6 at room temperature. The atomic positions (in fractional coordinates) and isotropic atomic displacement parameters were refined in the space group $P2_1/n$. (Note: $a = 5.6062(1)$Å; $b = 5.8553(1)$Å; $c = 8.0977(1)$Å; $\beta = 90.23(1)^\circ$; $R_{wp} = 11.6\,\%$; $R_B = 5.13\,\%$; $\chi^2 = 1.72$.)

Atom	Site	x	y	z	B(Å^2)	Occupancy
Sb	2c	0	1/2	0	0.40(3)	1.00
Ca1/Sm2	2d	1/2	0	0	0.99(3)	0.92(1)/0.08(1)
Sm1/Ca2	4e	0.0150(3)	0.0569(3)	0.2466(2)	0.59(4)	0.92(1)/0.08(1)
O1	4e	0.331(1)	0.293(1)	0.069(1)	0.60(1)	1.00
O2	4e	0.289(1)	0.318(1)	0.453(1)	0.60(1)	1.00
O3	4e	0.881(1)	0.443(1)	0.269(1)	0.60(1)	1.00

one we have obtained for Ca_2LnSbO_6 (Ln=La,Sm), show that the Ca^{2+} and Ln^{3+} cations are partially disordered in the A-site and at half of the B-site positions of the ABO_3 perovskite, and that the Ca^{2+}/Ln^{3+} and Ru^{5+} cations are located at the B-site regularly ordered; and, thus, those compounds should be represented by the general formula: $Ca_{2-x}Ln_x[Ln_{1-x}Ca_x]RuO_6$. The ratio of the Ln^{3+} located at the B-site varies with its cationic radius: according to their results, the larger Ln cations tend to occupy the A-site, whereas, the smaller Ln cations tend to go to the B-site.

Our laboratory X-ray powder diffraction measurements, thus, confirm their conclusions, but in two lanthanide members of the antimony family: that is, the lanthanide enters in the A-site position, displacing the Ca^{2+} cation to the B-site, but depending on the size of the lanthanide, the displacing effect is different: the bigger the size of the lanthanide the stronger the displacement. In particular, in our case, La^{3+} displaces all the Ca^{2+} it can, and the Sm^{3+}, being a little smaller than La^{3+}, is not able to displace all the Ca^{2+} to the B-site.

It is known that the bigger the radius of the cation in the B-site position the more distorted the structure is [74]; so, being La^{3+} bigger than Sm^{3+} we were expecting the La compound to be more distorted than the Sm compound. But we observed the opposite. This observation is also in accordance with the final distribution obtained in the case of Sm, in which in the A-site of the double perovskite we have $[Ca_{1+x}Sm_{1-x}]$ and in the La we have [CaLa]. This distribution makes effectively smaller the cubooctahedral space (A-site) in the former case; and, it is also known, that the smaller the size of the cation in the A-site, the more distorted the structure is.

We do not have a definitive explanation for this observation, but in our view, there are two competing factors giving rise to the observed new distribution: in the one hand, the size of the cations, as given by the ionic radius from Shannon [3], $r_{La^{3+}} > r_{Ca^{2+}} > r_{Sm^{3+}}$, in the two possible coordination schemes, XII (cubooctahedral) and VI (octahedral); and, in the other hand, the tendency of the cations to be surrounded by anions (electronegativity). To understand the origin of the distribution we have synthesized two points in the $Ca_{2-x}Sr_xLnSbO_6$ (Ln=La,Sm) and $(x = 0.5, 1.0)$.

12.2.2. $Ca_{2-x}Sr_x$LnSbO$_6$ (Ln=La,Sm) and $(x = 0.5, 1.0)$

The room temperature X-ray powder diffraction patterns of $Ca_{2-x}Sr_xLaSbO_6$ and $Ca_{2-x}Sr_xSmSbO_6$ are shown in Figure 3 (a) and (b), respectively. Based on a visual inspection of the room temperature X-ray powder diffractograms, as there is a continuous change in the position of the peaks and their form, which can see clearly in the insets of Figure 3 (a) and (b). It is clear that the substitution of Ca^{2+} cation by Sr^{2+} gives rise to continuous solid solutions. All diffractograms shown the monoclinic splitting and the primitive Bragg peaks correspond to the primitive monoclinic space group $P2_1/n$. in Table 3 summarizes the room temperature unit cell parameters, atomic positions, isotropic displacement parameters, factor of occupation and reliability factors of the Rietveld refinements for the studied compounds $Ca_{1.5}Sr_{0.5}LaSbO_6$, $CaSrLaSbO_6$, $Ca_{1.5}Sm_{0.5}SmSbO_6$ and $CaSrSmSbO_6$

TABLA 12.3: Crystal structure data and refinement results, at room temperature, for $Ca_{1.5}Sr_{0.5}LaSbO_6$, $Ca_{1.0}Sr_{1.0}LaSbO_6$, $Ca_{1.5}Sr_{0.5}SmSbO_6$ and $Ca_{1.0}Sr_{1.0}SmSbO_6$. The atomic positions (in fractional coordinates) and isotropic atomic displacement parameters were refined in the space group $P2_1/n$. The Wyckoff positions are the following: Sb (2c), Ca or Ca/Sm (2d), Sr/Ca/La, Sr/La or Sr/Sm/Ca (4e) and O1, O2 and O3 (4e).

Compound Agreement factors	Lattice Parameters a, b, c (Å)	Atom	x	y	z	B_{iso}(Å^2)	Occupancy
$Ca_{1.5}Sr_{0.5}LaSbO_6$	$a = 5.703(1)$	Sb	0	1/2	0	0.17(4)	1.00
	$b = 5.8864(1)$	Ca	1/2	0	0	0.17(4)	0.84(1)/0.16(1)
$R_{wp} = 15.4\,\%$	$c = 8.2065(1)$	Sr/Ca/La	0.0114(4)	0.0467(2)	0.2491(2)	0.44(4)	0.25/0.25/0.5
$R_B = 6.3\,\%$	$\beta = 89.93(1)^\circ$	O1	0.309(2)	0.299(2)	0.058(2)	1.05(5)	1.00
$\chi^2 = 2.35$		O2	0.306(2)	0.298(2)	0.451(2)	1.05(5)	1.00
		O3	0.903(2)	0.465(2)	0.249(2)	1.05(5)	1.00
$CaSrLaSbO_6$	$a = 5.7756(1)$	Sb	0	1/2	0	0.20(3)	1.00
	$b = 5.9020(1)$	Ca	1/2	0	0	0.20(3)	1.00
$R_{wp} = 13.0\,\%$	$c = 8.2448(1)$	Sr/La	0.0103(3)	0.0442(2)	0.2498(2)	0.79(3)	0.5/0.5
$R_B = 6.32\,\%$	$\beta = 89.86(1)^\circ$	O1	0.305(2)	0.276(2)	0.055(2)	1.04(4)	1.00
$\chi^2 = 2.63$		O2	0.278(2)	0.302(2)	0.452(2)	1.04(4)	1.00
		O3	0.900(2)	0.469(2)	0.262(2)	1.04(4)	1.00
$Ca_{1.5}Sr_{0.5}SmSbO_6$	$a = 5.6535(1)$	Sb	0	1/2	0	0.56(3)	1.00
	$b = 5.8692(1)$	Ca1/Sm2	1/2	0	0	0.74(3)	0.84(1)/0.16(1)
$R_{wp} = 15.4\,\%$	$c = 8.1375(1)$	Sr/Sm1/Ca2	0.0134(3)	0.0536(2)	0.2473(2)	0.88(3)	0.25/0.42(1)/0.33(1)
$R_B = 6.30\,\%$	$\beta = 90.07(1)^\circ$	O1	0.307(2)	0.296(2)	0.045(2)	1.01(8)	1.00
$\chi^2 = 2.35$		O2	0.305(2)	0.295(2)	0.436(2)	1.01(8)	1.00
		O3	0.891(2)	0.452(2)	0.242(2)	1.01(8)	1.00
$CaSrSmSbO_6$	$a = 5.7110(1)$	Sb	0	1/2	0	0.54(3)	1.000
	$b = 5.8856(1)$	Ca1/Sm2	1/2	0	0	0.94(3)	0.70(1)/0.30(1)
$R_{wp} = 13.3\,\%$	$c = 8.1932(1)$	Sr/Sm1/Ca2	0.0147(3)	0.0487(2)	0.2489(2)	0.98(3)	0.50/0.35(1)/0.15(1)
$R_B = 8.08\,\%$	$\beta = 89.93(1)^\circ$	O1	0.301(2)	0.259(2)	0.071(2)	0.81(8)	1.00
$\chi^2 = 2.46$		O2	0.275(2)	0.306(2)	0.445(2)	0.81(8)	1.00
		O3	0.893(2)	0.454(2)	0.265(2)	0.81(8)	1.00

in $P2_1/n$ space group.

Figure 4 gives the variation at room temperature of the (a) a, b and c lattice parameters, (b) monoclinic angle β, (c) the unit cell volume and (d) the ratio of the Ln at the B site as a function of the Sr content. From the figure, it is seen that the lattice parameters and the volume increase linearly with increasing of Sr concentration, on the other hand, the monoclinic angle β decreases. which is due to the chemical substitution of the bigger Sr^{2+} ions in the smaller Ca^{2+} sites. As a sequences the volume of the cubooctahedra space increase which reflects in the increasing of the lattice parameters. The increasing of the volume of the cubooctahedra A site leads to the decrease in the tilt systems and which is observed by decreasing of the monoclinic angle β. A clear evidence that the Vegard's law holds for these solid solutions.

Figure 4 (c) shows the ratio of the Ln cations at the B site of $Ca_{2-x}Sr_xLnSbO_6$ (Ln=La,Sm) as a function of Sr content. In the lanthanum compounds, the B site of are totaly occupied by the Ca cations which corresponds to the $[Ca_{1-x}Sr_xLa]CaSbO_6$ general formula. In the case of samarium compounds, the results of refinements show that Sm^{3+} ions partially occupy the B site, the ratio of occupancy of Sm^{3+} in B site increase with increasing of Sr content. In addition, they show that the B and B′ ions are regularly disordered in the NaCl-type. The B site is randomly occupied by Ca^{2+} and Sm^{3+} ions and the B′ site is occupied by only the Sb^{5+} ion. In previous works, we have observed

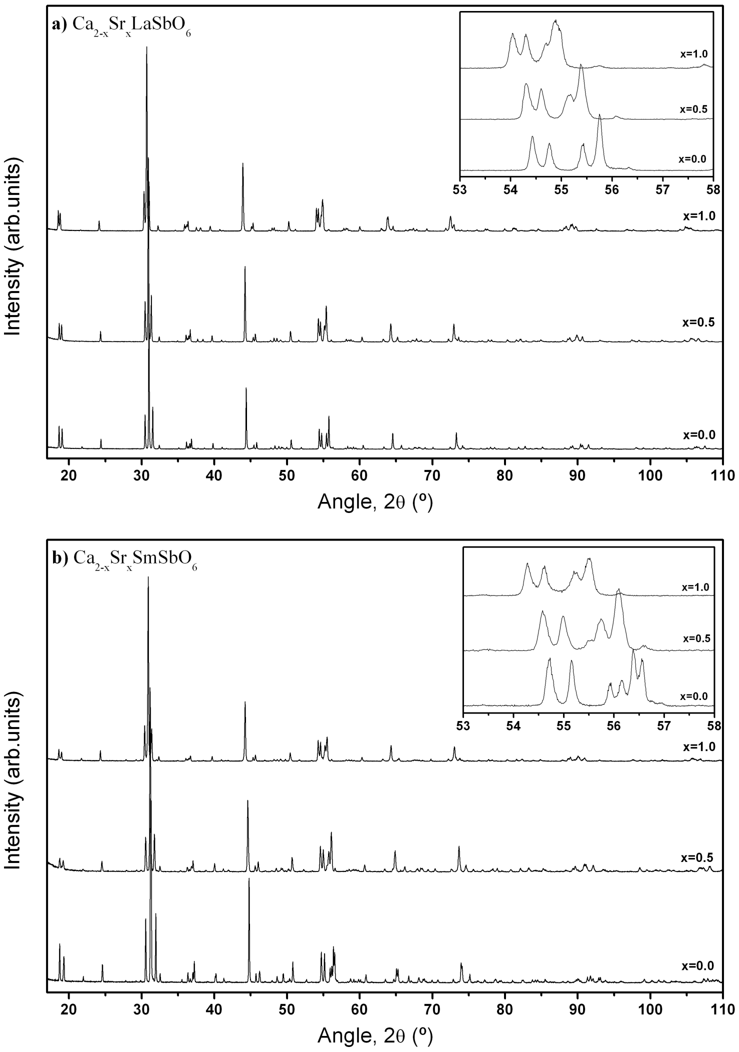

FIGURA 12.3: Evolution of the laboratory X-ray diffraction pattern at room temperature of $Ca_{2-x}Sr_xLaSbO_6$ (a) and $Ca_{2-x}Sr_xSmSbO_6$ (b) with $(x = 0.5, 1.0)$. In the insets, details from the X-ray powder diffraction patterns in 53-58° range, to show the continuous evolution of the pattern with increasing of Sr concentration.

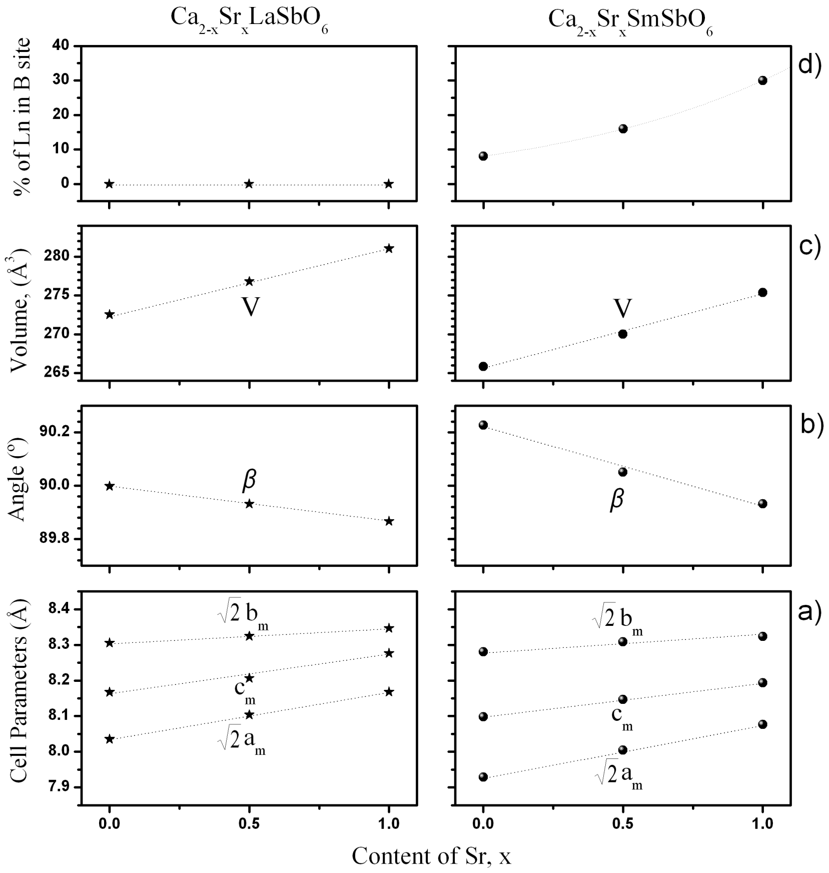

FIGURA 12.4: Evolution, as a function of increasing strontium content, $(x = 0, 0.5, 1)$, at room temperature, of the (a) unit cell parameters, (b) monoclinic angle (β), (c) unit-cell volume and (d) the ratio of the Ln at the B site of the synthesized materials $Ca_{2-x}Sr_xLaSbO_6$ (left panels) and $Ca_{2-x}Sr_xLaSbO_6$ (right panels) . Dotted line is a guide for the eyes.

a partial disordering between the M^{3+} and Sb^{5+} cations over the B sites [105, 108, 109], and this is the first time we observe the partial cation ordering over the A and B sites in double perovskite antimony family. In general the degree of the cation depends on the charge, size and polarization factors, but it can affected by the synthesis temperature, antisite can be reduced by using high temperature possible. In [110], we have studied the effect of the A type cation on the degree of ordering of the B and B′ cations in the B sites. High degree of ordering in rich Ca-rich double perovskite compounds is observed, due to the the thermal diffusivity of calcium in comparison of strontium. This factor affect in the same manner the cation ordering between the A and B sites observed in this study, these compounds are prepared in the same conditions with the same thermal treatments. High degree of cation ordering between the Sm^{3+} and Ca^{2+} over the A and B sites, in rich calcium compounds is observed.

12.3. High-temperature phase-transitions in Ca$_{2-x}$Sr$_x$LnSbO$_6$ (Ln=La,Sm) and $(x = 0, 0.5, 1)$

The thermal evolution of the structures of Ca$_{2-x}$Sr$_x$LnSbO$_6$ (Ln=La,Sm) and $(x = 0, 0.5, 1)$ was studied by means of conventional X-ray diffraction measurements at different temperatures. X-ray data were collected in 2θ from 15 to 120°, between 1170 and 1770K, with a temperature step 15K. In Figure 5 we show the scattered intensity of (422) cubic reflection in the 53-57° 2θ interval, projected and represented with shades of gray. We have plotted the experimental results for Ca$_2$LaSbO$_6$ in panel (a), Ca$_{1.5}$Sr$_{0.5}$LaSbO$_6$ in panel (b), CaSrLaSbO$_6$ in panel (c), Ca$_2$SmSbO$_6$ in panel (d), Ca$_{1.5}$Sm$_{0.5}$SmSbO$_6$ in panel (e) and CaSrSmSbO$_6$ in panel (f). This regions contain a group of diffraction peaks that have been identified as especially sensitive to the structural changes occurring in these family of compounds.

After examination of all diffractograms of Ca$_2$LaSbO$_6$, Ca$_2$SmSbO$_6$ and Ca$_{1.5}$Sm$_{0.5}$SmSbO$_6$, we observed no disappearing of diffraction peaks corresponding to primitive Bragg peaks reflections with indices of type h+k+l=2n+1 in all range of temperature. This shows that no change of primitive unit cell. In Figure 5, panels (a), (d) and (e), we noted the same a monoclinic splitting of reflections from 1170 to 1770K . Which shows no phase transition is produced. Analyzing the peak splitting, it becomes clear that at 1770K the unit cell is monoclinic. The experimental data show that the structure of Ca$_2$LaSbO$_6$, Ca$_2$SmSbO$_6$ and Ca$_{1.5}$Sm$_{0.5}$SmSbO$_6$ does not change significantly between ambient temperature and 1770K, and that there is no indication of any phase transitions in this temperature range.

In the case of Ca$_{1.5}$Sr$_{0.5}$LaSbO$_6$, CaSrLaSbO$_6$ and CaSrSmSbO$_6$. As seen in Figure 5, the distortion of the unit cells gets smaller at higher temperatures: the diffraction lines get closer to each other. At about 1695K, 1590K and 1620K in Ca$_{1.5}$Sr$_{0.5}$LaSbO$_6$, CaSrLaSbO$_6$ and CaSrSmSbO$_6$, respectively, as indicated in the figure, the splitting of the diffraction lines reduces appreciably. At those temperatures also, the reflections of the type hkl, with $h + k + l = 2n + 1$ also disappear in the patterns of these compounds. As mentioned, these reflections are characteristic for a primitive unit cell. These observations indicate that, at the mentioned temperatures, the structures transform from the monoclinic symmetry (at low temperature) to another structure of higher symmetry (at high temperature), not with a primitive cell. At about 1755, 1725 and 1650K, in Ca$_{1.5}$Sr$_{0.5}$LaSbO$_6$, CaSrLaSbO$_6$ and CaSrSmSbO$_6$, respectively, the splitting of the diffraction lines disappears, in a continuous way. This indicates the presence of another phase transition, in each case, that changes the structures from the intermediate to a higher symmetry one, cubic ($Fm\bar{3}m$).

In previous work, the structural analysis of similar materials Sr$_2$SmSbO$_6$ and Sr$_2$LaSbO$_6$ suggests that there is a two phase-transitions at high temperatures, the first one being discontinuous and the second one continuous as a following phase-transition sequence: $P2_1/n \rightarrow R\bar{3} \rightarrow Fm\bar{3}m$. In this work we have proposed that the intermediate rhombohedral tilt system is favored by the

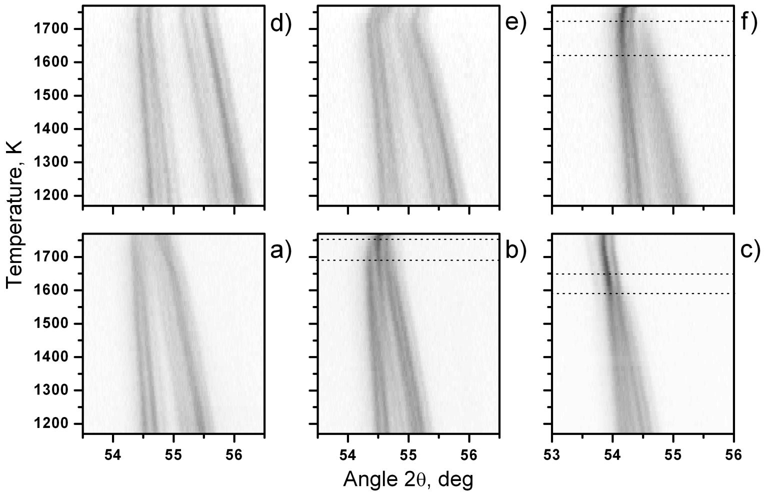

FIGURA 12.5: Thermal evolution of the the scattered intensity of (a) Ca_2LaSbO_6, (b) $Ca_{1.5}Sr_{0.5}LaSbO_6$, (c) $CaSrLaSbO_6$, (d) Ca_2SmSbO_6, (e) $Ca_{1.5}Sm_{0.5}SmSbO_6$ and (f) $CaSrSmSbO_6$ in the 53-57° 2θ interval, projected and represented with shades of gray. Black corresponds to high intensity, and white to low intensity. The horizontal lines are a guide to the eye, and mark the temperatures at which the distortions in compounds get smaller, first, and, then, disappear; thus, indicating the presence of two successive phase transitions.

presence of the big difference between the B cations' radii, more symmetric than the tetragonal tilt. So, basing in this work we attempted to refine the patterns at 1695K, 1590K and 1620K in $Ca_{1.5}Sr_{0.5}LaSbO_6$, $CaSrLaSbO_6$ and $CaSrSmSbO_6$, respectively, in the $R\overline{3}$ space group (tilt-system $a^-a^-a^-$). The results of refinement confirm that the observed discontinuous phase transition for both compounds is $P2_1/n \longrightarrow R\overline{3}$. And the patterns collected at temperatures higher than 1755, 1725 and 1650K, in $Ca_{1.5}Sr_{0.5}LaSbO_6$, $CaSrLaSbO_6$ and $CaSrSmSbO_6$, respectively, were well fit by a structural model with the space group $Fm\overline{3}m$, corresponding to the undistorted aristotype double perovskite structure (tilt-system $a^0a^0a^0$). Nevertheless, while the rhombohedral tilt system occurs in $Ca_{1.5}Sr_{0.5}LaSbO_6$, $CaSrLaSbO_6$ and $CaSrSmSbO_6$ double perovskites, this observation demonstrates a more prominent role of big difference between the B cations' radii in determining the intermediate tilt system.

Finally, in Fig. 6 we show the variation with the temperature of the lattice constants of Ca_2LaSbO_6 in panel (a), $Ca_{1.5}Sr_{0.5}LaSbO_6$ in panel (b), $CaSrLaSbO_6$ in panel (c), Ca_2SmSbO_6 in panel (d), $Ca_{1.5}Sm_{0.5}SmSbO_6$ in panel (e) and $CaSrSmSbO_6$ in panel (f). The monoclinic and hexagonal parameters have simply scaled to compare with edge of the centered cubic as it appears in the final structure.

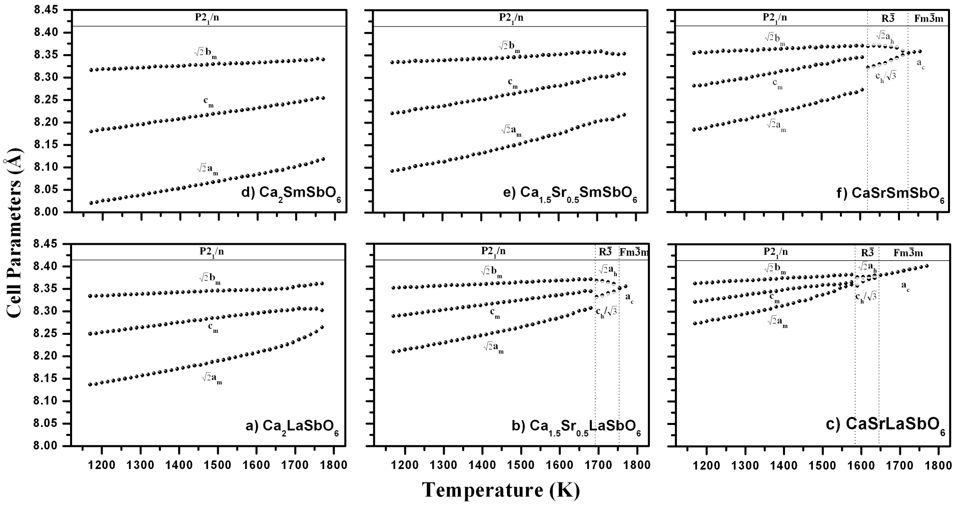

FIGURA 12.6: Temperature evolution of the lattice parameters of (a) Ca_2LaSbO_6, (b) $Ca_{1.5}Sr_{0.5}LaSbO_6$, (c) $CaSrLaSbO_6$, (d) Ca_2SmSbO_6, (e) $Ca_{1.5}Sm_{0.5}SmSbO_6$ and (f) $CaSrSmSbO_6$. We show the cell parameters of the trigonal phase in the hexagonal notation. The monoclinic and hexagonal parameters have simply scaled to compare with edge of the centered cubic.

12.4. Conclusions

As summary, we have studied the chemical size effect on the structure of $Ca_{2-x}Sr_xLnSbO_6$ (Ln=La,Sm) and $(x = 0, 0.5, 1)$. All six compounds crystallize in the monoclinic space group $P2_1/n$, with cation distribution $[Ca_{1-x}Sr_xLn]_ACaSbO_6$ general formula. The larger La cations occupy only the A-site, whereas, the Sm cations distribute between the A-site and B-site. The degree of Sm-Ca ordering decrease with increase of the Sr content. The Vegard's law holds for these solid solutions $Ca_{2-x}Sr_xLnSbO_6$ (Ln=La,Sm) and $(x = 0, 0.5, 1)$, due to the linear variation of lattice parameters at room temperature with increasing of Sr concentration. The high-temperature study revealed the following two phase-transition sequence $P2_1/n \rightarrow R\bar{3} \rightarrow Fm\bar{3}m$ in $Ca_{1.5}Sr_{0.5}LaSbO_6$, $CaSrLaSbO_6$ and $CaSrSmSbO_6$ double perovskites, this observation demonstrate the presence of rhombohedral tilt system as intermediate phase for the compounds have a big difference between radii of B cations' site. In Ca_2LaSbO_6 , Ca_2SmSbO_6 and $Ca_{1.5}Sm_{0.5}SmSbO_6$, no indication of any phase transitions from room temperature to 1770K was observed, due to high distortion at room temperature of these compounds.

Capítulo 13

A study of the crystal structures and the phase transitions of the ordered double perovskites Sr_2ScSbO_6 and Ca_2ScSbO_6

13.1. Introduction

In a previous work [105], we have studied the structures of Sr_2AlSbO_6 and Sr_2CoSbO_6 with the X-ray powder diffraction method. At room temperature the crystal structure of Sr_2AlSbO_6 is cubic ($Fm\bar{3}m$, No. 225). It was found that depending on the preparation conditions, the Al^{3+} and Sb^{5+} cations can be either entirely or partially ordered. In the case of the partially ordered Sr_2AlSbO_6 sample, the extension of cation ordering was estimated from the *hkl*-dependent broadening of the diffraction peaks and the results were interpreted as evidence of the formation of anti-phase domains in the material. Low-temperature Raman spectroscopic measurements demonstrated that the cubic phase of Sr_2AlSbO_6 is stable down to 79K. The room-temperature crystal structure of Sr_2CoSbO_6 was found to be trigonal (space group $R\bar{3}$, No. 148). At 470K, however, the material undergoes a continuous phase transition and its structure is converted to cubic (space group $Fm\bar{3}m$). The studied Sr_2CoSbO_6 sample was partially ordered, but unlike Sr_2AlSbO_6, no indication of the formation of anti-phase domains was observed.

In this work we have focused our attention on Sr_2ScSbO_6 and Ca_2ScSbO_6 ordered double perovskite oxides. To the best of our knowledge, this is the first time that the room-temperature structures of Sr_2ScSbO_6 and Ca_2ScSbO_6 are reported. Syntheses of Sr_2ScSbO_6 have been reported on two occasions [83, 114]; however, no space group and structural determination were performed. In the first study, Sr_2ScSbO_6 was reported as orthorhombic with unit cell parameters a=5.678Å; b=5.691Å; c=8.021Å [114]. The second work, reported Sr_2ScSbO_6 as tetragonal, with a=8.019Å; c=8.063Å [83]. Also, there are no previous studies on the possible induced phase transitions in both materials. The aim of this work is also to analyze the possible high temperature phase transitions in Sr_2ScSbO_6 and Ca_2ScSbO_6.

13.2. Room temperature crystal structures of Sr_2ScSbO_6 and Ca_2ScSbO_6

The ideal double perovskite with the general formula $A_2BB'O_6$ has a cubic symmetry with the space group $Fm\bar{3}m$. This symmetry is usually expected when the tolerance factor values t, $t = \frac{(r_{Sr}+r_O)}{\sqrt{2}(\bar{r}_{B,Sb}+r_O)}$ where $\bar{r}_{B,Sb}$ is the averaged ionic radius of the B and B′ cations, is close to unity. For the majority of double perovskites, however, the size of the A-cation is too small to fit in the cavity formed by the 12 anions. In such cases, tilting of the octahedra generally occurs, leading to a lower symmetry, and hence, for the structure distorted from prototype cubic symmetry, the value of t is $t < 1$. The tolerance factors, at room temperature, for Sr_2ScSbO_6 and Ca_2ScSbO_6 are obtained to be 0.969 and 0.897, respectively (calculated using the ionic radii suggested in [3]). These values suggest, in the one hand, that the room-temperature structures of both compounds should not be cubic, and, in the other hand, that the calcium compound will be more distorted than the strontium one.

The room-temperature data obtained for Sr_2ScSbO_6 from neutron powder diffraction (NPD) and X-ray powder diffraction (XRPD) measurements, refined simultaneously to determine the structure, are shown in figure 1a and 1b, respectively. The refinement process has been done, in a first approach, as usually: using the atomic coordinates of the atoms as the degrees of freedom of the structure. As will be explained below, in a second and definitive approach, we have used the new version of FullProf Suite program [40] to refine the structures, making use symmetry adapted modes. In figure 1a and 1b, many diffraction lines are clearly split, indicating that the unit cell of this material is not cubic, as expected. For example, two of the insets in figure 1 (a and b) show the splitting of the (800) cubic reflection. As a starting model for the Rietveld refinement, we have used the lowest symmetry space group usually encountered in the case of the ordered double perovskite oxides: the monoclinic structure with space group $P2_1/n$ suggested in [80] for one antimony oxide, with the following atomic position; Sb at 2c $(0, 1/2, 0)$, Sc at 2b $(1/2, 0, 0)$ and Sr, O1, O2 and O3 at 4e (x, y, z). The results of refinements are shown in figure 1, and the structural details of Sr_2ScSbO_6 at room temperature are given in Table 1. A large number of weak reflections are observed in both diffraction patterns. The enlarged portion of the profile shows the presence of the primitive (monoclinic) Bragg peaks (111/-111) at about 24.75 in XRPD data, (210/120) at 41.38° and (-212/212/-

TABLA 13.1: Crystal structure and R. factors for Sr_2ScSbO_6, the atomic positions were refined in space group $P2_1/n$ at room temperature from x-ray and E9 neutron data. The cell parameters are: a=5.6914(1)Å; b=5.6776(1)Å; c=8.0242(1); β= 90.03(1)○; V=259.30 (1)Å^3

Atom	Site	x	y	z	B(Å^2)	Occupancy
Sr	4e	0.0025(2)	0.0099(2)	0.2485(4)	0.49(3)	1.00
Sb	2c	0	1/2	0	0.28(3)	1.00
Sc	2d	1/2	0	0	0.31(5)	1.00
O1	4e	0.2641(2)	0.2690(2)	0.0270(4)	0.57(4)	1.00
O2	4e	0.2730(2)	0.2650(2)	0.4760(4)	0.57(4)	1.00
O3	4e	0.9511(5)	0.4946(1)	0.2424(4)	0.57(4)	1.00

Reliability factors (X-ray/neutron): $R_\mathrm{p} = 8.80/4.71\,\%$, $R_\mathrm{wp} = 16.4/6.13\,\%$, $\chi^2 = 1.55/1.83$, $R_\mathrm{Bragg} = 2.55/3.43$

TABLA 13.2: Crystal structure and R. factors for Ca_2ScSbO_6, the atomic positions were refined in space group $P2_1/n$ at room temperature from x-ray and E9 neutron data. The cell parameters are: a=5.5088(1)Å; b=5.6226(1)Å; c=7.8601(1); β= 90.02(1)○; V=243.46(1)Å^3

Atom	Site	x	y	z	B(Å^2)	Occupancy
Ca	4e	0.0150(9)	0.0461(4)	0.2490(4)	0.28(6)	1.00
Sb	2c	0	1/2	0	0.18(3)	1.00
Sc	2d	1/2	0	0	0.59(6)	1.00
O1	4e	0.292(2)	0.303(2)	0.052(2)	0.48(3)	1.00
O2	4e	0.299(2)	0.284(2)	0.444(2)	0.48(3)	1.00
O3	4e	0.908(2)	0.468(1)	0.244(1)	0.48(3)	1.00

Reliability factors: $R_\mathrm{p} = 10.9\,\%$, $R_\mathrm{wp} = 16.0\,\%$, $\chi^2 = 3.11$, $R_\mathrm{Bragg} = 3.55$

122/122) at 49.44° in NPD data, that violate the I-centering condition on the hkl reflections with $h+k+l$=2n.

The Rietveld refinement results of X-ray diffraction pattern data of Ca_2ScSbO_6 recorded at room temperature is shown in Figure 2. All diffraction lines are indexed based on a monoclinic symmetry with the $P2_1/n$ space group, the unit-cell being: a=5.5088(1)Å; b=5.6226(1)Å; c=7.8601(1)Å and β=90.02(1)°. A clear splitting of many peaks can be observed, inset of figure 2. Table 2 lists the final atomic parameters, cell parameters and isotropic atomic displacement parameters.

The monoclinic structure ($P2_1/n$ space group) is characterized by rock-salt like ordering, in this case, of the Sc^{3+} and Sb^{5+} cations, over alternative layers. The degree of cation ordering depends mostly on the charge difference, size, and polarization of B- and B'-site cations of the double perovskite oxide with the general formula $A_2BB'O_6$. It can also be affected by the synthesis tem-

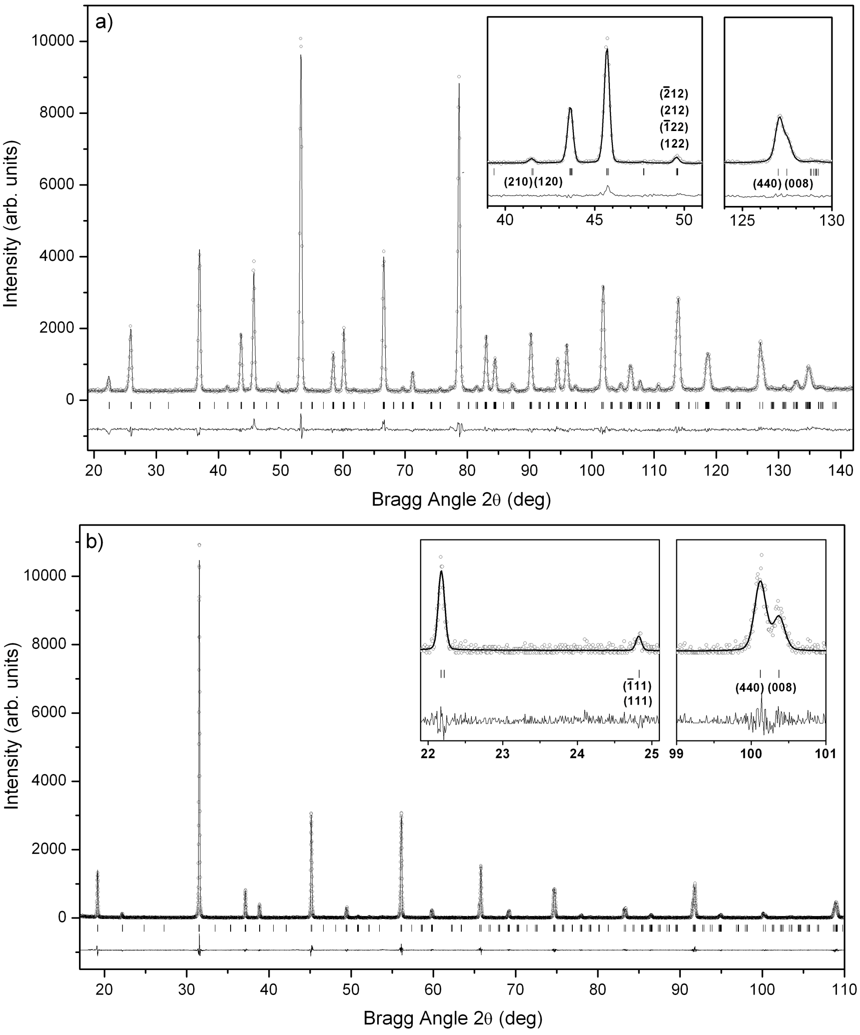

a)

b)

FIGURA 13.1: Experimental (symbols) and calculated (line) neutron profiles (top) and X-ray profiles (bottom) for the Rietveld refinement of Sr_2ScSbO_6 at room temperature using a structural model with $P2_1/n$ space group. Insets shows in detail the presence of the primitive Bragg peaks corresponding to the $P2_1/n$ symmetry.

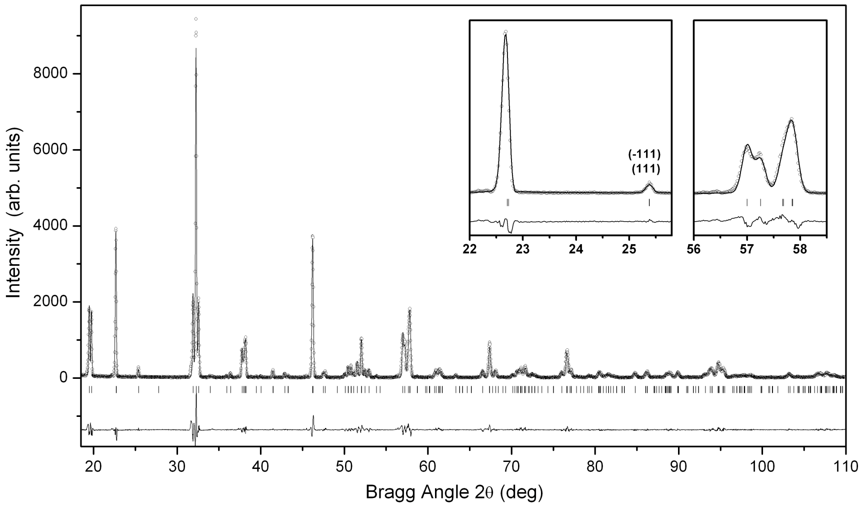

FIGURA 13.2: Experimental (symbols) and calculated (line) X-ray powder diffraction profiles for the Rietveld refinement of Ca_2ScSbO_6 at room temperature using a structural model with $P2_1/n$ space group. Insets shows in detail the presence of the primitive Bragg peaks corresponding to the $P2_1/n$ symmetry.

perature, sintering time and method of preparation. To eliminate the effect of these last factors on cation ordering, we have prepared our samples in the same conditions: method and temperature of preparation. The Sc and Sb atoms are totally ordered in the two distinct B sites, in both compunds, A_2ScSbO_6 (A=Sr,Ca). As mentioned, in two previous works [105, 108], we have studied the structure of Sr_2AlSbO_6, Sr_2CoSbO_6 and Sr_2CrSbO_6 compounds: the former materials showed a partial order in the B sites, 98 % and 80 %, respectively; and the latter, was nearly completely ordered, 99.2 %. The complete order of Sc/Sb reported in the present work is attributed to the significantly larger difference in the effective ionic radii of the $Sc^{3+} - Sb^{5+}$ (Δr =0.145Å), in comparison to that of the $Al^{3+} - Sb^{5+}$ (Δr =0.065Å) and $Co^{3+} - Sb^{5+}$ (Δr =0.010Å) differences. It is known, that the cation ordering increases with the increase of the difference in the effective radii of B-site cations. The ionic radii difference in the chromium compound ($Cr^{3+} - Sb^{5+}$; Δr =0.015Å) compound is a little bit greater than that of the Co compound, although the first one is nearly completely ordered and the last one is not; and, at the same time, the difference is four times lower than in the Al compound, being this nearly ordered. We conclude that Jahn-Teller character of the Cr^{3+} cation, although weak in comparison with Cu^{2+}, for instance, is enough to order the $Cr^{3+} - Sb^{5+}$ cations, despite the ionic radii difference is lower than the aluminum compound, being this less ordered.

Table 3 lists the main interatomic distances and angles for Sr_2ScSbO_6 and Ca_2ScSbO_6 phases at room temperature. The structural analysis of both compounds indicates that the Sc^{3+} and Sb^{5+} are octahedrally coordinated with the oxygen atoms. The typical Sc−O bond lengths of ScO_6 octahedra range between 2.04 and 2.10Å. Similarly, the Sb−O bond lengths of SbO_6 octahedra range between 1.96 and 2.01Å. The average $< Sc - O >$ and $< Sb - O >$ are also close to the calculated

TABLA 13.3: Main bond distances (Å) and selected angles (°) for Sr_2ScSbO_6 and Ca_2ScSbO_6 from XRPD at room temperature. rSc^{3+}(VI)=0.745Å rSb^{5+}(VI)=0.6Å.

	Sr_2ScSbO_6	Sr_2ScSbO_6
ScO_6 polyhedra		
Sc-O1 (×2)	2.045(2)	2.091(9)
Sc-O2 (×2)	2.057(2)	2.092(9)
Sc-O2 (×2)	2.085(2)	2.078(9)
Average distance	2.062(4)	2.087(4)
Predicted distance	2.145	2.145
SbO_6 polyhedra		
Sb-O1 (×2)	2.006(2)	1.997(9)
Sb-O2 (×2)	1.992(2)	1.992(9)
Sb-O3 (×2)	1.965(2)	1.995(9)
Average distance	1.988(4)	1.995(4)
Predicted distance	2.000	2.000
AO_n polyhedra		
A-O1 (×1)	2.746(2)	2.610(2)
A-O1 (×1)	2.622(3)	2.333(3)
A-O1 (×1)	3.113(4)	-
A-O1 (×1)	2.900(6)	2.811(5)
A-O2 (×1)	2.792(3)	2.564(2)
A-O2 (×1)	2.610(4)	2.352(2)
A-O2 (×1)	3.128(4)	-
A-O2 (×1)	2.849(6)	2.842(5)
A-O3 (×1)	2.940(8)	-
A-O3 (×1)	2.767(8)	2.447(7)
A-O3 (×1)	2.584(3)	2.372(9)
A-O3 (×1)	3.111(3)	3.207(9)
Average distance	2.847(6)	2.615(6)
Predicted distance	2.84	2.63
Sb-O1-Sc (×2)	165.6(5)	148.6(3)
Sb-O2-Sc (×2)	166.0(5)	149.0(4)
Sb-O3-Sc (×2)	164.1(4)	149.5(4)
<Sb-O-Sc>	165.2	149.0

values from the ionic radii, of 2.15Å and 2.00Å, respectively. The ScO_6 and SbO_6 octahedra are alternatively connected and extended in three dimensions. The A^{2+} cations are located in the cavities formed by the corner-sharing octahedra, the average of the A−O short distances 2.85Å is typical for Sr^{2+} cations in a twelve-coordinate environment and 2.62Å for Ca^{2+} in a eight-coordinate environment, this is commonly observed for compositions that include an A^{2+} cation which is too small to fill the twelve-fold coordination site, and results in a reduced eight-fold coordination environment for the A cation in the monoclinic structure. The mean average distance A−O decreases as Sr^{2+} is substituted by Ca^{2+}, which is consistent with the lower ionic radius of Ca^{2+}(1.23Å) compared to Sr^{2+}(1.44Å). This smaller size of Ca^{2+} is responsible for the larger monoclinic distortion.

Glazer proposed a simple notation for clarifying and describing the possible space groups of simple perovskites by allowing for octahedral tilting [24], and Woodward extended it to describe the double perovskites with the general formula $A_2BB'O_6$ [38]. Using this notation, a tilt system is

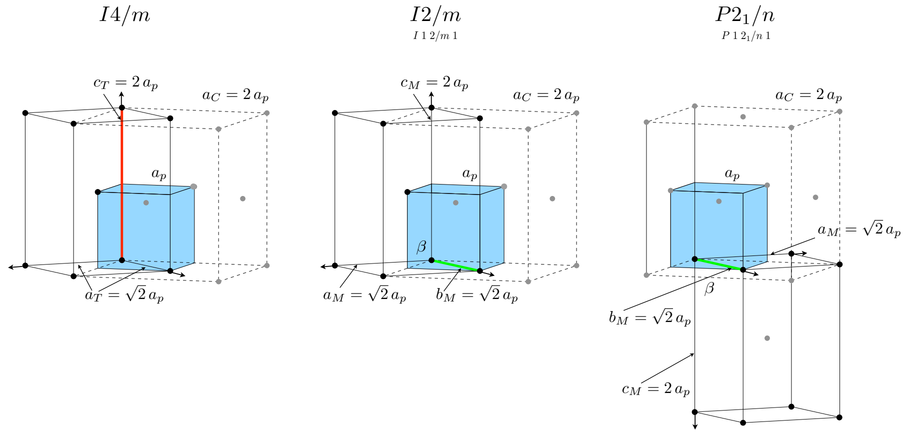

FIGURA 13.3: The relative orientation of the unit cell of the prototype cubic simple perovskite ($Pm\bar{3}m$) (blue) and those of the prototype cubic ($Fm\bar{3}m$) (dashed lines, the distorted tetragonal ($I4/m$) and the monoclinic ($I2/m$ and $P2_1/n$) of the double perovskites

described in terms of rotations of BO$_6$ octahedra around any of the cartesian axes; these axes are coincident with the three axes of the prototype unit cell of the cubic simple perovskite ($Pm\bar{3}m$ space group). In the general case of unequal angles of rotation around the x, y and z axes, the rotation scheme is specified as a, b and c degrees, with the sense of rotation in successive layers of octahedra perpendicular to the rotation axis given as superscripts. A positive superscripts indicates a tilt of the octahedra in successive layers in the same direction, i.e. an in-phase tilt, whereas a negative superscript indicates that the neighboring octahedra rotate in the opposite direction, i.e. an anti-phase tilt. When the unit cell of primitive perovskites ABO$_3$ is described as $a_p \times b_p \times c_p$, that of the double-type perovskites should be described as $2a_p \times 2a_p \times 2a_p$ (cubic) or $\sqrt{2}a_p \times \sqrt{2}a_p \times 2a_p$ (tetragonal or monoclinic). The relative orientation of the unit cell of the prototype cubic simple perovskite ($Pm\bar{3}m$) and those of the prototype cubic ($Fm\bar{3}m$) and the distorted tetragonal ($I4/m$) and monoclinic ($I2/m$ and $P2_1/n$) of the double perovskites are shown in figure 3. According to Glazer's notation, double perovskite-type structures with the space group $P2_1/n$ are described by the $a^+b^-b^-$ tilt system. Thus, this means that the $P2_1/n$ symmetry is achieved, from the cubic prototype by rotating the octahedra around the simple perovskite x axis the same amount for the the octahedra in successive layers; and a different amount around y and z axes (but the same around both), so that the octahedra in successive layers are rotated in an anti-phase manner. On the other hand, in figure 4 we show the projections, along the cubic (simple) perovskite axes, ($[100]_p$, $[010]_p$ and $[001]_p$), of a section of the unit cell of the structure of the double perovskite with A$_2$BB'O$_6$ general formula in the $Fm\bar{3}m$, $I4/m$, $I2/m$ and $P2_1/n$ space groups, to show that the difference amongst the structural models consists in the losing of one or more tilts around the mentioned simple perovskite axis.

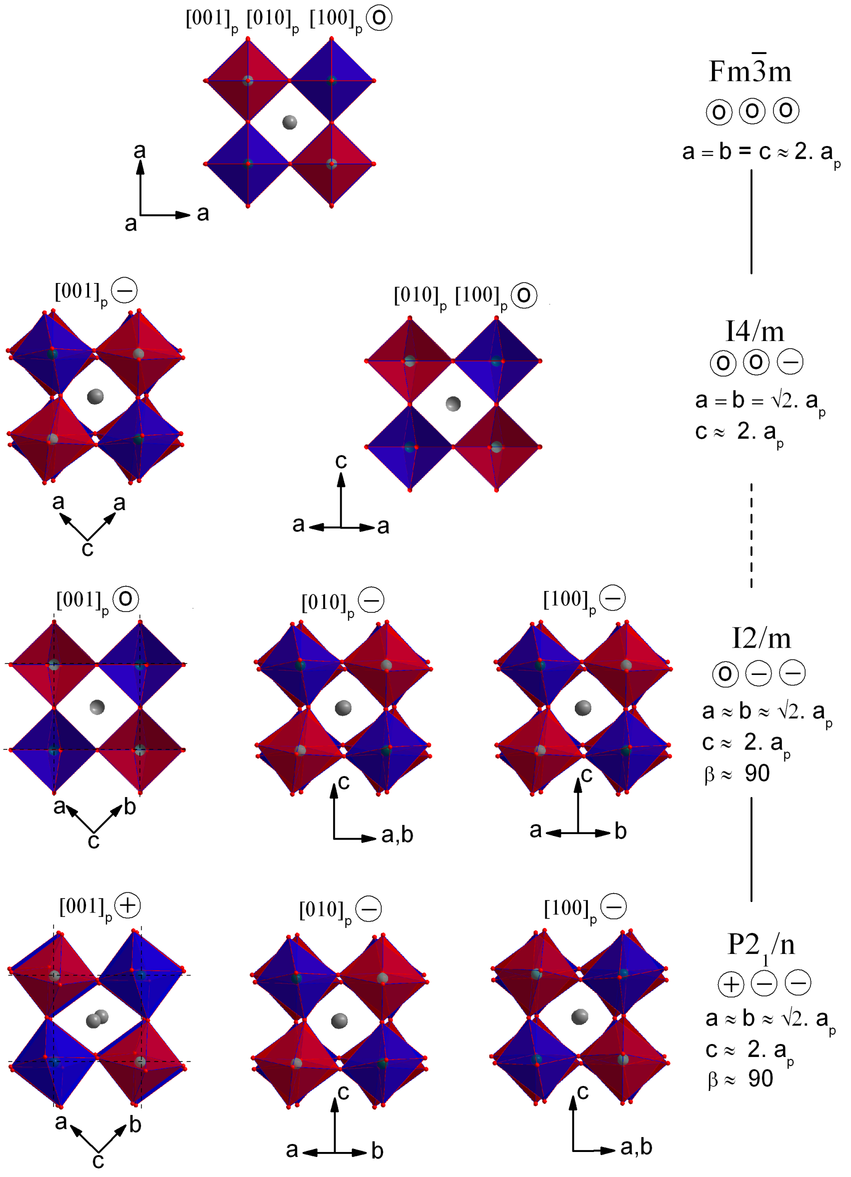
[001]p [010]p [100]p ⓞ
a
a
a
Fm3̄m
ⓞⓞⓞ
a = b = c ≈ 2. ap
[001]p ⊖
a
a
c
[010]p [100]p ⓞ
c
a
a
I4/m
ⓞⓞ⊖
a = b = √2. ap
c ≈ 2. ap
[001]p ⓞ
a
b
c
[010]p ⊖
c
a,b
[100]p ⊖
c
a
b
I2/m
ⓞ⊖⊖
a ≈ b ≈ √2. ap
c ≈ 2. ap
β ≈ 90
[001]p ⊕
a
b
c
[010]p ⊖
c
a
b
[100]p ⊖
c
a,b
P2$_1$/n
⊕⊖⊖
a ≈ b ≈ √2. ap
c ≈ 2. ap
β ≈ 90

FIGURA 13.4: Projections along the cubic (simple) perovskite axes, ([100]$_p$, [010]$_p$ and [001]$_p$), of a section of the unit cell of the structure of Sr$_2$ScSbO$_6$ in the $Fm\bar{3}m$, $I4/m$, $I2/m$ and $P2_1/n$ space groups showing in-phase (+), out-of-phase (-) rotations. ScO6 octahedra are shown red, SbO6 in bleu and Sr atoms in grey. Each structural transition corresponds to the appearance or/and the disappearance of these rotations.

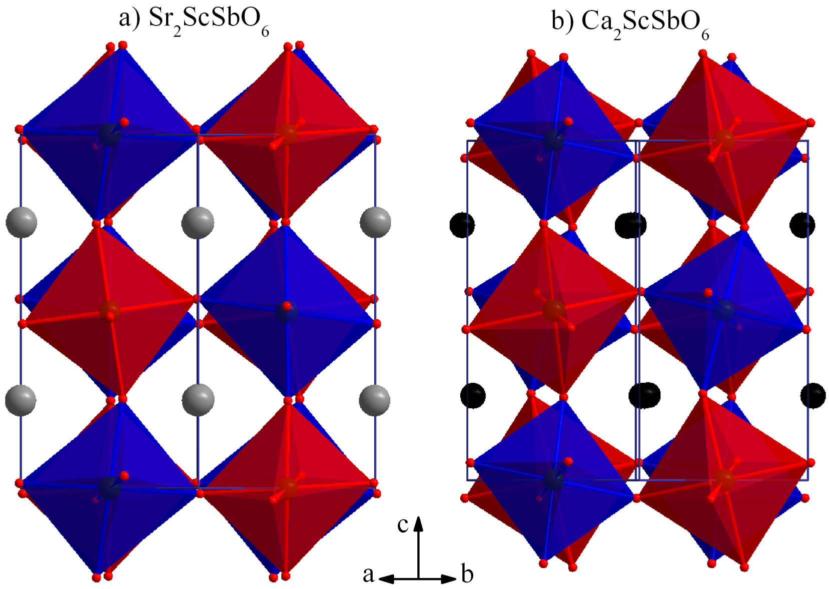

FIGURA 13.5: Crystal structure of Sr_2ScSbO_6 and Ca_2ScSbO_6 along [010]. ScO6 octahedra are shown red, SbO_6 in bleu, Sr atoms in grey and Ca atoms in black. The anti-phase (-) tilting is bigger in the calcium compound.

Figure 5 presents the projection of the room-temperature crystal structures of Sr_2ScSbO_6 and Ca_2ScSbO_6 along the [010] double perovskite monoclinic lattice vector. The appreciable tilt of the octahedra is inferred from the deviation of Sc−O−Sb angles from the ideal value (180°), the deviation of the angle is bigger in the case of Ca compound (149°) in comparison to the Sr compound (165°), which means that the Ca_2ScSbO_6 is more distorted than Sr_2ScSbO_6.

The structure of many materials can be seen as the result of a distortion with respect to a structure of higher symmetry: parent structure (virtual or real). A group-subgroup relation necessarily exists between their space groups, and the structural distortion that relates them can be identified as a symmetry breaking distortion. Usually small distortions (only of displacive type, in our case) imply that the parent phase can be thermally stabilized, and one or several structural phase transitions towards the arrangement of higher symmetry may happen as temperature increases.

The distortion present in a distorted structure (pseudo-symmetric) contains a primary component, corresponding to a mode or modes which are unstable in the parent high-symmetry configuration, and are fundamental for explaining the stability of the distorted structure. In addition, the distortion contains other secondary contributions of less importance, associated with modes which are allowed by symmetry and become frozen through coupling with the primary ones. (Those distortion modes are associated with different irreducible representations (irreps) of the parent space group.) The separation of the contributions of the different modes in a structural distortion is done using the symmetry-mode analysis. In this, two concepts have to be properly defined: (a) the structural distortion itself (displacement field) relating the parent and the distorted phases; which can be decomposed into two contributions: a homogeneous strain (elastic degrees of freedom) and an atomic displacement field (internal atomic degrees of freedom) given by the displacements of each atom in the low-symmetry structure with respect to its position in the parent structure. And (b) the basis with respect to which that displacement field can be decomposed and formed by the symmetry modes compatible with the symmetry break between the space groups of the parent phase and the analyzed phase.

The program AMPLIMODES, located in the Bilbao Crystallographic Server [115], and freely accessible via an internet connection, has a module that prepares a special input file (pcr-file) suitable for refining the powder diffraction data using the FullProf Package [40], irrespective of the source (XRPD or NPD), using symmetry-adapted modes instead of the usual approach that uses atomic coordinates [116]. This new approach takes full advantage of the symmetry-mode analysis performed by AMPLIMODES, as it uses the amplitudes of the symmetry-adapted modes as the refinable parameters (degrees of freedom) in the refinement process. Very recently, this approach, the module of AMPLIMODES and the new version of FullProf have been proven to be very efficient and very robust for refining powder diffraction data [117].

Given the parent (in our case, the prototype cubic phase, $Fm\bar{3}m$ space group) and the distorted structure (the room-temperature monoclinic symmetry, $P2_1/n$ space group), AMPLIMODES calculates the atomic displacements relating both structures, if their magnitudes lay within some tolerance range. A complete basis of symmetry-adapted distortion modes is then determined and defined. Then, the program decomposes the distortion in terms of this basis of symmetry modes, and calculates the amplitudes for each of the symmetry-adapted distortions. Modes are given in terms of atomic displacements in relative units for the atoms of the asymmetric unit of the distorted phase.

It is worth noting that for the symmetry-mode analysis AMPLIMODES does, it is not necessary to know a real parent structure. Starting from the distorted phase (H space group) one can construct an ideal parent structure whose symmetry group (G, with G>H) is determined by the structural pseudo-symmetry of the low-symmetry phase. The structural differences between that ideal parent structure and any other possible parent structure of this symmetry are due only to contributions of symmetry modes compatible with G, i.e. the totally symmetric modes. The contributions of the much more important symmetry-breaking distortion-modes present in the distorted phase do not depend on any choice of the atomic coordinates of the parent structure.

As a second approach in the refinement process, we have refine or room-temperature data using the symmetry adapted modes as degrees of freedom, instead of the atomic coordinates. The results are given in table 1(b): as can be readily appreciated, both structural models, atomic coor-

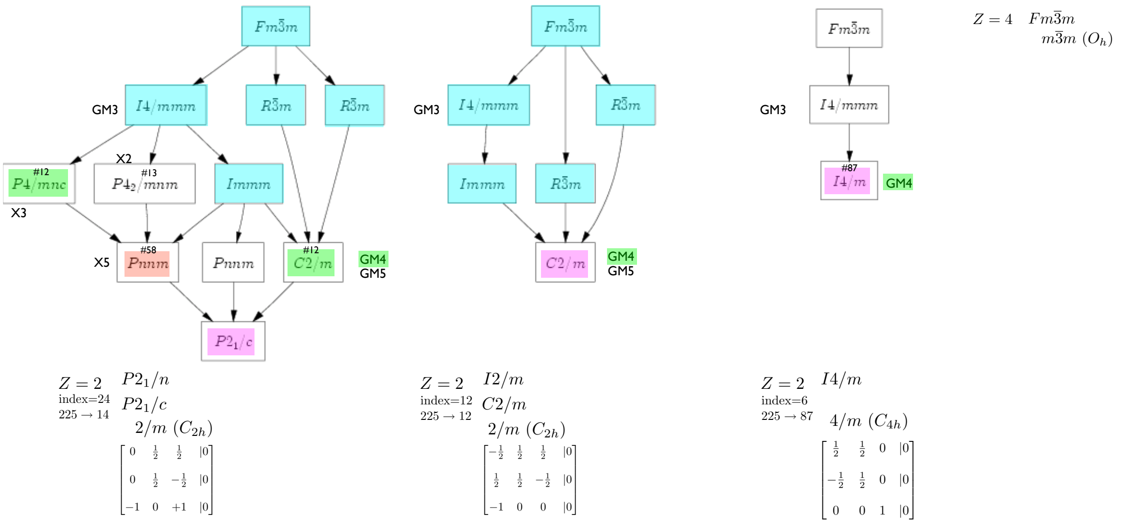
Fm3̄m
GM3
I4/mmm
R3̄m
R3̄m
X2
#12
P4/mnc
#13
P4$_2$/mnm
Immm
X3
X5
#58
Pnnm
Pnnm
#12
C2/m
GM4
GM5
P2$_1$/c
Z = 2 P2$_1$/n
index=24 P2$_1$/c
225 → 14
2/m (C$_{2h}$)
Fm3̄m
GM3
I4/mmm
R3̄m
Immm
R3̄m
C2/m
GM4
GM5
Z = 2 I2/m
index=12 C2/m
225 → 12
2/m (C$_{2h}$)
Fm3̄m
GM3
I4/mmm
#87
I4/m
GM4
Z = 4 Fm3̄m
m3̄m (O$_h$)
Z = 2 I4/m
index=6
225 → 87
4/m (C$_{4h}$)

```
Fm-3m to P21/n

Atoms       WP          Modes
O11         24e         GM1+(1) GM3+(1) GM4+(1) GM5+(2) X2+(1) X3+(1) X5+(2)
Sr1         8c          GM5+(2) X5+(1)


Summary of Amplitudes

K-vector    Irrep       Direction             Isotropy        Dimension   Amplitude(≈)
                                              Subgroup
(0,0,0)     GM1+        (a)                   Fm-3m (225)      1          0.2797
(0,0,0)     GM3+        (a,0)                 I4/mmm (139)     1          0.0023
(0,0,0)     GM4+        (a,a,0)               C2/m (12)        1          0.8104
(0,0,0)     GM5+        (-b,a,-a)             C2/m (12)        4          0.0390
(0,1,0)     X2+         (0,a,0)               P4_2/mnm (136)   1          0.0040
(0,1,0)     X3+         (0,a,0)               P4/mnc (128)     1          0.3872
(0,1,0)     X5+         (a,a,0,0,a,-a)        Pnnm (58)        3          0.1375

Global distortion: 0.9515 ≈
```

```
Fm-3m to I2/m

Atoms       WP          Modes
O11         24e         GM1+(1) GM3+(1) GM4+(1) GM5+(2)
Sr1         8c          GM5+(2)
Note: The primary mode is written in bold letters

Summary of Amplitudes

K-vector    Irrep       Direction             Isotropy        Dimension   Amplitude(≈)
                                              Subgroup
(0,0,0)     GM1+        (a)                   Fm-3m (225)     1           0.0456
(0,0,0)     GM3+        (a,0)                 I4/mmm (139)    1           0.0042
(0,0,0)     GM4+        (a,a,0)               C2/m (12)       1           0.5564
(0,0,0)     GM5+        (-b,a,-a)             C2/m (12)       4           0.0504

Global distortion: 0.5606 ≈
```

```
Fm-3m to I4/m

Atoms       WP          Modes
O11         24e         GM1+(1) GM3+(1) GM4+(1)
Note: The primary mode is written in bold letters

Summary of Amplitudes

K-vector    Irrep       Direction             Isotropy        Dimension   Amplitude(≈)
                                              Subgroup
(0,0,0)     GM1+        (a)                   Fm-3m (225)     1           0.0337
(0,0,0)     GM3+        (a,0)                 I4/mmm (139)    1           0.0056
(0,0,0)     GM4+        (0,0,a)               I4/m (87)       1           0.4998

Global distortion: 0.5010 ≈
```

FIGURA 13.6: The results of the mode analysis carried out by AMPLIMODES: the reference structure is the prototype cubic and the "low-symmetry"phase is the room-temperature NPD-data structure

dinates and amplitudes of the symmetry adapted modes as free parameters in the refinement, are fully coincident.

In figure 6 we show the results of the mode analysis carried out by AMPLIMODES: the reference structure is the prototype cubic (determined from the high-temperature XRPD data, see next section) and the "low-symmetry"phase is the room-temperature NPD-data structure (a panel in the figure).

There are six irreps of the $Fm\bar{3}m$ space group (the seventh irrep, GM^{1+}, is the totally symmetric) that can take part in the symmetry breaking from that space group to the room-temperature $P2_1/n$ monoclinic space group: GM^{3+}(1), GM^{4+}(1), GM^{5+}(4), X^{2+}(1), X^{3+}(1) and X^{5+}(3). The numbers in parenthesis indicate the number of modes transforming according to the irrep; thus, there are 11 modes (+1 totally symetric). The table with the modes label indicates the atoms, with their corresponding Wyckoff position in the reference structure, involved in the modes. Thus, the twelve

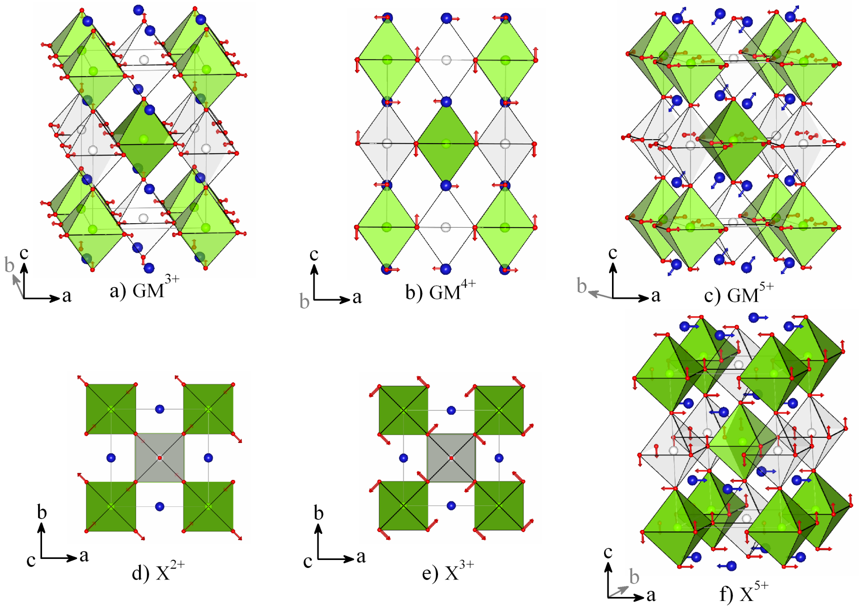

FIGURA 13.7: Representation of the polarization vectors of the six irreps of the $Fm\bar{3}m$ space group that can take part in the symmetry breaking from that space group to the room-temperature $P2_1/n$ monoclinic space group: GM^{3+}(a), GM^{4+}(b), GM^{5+}(c), X^{2+}(d), X^{3+}(e) and X^{5+}(f)

modes move only the oxygen atoms (24e), 8 (+1) modes, and the Sr atom (8c), 3 modes. As indicated in the table included in figure 6a, the GM irreps have a $(0,0,0)$ k-vector, which implies that they maintain the unit cell, and the X irreps have a $(0,1,0)$ k-vector, and, thus, the double, in the b direction, the unit cell. The isotropy group stands for the possible intermediate group, with a group-subgroup relation, between the reference and the distorted symmetry one. The atomic displacements the modes imply break the prototype symmetry to the isotropy group symmetry. The final result of the refinement is indicated as the value of the amplitude associated to each mode (this is the output of the FullProf program, as indicated in the table of figure 6a) or as the global amplitude value associated to each irrep. In figure 7 we show the polarization vectors of the different modes. To do: Description of the polarization vectors of the modes in terms of displacements.

Looking at the refinement final-values for the amplitudes, it is clear that there are only two amplitudes considerable higher than the rest: 0.8085 (GM^{4+}) and 0.3767 (X^{3+}), if we exclude the totally symmetric one, i.e. 0.2732 (GM^{1+}); all the others are at least one order of magnitude lower than those, negligible, thus; and, indeed, their associated sigmas indicate that they can be rounded to zero. That there are two amplitudes of considerably higher values than the rest could be inferred by the fact that there is no unique irrep that breaks the prototype symmetry down to the room-temperature one: there is no unique primary mode, necessarily there are two primary modes that must couple and give rise to the observed room-temperature broken symmetry. This coupling is

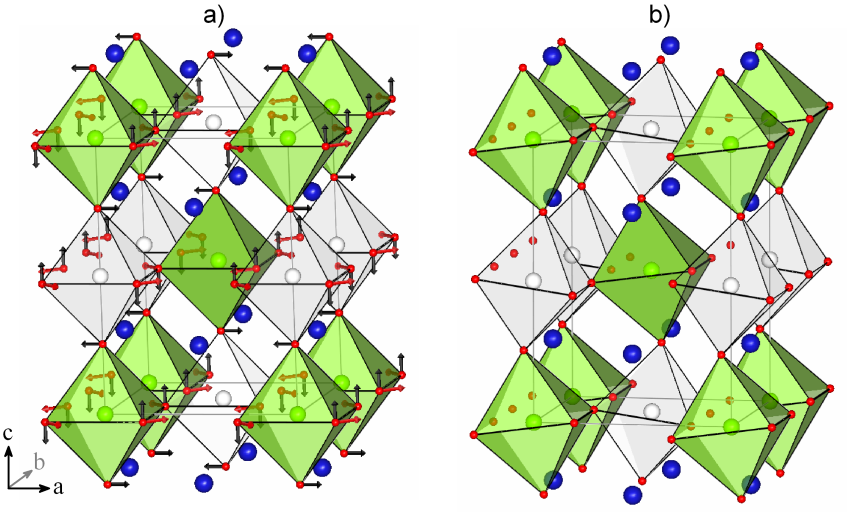

FIGURA 13.8: Representation of the new configuration resulting from the coupling of the unidimensional GM^{4+} and X^{3+} modes with the $a^+b^-b^-$ tilting scheme associated to $P2_1/n$: the atomic displacements implied by the two coupled primary modes can be interpreted, precisely, as the rotations (tilts) of the octahedra.

shown in figure 8(a). On the one hand, it is worth mentioning that the coupled primary modes only involve oxygen atoms. On the other hand, it is worth comparing the new configuration resulting from the coupling of the unidimensional GM^{4+} and X^{3+} modes with the $a^+b^-b^-$ tilting scheme associated to $P2_1/n$: the atomic displacements implied by the two coupled primary modes can be interpreted, precisely, as the rotations (tilts) of the octahedra (figure 8b). Hence, the physically more sensible (making full use of symmetry consideration restrictions) refinement procedure gives rise directly and naturally (the amplitudes of the non-primary modes round to zero) to the physically observed distortions.

13.3. High-temperature x-ray diffraction of Sr$_2$ScSbO$_6$ and Ca$_2$ScSbO$_6$

To search the phase transitions in Sr$_2$ScSbO$_6$ at high temperatures, we analyzed two narrow 2θ-intervals: 51.4° to 52.4°, and 98° to 101°, the first one corresponding to the monoclinic primitive Bragg peaks (131/-131/311/-311), and the second one corresponding to the (642) cubic reflection; in the temperature range from 300 to 780K, with a step of 5K. That 2θ-interval has been identified as especially sensitive to the structural changes occurring in this kind of materials. Figure 9 shows the evolution of diffraction intensities of these reflections with temperature. Figure 9c shows the disappearance of the primitive Bragg peaks, at about 400K, which no longer satisfy (for hkl) the $h+k+l$=2n reflection condition. This corresponds to a transition from the primitive space $P2_1/n$ to a

TABLA 13.4: Crystal structure data and refinement results for Sr_2ScScO_6 at 430K and 613K

Temp. space group Agreement factors	Lattice parameters	Atom	Site	x	y	z	B(Å^2)
430K ($I2/m$)	a=5.7021(1)Å	Ca	4i	0.4993 (1)	0	0.2494 (4)	0.69(3)
$R_p = 4.84\,\%$	b=5.6861(1)Å	Sb	2d	0	0	1/2	0.41(1)
$R_{wp} = 6.21\,\%$	c=8.0293(1)Å	Sc	2a	0	0	0	0.48(3)
$\chi^2 = 1.89$	β=89.96(1)°	O1	4i	-0.0485(8)	0	0.2559(9)	0.91(3)
$R_{Bragg} = 3.44$	V=260.33(1)Å^3	O2	8j	0.2564(9)	0.2555(1)	0.0236(3)	0.91(3)
613K ($I4/m$)	a=5.6929(1)Å	Ca	4d	0	1/2	1/4	0.91(4)
$R_p = 5.85\,\%$	c=8.0641(1)Å	Sb	2a	0	0	1/2	0.67(3)
$R_{wp} = 7.36\,\%$	V=261.35(1)Å^3	Sc	2b	0	0	0	0.72(4)
$\chi^2 = 2.72$		O1	4e	0	0	0.2562(9)	1.23(4)
$R_{Bragg} = 4.84$		O2	8h	0.2871(2)	0.2250(1)	0	1.23(4)

centered space group. It is worth noting that the monoclinic splitting observed at room temperature is maintained up to 560K, as we can see in figure 9a and 9b. These two facts are compatible with a continuous phase transition occurring at 400K from the room-temperature $P2_1/n$ monoclinic space group to an I-centered monoclinic space group: $I2/m$. To determine the structural changes, high-resolution diffraction measurements using neutron diffraction were performed at 430K. The pattern calculated using the $I2/m$ space group shows a good agreement with the experimental pattern (figure 10) and provides good agreement factors. In the inset of figure 10, we can see the missing of all diffraction peaks with indices of the type (hkl) and satisfying h+k+l=2n+1, present at low temperatures (inset figure 1a). In figure 9a and 9b, we observe the appearance, at 560K, of a shoulder on the low-angle side of the shown peak. This is very similar to that observe in the Sr_2MWO_6 family [41, 42, 43] and Sr_2CrSbO_6 [108], where this change was interpreted as an evidence of the material undergoing a discontinuous phase transition from a monoclinic structure to a tetragonal one, with the tetragonal $I4/m$ space group. The refinement of NPD pattern at 633K with $I4/m$ model gave a good fit of the diffraction profile and provided a good agreement factors as well. Structural details for Sr_2ScSbO_6 at 430K in $I2/m$, and at 613K in $I4/m$, are given in Table 4. The tetragonal distortion of the unit cell disappears in a continuous way and at about 660K the unit cell transforms from tetragonal to cubic, is essentially the same as that observed in other double perovskite materials presenting the $I4/m - Fm\bar{3}m$ phase transition.

To determine the variation of the lattice constants with the temperature in Sr_2ScSbO_6 at high temperatures, we obtained 42 X-ray powder diffraction profiles at different temperatures, in 2θ range from 15° to 120°, between 300K and 710K, with a step of 10K. The variation of unit cell parameters and space group symmetries of Sr_2ScSbO_6 with temperatures are shown in figure 11.

To determinate the presence of phase transitions and evolution of unit cell parameters with temperature in Ca_2ScSbO_6, x-ray data were collected in 2θ from 24 to 26 and from 91 to 96, between 300K and 1740K, with a temperature step 5K. The first interval corresponding to the primitive Bragg peaks reflections (111/-111) and the second interval of 2θ corresponding to the (642), as previously.

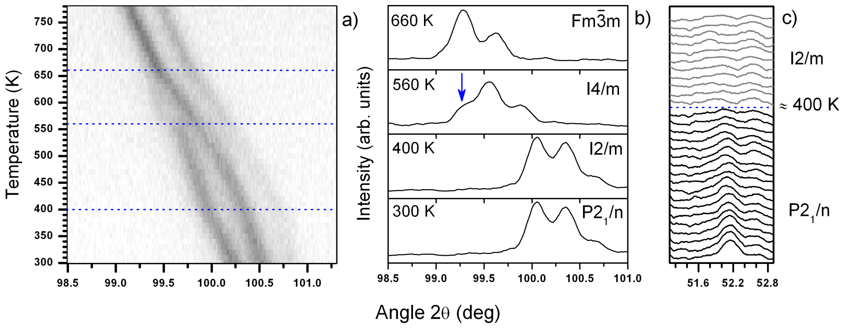

FIGURA 13.9: thermal evolution of the (642) cubic reflections (a,b) and the primitive Bragg peaks (c) of Sr$_2$ScSbO$_6$. In a) scattered intensity is represented with shades of gray –black corresponds to high intensity, and white, to low intensity. The tetragonal splitting existing in the temperature range from 560 to about660K can be observed. The shoulder appearing at 560K is marked with an arrow in (b) and, eventually, the tetragonal splitting disappears and the double reflection evolves to a single cubic one. (c) Thermal evolution of the primitive Bragg peaks (131/-131/311/-311) showing disappears of these peaks at about 400K.

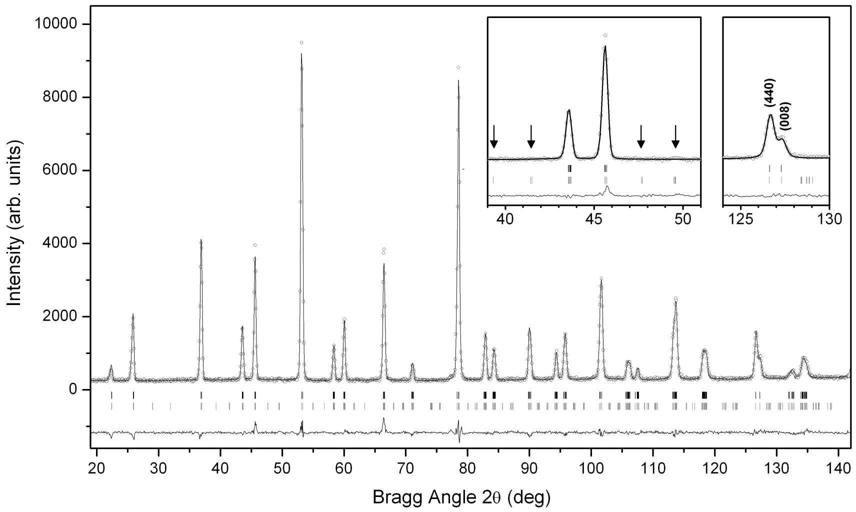

FIGURA 13.10: Experimental (symbols) and calculated (line) neutron profiles for the Rietveld refinement of Sr$_2$ScSbO$_6$ at 430K, using a structural model with $I2/m$ space group. Insets shows in detail the missing of the primitive Bragg peaks corresponding to the $P2_1/n$ symmetry.

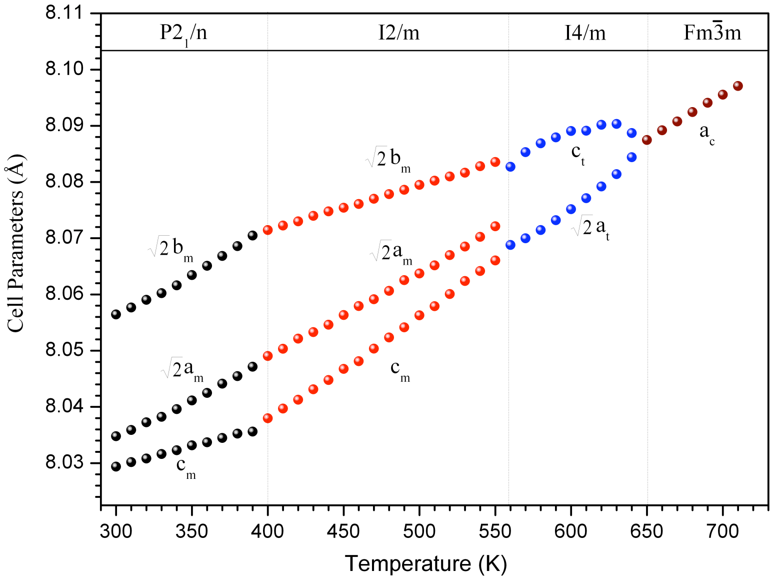

FIGURA 13.11: Variation of the lattice parameters of Sr_2ScSbO_6 with the temperature. The high temperature structure of this compound is cubic. Below 650K it transform to tetragonal. There is another phase transition at about 560K, changing the symmetry from tetragonal to cantered monoclinic $I2/m$ and the last transition from centered monoclinic $I2/m$ to primitive monoclinic $P2_1/n$ at about 400K.

Figure 12 shows the evolution of diffraction intensities of this reflection with temperature. From the profile shape characteristic reflections at 2θ from 91 to 96 in (figure 12b), it was concluded that up to 1740K Ca_2ScSbO_6 does not transform to the tetragonal lattice ($I4/m$ space group) like Sr_2ScSbO_6. This shows that there is no change of the monoclinic distortion in all this range of temperatures; and, analyzing the peak splitting, it becomes clear that at 1740K the unit cell is monoclinic. After examination of all diffractograms, we observed, about 1440K (figure 12a), the continuous desapearance of diffraction peaks corresponding to primitive Bragg reflections, with indices (hkl) of the type $h+k+l$=2n+1. This corresponds to a continuous phase transition from monoclinic $P2_1/n$ to monoclinic $I2/m$ at about 1440K. The evolution with temperature, from 720 to 1680K, of the refined lattice parameters for Ca_2ScSbO_6, are shown in figure 13. As deduced from the figure, the lattice parameters increasing countinuously with temperature, and the difference between $\sqrt{2}$a, $\sqrt{2}$b and c lattice parameters decreases. But no anomaly change is noted.

This sequence of structural phase transitions ($P2_1/n \rightarrow I2/m \rightarrow I4/m \rightarrow Fm\bar{3}m$) was previously reported for the fluoride Cs_2RbDyF_6 [118] and for the tellurium double perovskite Sr_2MnTeO_6 [48] and, as far as we know, this is the first time that it has been observed in the antimony double perovskite oxide family.

We have analyzed the temperature evolution of the two intermediate phases (the monoclinic ($I2/m$) and the tetragonal ($I4/m$) structures) present in Sr_2ScSbO_6 between the monoclinic $P2_1/n$

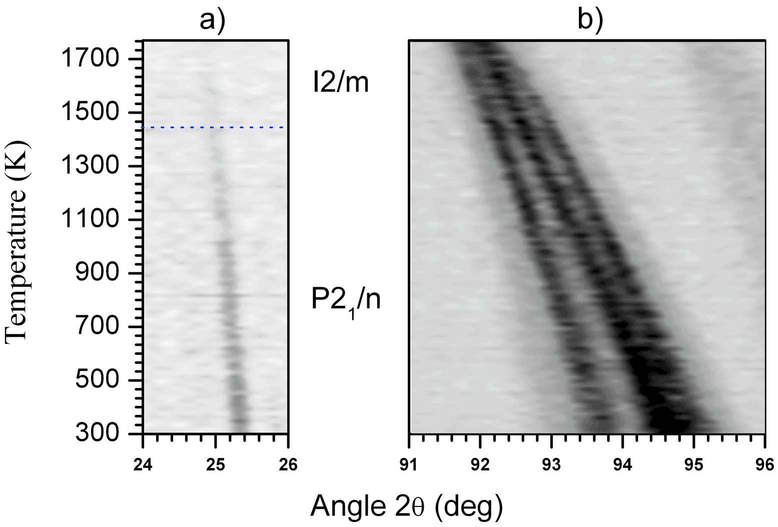

FIGURA 13.12: Temperature evolution of the (642) cubic reflection of Ca_2ScSbO_6. In (b) scattered intensity is represented with shades of dark corresponds to high intensity and light to low intensity. The monoclinic splitting existing in the temperature range from 300 to 1700K can be observed in (b). In (a) we observed dispersing of primitive Bragg peaks reflections at about 1440K.

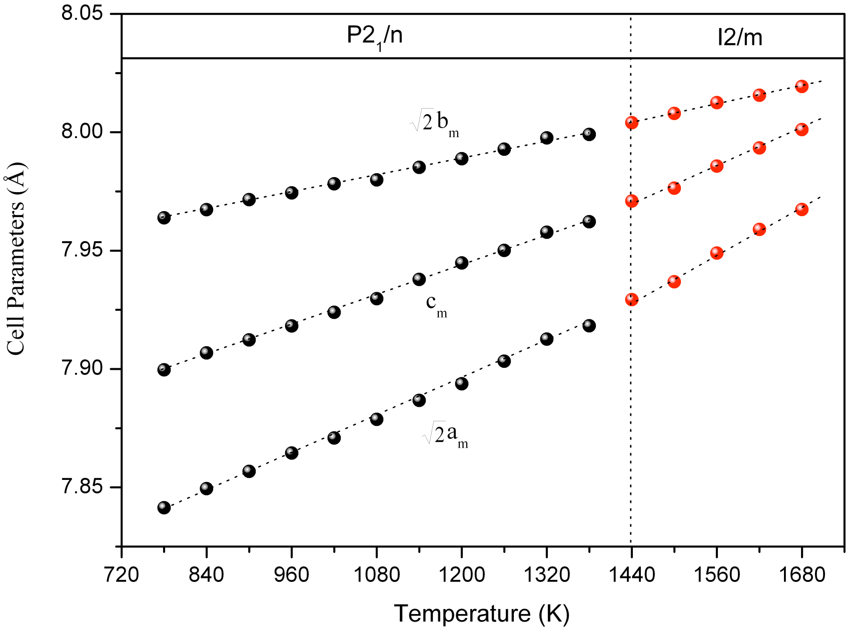

FIGURA 13.13: Variation of the unit cell parameters of Ca_2ScSbO_6 with the temperature. There is a phase transition at about 1440K, changing the symmetry from the primitive monoclinic $P2_1/n$ to the centered monoclinic $I2/m$.

room-temperature phase and the high-temperature $Fm\bar{3}m$ cubic parent phase, as deduced from the NPD data, using the AMPLIMODES program. All the data necessary to understand and to follow the analysis carried out by AMPLIMODES is shown in figure 6(b) and 6(c). We present no temperature evolution of the structure in the low-temperature monoclinic phase. The results of the analysis for the room-temperature phase has been recently published [117]. AMPLIMODES performs all the calculations in the conventional settings of the space groups, so in figure 6, together with the usual settings used for the space groups, we also show the conventional ones.

The analysis is made in the same manner as the experimental data are taken: starting from the low-temperature phase ($I2/m$, at 430K) and increasing the temperature ending up in the cubic phase. Although the (reduced) phase-transition sequence is $I2/m - I4/m - Fm\bar{3}m$, both low-lying phases will have the same parent phase as the reference. This implies that the reference phase for the monoclinic will not be the tetragonal, even if the experiment shows that the later lies between the former and the parent phase.

Nevertheless, due to experimental limitations related to the time-interval expended at each temperature at which data were collected, we did not reach the high-temperature cubic phase. In any case, as mentioned before in relation to the character of the parent phase, this fact does not limit at all the analysis, although, we will not be able to present a complete set of points ending at the high-temperature phase, even if the last measured temperature should correspond to the cubic phase. In a recent work [108], we also observed a similar shift between the phase-transition temperatures observed by XRPD and by NPD, but in that case we collected data quite inside the cubic phase. In the XRPD measurements we used the Bragg-Brentano geometry (flat sample) and in the NPD measurements bulky samples have to be used, as a routine. Our interpretation is that the bulk of the sample (NPD) had no time to transform completely, which means that, effectively, there is a temperature shift: the temperature values shown in figure 9 are the ones corresponding to the selected set points, but do not correspond to the sample-bulk temperature. Finally, there is a temperature difference between the temperature associated to the phase transition as deduced from the XRPD (TXRDP) and NPD (TNPD=TXRDP +30) data.

There are four irreps of the $Fm\bar{3}m$ space group (the fifth irrep, GM^{1+}, is the totally symmetric) that can take part in the symmetry breaking from that space group to the room-temperature $I2/m$ monoclinic space group: GM^{3+}(1), GM^{4+}(1) and GM^{5+}(4). It is worth noting that the output of SYMMODES [119] for the $Fm\bar{3}m$ to $I2/m$ symmetry braking is contained in the $Fm\bar{3}m$ to $P2_1/n$ symmetry breaking, as indicated in figure 6(b) by them blue color. Nevertheless, for this symmetry break, as there are two irreps, i.e. GM^{4+} and GM^{5+}, that break the symmetry down to $I2/m$, there are two possible primary order parameters. The final refinement results for the amplitude values of the modes involved in this symmetry break, shown in figure 6(b), indicate that from the possible two primary order parameters, in fact there is only one, GM^{4+}, whose amplitude is, as in the previous analysis, at least one order of magnitude greater than the rest of the amplitudes. The polarization vector associated with GM^{4+}, going down to $P2_1/n$ or going down just to $I2/m$ is the same, and it involves all the oxygen atoms in the monoclinic phases (three distinct in $P2_1/n$, and two distinct in $I2/m$). GM^{4+} is essentially a rotation of the octahedra around the b axis in the monoclinic cell; although it also deforms a little bit the octahedra: the amount of rotation of the oxygens in the *ab* plane, $(\approx 0.25, \approx 0.25, \approx 0)$ set of coordinates, and the one above and perpendicular to that plane, $(\approx 0, \approx 0, \approx 0.25)$ set of coordinates, are not the same. In figure 8(a) the red arrows indicate the polarization vector of the transforming according to the GM^{4+} irrep.

We have refined NPD data at 430K using the symmetry-adapted modes, FullAmplimodes, and the result for the final amplitudes of the (global) modes corresponding to the four irreps is shown in figure 6 (low-lying middle panel). According to those values, the totally symmetric irrep, has a very low value, which physically means (see above) that there is a small strain between the cubic cell and the monoclinic one. Amongst those irreps, GM^{4+} and GM^{5+} correspond to primary modes, in other words, they both (could) lower the cubic symmetry down to the monoclinic. But from the their amplitude values, it is clear that only GM^{4+} is responsible for the symmetry break, as its value is one order of magnitude bigger than the one corresponding to GM^{5+}. This mode involves only coordinates of the oxygens, as is represented in figure 7b; and the displacements shown in the mode pattern can be interpreted as tilts of the octahedra. The GM^{3+} symmetry mode is irrelevant for this phase transition: its amplitude values is two orders of magnitude lower than the primary mode one.

In the tetragonal ($I4/m$) to cubic ($Fm\bar{3}m$) phase transition there are two unidimensional modes (as in the previous cases, the third irrep, GM^{1+}, is the totally symmetric), all of them involving oxygens atoms at located at the 24e Wyckoff positions of the prototype cubic phase: $GM^{3+}(1)$ and $GM^{4+}(1)$. The GM^{3+} mode is responsible for the breaking of the symmetry to the $I4/mmm$ tetragonal space group (intermediate between the $Fm\bar{3}m$ and the $I4/m$, observed experimentally at high and low temperature, respectively). This mode involves the movements of all the oxygen atoms in the octahedra, in a way that the oxygens located in the (00z) positions move to the center of the octahedra; and the oxygen atoms located in the xy plane move outwards along the diagonals of the basal plane of the octahedra. On the other hand, the mode GM^{4+} is responsible for the breaking of the symmetry down to the $I4/m$ space group, and involves movements only of the oxygens located in the xy plane. We have refined NPD data at 590K using the symmetry-adapted modes, FullAmplimodes, and the result for the final amplitudes of the (global) modes corresponding to the four irreps is shown in figure 6(c) (low-lying right panel). It can be readily appreciated that the GM^{4+} mode amplitude is considerable and shows a clear evolution with temperature: diminishes as temperature increases, and at the transition temperature (660K) it reaches its lowest (non null) value. The amplitude of the other modes, the totally symmetric one (GM^{1+}) and GM^{3+} are negligible, of the order of magnitude of the error in the data. In relation to these high-temperature data, we had difficulties when we collected them, and in the case of the last two points shown in the figure we spent half the time as spent in the other points. This fact implied that the statistics of these diffractograms were different to the others. As a result, we had difficulties when refining all the diffractograms in a cyclic way using FullProf, so we decided to fix the amplitudes of GM^{1+} and GM^{3+} modes, and we only refined the amplitude of the primary mode. In this sense, the values for the non-primary modes in figure 14 in the tetragonal phase are fictitious. As mentioned before, in a previous work [108], we have obtained the same behavior; although, this time we have not enough data to see the complete disappearance of the primary mode associated to the tetragonal-to-cubic transition. As we mentioned in that work, this is the typical behavior of the primary order parameter of a continuous phase transition: continuous decreasing and a smooth change to zero at the critical temperature.

Indeed, in the same figure, in the right axis, we have plotted the evolution of the angle of rotation of the octahedra around the tetragonal axis (the only distortion allowed by symmetry in the $I4/m$ tetragonal phase, a0a0c- tilt system), and the angle of rotation of the octahedra around the [110] direction in the monoclinic phase (this direction coincides with the $[010]_p$ (figure 4) of the simple perovskite): this angle is the only distortion allowed in the monoclinic phase, $I2/m$ $a^0b^-b^-$ tilt system; in fact, by symmetry, the same distortion has to be present along the $[100]_p$ direction. The matching of the angle of rotation and the amplitude of the primary modes is perfect, in both phases, indicating that they are proportional (proportionality constants are approximately equal, 19.7) and, thus, showing that the rotation of the octahedra around the tetragonal and [110] monoclinic axis are the primary order parameters associated to the tetragonal-to-cubic and to the tetragonal-to-monoclinic phase transitions, respectively.

It is worth noting that despite the fact that the irreps of the primary modes lowering successively the symmetry from the cubic to the monoclinic ($I2/m$) are the same, and in both cases involve only oxygen atoms, and in both cases, as well, can be interpreted as tilts of the octahedra, the cubic-to-tetragonal phase transition is continuous, and the tetragonal-to-monoclinic is discontinuous. The discontinuous character of the last transition is related to the relative orientation of both space groups: $I2/m$ is a subgroup of $I4/m$, but when the two-fold axis is located in the same direction as the four-fold one. There is no way to go in a continuous manner from the tetragonal to the monoclinic symmetry when the two-fold axis is perpendicular to the four-fold axis, as it is the case in the tetragonal-to-monoclinic phase transition, as shown in figure 3.

Another interesting remark is that the amplitudes of the primary modes and of the non-primary modes vary in the same temperature interval, as shown in figure 14, but the formers show a trend in their variation, as expected, and the later show a chaotic variation: no trend at all (same of them are very close to zero). Moreover, the sigmas corresponding to the primary modes are one order of magnitude smaller than the ones of the non-primaries.

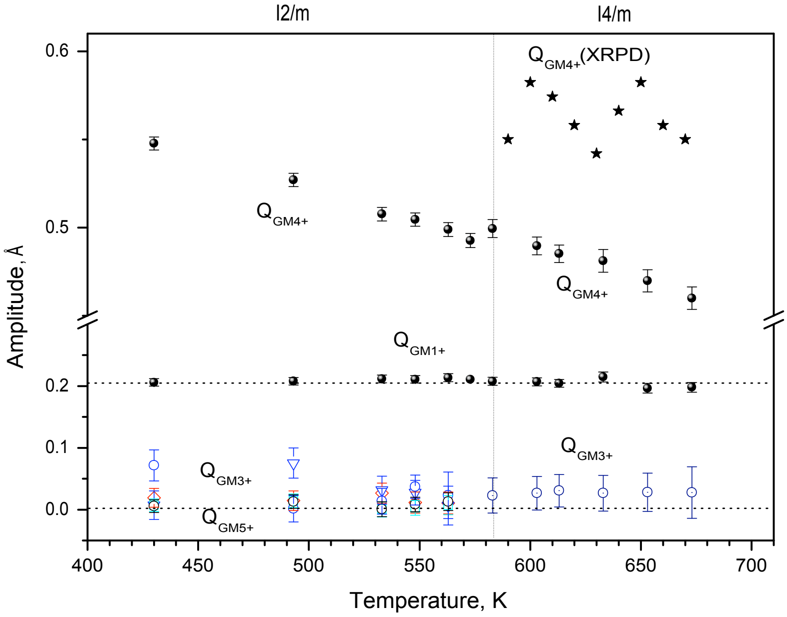

FIGURA 13.14: The temperature evolution of the amplitudes of the GM^{1+}, GM^{3+}, GM^{4+} and GM^{5+} modes, as obtained from refinement of the NPD data of Sr_2ScSbO_6, in comparison to the results obtained from XRPD data (stars). The temperature at which the monoclinic structure disappears is 585K.

13.4. Conclusions

The objective of this investigation is to determine the crystal structures and phase transitions with temperature of the two ordered double perovskite oxides Sr_2ScSbO_6 and Ca_2ScSbO_6. The crystal structures at room temperature of both compounds are determined for the first time and are refined in monoclinic space group $P2_1/n$ with a=5.6914(1)Å; b=5.6776(1)Å; c=8.0242 (1)Å and β=90.03(1)° for Sr containing compound and with a=5.5088(1)Å; b=5.6226(1)Å; c=7.8601(1)Å; β=90.02(1)° for Ca containing compound. Three phase transitions with temperature are observed in Sr_2ScSbO_6: $P2_1/n \rightarrow I2/m \rightarrow I4/m \rightarrow Fm\bar{3}m$, at about 400, 560 and 650K, respectively. The large distortion of Ca_2ScSbO_6 at room temperature leads to a higher temperature phase transition from $P2_1/n$ to $I2/m$ at about 1440K. This fact, it was not possible to observe the others phase transitions to the higher symmetries due to the instrument limitations.

Capítulo 14

A study of the crystal structures and the phase transitions of Sr_2FeSbO_6, $SrCaFeSbO_6$ and Ca_2FeSbO_6 double perovskite oxides

14.1. Introduction

In recent works, we have reported the room-temperature crystal structures and the possible phase transitions at low- and high-temperature of Sr_2MSbO_6 (M=Al,Co,Cr,Sc,Sm,La) and Ca_2ScSbO_6 [105, 108, 109, 110] members of the antimony double perovskite family. In the present work we report the synthesis, room-temperature crystal structure determination and phase transitions at low- and high-temperature of other three members of this family Sr_2FeSbO_6, $SrCaFeSbO_6$ and Ca_2FeSbO_6. To the best of our knowledge, no study has been carried out on the possible temperature induced phases transitions, or low- and high-temperature phases, of Sr_2FeSbO_6, Ca_2FeSbO_6 and of the new compound $SrCaFeSbO_6$.

Syntheses of Sr_2FeSbO_6 have been reported on several occasions; in table 1 we have summarized the available results from previous works to compare with our results. The first preparation of this compound was reported in [87], it was reported to have a cubic unit cell. According to [80, 120], the room-temperature structure of Sr_2FeSbO_6 was found to be of an ordered perovskite type, with the monoclinic $P2_1/n$ (No. 14, non-standard setting) space group; however, no structural determination was performed. The first structural determination, on the basis of neutron powder diffrac-

TABLA 14.1: Structural details of Sr_2FeSbO_6 and Ca_2FeSbO_6 compounds at room temperature. The data shown are as follows: space group, lattice constance and degree of ordering. 'PW' stands for present work.

Compound	Space group	a (Å)	b (Å)	c (Å)	β (°)	Degree of ordering (%)	Ref.
Sr_2FeSbO_6	Cubic	7.90					[87]
	$P2_1/n$	5.1635(2)	5.5954(2)	7.9001(2)	89.99(1)	84	[120]
	$P2_1/n$	5.6132(5)	5.5973(5)	7.9036(7)	90.01(1)	79.5	[80]
	$P2_1/n$	5.594(1)	5.571(1)	7.926(2)	90.09(0)	80	[81]
	$I2/m$	5.6163(1)	5.5959(1)	7.8994(2)	89.98(1)	89	[PW]
Ca_2FeSbO_6	Orthorhombic	5.54	5.47	7.74			[87]
	$P2_1/n$	5.5283(2)	5.4389(2)	7.7358(3)	90.00(2)		[120]
	$P2_1/n$	5.4389(1)	5.5380(1)	7.7403(1)	90.06(2)	93.4	[PW]

tion measurements, of this material was reported in [81]. The room-temperature crystal structure of this material was assigned the $P2_1/n$ space group, as in the previous work. But, examination of the reported diffraction profiles did not showed evidence for any reflection corresponding to primitive cell. This was the motivation to re-examine the room-temperature structure of this material, as another member of the antimony family we have been studying during the last years.

The first synthesis of Ca_2FeSbO_6 was reported in [87, 120]. In the first work, it was described as an orthorhombic structure, but without assigning the space group; and in the second work, the structure was described as monoclinic with the $P2_1/n$ space group, but the crystal structure was not determined.

14.2. Sr_2FeSbO_6

The room-temperature powder diffraction data of Sr_2FeSbO_6 obtained by X-ray and neutron diffraction are shown in figures 1a and 1b, respectively. As mentioned, the monoclinic $P2_1/n$ space group was assigned to this compound, but we could not observe the primitive Bragg reflections in our patterns. In the insets of Fig. 1 their expected positions are marked with arrows, making apparent the absence of such reflections, although the monoclinic splitting seemed to be clear. These facts, together with the the space-group assignation reported in [108], allow us to conclude that the correct space-group symmetry for Sr_2FeSbO_6 at room-temperature is $I2/m$.

The structure was refined, from neutron and X-Ray data, in space group $I2/m$, with the following atomic positions: Sb1/Fe2 at 2d(0,0,1/2); Fe1/Sb2 at 2a(0,0,0); Sr, O1 at 4i(x,0,z) and O2 at 8j(x,y,z). Details of the final refinement and atomic parameters are given in Table 2. The obtained unit cell parameters $a = 5.6134(1)$ Å; $b = 5.5935(1)$ Å; $c = 7.8976(2)$ Å and $\beta = 89.98(1)°$ are very similar to the unit cell parameters obtained in previous works, except for the very small value of the $a = 5.1635$ Å parameter given in [120], which may be due to a typing error. Due to the charge and the small difference in the ionic radii of the Fe^{3+} ($r = 0.645$ Å) and Sb^{5+} ($r = 0.60$ Å) [3], antisite disorder on Fe and Sb cations is observed. Our refinement results show that the degree of order in Sr_2FeSbO_6 sample is 89 %, a bit bigger than the order obtained in previous studies. This difference is expected to be due to the synthesis conditions: the high temperature of preparation, 1770K in our case, can increase the order.

Although Sr_2FeSbO_6 has been studied at low temperature to analyze the magnetic properties [80], no structural phase transition has been reported and, besides, this is the first time that the temperature-induced structural phase-transitions at high temperature are reported for this compound.

Hence, to search for the high-temperature phase transitions in our sample, we analyzed the two narrow 2θ intervals shown in Fig. 2: 101-103.5° and 110-113° corresponding to the (800) and (660) cubic ($Fm\bar{3}m$) reflections, respectively. These reflections have been identified as especially sensitive to the structural changes occurring in this material. As it can be concluded from the Fig. 2, Sr_2FeSbO_6 undergoes two successive temperature-induced phase transitions taking place approximately at 430 and 540K. At 430K we observed the appearance of a shoulder on the low angle side of the peak (Fig. 2a), this change is very similar to that observed in Sr_2CrSbO_6. The reflections shown in this figure are (440) and (008) in both space groups, $I2/m$ and $I4/m$, but as they are interchanged in position, the transition is obvious (see Figure 5, middle column, panels b and c [108]). This change was interpreted as an evidence for the first phase transition from monoclinic $I2/m$ to tetragonal $I4/m$. In Fig. 2b the continuous character of the second phase transition is even more easily appreciated: at low temperatures the reflection shown is composed by a triplet (due to the monoclinic distortion); this triplet merges into a single reflection above 540K, indicating the disappearance of this distortion, and the structure transforms, as expected, to the cubic prototype space group: $Fm\bar{3}m$. The analysis of the diffraction data in the temperature range from 430 to 530K shows that this phase is tetragonal, with body centred unit cell. The structural refinement at 430K with $I4/m$ space group has given good results (see Table 3).

The attempt to refine the diffraction pattern collected at 410K using a structural model with $I2/m$ and $I4/m$ space groups, separately, cannot reproduce the splitting observed at 2θ=107°, as we can see in Fig. 4a and 4c. These problems were successfully solved by performing a refinement based on the two symmetries. This material shows a two phase co-existance, (40 %) of $I2/m$ and (60 %) of $I2/m$, in the 400 to 420K temperature interval.

To clarify the structural changes occurring in Sr_2FeSbO_6 at low temperatures, high resolution diffraction measurements using neutron diffraction, D2B (ILL, Grenoble), were performed at low temperatures, 50, 100, 150, 200K (and also at high temperatures 300, 380, 410 and 440K, just for completeness). The temperature dependence of the structural parameters obtained from the Rietveld refinements are given in Table 3. The patterns obtained at 50K and 100K show the appearance of the primitive Bragg peaks, as we can see in Figure 3. This fact means that the material undergoes a continuous phase transition at about 100K from centred monoclinic space group $I2/m$ to primitive

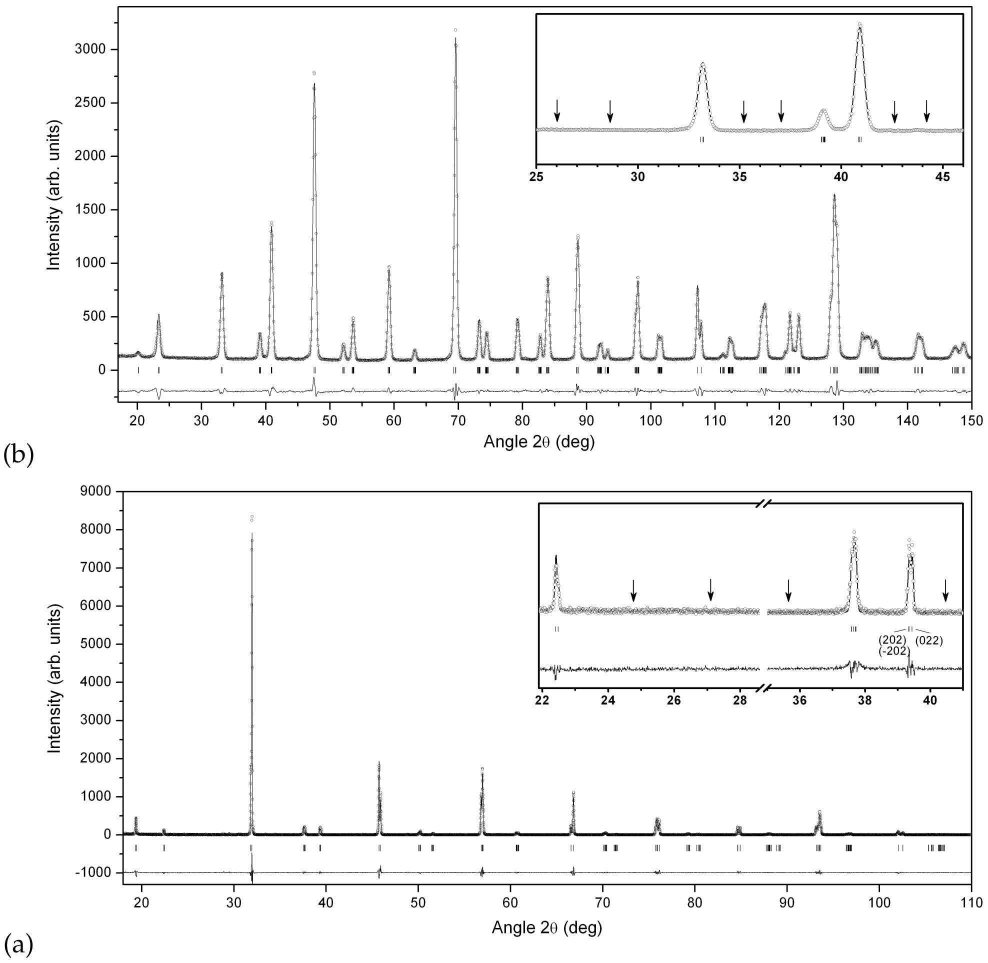

FIGURA 14.1: Experimental (symbols) and calculated (line) neutron profiles (top) and X-ray profiles (bottom) for the Rietveld refinement of Sr$_2$FeSbO$_6$ at room temperature using a structural model with $I2/m$ space group. Insets shows in detail the absence of the primitive bragg peak reflections with $h + k + \ell = 2n + 1$, their positions indicated by arrows, corresponding to the $P2_1/n$ symmetry.

TABLA 14.2: Crystal structure data and refinement results for Sr_2FeSbO_6, $SrCaFeSbO_6$ and Ca_2FeSbO_6 at room temperature determined using X-ray and neutron diffraction data.

Compound	Sr_2FeSbO_6	$SrCaFeSbO_6$	Ca_2FeSbO_6
Space group	$I2/m$	$P2_1/n$	$P2_1/n$
A	4i (x,0,z)	4e (x,y,z)	4e (x,y,z)
x	0.5003(1)	0.0029(4)	0.0096(8)
y	0	0.0202(3)	0.0435(3)
z	0.2541(8)	0.2516(2)	0.2495(3)
B (Å^2)	0.45(2)	0.81(3)	0.42(4)
Sb1/Fe2	2d (0,0,1/2)	2c (0,1/2,0)	2c (0,1/2,0)
B (Å^2)	0.10(1)	0.31(1)	0.07(1)
Fe1/Sb2	2a (0,0,0)	2d (1/2,0,0)	2d (1/2,0,0)
B (Å^2)	0.10(1)	0.56(6)	0.37(5)
Occupancy	0.89(1)/0.11(1)	0.94(1)/0.06(1)	0.94(1)/0.06(1)
O1	4i (x,0,z)	4e (x,y,z)	4e (x,y,z)
x	0.5003(1)	0.2793(3)	0.2955(2)
y	0	0.2712(6)	0.2964(2)
z	0.2541(8)	0.0520(4)	0.0449(5)
B (Å^2)	0.57(2)	0.88(9)	0.78(1)
O2	8j (x,y,z)	4e (x,y,z)	4e (x,y,z)
x	0.2492(3)	0.2735(2)	0.2961(2)
y	0.2560(1)	0.2910(8)	0.2913(2)
z	0.0211(2)	0.4875(5)	0.4516(5)
B (Å^2)	0.57(2)	0.88(9)	0.78(1)
O3		4e (x,y,z)	4e (x,y,z)
x		0.9444(8)	0.9102(2)
y		0.4875(5)	0.4764(1)
z		0.2352(3)	0.2516(1)
B (Å^2)		0.88(9)	0.78(1)
Cell parameters			
a (Å)	5.6163(1)	5.5384(4)	5.4389(1)
b (Å)	5.5959(1)	5.5499(3)	5.5380(1)
c (Å)	7.8994(1)	7.8447(5)	7.7403(1)
β (°)	89.99(1)	90.08(1)	89.94(1)
V (Å^3)	248.26(1)	241.11(1)	233.14(1)
Reliability factors	neutron/X-ray	X-ray	X-ray
R_p(%)	3.89/11.7	8.71	8.70
R_{wp}(%)	4.99/22.4	14.3	13.1
R_{exp}(%)	6.95/16.34	10.13	9.35
χ^2	0.51/1.87	1.98	1.96

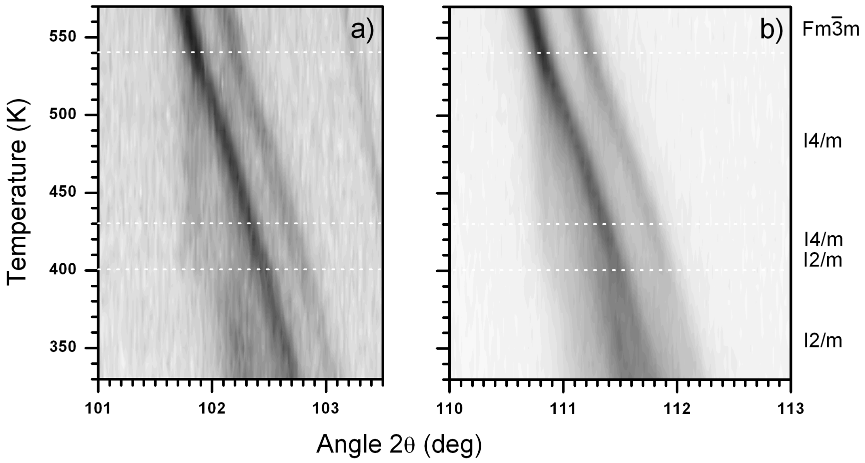

FIGURA 14.2: Temperature evolution of the (a)(800) and (b)(660) cubic reflections of Sr_2FeSbO_6 as obtained from XRPD experiments. The scattered intensity is represented in gray scale, where black (white) corresponds to high (low) intensity. In (a), two monoclinic reflections maintain as two tetragonal but with the positions interchanged, and, eventually, the tetragonal splitting disappears and the double reflection evolves to a single cubic one. (b) Temperature evolution of the (660) cubic reflections: the tetragonal splitting existing in the temperature range from 430K to about 540K can be observed.

monoclinic space group $P2_1/n$.

Thus, the structural analysis of Sr_2FeSbO_6 suggests that there is a tree phase transitions at low- and high-temperatures following the $P2_1/n$ - $I2/m$ - $I4/m$ - $Fm\bar{3}m$ phase-transition sequence. This phase transition sequence was previously reported for other member of the antimony family Sr_2ScSbO_6. Evolution of the refined lattice parameters and space group symmetries, are shown in Fig. 5.

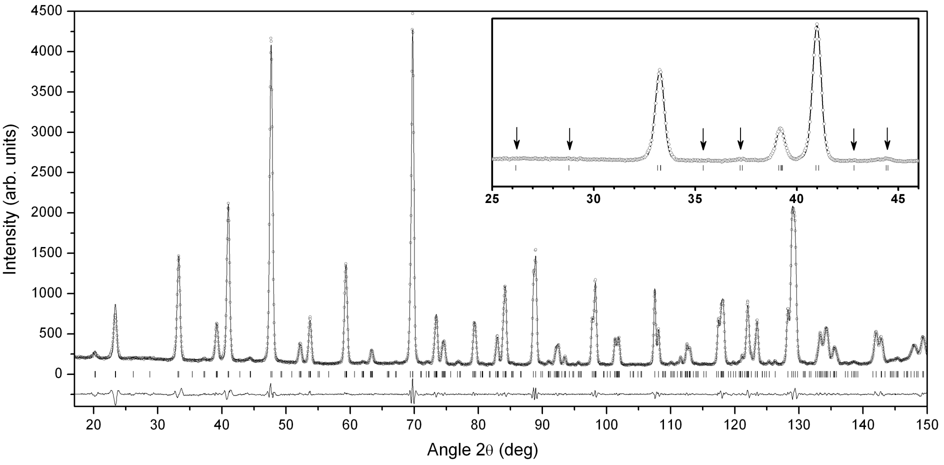

FIGURA 14.3: Observed NPD patterns (symbols), calculated (line) and difference profiles for the Rietveld refinement of Sr_2FeSbO_6 at 100K, using a structural model with $P2_1/n$ space group. Inset shows in detail the presence of the primitive bragg peak reflections with $h + k + \ell = 2n + 1$, their positions indicated by arrows, corresponding to the $P2_1/n$ symmetry.

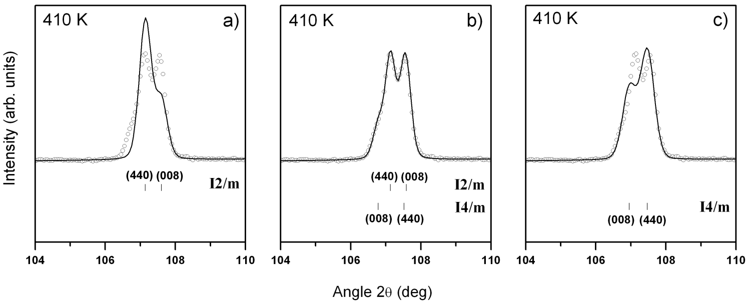

FIGURA 14.4: Experimental diffraction data for Sr_2FeSbO_6 at 410K (symbols) compared with the diffraction patterns calculated after refinement (lines) using structural models with symmetries $I2/m$ (a), $I4/m$ (c) and both symmetries (b). The mixture of the two symmetries reproduces correctly the splitting observed in the experiment.

TABLA 14.3: Crystal structure data and refinement results for Sr_2FeSbO_6 at different temperatures determined using neutron diffraction data.

Temperatures		50K	100K	150K	200K	380K	410K		440K
Space group		$P2_1/n$	$P2_1/n$	$I2/m$	$I2/m$	$I2/m$	$I2/m$(40 %)	$I4/m$(60 %)	$I4/m$
Sr	x	0.0004(4)	0.0005(4)	0.4982(4)	0.4997(4)	0.5006(6)	0.4979(3)	0	0
	y	0.0049(9)	0.0025(3)	0	0	0	0	1/2	1/2
	z	0.2485(2)	0.2492(2)	0.2509(2)	0.2503(2)	0.2519(3)	0.2484(5)	1/4	1/4
	B (Å^2)	0.62(2)	0.66(2)	0.69(1)	0.76(1)	1.11(1)	1.22(2)	1.14(2)	1.21(2)
Sb1/Fe2		2c(0,1/2,0)	2c(0,1/2,0)	2d(0,0,1/2)	2d(0,0,1/2)	2d(0,0,1/2)	2d(0,0,1/2)	2d(0,0,1/2)	2d(0,0,1/2)
	B (Å^2)	0.41(1)	0.38(2)	0.36(1)	0.42(1)	0.54(1)	0.60(1)	0.63(2)	0.63(1)
Fe1/Sb2		2d(1/2,0,0)	2d(1/2,0,0)	2a(0,0,0)	2a(0,0,0)	2a(0,0,0)	2a(0,0,0)	2a(0,0,0)	2a(0,0,0)
	B (Å^2)	0.41(1)	0.38(2)	0.36(1)	0.42(1)	0.54(1)	0.60(1)	0.63(2)	0.63(1)
O1	x	0.2631(9)	0.2620(1)	-0.0456(3)	-0.0445(3)	-0.0391(4)	-0.0541(7)	0	0
	y	0.2654(9)	0.2631(9)	0	0	0	0	0	0
	z	0.0216(8)	0.0228(1)	0.2481(9)	0.2525(8)	0.2489(9)	0.2492(9)	0.2555(7)	0.2532(7)
	B (Å^2)	0.71(1)	0.69(1)	0.74(2)	0.81(1)	1.23(2)	1.31(1)	1.31(2)	1.39(1)
O2	x	0.2574(1)	0.2566(2)	0.2492(3)	0.2509(8)	0.2539(9)	0.2410(4)	0.2749(2)	0.2750(5)
	y	0.2533(9)	0.2527(9)	0.2560(1)	0.2446(7)	0.2465(8)	0.2593(6)	0.2235(5)	0.2254(5)
	z	0.4754(9)	0.4766(9)	0.0211(2)	0.0221(1)	0.0192(2)	0.0184(3)	0	0
	B (Å^2)	0.71(1)	0.69(1)	0.74(2)	0.81(1)	1.23(2)	1.31(1)	1.31(2)	1.39(1)
O3	x	0.9549(4)	0.9547(3)						
	y	0.4986(2)	0.4983(5)						
	z	0.2492(2)	0.2493(2)						
	B (Å^2)	0.71(1)	0.69(1)						
Cell parameters	a (Å)	5.6107(1)	5.6120(1)	5.6142(1)	5.6152(1)	5.6181(1)	5.6191(2)	5.5994(1)	5.5995(1)
	b (Å)	5.5846(1)	5.5860(1)	5.5883(1)	5.5908(1)	5.6014(1)	5.6032(2)		
	c (Å)	7.8867(1)	7.8870(5)	7.8872(1)	7.8902(1)	7.9094(1)	7.9120(2)	7.9448(1)	7.9545(1)
	β (°)	89.98(1)	90.01(1)	89.99(1)	89.99(1)	89.99(1)	90.01(1)		
	V (Å^3)	247.12(1)	247.24(1)	247.46(1)	247.70(1)	248.90(1)	249.10(1)	249.10(1)	249.41(1)
Reliability factors	R_p (%)	3.89	3.74	3.91	3.99	3.83	4.42	4.42	3.99
	R_{wp} (%)	5.04	4.85	5.09	5.40	5.11	6.16	6.16	5.42
	R_{exp} (%)	5.91	5.92	5.96	5.99	5.87	5.89	5.89	5.87
	χ^2	0.73	0.67	0.72	0.81	0.76	1.10	1.10	0.85

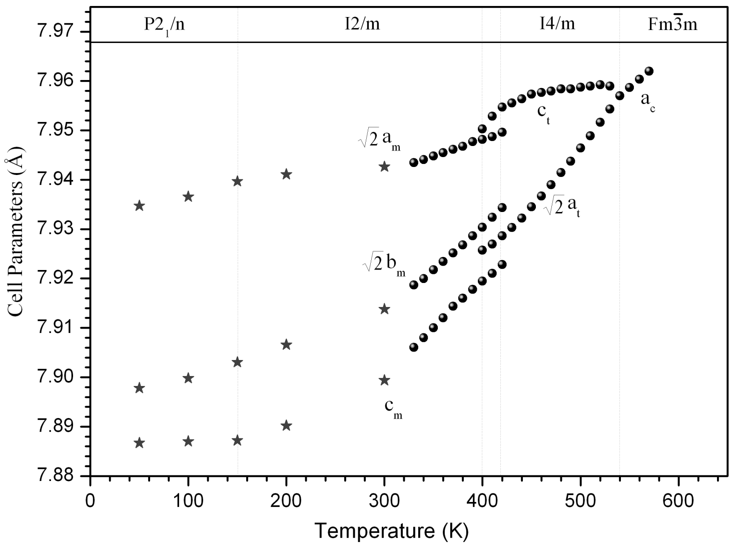

FIGURA 14.5: Variation of the lattice parameters of Sr_2FeSbO_6 with the temperature. The high temperature structure of this compound is cubic. Below 540K it transforms to tetragonal. There is another phase transition at about 420K, changing the symmetry from tetragonal to monoclinic with coexistence of both symmetries between 400 and 420K.

14.3. SrCaFeSbO$_6$

The diffraction pattern collected for $SrCaFeSbO_6$ at room temperature is shown in Fig. 6. The splitting of the diffraction lines is not clear and it can seen the presence of superstructure reflections arising from the presence of rock salt type ordering between B-site cations. In the same way, we observe the presence of the primitive Bragg peak. Due to all that, the refinements of the XRPD data were undertaken using all possible space groups for double perovskite generated by tilting of the octahedra in combination with 1:1 cation ordering $Pnnn$, $Pn\bar{3}$, $P4_2/nnm$, $P4/mnc$, $P4_2/n$ and $P2_1/n$. The four first space groups cannot describe the reflections characteristic of A-cation displacements observed in our experimental diffraction data. As result only $P4_2/n$ and $P2_1/n$ have been tested in our refinements. The results of Rietveld refinements of X-ray diffraction pattern data are shown in Fig. 6. It is obvious that the $P4_2/n$ cannot reproduce correctly the splitting of the (222) cubic reflection observed in the experimental diffraction data at about 2θ=39.8°. Also, the model based on the $P4_2/n$ space group gives poor R-factors: $R_p = 10.1\,\%$; $R_{wp} = 16.5\,\%$; $R_{exp} = 9.73\,\%$; $\chi^2 = 2.86$, in comparison with those obtained using the $P2_1/n$ model: $R_p = 8.71\,\%$; $R_{wp} = 14.3\,\%$; $R_{exp} = 10.13\,\%$; $\chi^2 = 1.98$. Based on these facts, we suggest that the room temperature structure of $SrCaFeSbO_6$ is better described in a $P2_1/n$ primitive monoclinic space group, with unit-cell $a = 5.5384(4)$ Å; $b = 5.5499(3)$ Å; $c = 7.8447(5)$ Å; β=90.08(1)°. The results of the refinements are given in Table 2. The obtained cell parameters are very close to each other and $\sqrt{2}a \simeq c$, which is

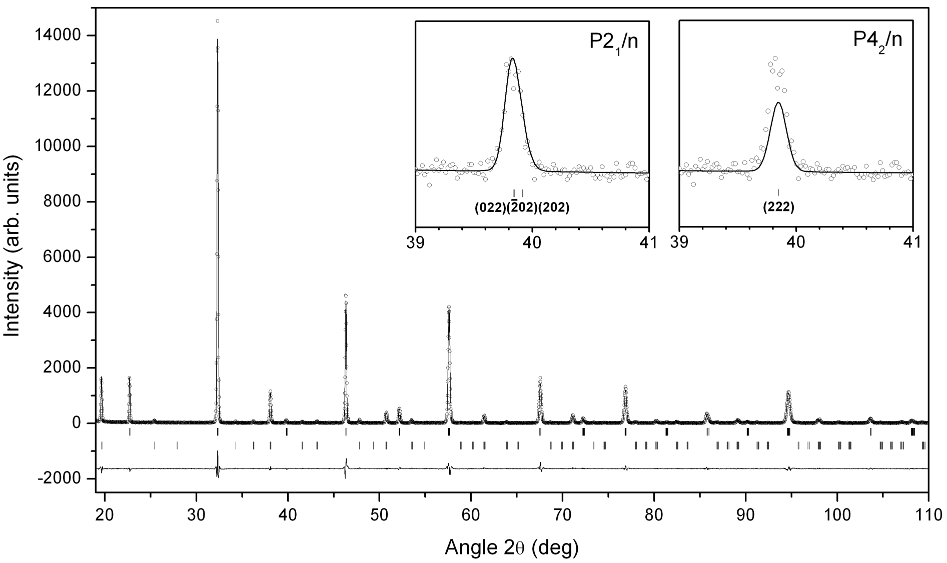

FIGURA 14.6: Experimental (symbols) and calculated (line) X-ray powder diffraction profiles for the Rietveld refinement of SrCaFeSbO$_6$ at room temperature using a structural model with $P2_1/n$ space group. The bars in the lower part of the graphics represent the Bragg peak positions. The upper set of bars correspond to the simple perovskite structure (sub-cell) and the lower set of bars gives the positions of peaks arising from the presence of the B-site cation ordering (super cell). Insets show a section of the diffractogram comparing the results of the refinement using the $P2_1/n$ and $P4_2/n$ space groups. The structural model in $P2_1/n$ fits better the peaks intensity.

an indication of a high degree of pseudo-tetragonal character of the metric, but the distortion angle β was found different to 90°. The refinement results show that the degree of ordering between the Fe and Sb cations in SrCaFeSbO$_6$ sample is 94 %.

To study the temperature induced phase-transitions, several patterns were collected from room temperature to 1270K using laboratory X-Rays. Unfortunately, due to pseudosymmetry observed at room temperature, the small difference between the cell parameters and the resolution limited instrument, it was not possible to determine the phase transitions in this compound.

14.4. Ca$_2$FeSbO$_6$

The Rietveld refinement of X-ray diffraction pattern data of Ca$_2$FeSbO$_6$ recorded at room temperature is shown in Fig. 7. All diffraction lines are indexed based on a monoclinic model with the $P2_1/n$ space group, and unit-cell parameters: $a = 5.4389(1)$ Å; $b = 5.5380(1)$ Å; $c = 7.7403(1)$ Å; β=90.06(2)°. A very clear splitting of all peaks is observed, including the peaks at low angles, as

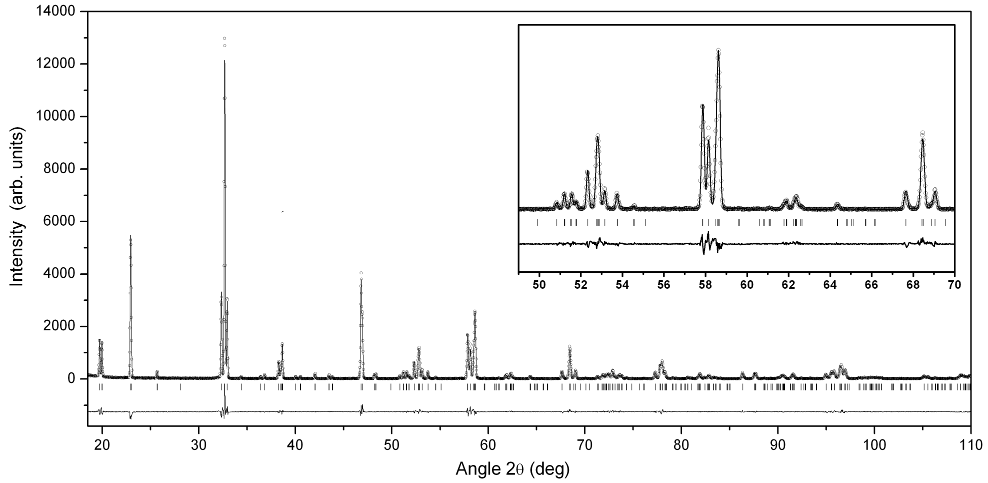

FIGURA 14.7: Observed X-ray patterns (symbols), calculated (line) and difference profiles for the Rietveld refinement of Ca_2FeSbO_6 at room temperature using a structural model with $P2_1/n$ space group.

the (111) cubic reflection, at about 2θ=20°: two monoclinic peaks (011) and (101/$\bar{1}$01) are clearly observed. Table 2 lists the final atomic parameters, cell parameters, isotropic atomic displacement parameters, occupations and reliability factors.

Refinement of the anti-site degree level (Fe at Sb sites, and vice versa) allowed us to evaluate the degree of long-range ordering to be 94 %, the same value obtained for $SrCaFeSbO_6$. Worth noticing is the high order obtained in this material in comparison to that of the strontium compound Sr_2FeSbO_6. This result means that there is an effect of the A cation on the order of Fe and Sb cations in the B-sites. Under carefully controlled synthesis conditions, anti-site disorder can be reduced by using the highest possible temperature. In the preparation of these samples, we have used the same thermal treatments, although the ordering degree obtained is very different. One of the possible reasons for that could be the thermal conductivity of the A-site cations: thermal conductivity of calcium (190 $W{\cdot}m^{-1}K^{-1}$) is very high in comparison to that of strontium (49 $W{\cdot}m^{-1}K^{-1}$) [121]. The high conductivity of Ca could reduce the temperature gradient within the crucible and the temperature of the bulk in the crucible would be better homogenized. In this way the effective formation temperature would be higher, facilitating the ordering of the B-site cations.

To determine the presence of phase transitions and evolution of unit cell parameters with temperature, X-ray data were collected in 2θ from 15 to 120°, between ambient temperature and 1470K, with a temperature step 10K. After examination of all patterns, we observed no disappearance of diffraction peaks corresponding to primitive Bragg reflections with indices of type ($hk\ell$) with $h + k + \ell = 2n + 1$, in the whole temperature range. This shows that primitive unit-cell is preserved, at least, up to the measured temperature. Moreover, the splitting of the reflections is

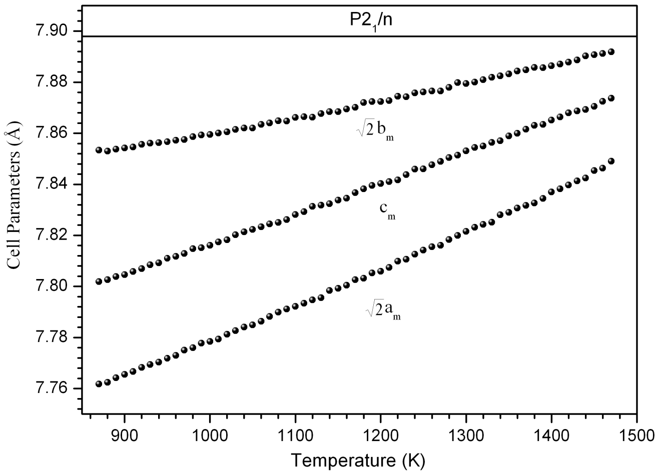

FIGURA 14.8: Variation of the lattice parameters of Ca_2FeSbO_6 with the temperature. The lattice parameters increase with temperature, and we observe the same decreasing of the difference between $\sqrt{2}a$, $\sqrt{2}b$ and c parameters, but no anomalous change is noted.

also maintained in the whole temperature range measured, which shows that no cubic phase is produced. Hence, it becomes clear that at 1470K the unit cell is monoclinic. The experimental data show that the structure of Ca_2FeSbO_6 does not change significantly between ambient temperature and 1470K, and that there with temperature for Ca_2FeSbO_6 from 830K to 1470K are shown in figure 8. As seen Fig. 8, the lattice parameters increase with temperature; at the same time, we observe a decreasing of the difference between $\sqrt{2}a$, $\sqrt{2}b$ and c parameters; but, no anomalous change is noted.

14.5. Conclusions

Samples of Sr_2FeSbO_6, $SrCaFeSbO_6$ and Ca_2FeSbO_6 were synthesized and their crystal structure determined from x-ray powder diffraction data using the Rietveld method. At ambient temperature, the crystal structure of Sr_2FeSbO_6 was found to be monoclinic with the space group $I2/m$, which is different from the previously reported $P2_1/n$ space group. For $SrCaFeSbO_6$ and Ca_2FeSbO_6, the crystal structures were determined to be monoclinic with $P2_1/n$ space group. The Sr_2FeSbO_6 presents tree phase transitions the first one is continuous at 540K from $Fm\overline{3}m$ to tetragonal $I4/m$, the second one is discontinuous from $I4/m$ to $I2/m$, with a co-existence of both symmetries between 400 and 420K and the third one is continuous at 100K from $I2/m$ to $P2_1/n$. The experimental data show that the structure of Ca_2FeSbO_6 does not change significantly between ambient temperature and 1470K, and that there is no indication of any phase transitions in this temperature range.

Capítulo 15

A study of the crystal structures and the phase transitions of Sr_2MSbO_6 (M=Al,Co,Cr,Ga,Mn,Fe,Sc,Sm,La) double perovskite oxides

15.1. Introduction

Structural data of previously studied Sr_2MSbO_6 (M=Al,Co,Cr,Ga,Mn,Fe,Sc,Sm,La) double perovskite oxides are summarized in Table 1. All materials were prepared by solid state reaction method with the exception of the Al-containing material for which the sol-gel method was also used [105]. The table shows the synthesis temperatures, ionic radii suggested in [3], the size difference between the M and Sb cations $\Delta r=|r_{M^{+3}} - r_{Sb^{5+}}|$, the degree of ordering between the M^{3+} and Sb^{5+} cations over the B-sites of the perovskite structure, the tolerance factors $t = \frac{(r_{Sr}+r_O)}{\sqrt{2}(\bar{r}_{M,Sb}+r_O)}$ where $\bar{r}_{M,Sb}$ is the averaged ionic radii of the M^{3+} and Sb^{5+} cations in the double perovskite [66], and the reported symmetry at room temperature.

As seen in Table 1, only the Al-containing material of this family has a cubic structure at room temperature and a tolerance factor well above 1. Sr_2CoSbO_6 and Sr_2GaSbO_6 are two materials with tolerance factors very close to 1 and with trigonal and tetragonal asymmetries, respectively. The rest of the materials are monoclinic and with tolerance factors below 1. It seems clear that the reduction of the tolerance factor (as the ionic radius of the M^{3+} cation increases) causes a evolution of the symmetries of the room-temperature structures of the members of this antimony family that can be described by the following phase-transition sequence: $Fm\bar{3}m \rightarrow R\bar{3} \rightarrow I4/m \rightarrow I2/m \rightarrow P2_1/n$. The compounds Sr_2CrSbO_6 and Sr_2MnSbO_6 do not follow the general trend, due to their Jahn-Teller character.

*Prepared by sol-gel method. **No attempt to refine the order- disorder in these papers. ***These results will be published elsewhere.

Syntheses of Sr_2GaSbO_6 have been reported on two occasions. According to [83], the room temperature symmetry of this compound is tetragonal. On the basis of X-ray powder diffraction measurements [82], the $I4/m$ tetragonal space group was assigned to the room-temperature strucutre of this compound. Complete cation ordering of Ga^{3+} and Sb^{5+} was observed in this study. According to it, at high temperature Sr_2GaSbO_6 undergoes a phase transition from $I4/m$ to $Fm\bar{3}m$, at about 723K. There are no previous studies on the low-temperature structural modifications of this material. The size difference between Ga and Sb is 0.020Å. According to table 1, with this difference the gallium compound should be placed in the range where there is partial order between the M and Sb cations over the B sites. To clarify this point and to study the possible phase transitions at low- and high-temperatures, we have decided to re-investigate this compound.

Sr_2MnSbO_6 was extensively studied in the past and its structural, electric and magnetic properties are considered well known [122, 123, 124]. The crystal structure at room temperature has been reported several times [122, 123, 124]. It was found to have the $I4/m$ space group at room temperature. The degree of cation ordering (Mn^{3+} and Sb^{5+}) increases as the temperature of preparation increases (Table 1). There is one phase transition at high temperature observed previously in Sr_2MnSbO_6: it changes the symmetry from tetragonal $I4/m$ to $Fm\bar{3}m$. There is a difference of $\approx$70 K between the reported phase-transition temperature values: 750 and 820K, in works [122] and [124], respectively; and there is also a difference in the cation ordering degree reported in both works: 64 % and 58.6 %, respectively. The origin of the difference of the phase-transition temperatures could be due to the different techniques used in those works. Concerning this compound, the aim of the present study was to analyze the low-temperature range to detect the possible phase transitions; for completeness, we also measured it at high temperatures.

15.2. Results and Discussion

15.3. Sr_2GaSbO_6

To study the room temperature structure and the phase transition at high temperatures, a complete diffraction patterns were obtained (D2B) at different temperatures between room temperature and 800K, with a step of 50K.

TABLA 15.1: Structural details and preparation conditions of Sr_2MSbO_6 compounds. The data shown are as follows: Highest temperature of treatment; ionic radii in [3]; Δr=$|r_{M^{+3}} - r_{Sb^{5+}}|$; experimentally observed degree of cation ordering; tolerance factor; symmetry of the crystal structure at room temperature and literature reference. PW stands for present work.

Compound	S.T.(K)	I.R(Å)	Δr(Å)	D.O.(%)	t	SG. at 300K	Ref.
Sr_2AlSbO_6	1770	0.535	0.065	98	1.021	$Fm\overline{3}m$	[105]
	1375*			91		$Fm\overline{3}m$	[105]
Sr_2CoSbO_6	1570-1620	0.610	0.010	77	1.002	$R\overline{3}m$	[18]
	1770			80		$R\overline{3}$	[105]
Sr_2CrSbO_6	1420	0.615	0.015	100**	1.000	$P2_1/n$	[96]
	1770			99.4		$I2/m$	[108]
Sr_2GaSbO_6	1570-1870	0.620	0.020	-	0.999	Tetragonal	[83]
	-			100**		$I4/m$	[82]
	1770			96		$I4/m$	PW
Sr_2MnSbO_6	1370	0.645	0.045	58.6	0.993	$I4/m$	[122]
	1670			64		$I4/m$	[123]
	1550			58.4		$I4/m$	[124]
	1770			65		$I4/m$	PW
Sr_2FeSbO_6	1570	0.645	0.045	80	0.993	$P2_1/n$	[80]
	-			80		$P2_1/n$	[81]
	1770			89		$I2/m$	***
Sr_2ScSbO_6	1770	0.745	0.145	100	0.969	$P2_1/n$	***
Sr_2InSbO_6	1470	0.800	0.200	100	0.956	$P2_1/n$	[84]
Sr_2YSbO_6	1545	0.900	0.300	100	0.934	$P2_1/n$	[84]
Sr_2HoSbO_6	1670	0.901	0.301	100	0.934	$P2_1/n$	[85]
Sr_2DySbO_6	1670	0.912	0.312	100	0.931	$P2_1/n$	[85]
Sr_2SmSbO_6	1770	0.958	0.358	100	0.922	$P2_1/n$	[109]
Sr_2LaSbO_6	1770	1.032	0.432	100	0.910	$P2_1/n$	[109]

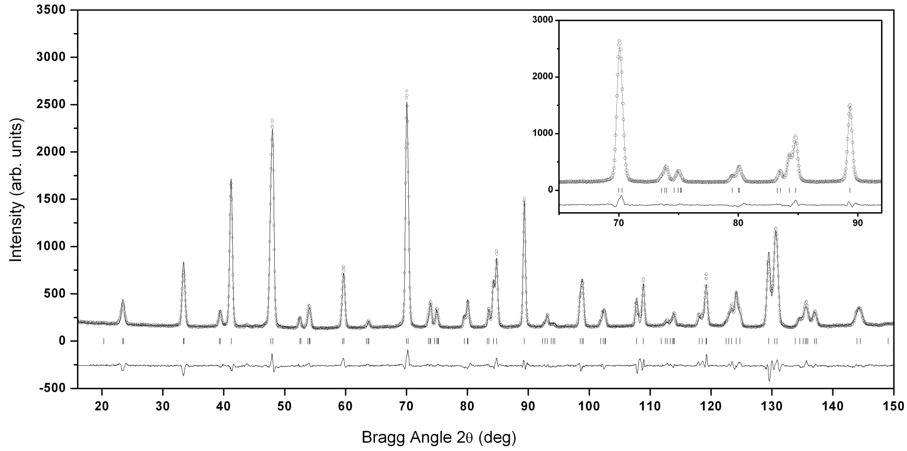

FIGURA 15.1: Observed X-ray patterns (symbols), calculated (line) and difference profiles for the Rietveld refinement of Sr_2GaSbO_6 at room temperature using a structural model with $I4/M$ space group.

The room-temperature neutron powder diffraction data obtained for Sr_2GaSbO_6 are shown in Figure 1. The data were refined in the $I4/m$ space group using symmetry adapted modes, FullAmplimodes, instead of the atomic coordinates. As a starting model for the Rietveld refinement, we used the lowest symmetry space group usually encountered in the case of the ordered double perovskite oxides [105]: the tetragonal structure with space group $I4/m$ suggested in [108] for one antimony oxide, with the following atomic position; Sb at 2a $(0,0,0)$, Sc at 2b $(0,0,1/2)$ and Sr at 4d $(0,1/2,1/4)$, O1 at 4e $(0,0,z)$ and O2 at 8h $(x,y,0)$. The results of refinements are shown in Figure 1, and the structural details of Sr_2GaSbO_6 at room temperature are given in Table 2. The refinement of the level of anti-site defects (Ga at Sb sites, and vice versa) allowed us to evaluate the degree of long-range ordering as 96 %, not total ordering as mentioned in [82].

In the tetragonal ($I4/m$) to the cubic ($Fm\bar{3}m$) phase transition there are three irreps unidimensional modes GM^{1+}, GM^{3+} and GM^{4+}. As we have reported in [108], the GM^{4+} mode is responsible for the symmetry breaking from $Fm\bar{3}m$ (totally symmetric) to room-temperature $I4/m$ tetragonal space group. The final values at room temperature of the amplitudes are GM^{1+}=0.122(2), GM^{3+}=0.075(9) and GM^{4+}=0.423(3). In Figure 2 we show the variation of the amplitude of GM^{4+} mode with the temperature as obtained from the refinements. The amplitudes decreases continuously with the temperature and at about 660K becomes equal to zero, the value at which the cubic symmetry is attained.

The patterns collected at 700, 750 and 800K were well fit by a structural model with the space group $Fm\bar{3}m$. The Rietveld refinement of the neutron powder diffraction pattern data recorded at 700K, using a structural model with $Fm\bar{3}m$ space group is shown in Figure 3. As we can seen in the inset of this figure the tetragonal splitting observed at room temperature has disappeared at this temperature. The structural details at different temperatures are summarized in Table 2.

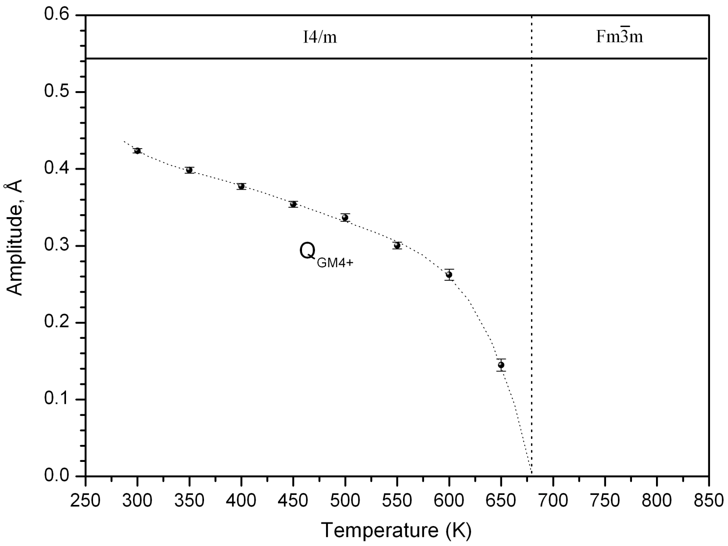

FIGURA 15.2: The temperature evolution of the amplitudes of the GM^{4+} as obtained from refinements of neutron powder diffraction data by Fullprof. The amplitudes decreases continuously with the temperature and at about 660K becomes equal to zero.

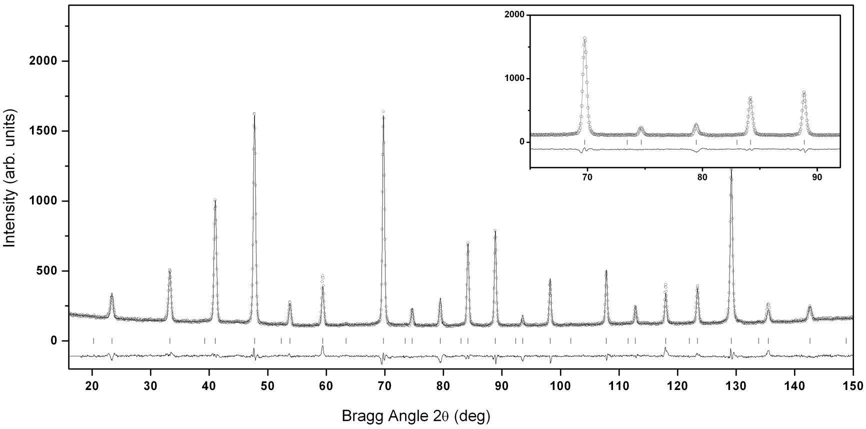

FIGURA 15.3: Observed NPD patterns (symbols), calculated (line) and difference profiles for the Rietveld refinement of Sr_2GaSbO_6 at 700 K, using a structural model with $Fm\bar{3}m$ space group. Inset shows in detail the disappears of the tetragonal splitting observed at room temperature.

TABLA 15.2: Crystal structure data and refinement results for Sr_2GaSbO_6 at different temperatures determined using neutron diffraction data.

Temp.		300K	350K	400K	450K	500K	550K	600K	650K	700K	750K	800K
S.G.		$I4/m$	$I4/m$	$I4/m$	$I4/m$	$I4/m$	$I4/m$	$I4/m$	$I4/m$	$Fm\bar{3}m$	$Fm\bar{3}m$	$Fm\bar{3}m$
Sr		4d(0,1/2,1/4)	(0,1/2,1/4)	(0,1/2,1/4)	(0,1/2,1/4)	(0,1/2,1/4)	(0,1/2,1/4)	(0,1/2,1/4)	(0,1/2,1/4)	8c(1/4,1/4,1/4)	(1/4,1/4,1/4)	(1/4,1/4,1/4)
	B (Å^2)	0.47(2)	0.58(3	0.72(3)	0.82(3)	0.84(3)	0.92(3)	1.27(3)	1.41(3)	1.40(4)	1.49(4)	1.59(4)
Sb1/Ga2		2a(0,0,0)	(0,0,0)	(0,0,0)	(0,0,0)	(0,0,0)	(0,0,0)	(0,0,0)	(0,0,0)	4a(0,0,0)	(0,0,0)	(0,0,0)
	B (Å^2)	0.36(2)	0.35(3)	0.33(3)	0.35(3)	0.34(3)	0.42(3)	0.50(3)	0.54(3)	0.62(3)	0.55(3)	0.50(3)
Occuoancy		0.96/0.04(1)	0.96/0.04(1)	0.96/0.04(1)	0.96/0.04(1)	0.96/0.04(1)	0.96/0.04(1)	0.96/0.04(1)	0.96/0.04(1)	0.96/0.04(1)	0.96/0.04(1)	0.96/0.04(1)
Ga1/Sb2		2b(0,0,1/2)	(0,0,1/2)	(0,0,1/2)	(0,0,1/2)	(0,0,1/2)	(0,0,1/2)	(0,0,1/2)	(0,0,1/2)	4b(1/2,1/2,1/2)	(1/2,1/2,1/2)	(1/2,1/2,1/2)
	B (Å^2)	0.34(2)	0.33(3)	0.31(3)	0.35(3)	0.32(3)	0.40(3)	0.47(3)	0.51(3)	0.57(3)	0.50(3)	0.55(3)
Occuoancy		0.96/0.04(1)	0.96/0.04(1)	0.96/0.04(1)	0.96/0.04(1)	0.96/0.04(1)	0.96/0.04(1)	0.96/0.04(1)	0.96/0.04(1)	0.96/0.04(1)	0.96/0.04(1)	0.96/0.04(1)
O1	x	0	0	0	0	0	0	0	0	0.2492(6)	0.2499(8)	0.2492(6)
	y	0	0	0	0	0	0	0	0	0	0	0
	z	0.2425(9)	0.2424(2)	0.2457(2)	0.2480(3)	0.2494(2)	0.2390(4)	0.2500(2)	0.2495(7)	0	0	0
	B (Å^2)	0.70(2)	0.73(2)	0.88(2)	0.97(2)	1.06(3)	1.12(3)	1.53(3)	1.70(3)	1.92(3)	1.97(3)	2.05(3)
O2	x	0.2768(7)	0.2767(1)	0.2742(2)	0.2735(2)	0.2675(2)	0.2750(2)	0.2705(5)	0.2619(5)			
	y	0.2244(7)	0.2274(1)	0.2275(2)	0.2297(2)	0.2259(2)	0.2380(2)	0.2355(5)	0.2441(5)			
	z	0	0	0	0	0	0	0	0			
	B (Å^2)	0.70(2)	0.73(2)	0.88(2)	0.97(2)	1.06(3)	1.12(3)	1.53(3)	1.70(3)			
Cell	a (Å)	5.5493(1)	5.5541(1)	5.5583(1)	5.5628(1)	5.5674(1)	5.5722(1)	5.5770(1)	5.5824(2)	7.9014(1)	7.9060(2)	7.9105(2)
para.	c (Å)	7.9018(1)	7.9035(1)	7.9039(2)	7.9037(2)	7.9035(2)	7.9024(3)	7.9006(3)	7.9007(5)			
	V (Å^3)	243.33(1)	243.80(1)	244.19(1)	244.58(1)	244.98(1)	245.36(1)	245.73(1)	246.21(1)	493.30(1)	494.16(1)	495.01(1)
Rel.	R_p (%)	3.91	3.61	3.31	3.28	3.39	3.29	3.64	3.49	3.43	3.51	3.29
fact.	R_{wp} (%)	5.34	4.61	4.22	4.18	4.34	4.26	4.88	4.71	4.74	4.81	4.58
	R_{exp} (%)	6.46	7.54	7.59	7.61	7.63	7.66	7.77	7.79	7.80	7.82	7.85
	χ^2	0.68	0.37	0.31	0.30	0.32	0.31	0.39	0.36	0.37	0.38	0.34

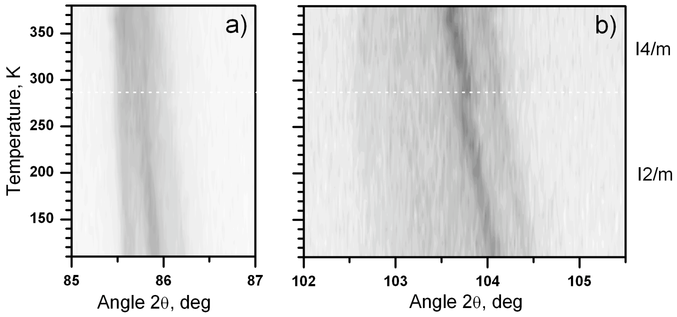

FIGURA 15.4: Thermal evolution of the (a) (444), (b) (800) cubic reflections as obtained from XRPD experiments. The scattered intensity is represented with shades of gray –black corresponds to high intensity, and white, to low intensity. In (a), the $I2/m$ monoclinic triplet [(044),(-404),(404)] converts to a single $I4/m$ tetragonal reflection: (044). In (b), two monoclinic reflections maintain as two tetragonal but with the positions interchanged, and, eventually, the tetragonal splitting disappears and the double reflection evolves to a single cubic one.

To study the low-temperatures phase transition in Sr_2GaSbO_6, we collected XRPD data between 380K and 110K with steep of 10K. The refinement of the data show that this material undergoes a discontinuous phase transition, at about 285K, from the tetragonal $I4/m$ space group to monoclinic one; as the cell centering is maintained (there are no primitive reflections appearing), we have used the $I2/m$ space-group model as the starting point for the refinements, which, on the other hand was one of the expected low-temperature symmetries.

In figure 4 we show a thermal evolution of the scattering intensity for two 2θ intervals corresponding to (a) (444) and (b) ((800) cubic reflections. As seen from this figure, at about 285K produce the splitting of the single reflection observed at room temperature at about 2θ=85.7° (figure 4a). In figure 4b the discontinuous character of this phase transition is easily appreciable by the interchanging of the position of the two reflections (440) and (800) exists in both symmetries $I4/m$ and $I2/m$.

In figure 5 we plot the temperature dependence of the unit cell parameters, in the whole temperature range from 110 to 800K, as obtained from the refinement. The high temperature structure of this compounds is cubic with $Fm\bar{3}m$ space group; below 650K it transforms to tetragonal $I4/m$; and at 280K the compounds transforms to monoclinic $I2/m$.

15.4. Sr$_2$MnSbO$_6$

The room-temperature data obtained for Sr_2MnSbO_6 from NPD(E9) and XRPD measurements, refined simultaneously to determine the structure, are shown in figure 6a and 6b, respectively. The

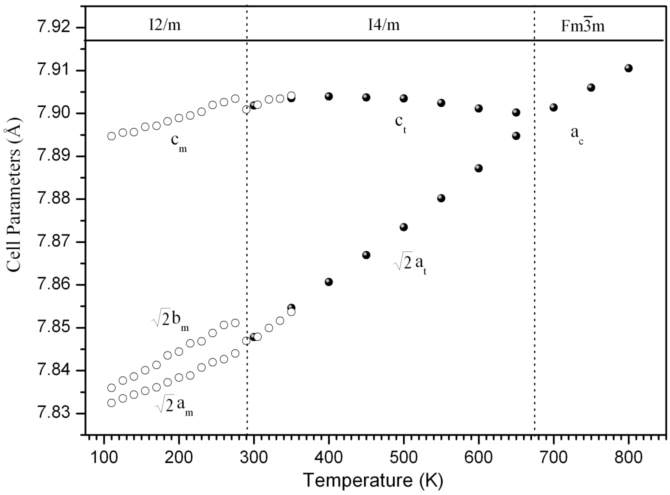

FIGURA 15.5: Variation of the lattice parameters of Sr_2GaSbO_6 with the temperature as obtained from XRPD and NPD measurement; open circles up 350K, were obtained in the low-temperatures XRPD measurement, and solid circles from 300 to 800K obtained with high-temperature NPD measurement. The high temperature structure of this compound is cubic ($Fm\bar{3}m$); below 650K it transforms to tetragonal ($I4/m$); and at 280K the compound transforms to monoclinic ($I2/m$).

refinement of the structure showed that the symmetry of the compound is $I4/m$, in accordance with previous works. The result of the structural refinement are shown in Table 3. The degree of ordering of Mn^{3+} and Sb^{5+} obtained from the refinement is 65 %.

Low-temperature neutron powder-diffraction data from Sr_2MnSbO_6 were collected on the same diffractometer (E9) at 15, 50, 100, 150, 200 and 250K. The results of the low-temperature pattern refinements showed that the room temperature $I4/m$ tetragonal symmetry is stable down to 15K: no significant changes were observed. The structural details at different temperatures are summarized in Table 3.

The study of Sr_2MnSbO_6 at high temperatures showed that the material undergoes a continuous phase transition. At about 700K the unit cell transforms from tetragonal to cubic, see figure 7. Figure 8 show the variation of the unit cell parameters, in the whole temperature range from 15 to 860K,

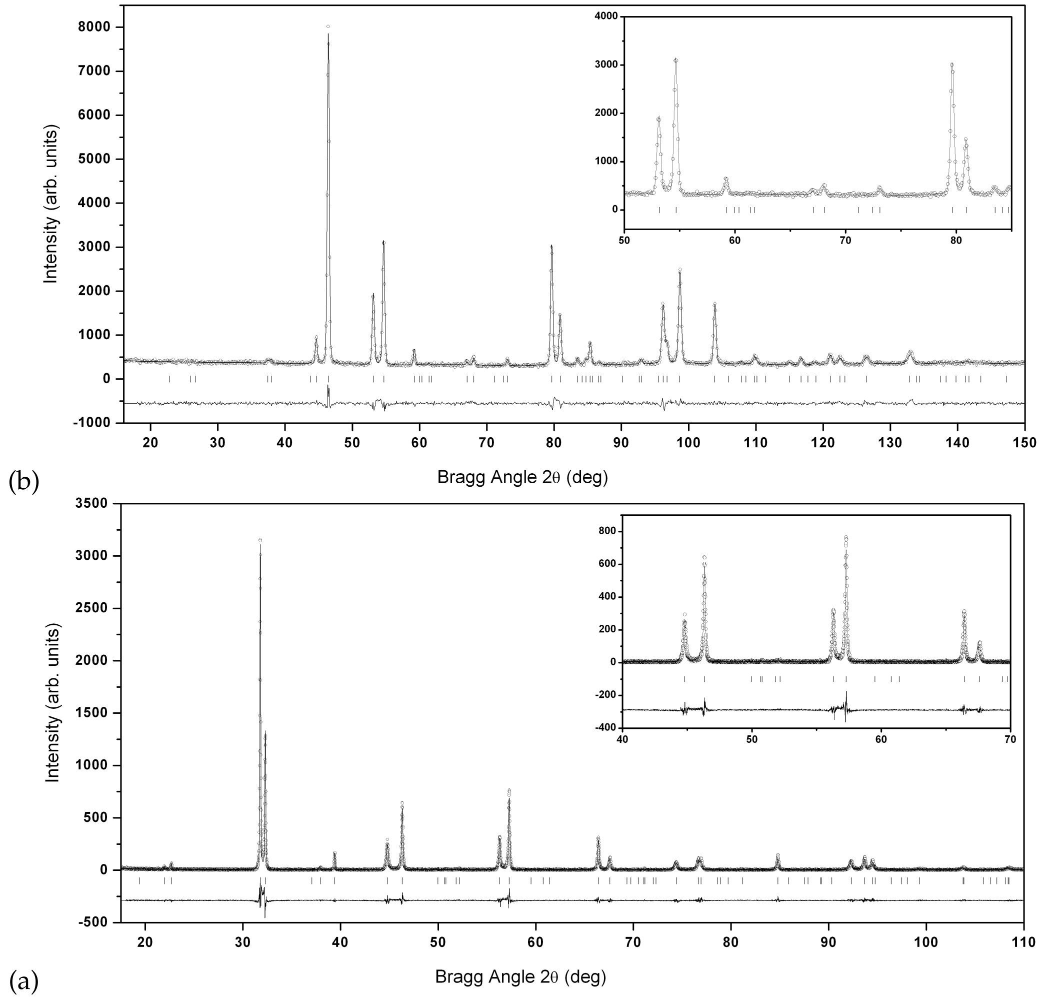

FIGURA 15.6: Experimental (symbols) and calculated (line) neutron profiles (top) and X-ray profiles (bottom) for the Rietveld refinement of Sr_2MnSbO_6 at room temperature using a structural model with $I4/m$ space group.

TABLA 15.3: Crystal structure data and refinement results for Sr_2MnSbO_6 at different temperatures determined using neutron diffraction data.

Temperatures		15K	50K	100K	150K	200K	250K	300K
Space group		$I4/m$	$I4/m$	$I4/m$	$I4/m$	$I4/m$	$I4/m$	$I4/m$
Sr		4d(0,1/2,1/4)	4d(0,1/2,1/4)	4d(0,1/2,1/4)	4d(0,1/2,1/4)	4d(0,1/2,1/4)	4d(0,1/2,1/4)	4d(0,1/2,1/4)
	B (Å^2)	0.66(7)	0.65(6)	0.73(8)	0.84(5)	0.89(7)	0.87(7)	0.96(9)
Sb1/Mn2		2a(0,0,0)	2a(0,0,0)	2a(0,0,0)	2a(0,0,0)	2a(0,0,0)	2a(0,0,0)	2a(0,0,0)
	B (Å^2)	0.37(6)	0.45(7)	0.49(6)	0.47(6)	0.54(6)	0.55(5)	0.54(5)
Occupancy		0.65(1)/0.35(1)	0.65(1)/0.35(1)	0.65(1)/0.35(1)	0.65(1)/0.35(1)	0.65(1)/0.35(1)	0.65(1)/0.35(1)	0.65(1)/0.35(1)
Mn1/Sb2		2b(0,0,1/2)	2b(0,0,1/2)	2b(0,0,1/2)	2b(0,0,1/2)	2b(0,0,1/2)	2b(0,0,1/2)	2b(0,0,1/2)
	B (Å^2)	0.45(6)	0.43(7)	0.43(6)	0.47(6)	0.44(6)	0.43(5)	0.44(5)
Occupancy		0.65(1)/0.35(1)	0.65(1)/0.35(1)	0.65(1)/0.35(1)	0.65(1)/0.35(1)	0.65(1)/0.35(1)	0.65(1)/0.35(1)	0.65(1)/0.35(1)
O1	x	0	0	0	0	0	0	0
	y	0	0	0	0	0	0	0
	z	0.2412(1)	0.2411(1)	0.2416(6)	0.2439(4)	0.2438(4)	0.2456(8)	0.2454(6)
	B (Å^2)	0.71(5)	0.76(5)	0.81(5)	0.85(5)	0.86(5)	0.92(5)	1.07(5)
O2	x	0.2847(4)	0.2862(3)	0.2831(5)	0.2834(7)	0.2750(6)	0.2840(6)	0.2808(6)
	y	0.2160(4)	0.2174(4)	0.2166(5)	0.2169(6)	0.2165(5)	0.2203(7)	0.2196(5)
	z	0	0	0	0	0	0	0
	B (Å^2)	0.71(5)	0.76(5)	0.81(5)	0.85(5)	0.86(5)	0.92(5)	1.07(5)
Cell parameters	a (Å)	5.5340(1)	5.5342(1)	5.5356(1)	5.5383(1)	5.5420(1)	5.5460(1)	5.5512(1)
	c (Å)	8.0677(2)	8.0673(2)	8.0674(2)	8.0673(2)	8.0661(2)	8.0635(2)	8.0602(2)
	V (Å^3)	247.07(1)	247.08(1)	247.21(1)	247.44(1)	247.74(1)	248.02(1)	248.38(1)
Reliability factors	R_p(%)	5.57	5.30	5.29	5.26	4.98	5.28	4.54
	R_{wp}(%)	6.99	6.62	6.66	5.42	6.62	6.68	5.82
	R_{exp}(%)	4.78	4.77	4.76	4.76	5.87	4.76	4.78
	χ^2	2.14	1.93	1.96	1.93	0.85	1.97	1.48

15.5. Cation ordering of Sr_2MSbO_6 (M=Al,Co,Cr,Ga,Mn,Fe,Sc,Sm,La)

The degree of cation ordering over the M and M′ positions of the double perovskite depends mostly on the charge, size and polarization properties of the the M-site cations. If the charge difference between the M and M′ cation is greater than 2, the order is complete: thus, double perovskites of the tungsten family have always shown complete ordering of M^{2+} and W^{6+} cations [41, 43, 74]. However, in the antimony family, the charge difference between M^{3+} and Sb^{5+} cations is smaller, and various degrees of order of the M^{3+} octahedral site cations are observed. As seen in Table 1, a complete ordering is observed for compounds with size difference between the M and Sb cations bigger than 0.145Å, and a partial ordering is observed for size difference smaller than 0.065Å. In [82, 96], the authors refined the structures of Sr_2CrSbO_6 and Sr_2GaSbO_6 assuming complete cation ordering, but the authors could not explicitly state if a partially ordered refinement was tried. In our samples, the degrees of this ordering deduced from the final refinement are 99.4 % and 96 % for Sr_2CrSbO_6 and Sr_2GaSbO_6, respectively.

The degree of cation ordering can be also affected by the synthesis temperature, sintering time and the method of preparation. In [105], we have studied the cation ordering of Sr_2AlSbO_6. It was found that the degree of ordering tends to increase with increasing temperature of synthesis. A similar result was obtained for Sr_2CoSbO_6, Sr_2MnSbO_6 and Sr_2FeSbO_6, higher degrees of order are obtained in our samples due to the higher temperature of preparation 1770K.

Another objective of this work is to study the evolution of the order between the M^{3+} and Sb^{5+} cations over the B and B′ sites, in these compounds, in function of their size difference. For that we have prepared these samples in the same conditions, for eliminate the influence of this factor. In previous works, we have demonstrated, for the first time, the presence of the influence of the thermal conductivity of the elements about the degree of ordering, higher degree of ordering for higher values of thermal conductivity. The thermal conductivities of Al, Co, Cr, Ga, Mn and Fe are 237, 100, 93.7, 40.6, 7.82 and, 80.2 $Wm^{-1}K^{-1}$, respectively [121]. As we can seen in table 1, the Mn and Fe cations have the same ionic radii 0.645Å, but these compounds present two different degree of ordering about 65 % for Sr_2MnSbO_6 and 89 % for Sr_2FeSbO_6. The small degree of ordering obtained for Sr_2MnSbO_6, could be due to the small value of thermal conductivity of Mn($7.82Wm^{-1}K^{-1}$) in comparison to that of the Fe ($80.2Wm^{-1}K^{-1}$). In this case we have the influence of two antagonistic factors, for that we cannot have a continued evolution of the degree of ordering with the difference of size.

15.6. Phase transition of Sr_2MSbO_6 (M=Al,Co,Cr,Ga,Mn,Fe,Sc,Sm,La)

Figure 9 shows the phase transition temperatures as a function of the tolerance factor t. From this figure, we conclude that the phase transition temperatures increase with decreasing of the value of

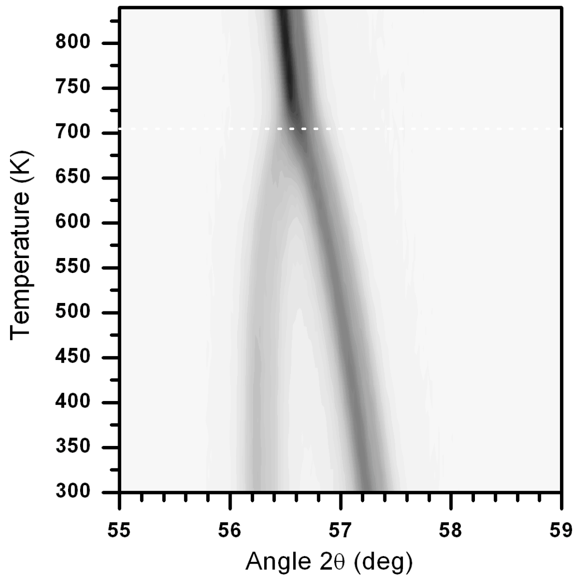

FIGURA 15.7: hermal evolution of the the scattered intensity in the 55-29° 2θ interval, projected and represented with shades of gray. Black corresponds to high intensity, and white to low intensity. The horizontal lines are a guide to the eye, and mark the temperatures at which the tetragonal distortion disappear; thus, indicating the presence of phase transition from tetragonal to cubic at 700K in Sr$_2$MnSbO$_6$. (204 y 312 tetra transform to 422)

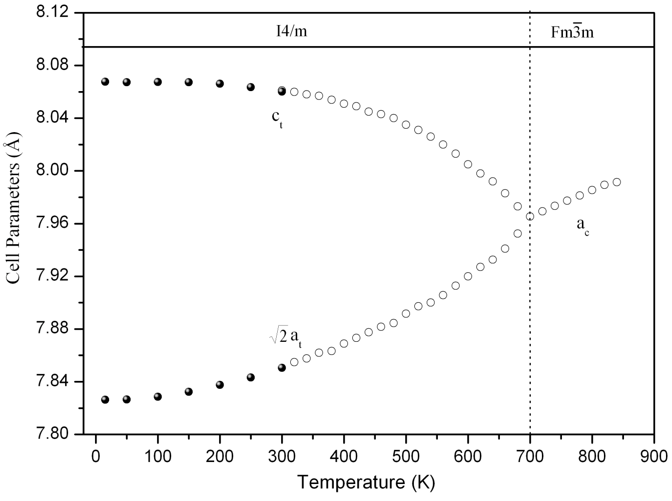

FIGURA 15.8: Variation of the lattice parameters of Sr$_2$MnSbO$_6$ with the temperature as obtained from XRPD and NPD measurement; solid circles up 300K, were obtained in the low-temperatures NPD measurement, and open circles from 300 to 860K obtained with high-temperature XRPD measurement. The high temperature structure of this compound is cubic ($Fm\overline{3}m$); below 700K it transforms to tetragonal ($I4/m$).

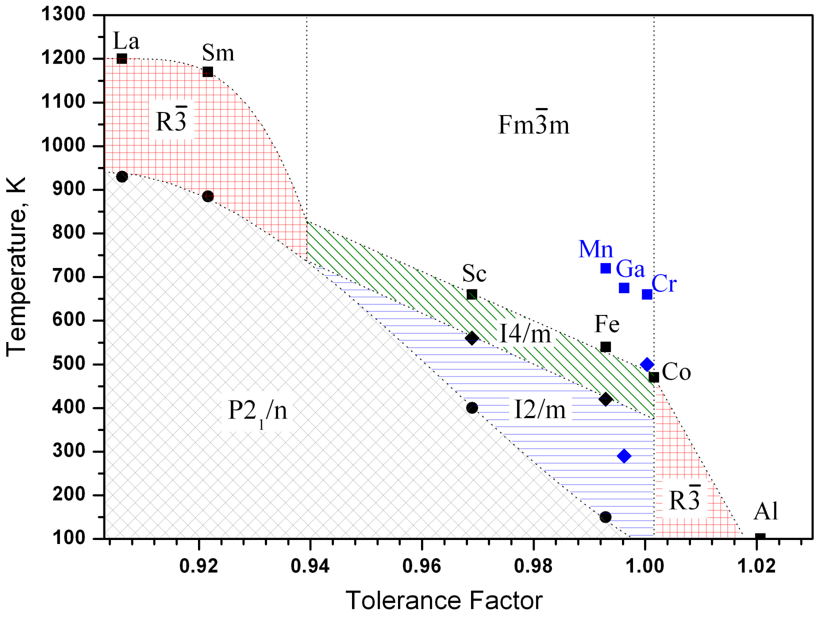

FIGURA 15.9: Phase transition temperatures of Sr_2MSbO_6 compounds, as a function of their tolerance factors.

the tolerance factor t. These results are similar to those observed in Sr_2MWO_6. But, in the tungsten family we have observed only one sequence phase transition $P2_1/n - I4/m - Fm\bar{3}m$. However, the intermediate phase, between the monoclinic and the cubic structures, depends the size difference between the M and Sb cations. In the antimony family there are two sequences phase transition:

(I) For big size difference between the M and Sb cations, we observed a rhombohedral phase, as intermediate phase with the phase transition sequence: $P2_1/n - R\bar{3} - Fm\bar{3}m$.

(II) for small size difference between the M and Sb cations, a tetragonal intermediate phase is obtained as the following phase transition sequence $P2_1/n - I2/m - I4/m - Fm\bar{3}m$.

There is three exceptions for Sr_2CrSbO_6, Sr_2GaSbO_6 and Sr_2MnSbO_6 compounds. These materials present higher temperatures of transition in comparison with the other compounds with similar values of the tolerance factor.

The Sr_2CrSbO_6 and Sr_2MnSbO_6 have a tolerance factors similar to that of Sr_2CoSbO_6 and Sr_2FeSbO_6; respectively. The higher temperatures of transition observed of these compounds due to the Jahn-teller effect presented in this materials.

15.7. Conclusions

Sr_2GaSbO_6 and Sr_2MnSbO_6 with the double perovskite structure have been synthesized by the conventional solid state reaction process. The data presented in this work allow us to confirm that the room temperature structure of both compounds described with the $I4/m$ space group. The crystal structures and phase transitions at low- and high-temperature were determined from Rietveld refinements of X-ray and neutron powder diffraction data.

Parte IV

Conlusiones y Trabajo Futuro

Conclusiones

El experimentador que no sabe lo que está buscando no comprenderá lo que encuentra.

Claude Bernard (1813-1878)

En esta memoria se ha presentado la síntesis, el estudio estructural y las transiciones de fase en las perovskitas dobles de fórmulas generales:

- ◇ Sr_2MWO_6 (M = Mn, Cd),
- ◇ $Sr_2Cd_{1-x}Ca_xWO_6$ $(0 \leq x \leq 1)$,
- ◇ Sr_2MSbO_6 (M = Al, Co, Cr, Ga, Mn, Fe, Sc, Sm, La),
- ◇ Ca_2MSbO_6 (M = Fe, Sc, Sm, La)
- ◇ $Ca_{2-x}Sr_xLnSbO_6$ (Ln = La, Sm) y $(x = 0.5, 1)$

Los trabajos recogidos en la presente memoria permiten extraer las siguientes conclusiones de caracter general, sin hacer referencia a conclusiones específicas relativas a cada material:

(I) Se han sintetizado y estudiado 29 compuestos perovskitas dobles de la familia de wolframio y de la familia de antimonio. De éstos, 22 se sintetizan por primera vez.

(II) Se ha sintetizado por la primera vez un monocristal de la familia de wolframio: Sr_2CaWO_6.

(III) Se han determinado las estructuras a temperatura ambiente y las transiciones de fases a bajas y altas temperaturas de esos compuestos, mediante medidas de difracción de rayos X y de neutrones.

(IV) La utilización de otro método de preparación diferente al cerámico, el método de co-precipitation, permite preparar con un grado óptimo de pureza los compuestos de familia de wolframio.

(V) La familia de wolframio presenta un orden completo entre los cationes M^{2+} y W^{6+} en las posiciones B y B′, debido a la diferencia entre los estado de oxidación de ambos cationes.

(VI) Mediante varias técnicas, EPR, XAS y XRPD, se ha confirmado que a 870 K, en aire, se produce la siguiente transformación irreversible:

$$Sr_2Mn^{2+}W^{6+}O_6 \rightarrow Sr_2Mn^{3+}W^{6+}O_{6+\delta}$$

(VII) En la familia de antimonio, y dependiendo del tamaño del cation M^{3+}, se observa un ordenamiento total o parcial entre aquel y el catión Sb^{5+}:

- ◇ Se obtiene un ordenamiento completo para M^{3+}=Sc,Sm,La;
- ◇ Se obtiene un ordenamiento parcial para M^{3+}=Al,Co,Cr,Ga,Mn,Fe.

(VIII) La utilización de altas temperaturas de preparación permite obtener muestras con un mayor grado del orden entre los sitios B y B′ y entre los sitios A y B, en el caso que estos cationes presenten orden parcial en la familia de antimonio.

(IX) Todo parece indicar que la conductividad térmica de los elementos en las posiciones A también puede afectar (controlar) el grado de ordenamiento final en las posiciones B y B′: las muestras con Fe de la familia de antimonio se ordenan conforme van teniendo más cantidad de Ca. El Ca tiene una conductividad térmica más alta que el Sr, lo que asegura que en el proceso de síntesis la temperatura es más alta y homogénea, lo que facilita el grado de ordenamiento.

(X) Se han refinado las estructuras a temperatura ambiente de los compuestos obtenidos en este trabajo. Los compuestos de la familia de wolframio $Sr_2Mn^{2+}W^{6+}O_6$, $Sr_2Cd_{1-x}Ca_xWO_6$ ($0 \leq x \leq 1$) se cristalizan en el mismo grupo espacial monoclínico $P2_1/n$; mientras que el compuesto $Sr_2Mn^{3+}W^{6+}O_{6+\delta}$ se cristaliza en el grupo espacial tetragonal $I4/m$.

(XI) Los compuestos de la familia de antimonio presentan una gran variedad de los grupos espaciales a temperatura ambiente dependiendo del tamaño del cation M^{3+}:

- ◇ Cúbico $Fm\overline{3}m$ para Sr_2AlSbO_6;
- ◇ Trigonal $R\overline{3}$ para Sr_2CoSbO_6;
- ◇ Tetragonal $I4/m$ para Sr_2GaSbO_6 y Sr_2MnSbO_6;
- ◇ Monoclínico $I2/m$ para Sr_2CrSbO_6 y Sr_2FeSbO_6;
- ◇ Monoclínico $P2_1/n$ para Sr_2MSbO_6 (M=Sc,Sm,La), Ca_2MSbO_6 (M=Fe,Sc,Sm,La) y $Ca_{2-x}Sr_xLnSbO_6$, con (Ln=La,Sm) y $(x = 0.5, 1)$.

(XII) El proceso de refinamiento de las estructuras a diferentes temperaturas se ha hecho de dos maneras diferentes:

- ◇ modo clásico: usando las coordenadas atómicas de los átomos como los grados de libertad de la estructura
- ◇ mediante modos: usando los *modos adaptados a la simetría* como los grados de libertad de la estructura.

(XIII) Los resultados del estudio de las transiciones de fase muestran que:

- ◇ En la familia de wolframio (figura 1):
  - la representación de las temperaturas de las transiciones de fase observadas en los compuestos Sr_2MWO_6 (M=Ni,Co,Mg,Mn,Cd,Ca) en función del factor de tolerancia t, muestra una tendencia general de disminución de las temperaturas de transición según el factor se aproxima a 1
  - muestra también que el rango de la existencia de la fase intermedia (tetragonal) entre la fase de temperatura ambiente y prototipo de alta temperatura es más amplio para valores de t mayores
  - el compuesto Sr_2MgWO_6 es una excepción: no sigue a la tendencia general

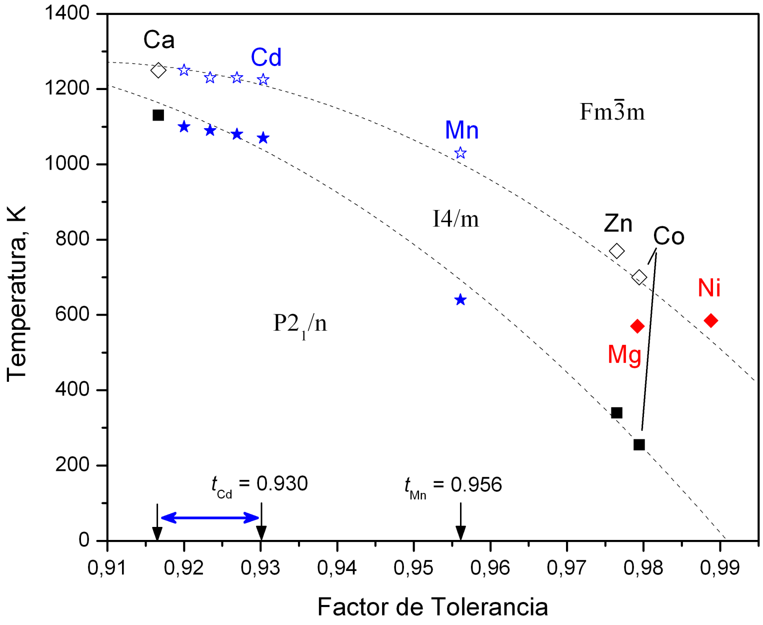

FIGURA 10:

- En la familia del antimonio (figura 2):
  - dependiendo del tamaño relativo de los cationes M^{3+} y Sb^{5+}, los miembros de esta familia presentan dos tipos de transiciones de fase en todo el rango de temperatura:
    - $P2_1/n - I2/m - I4/m - Fm\overline{3}m$
      con una simetría intermedia tetragonal por los cationes M^{3+} de tamaños catiónicos similares al tamaño del Sb^{5+}
    - $P2_1/n - R\overline{3} - Fm\overline{3}m$
      con una simetría intermedia trigonal por cationes M^{3+} que presentan una diferencia grande de sus tamañas catiónicos al respecto del Sb^{5+}
  - la representación de las temperaturas de las transiciones de fase observadas en los compuestos Sr_2MSbO_6 (M=Al,Co,Cr,Ga,Mn,Fe,Sc,Sm,La) en función del factor de tolerancia t, muestra una tendencia general de disminución de las temperaturas de transición según la aumenta el factor de tolerancia
  - en los compuestos Sr_2CrSbO_6, Sr_2GaSbO_6 and Sr_2MnSbO_6, la simetría a temperatura ambiente y las temperaturas de transiciones de fase no siguen a la tendencia observada por los otros compuestos

En los compuestos con Mn y Cr, estas diferencias se deben al efecto *Jahn-Teller* que presentan estos cationes; pero en el caso del Ga no está claro porqué se comporta de manera diferente al resto: puede que el grado del orden entre los Ga y Sb afecte a la simetría de temperatura ambiente y, en consecuencia, a las temperaturas de las transiciones

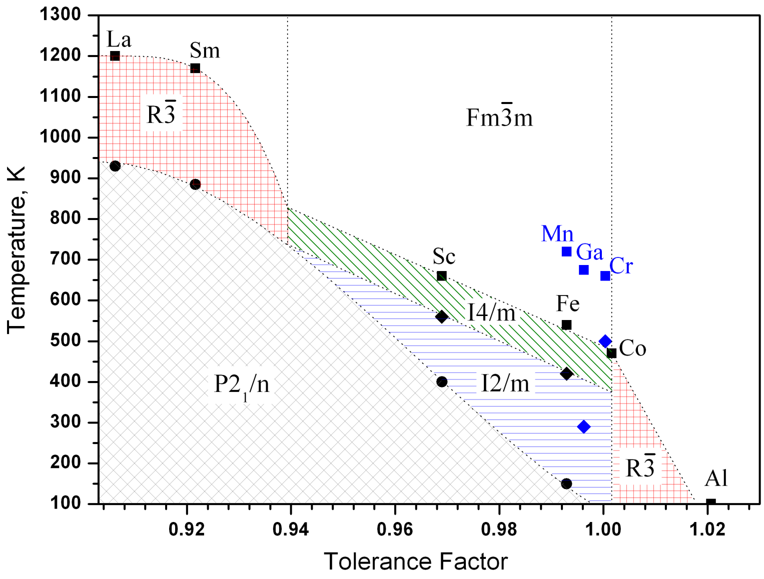

FIGURA 11:

Trabajo futuro: Para completar el estudio realizado en la familia de antimonio, se va a proceder a la síntesis y a la caracterización experimental (estructura a temperatura ambiente y transiciones de fase inducidas por la temperatura) de nuevos materiales pertenecientes a esta familia y con la siguinete fórmula general: Sr_2RSbO_6 (R=tierras raras: Nd, Eu, Dy, Er, Ho, Y, Yb, In).

Estos nuevos materiales permitirán aclarar los siguientes puntos:

- ◇ cuál es la forma real del diagrama de fase (temperaturas de transición – factor de tolerancia) en la zona de bajos factores de tolerancia, entre el Sm y el Sc; esto es, si se mantiene una fase intermedia ($R\bar{3}$) y hasta dónde, o si se mantienen dos fases itermedias ($I2/m$ y $I4/m$) y hasta dónde, en el eje del fator de tolerancia
- ◇ si, lo mismo que ocurre en la familia del wolframio, las transiciones de fase observadas tienen un origen principalmente geométrico, ya que los cationes Er, Ho e Y tienen el mismo radio iónico, y por lo tanto, los correspondientes compuestos presentan el mismo factor de tolerancia, con lo que se espera que presenten la misma secuencia de transiciones de fase y a las mismas temperaturas
- ◇ el grado de ordenamiento de los cationes en las posiciones de tipo B y B′ para los materiales nuevos, y para toda la familia

Además, también se sintetizará el compuesto Sr_2AsAbO_6, ya que su correspondiente factor de tolerancia es 0.991, lo que permitirá aclarar cuál es la forma del diagrama de fase en la zona alta del factor de tolerancia, por encima del correspondiente a compuesto con Co.

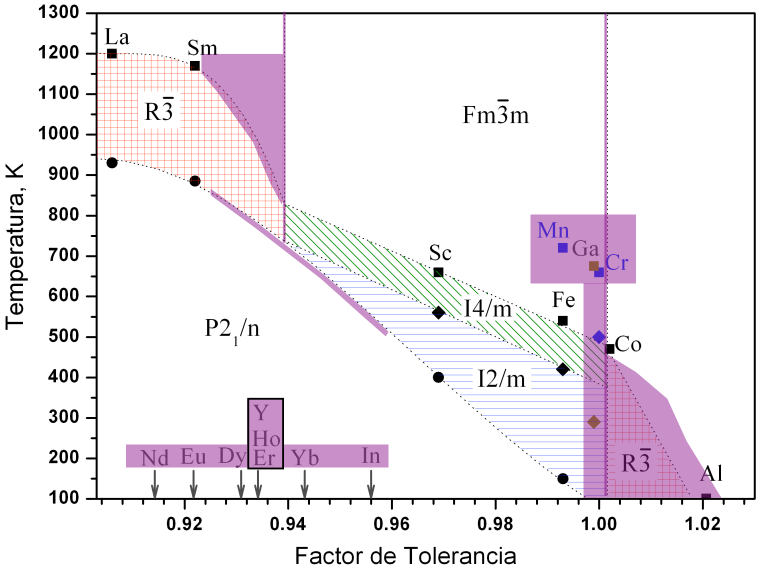

Bibliografía

[1] R.H. Buttner and E.N. Maslen (1992) *Acta Cryst.* B**48** 639-644.

[2] I. Ahmeda, S.G. Erikssonb, E. Ahlberga, C.S. Kneea, M. Karlssonc, A. Maticc, D. Engbergc and L. Börjesson (2007) *Solid State Ionics* **178** 515-520

[3] R.D. Shannon (1976) *Acta Cryst.* A**32** 751

[4] B. Jannot, C.E. Filippini and J. Bouillot 1984 *J. Solid State Chem.* **17** 1329-1337

[5] K-I. Kobayashi, T. Kimura, H. Sawada, K. Terakura and Y. Tokura (1998) *Nature* **395** 677-680

[6] M. DeMarco, H.A. Blackstead, J.D. Dow, M.K. Wu, D.Y. Chen, E.Z. Chien, H. Haka, S. Toorongian and J. Fridmann (2000) *Phys. Rev.* B **62** 14301-14303

[7] G. Baldinozzi, Ph. Sciau and P.-A. Buffat (1993) *Solid State Commun.* **86** 541

[8] I. Barbur and I. Ardelean (2001) *Phase Transitions* **74** 367-373

[9] I.N. Flerov, M.V. Gorev, K.S. Aleksandrov, A. Tressaud, J. Grannec and M. Couzi (1998) *Mater. Sci. Eng.* R **24** 81

[10] Q. Wang, B. Gu and X. Zhang 1990 *Phys. Stat. Sol.*(b) **161** 537-542

[11] M.T. Anderson and K.R. Poeppelmeier (1991) *Chem. Mater.* **3** 476-482

[12] J.A. Alonso, J.L. García-Muñoz, M.T. Fernández-Díaz, M.A.G. Aranda, M.J. Martínez-Lope and M.T. Casais (1999) *Phys. Rev. Lett.* **82** 3871-3874

[13] D.E. Cox and A.W. Sleight (1979) *Acta Crystallogr.* B**35** 1-10

[14] M.T. Anderson, K.B. Greenwood, G.A. Taylor and K.R. Poeppelmeier (1993) *Progr. Sol. State Chem.* **22** 197-233

[15] M. Gateshki, PhD, University of Basque Country (2003)

[16] Y. Todate (1999) *J. Phys. Chem. Solids* B **60** 1173

[17] Y. Tomioka, T. Okuda, Y. Okimoto, R. Kumai and K-I. Kobayashi (2000) *Phys. Rev.* B **61** 422

[18] V. Primo-Martín and M. Jansen (2001) *J. Solid State Chem.* **157** 76-85

[19] O. Chmaissem, R. Kruk, B. Dabrowski, D.E. Brown, X. Xiong, S. Kolesnik, J.D. Jorgensen and C.W. Kimball (2000) *Phys. Rev.* **B62** 14197

[20] J.P. Zhou, R. Dass, H. Q. Yin, J.-S. Zhou, L. Rabenberg and J.B. Goodenough (2000) *J. Appl. Phys.* **87** 5037

[21] C. Ritter, M.R. Ibarra, L. Morellon, J. Blasco, J. García and J. M. De Teresa (2000) *J. Phys.: Cond. Matter* **12** 8295

[22] Y. Moritomo, Sh. Xu, A. Machida, T. Akimoto, E. Nishibori, M. Takata, M. Sakata and K. Ohoyama (2000) *J. Phys. Soc. Japan* **69** 1723

[23] Y. Teraoka, M.-D. Wei and S. Kagawa (1998) *J. Mater. Chem.* **8** 2323-2325

[24] A.M. Glazer (1972) *Acta Cryst.* B**28** 3384-3392

[25] A.M. Glazer (1975) *Acta Cryst.* A**31** 756-762

[26] K.S. Aleksandrov and S.V. Misyul (1980) *Sov. Phys. Crystallogr.* **26** 612-618

[27] P.M. Woodward (1997) *Acta Cryst.* B**53** 32

[28] C.J. Howard, H.T. Stokes (1998) *Acta Cryst.* B**54** 782

[29] D. Reinen and H. Weitzel (1976) *Z. Anorg. Allg. Chem.* **424** 31

[30] M.C. Foster, R.M. Nielson and S.C. Abrahams (1997) *J. Appl. Phys.* **82** 3076

[31] D. Reinen, H.O. Wellern and J. Wegwerth (1997) *Z. Phys.* B**104** 595-600

[32] B.N. Figgis and M.A. Hitchman (2000) *Ligand Field Theory and Its Applications* (John Wiley & Sons) p 149

[33] P. Shiv Halasyamani, K.R. Poeppelmeier (1998) *Chem. Mater.* **10** 2753

[34] K.S. Aleksandrov and J. Bartolomé (2001) *Phase Transitions* **74** 255-335

[35] H. T. Stokes, E. H. Kisi, D. M. Hatch and C. J. Howard (2002) *Acta Cryst.* B**58** 934-938

[36] S.-T. Hong, J.-H. Park and J.-H. Choy (1995) *J. Phys. Chem.* **99** 6176

[37] J.-H. Choy, S.-T. Hong, K.-S. Choi (1996) *J. Chem. Soc., Faraday Trans.* **92** 1051

[38] C.J. Howard, B.J. Kennedy and P.M. Woodward (2003) *Acta Cryst.* B**59** 463-471

[39] J. Ihringer and S.C. Abrahams 1984 *Phys. Rev.* B**30** 6540-6548

[40] J. Rodríguez-Carvajal 1993 *Physica* **192** 55-69

[41] M. Gateshki, J.M. Igartua and E. Hernández-Bocanegra (2003) *J. Phys.: Cond. Matter* **15** 6199-6217

[42] M. Gateshki and J.M. Igartua (2003) *J. Phys.: Cond. Matter* **15** 6749-6757

[43] M. Gateshki and J.M. Igartua (2004) *J. Phys.: Cond. Matter* **16** 6639-6649

[44] B. Manoun, J. M. Igartua, M. Gateshki and S. K. Saxena (2004) *J. Phys.: Cond. Matter* **16** 8367-8376

[45] Ravel B and Newville M 2005 *J. Synchrotron Rad.* **12** 537

[46] A. Muñoz, J.A. Alonso, M.T. Casais, M.J. Martínez-López and M.T. Fernádez-Díaz (2002) *J. Phys.: Cond. Matter* **14** 8817-8830

[47] A. Dhahri, J. Dhahri and M. Oumezzine (2009) *Materials Letters* **63** 121-123

[48] L.O. Martin, J.P. Chapman, E. Hernández-Bocanegra, M. Insausti, M.I. Arriortua and T. Rojo (2004) *J. Phys.: Cond. Matter* **16** 3879-3888

[49] L.O. Martin, J.P. Chapman, G. Cuello, J. González-Calbet, M.I. Arriortua and T. Rojo (2004) *Z. Anorg. Allg. Chem.* **631** 2127-2130

[50] T.K. Mandal and J. Gopalakrishnan (2005) *Chem. Mater.* **17**, 2310-2316

[51] M.W. Lufaso and P.M. Woodward (2001) *Acta Cryst.* **B57** 725-738

[52] Z. Fu (1991) *Science in China* A **34** 455

[53] P. Shiv Halasyamani and K.R. Poeppelmeier (1998) *Chem. Mater.* **10** 2753

[54] Q. Zhou, B.J. Kennedy, C.J. Howard, M.M. Elcombe and A.J. Studer (2005) *Chem. Mater.* **17** 5357-5365

[55] Q. Zhou, B.J. Kennedy and M.M. Elcombe (2006) *Physica B: Condensed Matter.* **385-386** 190-192

[56] M.C.L. Cheah, B.J. Kennedy, R.L. Withers, M.Yonemura and T. Kamiyama (2006) *J. Solid State Chem.* **179** 2487-2494

[57] Q. Zhou, B.J. Kennedy, K.S. Wallwork, M.M. Elcombe, Y. Lee and T. Vogt (2005) *J. Solid State Chem.* **178** 2282-2291

[58] P.J. Saines and B.J. Kennedy (2008) *J. Solid State Chem.* **181** 298-305

[59] L.H. Brixner (1960) *J. Phys. Chem* **64** 165

[60] A.K. Azad, S. Ivanov, S.G. Eriksson, H. Rundlöf, J. Eriksen, R. Mathieu and P. Svedlindh (2001) *J. Magnetism and Magnetic Materials* **237** 124-134

[61] A. Muñoz, J.A. Alonso, M.T. Casais, M.J. Martínez-López and M.T. Fernádez-Díaz (2002) *J. Phys.: Cond. Matter* **14** 8817-8830

[62] M.W. Lufaso, P.W. Barnes and P.M. Woodward (2006) *Acta Cryst.* **B62** 397-410.

[63] J.J. Blanco, M. Insausti, L. Lezama, J.P. Chapman, I. Gil De Muro and T. Rojo (2004) *J. Solid State Chem.* **177** 2749-2755

[64] M.C. Viola, M.J. Martínez-Lope, J.A. Alonso, J.L. Martínez, J.M. De Paoli, S. Pagola, J.C. Pedregosa, M.T. Fernández-Díaz and R.E. Carbonio (2003) *Chem. Mater.* **15** 1655-1663

[65] R.H. Mitchell (2002) *Perovskites. Modern and Ancient* Almaz Press

[66] V.M. Goldschmidt (1926) *Str. Nor. Vidensk-Akad. Oslo* **1** 1

[67] N.E. Brese and M. O'Keeffe (1991) *Acta Cryst.* B**47** 192-197

[68] Accumulated Table of Bond Valence Parameters Version 2.2 Prepared by I.D. Brown, McMaster University, Hamilton, Ontario, Canada. Available at www.ccp14.ac.uk/ccp/web-mirrors/i_d_brown.

[69] I. N. Flerov, M. V. Gorev and V N Voronov (1996) *Phys. Solid State* **38** 396-401

[70] S.J. Patwe, S.N. Achary, M.D. Mathews and A.K. Tyagi (2005) *J. Alloys and Compounds* **390** 396-401

[71] D.D. Khalyavin, A.M.R. Senos and P.Q. Mantas (2004) *Powder Diffraction* **19** 280-283

[72] S.N. Achary, K.R. Chakraborty, S.J. Patwe, A.B. Shinde, P.S.R. Krishnaa and A.K. Tyagi (2006) *Mat. Res. Bull.* **41** 674-682

[73] A. Faik, J.M. Igartua, G.J. Cuello, F. Jiménez-Villacorta, G.R.Castro and L. Lezama (2009) *Journal of Molecular Structure* DOI: 10.1016/j.molstruc.2009.06.008

[74] M. Gateshki, J.M. Igartua and A. Faik (2007) *J. Solid State Chem.* **180** 2248-2255

[75] Faik A, Igartua J M and Pizarro J L 2009 *Journal of Molecular Structure* **920** 196-201

[76] Azad A K and Eriksson S G 2003 *Solid State Commun.* **126** 503-508

[77] Karppinen M, Yamauchi H, Yasukawa Y, Lindén J, Chan T S, Liu R S and Chen J M 2003 *Chem. Mater.* **15** 4118

[78] Bardelli F, Meneghini C, Mobilio S, Ray S and Sarma D D 2005 *Phys. Scripta* **115** 475

[79] Lin Q, Greenblatt M and Croft M 2005 *J. Sol. State Chem.* **178** 1356

[80] E.J. Cussen, J.F. Vente, P.D. Battle and T.C. Gibb (1997) *J. Mater. Chem.* **7** 459-463

[81] N. Kashima, K. Inoue, T. Wada and Y. Yamaguchi (2002) *Appl. Phys. A* **74** S805-S807

[82] M.W. Lufaso, R.B. Macquart, Y. Lee, T. Vogt and H.C. Loye (2006) *J. Phys. Condens. Matter* **18** 8761-8780

[83] A. Tauber, S.C. Tidow, R.D. Finnegan and W.D. Wilber (1996) *Physica C* **256** 340-344

[84] W.T. Fu and D.J.W. Ijdo (2005) *Solid State Communications* **134** 177-181

[85] H. Karunadasa, Q. Huang, B.G. Ueland, P. Schiffer and R.J. Cava (2003) *PNAS* **V100** 8097-8102

[86] M. Lufaso, P. M. Woodward and J. Goldberger (2004) *J. Solid State Chem.* **177** 1651-1659

[87] G. Blasse (1965) *J. Inor. Nucl. Chem.* **27** 993-1003

[88] G. Blasse (1965) *J. Appl. Phys.* **36** 879

[89] Paris W. Barnes (2003) PhD. Dissertation, The Ohio State University
"Exploring Structural Changes And Distortions In Quaternary Perovskites And Defect Pyrochlores Using Powder Diffraction Techniques"
(http://www.ohiolink.edu/etd/view.cgi?osu1064346592)

[90] W.T. Fu, R. de Gelder and R.A.G. Graaff (1997) *Materials Research Bulletin* **32** 657-662

[91] W.T. Fu (2000) *Solid State Communications* **116** 461-464

[92] P.M. Woodward, R.D. Hoffmann and A.W. Sleight (1994) *J. Mater. Res.* **9** 2118-2127

[93] A. Faik, M. Gateshki, J.M. Igartua, J.L. Pizarro, A. Grzechnik, M. Insausti, R. Kaindl (2008) *J. Sol. State Chem.* **V181** 1759-1766

[94] A. Sleight, R. Ward (1964) *Inorg. Chem* **3** 292

[95] P.W. Woodward (1997) *Ph.D. Dissertation, Oregon State University, Corvallis, OR*

[96] M. Retuerto, M. García-Hernández, M.J. Martínez-Lope, M.T. Fernández-Díaz, J.P. Attfield and J.A. Alonso (2007) *J. Mater. Chem.* **17** 3555-3561

[97] G.Y. Liu, G.H. Rao, X.M. Feng, H.F. Yang, Z.W. Ouyang, W.F. Liu, J.K. Liang (2003) *J. Alloys Compd.* **V353** 42-47

[98] R.S. Liu, T.S. Chan, S.F. Hu, J.G. Lin, C.Y. Huang (2002) *J. Magn. Magn. Mater.* **239** 164-166

[99] A. Pena, J. Gutiérrez, L.M. Rodríguez-Martínez, J.M. Barandiarán, T. Hernández, T. Rojo (2003) *J. Magn. Magn. Mater.* **254-255** 586-588

[100] E. Kroumova, M.I. Aroyo, J.M. Pérez-Mato, S. Ivantchev, J.M. Igartua and H. Wondratschek (2001) *J. Appl. Cryst.* **34** 783-784

[101] J.M. Igartua, M.I. Aroyo and J.M Pérez-Mato (1996) *Phys. Rev. B* **54** 12744-12752

[102] E. Kroumova, M.I. Aroyo, J.M. Pérez-Mato and R. Hundt (2001) *Acta Cryst. B* **57** 599-601

[103] M.I. Aroyo, J.M. Pérez-Mato, C. Capillas, E. Kroumova, S. Ivantchev, G. Madariaga, A. Kirov and H. Wondratschek (2006) *Z. Kristallogr.* **221 (1)** 15-27

[104] A. Tressaud, S. Khaïroun, J. P. Chaminade and M.Couzi (1986) *Phys. Status Solid* **98** 98 417

[105] A. Faik, J.M. Igartua, M. Gateshki and G.J. Cuello (2009) *J. Solid State Chem.* **181** 1759-1766

[106] Brown and Altermatt (1985) *Acta Cryst.* **B41** 244-247

[107] P.J. Saines, J.R. Spencer, B.J. Kennedy, Y. Kubota, C. Minakata, H. Hano, K. Kato and M. Takata (2007) *J. Solid State Chem.* **180** 3001-3007

[108] A. Faik, J.M. Igartua, M. Gateshki and G.J. Cuello (2009) *J. Solid State Chem.* **182** 1717-1725

[109] A. Faik, E. Iturbe-Zabalo, I. Urcelay and J.M. Igartua (2009) *J. Solid State Chem.* doi:10.1016/j.jssc.2009.07.021

[110] A. Faik, J.M. Igartua and G.J. Cuello (2009) *Submited to J. of Molecular Structure.*

[111] A. Faik, J. M. Igartua, D. Orobengoa, J. M. Perez-Mato and M. I. Aroyo (2009) *Submited to J. Solid State Chem.*

[112] M. Retuerto, J.A. Alonso, M. Garcia-Hernandez and M.J. Martinez-Lope (2006) *Solid State Communications* **139** 19-22

[113] Chiho Sakai, Yoshihiro Doi and Yukio Hinatsu (2006) *Journal of Alloys and Compounds* **408-418** 608-612

[114] V.V. Wittmann, G. Rauser and S. Kemmier-Sack (1981) *Z. Anorg. Allg. Chem.* **482** 143

[115] D. Orobengoa, C. Capillas, M.I. Aroyo and J.M. Perez-Mato (2009) *J. Appl. Cryst.* **42** to be published

[116] D. Orobengoa, J. Rodríguez-Carvajal, J.M. Perez-Mato, M.I. Aroyo, A. Faik and J.M. Igartua (2009) *Acta Cryst.* **A65** s328

[117] J.M. Perez-Mato, J. Rodríguez-Carvajal, A. Faik and J.M. Igartua (2009) to be published

[118] K.S. Aleksandrov, S.V. Melnikonova and S.V. Misjul (1987) *Acta Cryst.* **104** 104-545

[119] C. Capillas, E. Kroumova, M.I. Aroyo, J.M. Perez-Mato, H.T. Stokes and D.M. Hatch (2003) *J. Appl. Cryst.* **36** 953-954

[120] P.D. Battle, T.C. Gibb, A.J. Herod and J.P. Hodges (1995) *J. Mater. Chem.* **5** 75-78

[121] EniG. Periodic Table of the Elements 2008, KTF-Split. (www.periodni.com)

[122] M. Cheah, P.J. Saines, B.J. Kennedy (2006) *J. Solid State Chem.* **179** 1775-1781

[123] T.K. Mandal, V.V. Poltavets, M. Croft, M. Greenblatt (2008) *J. Solid State Chem.* **181** 2325-2331

[124] S.A. Ivanov, P. Nordblad, R. Tellgren, A. Hewat (2009) *Mater. Res. Bull.* **44** 822-830

Publicaciones

(I) M. Gateshki, J.M. Igartua and **A. Faik**
"*Crystal structures and phases transitions of* Sr_2CdWO_6"
J. of Solid State Chemistry, 180 (2007) 2248-2255.

(II) **A. Faik**, M. Gateshki, J.M. Igartua, J L Pizarro, A. Grzechnik, R. Kaindl and M. Insausti,
"*Crystal structures and cation ordering of* Sr_2CoSbO_6 *and* Sr_2AlSbO_6"
J. of Solid State Chemistry, 181 (2008) 1759- 1766.

(III) **A. Faik**, J.M. Igartua and J.L. Pizarro
"*Synthesis, Structures and Temperature-induced Phase Transitions of the* $Sr_2Cd_{1-x}Ca_xWO_6$ *(*$0 \leq x \leq 1$*) Double Perovskite Tungsten Oxides*"
J. of Molecular Structure, 920 (2009) 196-201.

(IV) **A. Faik**, J.M. Igartua, M. Gateshki, and G.J. Cuello
"*Crystal Structures and phase transitions of* Sr_2CrSbO_6"
J. of Solid State Chemistry, 182 (2009) 1717-1725.

(V) **A. Faik**, J.M. Igartua, G.J. Cuello, F. Jiménez-Villacorta, G.R. Castro and L. Lezama
"*Crystal structures and temperature-induced phase transitions of* $Sr_2Mn^{2+}W^{6+}O_6$*, and of its transformation to* $Sr_2Mn^{3+}W^{6+}O_{6+\delta}$"
J. of Molecular Structure, 933 (2009) 53-62.

(VI) **A. Faik**, E. Iturbe-Zabalo, I. Urcelay and J. M. Igartua
"*Crystal structures and high-temperature phase transitions of the new ordered double perovskites* Sr_2SmSbO_6 *and* Sr_2LaSbO_6"
J. of Solid State Chemistry, (2009) In press, DOI: 10.1016/j.jssc.2009.07.021.

(VII) D. Orobengoa, J. Rodríguez-Carvajal, J.M. Perez-Mato, M.I. Aroyo, **A. Faik** and J.M. Igartua
"*Solving Crystal Structures Using Symmetry-Mode Collective Coordinates*"
Acta Cryst., A65 (2009) s328

(VIII) **A. Faik**, J. M. Igartua and G. J. Cuello
"*A study of the crystal structures and the phase transitions of* Sr_2FeSbO_6*,* $SrCaFeSbO_6$ *and* Ca_2FeSbO_6

double perovskite oxides"
Submitted to J. of Molecular Structure.

(IX) G. Madariaga, **A. Faik**, T. Brezcewski and J. M. Igartua
"Crystal growth and twinned crystal structure of Sr_2CaWO_6*"*
Submitted to Acta Crystallographica B

(X) **A. Faik**, J. M. Igartua, D. Orobengoa, J. M. Perez-Mato and M.I. Aroyo
"A study of the crystal structures and the phase transitions of the ordered double perovskites Sr_2ScSbO_6 *and* Ca_2ScSbO_6*"*
In preparation.

(XI) **A. Faik**, E. Iturbe-Zabalo, I. Urcelay and J. M. Igartua
"Cationic ordering and role of the A-site cation on the structure of the new double perovskites $Ca_{2-x}Sr_xLaSbO_6$ *and* $Ca_{2-x}Sr_xSmSbO_6$ $(x = 0, 0.5, 1)$*"*
In preparation.

Resumen

Los óxidos mixtos con estructura tipo perovskita doble $A_2BB'O_6$ presentan gran interés desde el punto de vista científico y tecnológico debido a la gran variedad de propiedades que poseen: superconductoras, catalíticas, magnéticas y magnetorresistentes, por ejemplo. La temperatura es un variable que permite modificar la simetría de la estructura cristalina y, consecuentemente, las propiedades físicas del material.

El trabajo describe la síntesis, caracterización estructural y de las transiciones de fase en nuevos materiales de dos familias de perovskitas dobles: la familia de wolframio ($Sr_2M^{2+}W^{6+}O_6$) y la familia de antimonio ($A_2M^{3+}Sb^{5+}O_6$). Se ha llevado a cabo la síntesis de 29 compuestos, 22 de ellos sintetizados por primera vez. Los compuestos se han caracterizado mediante técnicas de difracción de rayos X y de neutrones, determinando su estructura cristalina a temperatura ambiente, así como las posibles transiciones de fase a bajas y altas temperaturas, y en algunos casos, también las estructuras de altas y bajas temperaturas.

Los materiales de la familia de wolframio estudiados en este trabajo presentan un ordenamiento total entre los cationes M^{2+} y W^{6+} en los sitios B y B′ de la perovskita doble ($A_2BB'O_6$); y presentan, además, una única secuencia de transiciones de fase a altas temperaturas:

$$P2_1/n \rightarrow I4/m \rightarrow Fm\bar{3}m.$$

Las temperaturas de las transiciones de fase observadas en estos compuestos en función del factor de tolerancia (t), muestran una tendencia general de disminución según t se aproxima a 1. En esta familia, se observa, también, que el rango de existencia de la fase tetragonal intermedia es más amplio para valores de t mayores.

Con respecto de la familia de antimonio, el ordenamiento catiónico en los sitios A y B, de una parte, y en los sitios B y B′ de otra, depende del tamaño de los cationes. Los compuestos de esta familia presentan una gran variedad de grupos espaciales a temperatura ambiente: $P2_1/n$, $I2/m$, $I4/m$, $R\bar{3}$ y $Fm\bar{3}m$. Además, dependiendo de la diferencia entre los tamaños de los cationes M^{3+} y Sb^{5+}, los compuestos presentan dos secuencias de transiciones de fase en todo el rango de temperatura:

$$P2_1/n \rightarrow I2/m \rightarrow I4/m \rightarrow Fm\bar{3}m,$$

la misma que en la familia del wolframio pero con una simetría intermedia monoclínica $I2/m$ (compuestos con cationes M^{3+} de tamaños similares al del Sb^{5+}); y

$$P2_1/n \rightarrow R\bar{3} \rightarrow Fm\bar{3}m,$$

con una simetría intermedia trigonal en vez de tetragonal, como en la familia del wolframio (compuestos con cationes M^{3+} de tamaños mayores que el del Sb^{5+}). En esta familia, las temperaturas de las transiciones de fase disminuyen conforme aumenta t.